Reaction Kinetics of Biogenic Solid Fuels under Process Conditions of Technical Entrained-Flow Gasifiers

zur Erlangung des akademischen Grades eines
DOKTORS DER INGENIEURWISSENSCHAFTEN (Dr.-Ing.)

von der KIT-Fakultät für Chemieingenieurwesen und Verfahrenstechnik des
Karlsruher Instituts für Technologie (KIT)
genehmigte

DISSERTATION

von
Dipl.-Ing. Christoph Schneider
aus Auschwitz in Polen

Tag der mündlichen Prüfung: 01.10.2021

Erstgutachter: Prof. Dr.-Ing. Thomas Kolb

Zweitgutachter: Prof. Dr. techn. Hermann Hofbauer

Dedication

Meinen Eltern.

Acknowledgements

The present doctoral thesis was created during my activity as a research assistant at Engler-Bunte-Institute Fuel Technology (EBI ceb) at Karlsruhe Institute of Technology (KIT) with the financial support by the Helmholtz Association of German Research Centers (HGF), within the research program Energy Efficiency, Materials and Resources (EMR), and the Deutsche Forschungsgemeinschaft (DFG, 121384/22-1). The work contributes to the Helmholtz Virtual Institute for Gasification Technology (HVI GasTech, VH-VI-429).

I would like to gratefully acknowledge my supervisor Prof. Dr.-Ing. Thomas Kolb for the confidence he displayed in me and many fruitful discussions that helped me to establish critical thinking and to conduct research in a professional manner. Furthermore, I would like to thank Prof. Dr. techn. Hermann Hofbauer for his kind interest in this thesis and for agreeing to act as a second examiner.

I want to address special thanks to all my colleagues and students at EBI ceb for the support as well as many helpful discussions.

Finally, I would like to express my deepest gratitude to my parents, Joachim and Dorothee, and my wife Tingting for enabling my doctoral thesis while always being supportive in rough and exhausting times. Thank you very much!

Abstract

This doctoral thesis is a cumulative dissertation consisting of five research articles. These articles are concerned with entrained-flow gasification which is an enabling technology for production of chemical energy carriers from biogenic and anthropogenic waste streams in the context of a circular economy. The present work aims to determine gasification kinetics at process conditions relevant for entrained-flow gasifiers, i.e. elevated pressure, high temperature and high heating rates. The gasification experiments are conducted using biomass chars that have been produced under process conditions of technical entrained-flow gasifiers. In the flame zone of the entrained-flow gasifier, the solid fuel undergoes devolatilization at high temperatures, high heating rates and short residence times. The pyrolysis conditions during this step determine char properties and reactivity for the subsequent heterogeneous gasification reaction. In order to design gasifiers that achieve complete char conversion, kinetic data for the gasification reactions with CO_2 and H_2O at high pressure is required.

First, the evolution of morphology, concentration of catalytically active ash components and number of active sites during heterogeneous gasification of a char particle with CO_2 are analyzed. Furthermore, the influence of these parameters on char reactivity and the course of conversion rate as a function of carbon conversion is investigated. As a result, catalytically active ash components that are usually found in biomass (e.g. calcium, potassium) affect char reactivity significantly and determine the course of the conversion rate. Their influence on the gasification behavior with CO_2 in the microkinetic regime may be regarded as superior as compared to char morphology.

Second, the influence of pyrolysis conditions on char properties, i.e. micropore surface area, graphitization of the carbon matrix and ash dispersion, during high-temperature pyrolysis in a drop-tube reactor is investigated. Moreover, the effect of calcium dispersion and graphitization degree on the gasification reactivity with CO_2 is discussed. Results show that thermal deactivation can be observed for the chars produced up to 1400 °C due to increasing graphitization degree and decreasing calcium dispersion. For the char produced at 1600 °C (P1600), however, char reactivity increases drastically despite showing the highest graphitization degree and the lowest micropore surface area. This phenomenon is caused by the formation of a thin CaO layer during pyrolysis selectively catalyzing the char-CO_2 gasification reaction.

Based on these experimental results, heterogeneous gasification kinetics are determined for chars with distinct properties to show the influence of thermal history on the reactivity in the gasification regime of the reactor. For the determination of gasification kinetics at elevated pressure, a novel single-particle reactor with forced flow-through conditions was designed and built in the frame of this work reducing diffusional effects at the char particle surface to a minimum. Gasification experiments at elevated pressure with CO_2, H_2O and its mixture are carried out using two high-temperature beech wood chars (P1400 & P1600). Modeling of gasification kinetics is successfully conducted using a power law approach. However, an observed saturation during gasification of P1600 applying high CO_2 partial pressures is better described by a Langmuir-Hinshelwood approach.

Concerning the gasification experiments in mixed CO_2/H_2O atmospheres, increasing the CO_2 partial pressure starting from pure steam as feed gas leads to a higher reactivity for both chars. The reaction rate for mixed gasification can be expressed by addition of the single atmosphere reaction rates suggesting a separate active site mechanism in the low pressure area. For higher H_2O and CO_2 partial pressures, however, P1600 reactivity stagnates due to lower specific surface area and higher graphitization degree i.e. lower amount of carbon active sites. Here, a common active sites mechanism can be assumed.

Zusammenfassung

Die vorliegende Doktorarbeit ist eine kumulative Dissertation bestehend aus fünf wissenschaftlichen Veröffentlichungen. Diese Veröffentlichungen befassen sich mit der Flugstromvergasung, die eine Schlüsseltechnologie für die Produktion von chemischen Energieträgern aus Abfallströmen unter dem Aspekt einer Kreislaufwirtschaft ist. Das Ziel dieser Arbeit ist die Bestimmung der Vergasungskinetik unter technisch relevanten Prozessbedingungen für die Flugstromvergasung, das heißt hohe Drücke, hohe Temperaturen und hohe Aufheizraten. Die Vergasungsexperimente werden mit Biomassekoksen durchgeführt, die unter typischen Prozessbedingungen technischer Flugstromvergaser produziert wurden. In der Flammenzone des Flugstromvergasers durchläuft der Festbrennstoff eine Pyrolyse bei hohen Temperaturen/Aufheizraten und kurzen Verweilzeiten. Die Pyrolysebedingungen in diesem Prozessschritt bestimmen Kokseigenschaften und Reaktivität für die folgenden heterogenen Vergasungsreaktionen. Für die Auslegung technischer Flugstromvergaser mit dem Ziel eines vollständigen Feststoffumsatzes ist es entscheidend, über kinetische Daten für die Vergasungsreaktionen mit CO_2 und H_2O zu verfügen.

Im ersten Teil der vorliegenden Arbeit wird die Entwicklung der Morphologie, die Konzentration katalytisch aktiver Aschekomponenten sowie die Anzahl aktiver Zentren während der heterogenen Vergasungsreaktion eines Kokspartikels mit CO_2 analysiert. Des Weiteren wird der Einfluss dieser Kokseigenschaften auf Reaktivität und Verlauf der Vergasungsreaktion als Funktion des Umsatzes untersucht. Die Ergebnisse deuten darauf hin, dass katalytisch aktive Aschekomponenten, die gewöhnlich in Biomasse vorgefunden werden (z.B. Calcium, Kalium), einen erheblichen Einfluss auf Reaktivität und Umsatzratenverlauf haben. Der Einfluss der Aschekomponenten auf die Vergasungsreaktion mit CO_2 im mikrokinetischen Gebiet kann im Vergleich zur Morphologie als überlegen angesehen werden.

Im zweiten Teil wird der Einfluss der Pyrolysebedingungen auf die Kokseigenschaften Mikroporenoberfläche, Graphitisierung der Kohlenstoffmatrix und Aschedispersion während der Hochtemperaturpyrolyse in einem Fallrohrreaktor untersucht. Darüber hinaus wird die Auswirkung der Calcium Dispersion und der Graphitisierung auf die Reaktivität der Biomassekokse während der Vergasung mit CO_2 herausgearbeitet. Die Ergebnisse zeigen, dass eine stetig steigende thermische Desaktivierung jener Kokse beobachtet werden kann, die bis zu einer Pyrolysetemperatur von 1400 °C hergestellt wurden. Die Desaktivierung ist vorwiegend auf eine Erhöhung der Graphitisierung und eine Erniedrigung der Calcium Dispersion zurückzuführen. Jedoch

ist beim Koks, der bei 1600 °C produziert wurde (P1600), ein sprunghafter Anstieg der Reaktivität zu beobachten, obwohl dieser den höchsten Grad des Graphitisierung und die niedrigste Mikroporenoberfläche aufweist. Dieses Phänomen ist durch die Ausbildung eines dünnen CaO-Films während der Pyrolyse bei 1600 °C versursacht, der selektiv die Vergasungsreaktion von P1600 mit CO_2 katalysiert.

Auf Basis dieser experimentellen Ergebnisse wird die heterogene Vergasungskinetik zweier Biomassekokse mit stark unterschiedlichen Eigenschaften bestimmt, um den Einfluss der thermischen Vorbehandlung auf das Vergasungsverhalten darzulegen. Zur experimentellen Bestimmung der Vergasungskinetik bei erhöhtem Druck wurde im Rahmen dieser Arbeit ein neuartiger Einzelpartikel-Reaktor entworfen und gebaut, in dem die Kokspartikel vom Reaktionsgas durchströmt werden, um etwaige Diffusionslimitierungen auf ein Minimum zu reduzieren. Vergasungsexperimente bei erhöhtem Druck werden mit CO_2, H_2O und in Gemischen der beiden Reaktionsgase mit Hochtemperatur-Buchenholzkoksen (P1400 & P1600) durchgeführt. Die Vergasungskinetik wird erfolgreich mithilfe eines Potenzansatzes modelliert. Jedoch wird während der Vergasung von P1600 bei hohen CO_2 Partialdrücken eine Sättigung der Koksoberfläche beobachtet, die besser mittels Langmuir-Hinshelwood-Ansatz beschrieben werden kann.

Hinsichtlich der Vergasungsexperimente in gemischten CO_2/H_2O Atmosphären führt eine Zugabe von CO_2 und damit eine Erhöhung des CO_2 Partialdrucks beginnend bei der reinen H_2O Vergasung zu einer höheren Vergasungsgeschwindigkeit für beide Biomassekokse. Im niedrigen Druckbereich kann die Reaktionsgeschwindigkeit der Gemisch-Vergasung mittels Addition der beiden Einzelatmosphären-Reaktionsgeschwindigkeiten für beide Koksproben ausgedrückt werden. Dies lässt die Vermutung zu, dass in diesem Druckbereich unterschiedliche aktive Zentren auf der Koksoberfläche für die Vergasungsreaktion mit CO_2 und H_2O verantwortlich sind. Bei einer weiteren Erhöhung der Partialdrücke der Reaktionsgase stagniert jedoch die Reaktivität von P1600 aufgrund der niedrigeren spezifischen Oberfläche und der höheren Graphitisierung, wodurch eine niedrigere Anzahl aktiver Kohlenstoffzentren auf der Koksoberfläche vorzufinden ist. Somit kann hier vermutet werden, dass CO_2 und H_2O um gemeinsame aktive Zentren auf der Koksoberfläche konkurrieren.

Table of contents

List of symbols and abbreviations

Symbol	Description	Unit
a, b, c, r, s, t, u, v	Stoichiometric factors	-
A	Specific surface area	$m^2\ g^{-1}$
A_{MSA}	Micropore surface area	$m^2\ g^{-1}$
c	Concentration	$mol\ m^{-3}$
c_{C_f}	Concentration of carbon active sites	$mol\ mol^{-1}$
c_∞	Concentration in the bulk phase	$mol\ m^{-3}$
d_{002}	Distance between two graphene layers	m
D_{AB}	Binary diffusion coefficient	$m^2\ s^{-1}$
D_{CaO}	Dispersion of superficial calcium oxide	$mol\ g^{-1}$
D_{eff}	Effective diffusion coefficient	$m^2\ s^{-1}$
D_{Kn}	Knudsen diffusion coefficient	$m^2\ s^{-1}$
d_{pore}	Pore diameter	m
$\frac{dm_C}{dt}$	Mass loss rate	$g\ s^{-1}$
$\frac{dX}{dt}$	Conversion rate	s^{-1}
E_A	Activation energy	$J\ mol^{-1}$
$E_{A,micro}$	Microkinetic activation energy	$J\ mol^{-1}$
$E_{A,obs}$	Observed activation energy	$J\ mol^{-1}$
$F(X_C)$	Structural term	-
ΔH_R^0	Reaction enthalpy at standard conditions	$J\ mol^{-1}$
k	Specific rate constant	s^{-1}
$k_{0,i}$	Pre-exponential factor	Various
k_i	Arrhenius rate coefficient	Various
k_{pyr}	Pyrolysis rate constant	s^{-1}
L_a	Radial expansion of graphene layers	m
$L_{a,0}$	Radial expansion of graphene layers of primary char	m
l_c	Characteristic length	m
$l_{H1\text{-}H3}$	Length of heating zones	m
$\widetilde{M}_C$	Molar mass of carbon	$g\ mol^{-1}$

m_C	Remaining carbon mass at a certain time t	g
$m_{C,0}$	Initial mass of fixed carbon	g
n_C	Remaining carbon molar amount at a certain time t	mol
$n_{C,0}$	Initial molar amount of fixed carbon	mol
n_i	Reaction order	-
p	System pressure	bar
p_i	Partial pressure of component i	bar
p_{rel}	Relative pressure	-
p_{tot}	Total pressure	bar
R	Chemical rate coefficient	s^{-1}
R_0	Initial conversion rate	s^{-1}
R_{1000}	Reactivity of chars produced at 1000 °C and 1 s	s^{-1}
R_U	Universal gas constant	J mol^{-1} K^{-1}
R_m	Specific conversion rate (reactivity)	s^{-1}
R_X	Conversion rate	s^{-1}
r^*	Dummy reaction rate (r^* = 1 mol g^{-1} s^{-1})	mol g^{-1} s^{-1}
r_i	Reaction rate (i = CO_2, H_2O, mix)	mol g^{-1} s^{-1}
r_{eff}	Effective reaction rate	mol g^{-1} s^{-1}
T	Temperature	K
T_{Gas}	Gas temperature	K
t	Time	s
V	Volume	m^3
V_{ads}	Adsorbed Volume	ml g^{-1}
V_{diff}	Differential pore volume	ml g^{-1}
Xc	Carbon conversion	-
$x_{reactive+catalytic}$	Reactive and catalytically active sites	
y_i	Volume fraction of component i	-
Greek symbols		
$\alpha,\beta,\gamma,\delta,\chi,\zeta,\omega$	Stoichiometric factors	-
ε	Porosity	-
η	Effectiveness factor	-
ϕ	Thiele modulus	-
τ	Tortuosity	-

Subscripts	Description
0	At the beginning of an experiment
C	Carbon
C_f	Fixed Carbon
CO_2	Concerning CO_2 gasification
f	Fixed carbon (in chemical reaction equation)
H_2O	Concerning H_2O gasification
i	Indexed variable
mix	Concerning mixed gasification in CO_2/H_2O atmosphere
pyr	Pyrolysis

Abbreviations	Description
AAEM	Alkaline and alkaline earth metals
AC	Activated carbon
ad	Air-dried
approx.	Approximately
ASA	Active surface area
ASIM	Active site / intermediate model
BET	Brunauer-Emmett-Teller
BSU	Basic structural units
CL	Chinar leaves
CPD	Chemical Percolation Depolymerisation model
DAE	Distributed activation energy
daf	Dry ash free
DFG	Deutsche Forschungsgemeinschaft
DFT	Density functional theory
diff	By difference
DR	Dubinin-Radushkevich
DTG	Differential thermogravimetry
DTR	Drop-tube reactor
EBI ceb	Engler-Bunte-Institute – Fuel Technology

EFG	Entrained-flow gasification
el.	Electrical heating
EMR	Energy Efficiency, Materials and Resources
Eq.	Equation
EU	European Union
FBR	Fluidized-bed reactor
FFB	Free-fall fixed-bed reactor
FG-DVC	Functional Group – Depolymerisation Vaporization Crosslinking model
Fig.	Figure
GC	Gas chromatograph
GSCM	Generalized shrinking core model
HGF	Helmholtz Association of German Research Centers
HK06	Primary char
HR	Heating rate
HRTEM	High resolution transmission electron microscopy
HSR	Heated strip reactor
HVI GasTech	Helmholtz Virtual Institute for Gasification Technology
ICP-OES	Inductively coupled plasma optical emission spectrometry
IR	Infrared spectroscopy
ITC	Institute for Technical Chemistry
IUPAC	International Union of Pure and Applied Chemistry
KIT	Karlsruhe Institute of Technology
LH	Langmuir-Hinshelwood
MFC	Mass flow controller
MPM	Multi pore model
MS	Mass spectrometer
n.a.	Not available
NMR	Nuclear magnetic resonance
P1400, P1600	Secondary chars produced at 1400 °C and 1600 °C
PNS	Pistachio nut shell
ppm	Parts per million
PS	Pine sawdust
pSPR	Pressurized single-particle reactor

(p)TGA	(Pressurized) Thermogravimetric analyzer
RPM	Random pore model
RS	Rice straw
RSA	Reactive surface area
RWTH	Rheinisch-Westfälische Technische Hochschule
SAED	Selected area electron diffraction
SCM	Shrinking core model
SEM	Scanning electron microscope
SFOR	Single first order reaction
SSA	Specific surface area
SSC	Stable surface complexes
STYX	Screw pyrolysis reactor
TEM	Transmission electron microscope
TGA	Thermogravimetric analyzer
TK	Transient kinetics
TPD	Temperature-programmed desorption
TPR	Temperature-programmed reaction
TSA	Total surface area
TSC	Total surface complexes
UCM	Uniform Conversion Model
WC1600(n)	Secondary char, biogenic model fuel pyrolyzed at 1600°C
WC500	Primary char
WMR	Wire-mesh reactor
WS	Walnut shells
vol.	Volume
wt.	Weight
XRD	X-ray diffraction

1 Introduction and scope

Anchored in the European Green Deal, the European Union (EU) proposed an action plan in order to introduce a new growth strategy that will transform the EU into a modern, resource-efficient, competitive and sustainable economy [1]. The main objective is to achieve net zero emissions of greenhouse gases by 2050 while decoupling economic growth from the use of fossil resources. Reaching this target will require action by all sectors of the economy, including the investment in environmentally friendly technologies that help to increase the efficient use of resources by moving to a clean, circular economy.

The bioliq® process, which was developed at Karlsruhe Institute of Technology (KIT), allows for the sustainable production of synthetic fuels from dry biomass residues [2]. Fig. 1.1 shows a schematic flow diagram of the bioliq® process chain. This multistage process accounts for a de-centralized pyrolysis step turning raw biomass into a pumpable and storable bio-slurry (biosyn-crude®) comprised of pyrolysis-oil and char with high energy density. Furthermore, it requires a large centralized entrained-flow gasification (EFG) unit (5 MW) coupled with fuel synthesis that benefits from economies of scale.

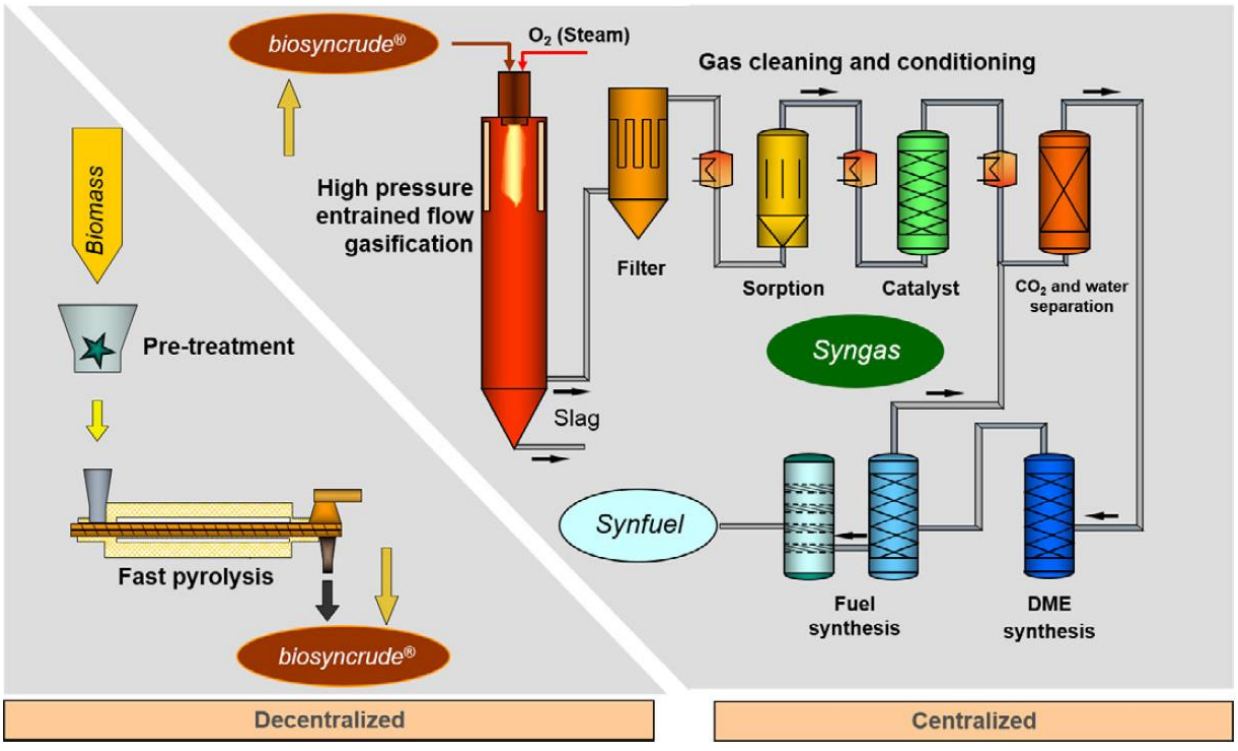

Fig. 1.1. Schematic flow diagram of the KIT bioliq ® process [2].

EFG is one of the key enabling technologies of the Green Deal for the conversion of waste and biomass to chemical energy carriers to ensure a closed carbon cycle. In the high-pressure entrained-flow gasifier of the bioliq® process, the biosyncrude® is converted into a tar-free synthesis gas at pressures of up to 80 bar and temperatures above 1200 °C. In order to identify the physical and thermo-chemical process steps dominating entrained flow gasification, Fig. 1.2 (left) shows a typical droplet/particle trajectory pattern as derived from the numerical simulation of a slurry-fed EFG [3]. The colors of the trajectories represent different physical and thermo-chemical process steps i.e.:

1. Cyan: Atomization, heating-up, evaporation and decomposition of the slurry
2. Orange: Heating-up and (secondary) pyrolysis of the solid fuel particle (primary char)
3. Red: Gasification of the solid fuel particle (secondary char) with CO_2 and H_2O
4. Blue: Ash / slag-forming particles impinging on the gasifier walls or leaving the gasifier with the syngas flow

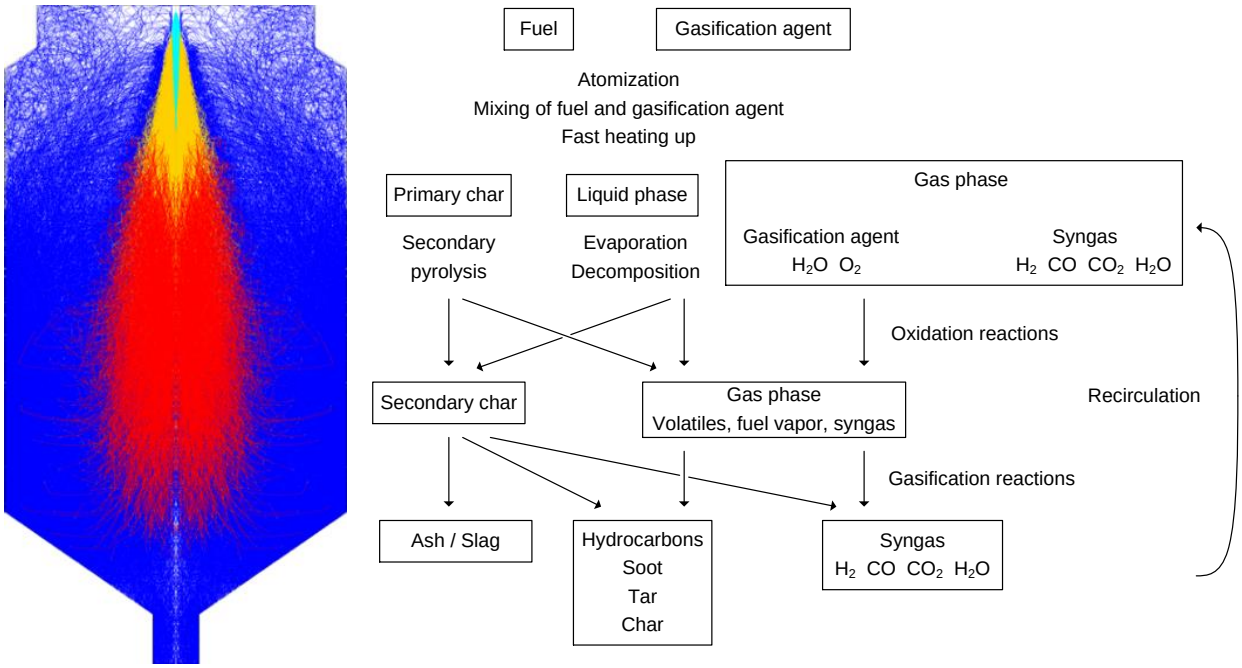

Fig. 1.2. Left: Trajectories of bio-slurry droplets in an entrained-flow gasifier. Right: Sub-processes and species relevant for entrained-flow gasification of slurry; adapted from [3,4].

In Fig. 1.2 (right), a detailed overview of the sequence of sub-processes and intermediate species relevant for EFG is depicted. The slurry is atomized close to the burner nozzle within the highly turbulent gas jet which is enveloped by the gas flame burning recirculated synthesis gas with

oxygen at very high temperatures. The liquid fraction of the suspension fuel evaporates and the vapors react with O_2, CO_2 and H_2O. The solid fuel fraction (primary char) undergoes secondary pyrolysis at high temperatures and high heating rates. The resulting secondary char penetrates through the highly reactive zone into the downstream gasification zone where the endothermic gasification reactions occur that determine syngas quality and fuel conversion efficiency.

The main objective of this work is to determine heterogeneous gasification kinetics in the micro-kinetic regime at elevated pressure using secondary chars that have been produced under process conditions of technical entrained-flow gasifiers i.e. high temperatures, high heating rates and short residence times. The interpretation of measured gasification rates is based on the analyzed char properties i.e. morphology, graphitization degree of the carbon matrix as well as composition and dispersion of catalytic ash components.

The present work is a cumulative dissertation consisting of five scientific articles of which three were written as first author and two were published as co-author. Beyond the published research, chapter 4 .1 contains additional research concerning the evolution of morphology and the effect of inorganic matter during gasification of biomass char. Furthermore, a brief literature review (see chapter 2) is presented and the most important results of the five scientific articles are summarized in chapter 4. For a more detailed and comprehensive illustration, the publications attached to this thesis can be consulted.

In order to achieve the above-mentioned objective, the following **research questions** will be answered in the frame of this work:

Question 1: *Which biogenic char properties affect heterogeneous gasification reactions predominantly and how do they change upon char gasification?* (Papers **III** & **IV** and chapter **4.1**)

Question 2: *How are biogenic char properties influenced by secondary pyrolysis during entrained-flow gasification?* (Paper **II** and chapter **4.2**)

Question 3: *Which experimental set-ups are suitable for the determination of heterogeneous gasification kinetics and which experimental set-up can be applied for the determination of gasification kinetics at elevated pressure?* (Papers **I** & **V** and chapter **4.3**)

Question 4: *What is the dominating reaction mechanism during mixed gasification of biogenic solid fuels in a CO_2/H_2O atmosphere at elevated pressure?* (Paper **I** and chapter **4.3**)

2 Literature review

2.1 Pyrolysis of solid fuels

2.1.1 Fundamentals

Pyrolysis describes the thermal decomposition of chemical compounds at elevated temperatures in an inert atmosphere. Cracking of large molecules occurs producing permanent gases (CO, CO_2, H_2, etc.), light hydrocarbons (C_uH_v), tars or heavy hydrocarbons ($C_rH_sO_t$) and solid char (C) (see Eq. R1) [5]. Devolatilization is often used as synonym for pyrolysis. However, devolatilization describes the release of volatile matter from a solid fuel which does not necessarily have to occur in an inert atmosphere but rather as a first step in a technical gasification process [6]. A general reaction equation can be presented in a simplified form as follows [7]:

$$C_aH_bO_c \xrightarrow{k_{pyr}} \alpha\ C_rH_sO_t + \beta\ C_uH_v + \gamma\ C + \delta\ CO + \chi\ CO_2 + \zeta\ H_2O + \omega\ H_2 \qquad (R1)$$

The solid feedstock is represented as $C_aH_bO_c$ and undergoes devolatilization with a chemical reaction rate constant k_{pyr}.

In literature, a great variety of different pyrolysis models with differing degrees of complexity can be found. Simple expressions estimating volatile yield are e.g. single-first order reaction models (SFOR), two competing reactions / multi-step models or distributed activation energy models (DAE) [8]. More phenomenological models i.e. FLASHCHAIN [9], Functional Group - Depolymerisation Vaporization Crosslinking model (FG-DVC) [10] and Chemical Percolation Depolymerisation model (CPD) [11] account for the chemical structure of the solid fuel and have originally been developed for coal. These models aim for the prediction of pyrolysis rates and yields / composition of tars and light gases based on the fuel properties that can be determined by e.g. ^{13}C nuclear magnetic resonance (NMR) measurements or proximate and ultimate analysis. Recently, attempts have been made to extend these models applying additional fuels beside coal. Especially the CPD model has been successfully adjusted to model pyrolysis of biomass, black liquor, rigid polyurethane, removable epoxy foams and waste tires [12].

2.1.2 Influence of pyrolysis temperature and residence time on char reactivity

During devolatilization in the flame zone of the entrained-flow gasifier, the char undergoes various changes concerning physico-chemical properties i.e. morphology, carbon matrix and inorganic ash components. In this context, high temperatures and long residence times typically lead

to a loss of reactivity in the subsequent gasification process. This effect is called thermal deactivation or "thermal annealing" and is the consequence of thermal stress during pyrolysis and gasification of fossil [13–19] or biomass-based solid fuels [8,19–22].

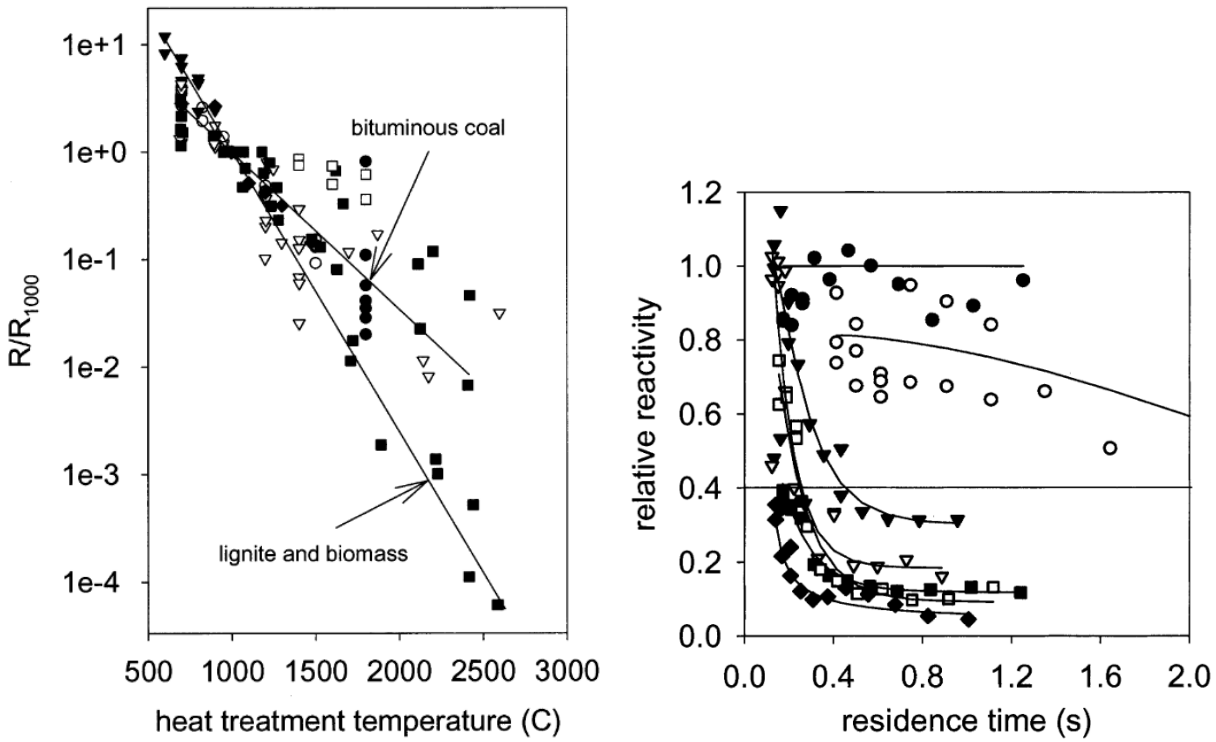

Fig. 2.1. Left: Effect of heat treatment on combustion reactivity of carbonaceous materials. R_{1000} represents reactivity of corresponding coal char pyrolyzed at 1000 °C for 1 s [23]. Right: Reactivity of Cerrejon coal chars after pyrolysis in an entrained-flow reactor at various temperatures and residence times. Relative reactivity based on char pyrolyzed at 700 °C for 1 s. Pyrolysis temperatures are ● 700 °C, ○ 900 °C, ▼ 1000 °C, ▽ 1100 °C, ■ 1200 °C, □ 1300 °C, ♦ 1475 °C [23].

Feng et al. [23] summarize various publications investigating thermal deactivation of coals and biomass and its effect on the subsequent gasification or combustion process. Fig. 2.1 (left) shows the effect of heat treatment temperature on the combustion reactivity of different carbonaceous materials in varying oxygen concentrations. Here, R_{1000} represents the combustion reactivity of the char produced at a temperature of 1000 °C and 1 s residence time. For the pyrolysis experiments, different experimental set-ups and conditions were applied. A detailed description of the pyrolysis and combustion experiments can be found in Feng et al. [23]. According to Fig. 2.1 (left), the reactivity of the fuels investigated decreased several orders of magnitude due to thermal stress, strongly dependent on the nature of the fuel. Biomass based fuels and low rank coals exhibit a much faster decrease in reactivity with increasing pyrolysis temperature than high rank

coals. Therefore, a potential thermal deactivation during the devolatilization step in a technical application has strong influence on the subsequent gasification or combustion reaction rate.

Fig. 2.1 (right) shows the loss of reactivity of Cerrejon coal pyrolyzed in an entrained-flow reactor as a function of residence time [23]. The relative reactivity of the chars is based on a reference char that was produced at 700 °C for 1 s. As can be seen, there is a combined effect of temperature and residence time on thermal deactivation. For pyrolysis temperatures higher than 900 °C, char reactivity decreases initially fast within the first 400 ms. Subsequently, no significant change in reactivity with increasing residence time was observed. Feng et al. [23] concluded that after 500 ms of pyrolysis, temperature was more important than residence time concerning thermal deactivation of the chars investigated.

2.1.3 Influence of heating rate on char reactivity

Not only peak temperature and residence time, but also heating rate during pyrolysis is an important parameter concerning char reactivity in a subsequent gasification or combustion process. In general, char reactivity increases with higher heating rate during pyrolysis [20,24–29]. Cetin et al. [26,28] conducted pyrolysis experiments with different biomass types in a wire-mesh reactor (WMR) and a tubular reactor at 950 °C. The authors report that chars generated in the WMR at a high heating rate of 500 K min^{-1} have higher gasification reactivity towards CO_2 by a factor of approx. two than chars produced in the tubular reactor at 20 K min^{-1}. They conclude that chars produced at high heating rates have higher specific surface areas and thus, exhibit higher reactivity towards heterogeneous gasification reactions. Other authors also state that the heating rate has influence on the constitution of the carbon matrix [25] and the dispersion of inorganic ash components on the char surface that can act as a catalyst during gasification reaction [29]. A detailed description of physical and chemical char properties affecting gasification reactivity will be addressed in chapter 2.3.

For slow heating rates, the volatile pyrolysis products are released through the natural porosity of the char particle and no major changes in particle morphology are observed [30]. On the other hand, fast volatile release produces substantial internal overpressure and coalescence of smaller pores leading to the loss of the original cellular structure, large internal cavities and more open structure [31–33]. Fig. 2.2 shows scanning electron microscopy (SEM) images of hazelnut shells with a particle fraction of 100 – 150 µm as received (a), pyrolyzed at low heating rate (0.5 K s^{-1}) in a TGA (b) and treated at high heating rate ($2 \cdot 10^4$ K s^{-1}) in a "Pyroprobe" up to 1000 °C [34]. The

hazelnut particle in Fig. 2.2 (a) shows a lamellar structure with wide fractures and a diffuse superficial microporosity. The hazelnut char in Fig. 2.2 (b) maintains the same size, shape and traces of lamellar structure as the parent material. At high heating rates (see Fig. 2.2 (c)), however, the char particle swells, the solid material is molten and the fissures are joined.

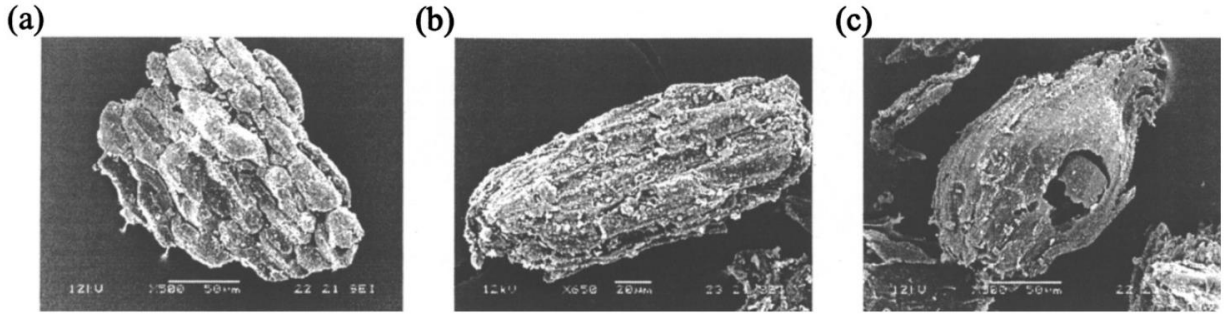

Fig. 2.2. SEM images of hazelnut shells as received (a), and its chars produced at low heating rate (b) and high heating rate (c) [34].

2.1.4 Influence of pyrolysis pressure on char reactivity

The influence of pyrolysis pressure on char reactivity was not investigated in the frame of this work. However, its effect on char reactivity cannot be neglected. Several authors investigated the influence of pyrolysis pressure on char structure and reactivity. No conclusive statement concerning pressure influence on the pyrolysis process can be found in literature. A short summary of selected references investigating the effect of pyrolysis pressure on char reactivity can be found in the appendix A.

2.2 Heterogeneous gasification of solid fuels

2.2.1 Fundamentals

Gasification describes the thermochemical conversion of a carbonaceous solid fuel into a combustible product gas, which is often referred to as synthesis gas. The main components of the obtained gas are hydrogen (H_2) and carbon monoxide (CO), while other components such as carbon dioxide (CO_2), water (H_2O), methane (CH_4) and other hydrocarbons are also present to a certain extent depending on the gasification conditions and the reactor type used. Common gasifying agents are steam, oxygen and air [35]. The most relevant heterogeneous gas-solid reactions during technical gasification processes can be expressed as follows [35]:

$$C + O_2 \rightarrow CO_2 \qquad \Delta H_R^0 = -393.5 \frac{kJ}{mol} \qquad (R2)$$

$$C + \frac{1}{2} O_2 \rightarrow CO \qquad \Delta H_R^0 = -110.5 \frac{kJ}{mol} \qquad (R3)$$

} combustion

$$C + CO_2 \rightleftharpoons 2\,CO \qquad \Delta H_R^0 = +159.6 \frac{kJ}{mol} \qquad (R4)$$

$$C + H_2O \rightleftharpoons CO + H_2 \qquad \Delta H_R^0 = +118.5 \frac{kJ}{mol} \qquad (R5)$$

$$C + 2\,H_2 \rightleftharpoons CH_4 \qquad \Delta H_R^0 = -87.5 \frac{kJ}{mol} \qquad (R6)$$

} gasification

R2 and R3 represent complete and partial oxidation of the carbonaceous solid fuel, respectively. R4 – R6 show the heterogeneous gasification reactions i.e. Boudouard reaction, heterogeneous water-gas reaction as well as hydrogasification. In an autothermal gasifier, a small fraction of the fuel is combusted (R2 & R3) in order to provide the thermal energy for the endothermic gasification reactions (R4 & R5). The resulting CO_2 can act as a gasifying agent further downstream in the gasifier. On the other hand, allothermal gasification processes rely on heat supply from outside the gasification reactor [35].

As a basis for the modeling of gasification kinetics (see chapter 2.2.3), the time dependent carbon conversion $X_C(t)$ needs to be defined. This can either be achieved by using molar amounts n_C or on a mass basis m_C [36].

$$X_{\mathrm{C}}(t) = \frac{n_{\mathrm{C},0} - n_{\mathrm{C}}(t)}{n_{\mathrm{C},0}} = \frac{m_{\mathrm{C},0} - m_{\mathrm{C}}(t)}{m_{\mathrm{C},0}} \tag{2-1}$$

Here, $n_{\mathrm{C},0}$ represents the molar amount of carbon in the char particle at the beginning of the gasification while $n_{\mathrm{C}}(t)$ is the amount at a certain time t. In order to describe the dynamics of the gasification process, the time dependent specific conversion rate R_{m} is defined [20].

$$R_{\mathrm{m}} = -\frac{1}{m_{\mathrm{C}}(t)}\frac{dm_{\mathrm{C}}}{dt} = \frac{1}{1 - X_{\mathrm{C}}(t)}\frac{dX_C}{dt} \tag{2-2}$$

As with any chemical gas-solid reaction, the gasification rate of carbonaceous materials depends on temperature and partial pressure of the reactant gases (see chapter 2.2.2). But contrary to gas-solid reactions on a catalyst surface, the carbonaceous solid fuel may vary its chemical and physical properties throughout the conversion process affecting the observed gasification rate [37]. The variation of char properties during the gasification reaction is considered using a structural term $F(X_{\mathrm{C}})$ depending on the carbon conversion degree. Subsequently, the conversion rate R_{X} consisting of a rate coefficient $R(T,p)$ (chemical kinetic term [38]) and a structural term $F(X_{\mathrm{C}})$ can be written as follows [39].

$$R_X = \frac{dX_{\mathrm{C}}}{dt} = R(T,p)\, F(X_{\mathrm{C}}) \tag{2-3}$$

Depending on the underlying particle conversion model, the structural term is defined differently. In the frame of this work, the uniform conversion model (UCM) was used due to its simplicity and the application for modeling the gasification reaction in the microkinetic regime. The UCM treats the solid fuel particle as a homogeneous body where the gasification reactions occur uniformly [40,41]. A linear decrease in carbon mass throughout the conversion process is considered resulting in a structural term of $F(X_{\mathrm{C}}) = 1 - X_{\mathrm{C}}$ and the following expression [40].

$$R_X = \frac{dX_{\mathrm{C}}}{dt} = R_0\,(1 - X_{\mathrm{C}}) \tag{2-4}$$

$$R_0 = \left.\frac{dX_{\mathrm{C}}}{dt}\right|_{X_{\mathrm{C}}=0} \tag{2-5}$$

$$X_{\mathrm{C}}(t) = 1 - \exp(-R_0\, t) \tag{2-6}$$

R_0 is defined as the initial conversion rate and can be determined experimentally. Eventually, the reaction rate r_i is formulated using the initial conversion rate R_0 and the molar mass of carbon

$\widetilde{M}_{\mathrm{C}}$. Here, i represents an indexed variable representing the corresponding gasification agent (CO_2, H_2O, mix).

$$r_i = \frac{R_0}{\widetilde{M}_{\mathrm{C}}} \tag{2-7}$$

In literature, a vast amount of different particle conversion models is available. By means of one-equation particle models e.g. shrinking core model (SCM) [42] or random pore model (RPM) [43], an attempt is made to describe the changes in char morphology throughout the conversion process. Discrete particle models such as generalized shrinking core model (GSCM) [42] and the multi pore model (MPM) [44,45] aim to describe the evolution of specific surface area and pore structure using spatially resolved data of particle structure as well as conservation and model equations. Hence, the morphological changes in the particle can be modeled and observed locally. The last group of particle models can be indicated as kinetic models since their objective is to describe the changes in microkinetic reaction rate due to changes in chemical properties of the char i.e. carbon matrix or catalytically active ash components. As an example, the active site/intermediate model (ASIM) [46] can be cited where a reaction scheme for a calcium catalyzed gasification reaction is developed and modeled.

2.2.2 Heterogeneous gas-solid reactions

The reaction equations presented in chapter 2.2.1 (R2 – R6) are heterogeneous gas-solid reactions. Thus, the chemical reaction between reactant gas and solid fuel takes place on the surface of the solid material. The individual steps of a heterogeneous gas-solid reaction on a porous catalyst are depicted Fig. A.8 (see appendix) [47]. These transport processes and reaction steps can also be applied to heterogeneous conversion of carbonaceous fuels with oxidizing agents [48]. The seven steps can be described as follows:

1. Diffusion of the reactant gases through the boundary layer surrounding the particle (film diffusion).
2. Intraparticle diffusion of the reactant gases into the pores to the active sites (pore diffusion).
3. Adsorption of the reactant gases onto active sites.
4. Surface reactions involving formation or conversion of adsorbed species at active sites.
5. Desorption of product gases from active sites.
6. Intraparticle diffusion of the product gases through the pores to the boundary layer.
7. Diffusion of the product gases across the boundary layer surrounding the particle.

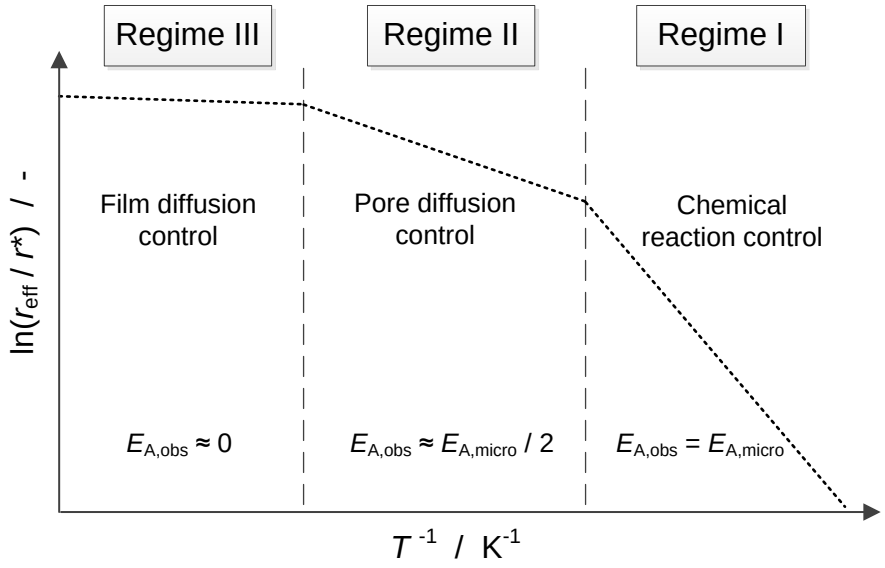

Fig. 2.3. The three regimes representing the dominating mechanisms for heterogeneous reactions with porous carbonaceous materials as a function of temperature; adapted from [49].

According to these seven steps, different regimes of rate control are existent, including: chemical reaction kinetics control (regime I, steps 3 – 5, also known as microkinetics [47]), pore diffusion control (regime II, steps 2 and 6) and film diffusion control (regime III, steps 1 and 7). Fig. 2.3 illustrates an Arrhenius diagram showing the effective (or observed) reaction rate of a porous carbonaceous material as a function of temperature. The figure is divided into three regimes, where the reaction is governed by different mechanisms according to Rossberg & Wicke [48].

In regime I, the effective reaction rate is solely affected by the before-mentioned steps 3 – 5 due to constant reactant gas concentration throughout the particle. Here, an increase in temperature leads to higher effective reaction rates with a slope that is proportional to the microkinetic activation energy $E_{A,micro}$. At a certain temperature, due to the exponential temperature dependency of chemical reactions (see Eq. 2-8), the effective reaction rate becomes so fast that mass transport phenomena must be taken into account. In the resulting regime II, the dominant factor limiting the effective reaction rate is diffusion of the reactant gas through the porous particle. The observed activation energy is approx. $E_{A,micro}$ / 2 in this regime. At even higher temperatures (regime III), the resistance of the external mass transport (film diffusion) is the predominant process limiting the reaction rate. Due to the weak temperature dependency of the diffusive mass transport as compared to the chemical reaction, the effective reaction rate increases only slightly with temperature [50].

Temperature dependency of the chemical reaction (regime I) can be modeled using the rate constant k_i and an Arrhenius approach [51].

$$k_i(T) = k_{0,i} \exp\left(-\frac{E_A}{R_U\, T}\right) \tag{2-8}$$

Here, $k_{0,i}$ represents the pre-exponential factor, E_A the activation energy, R_U the universal gas constant and T the reaction temperature. The rate of the gasification reaction r_i can be modeled using a simple nth-order approach with p_i being the partial pressure of the reactant gas and n_i the reaction order [51]. A more detailed description of possibilities to model heterogeneous gasification kinetics is presented in chapter 2.2.3.

$$r_i(T, p_i) = k_i(T)\, p_i^{n_i} \tag{2-9}$$

2.2.3 Determination and modeling of heterogeneous gasification kinetics

"The heterogeneous gasification of char particles is controlled by process parameters, i.e. temperature, partial pressure of the reactant gas and process pressure as well as the chemical and physical properties of the char. Char properties affecting the conversion rate during gasification mainly include surface area and porosity, graphitization of the carbon matrix and inorganic ash components [25,52–55]. Generally, the heterogeneous char gasification reactions with CO_2 and H_2O can be described by an oxygen exchange mechanism [56]." [57]

Concerning CO_2 gasification, the following reaction mechanism is widely accepted [56,58].

$$C_f + CO_2 \xrightarrow{k_1} C(O) + CO \tag{R7}$$

$$C(O) + CO \xrightarrow{k_2} C_f + CO_2 \tag{R8}$$

$$C(O) \xrightarrow{k_3} CO \tag{R9}$$

C_f represents an active site on the char surface and C(O) a carbon oxygen intermediate. $k_{1\text{-}3}$ are Arrhenius rate constants. The presence of CO exerts an inhibitory effect by lowering the concentration of the C(O) carbon oxygen intermediate (R8). Assuming steady-state conditions and that the rate of reaction is described by the rate of desorption of the carbon oxygen intermediate (R9), a Langmuir-Hinshelwood (LH) approach can be applied [56].

$$r_{\mathrm{CO_2}}(T, p_{\mathrm{CO_2}}, p_{\mathrm{CO}}) = \frac{k_1\, p_{\mathrm{CO_2}}}{1 + \frac{k_2}{k_3}\, p_{\mathrm{CO}} + \frac{k_1}{k_3}\, p_{\mathrm{CO_2}}} \tag{2-10}$$

For low CO concentrations, the inhibitory effect of CO can be neglected and the CO partial pressure p_{CO} is set to null [59]. Moreover, a simplified global kinetic model can be applied:

$$r_{\mathrm{CO_2}}(T, p_{\mathrm{CO_2}}) = k_{0,\mathrm{CO_2}} \exp\left(-\frac{E_{\mathrm{A,CO_2}}}{R_{\mathrm{U}}\, T}\right) p_{\mathrm{CO_2}}^{n_{\mathrm{CO_2}}} \tag{2-11}$$

"The reaction of carbon with steam proceeds similarly to the Boudouard reaction but has more possible inhibition steps as summarized by Hüttinger & Merdes [60].

$$\mathrm{C_f + H_2O \xrightarrow{k_4} C(O) + H_2} \tag{R10}$$

$$\mathrm{C(O) + H_2 \xrightarrow{k_5} C_f + H_2O} \tag{R11}$$

$$\mathrm{C(O) \xrightarrow{k_6} CO} \tag{R12}$$

$$\mathrm{C_f + H_2 \xrightarrow{k_7} C(H_2)} \tag{R13}$$

$$\mathrm{C(H_2) \xrightarrow{k_8} C_f + H_2} \tag{R14}$$

$$\mathrm{C_f + \frac{1}{2}\, H_2 \xrightarrow{k_9} C(H)} \tag{R15}$$

$$\mathrm{C(H) \xrightarrow{k_{10}} C_f + \frac{1}{2}\, H_2} \tag{R16}$$

Basically, the reaction steps can be subsumed into two main processes: the oxygen exchange mechanism (see R10 – R12) and possible hydrogen inhibition reactions (see R13 – R16). Again, $k_{4\text{-}10}$ are Arrhenius rate constants while C(H) and $\mathrm{C(H_2)}$ represent carbon hydrogen intermediates. Hydrogen not only inhibits the reaction by lowering the amount of C(O) carbon oxygen intermediates (see R11) but also by direct adsorption on carbon active sites $\mathrm{C_f}$ associatively (see R13) or dissociatively (see R15).

However, the experimental data presented within this work was obtained in a simplified system containing very low amounts of product gases. Thus, this paper focusses on the oxygen exchange

mechanism (see R10 – R12) while inhibitory effects via adsorption of H_2 were not explicitly investigated leading to a simplified rate expression (see Eq. 2-12). This approach is also consistent with previous experimental studies where kinetic parameters for the carbon steam reaction is determined [59,61].

$$r_{\mathrm{H_2O}}\left(T, p_{\mathrm{H_2O}}, p_{\mathrm{H_2}}\right) = \frac{k_4\, p_{\mathrm{H_2O}}}{1 + \frac{k_5}{k_6}\, p_{\mathrm{H_2}} + \frac{k_4}{k_6}\, p_{\mathrm{H_2O}}} \tag{2-12}$$

Again, for low H_2 concentrations, the inhibitory effect of H_2 is negligible and H_2 partial pressure $p_{\mathrm{H_2}}$ can be set to zero [59]." [57]

Hence, a simplified global kinetic model can be applied as well:

$$r_{\mathrm{H_2O}}\left(T, p_{\mathrm{H_2O}}\right) = k_{0,\mathrm{H_2O}} \exp\left(-\frac{E_{\mathrm{A,H_2O}}}{R_{\mathrm{U}}\, T}\right) p_{\mathrm{H_2O}}^{n_{\mathrm{H_2O}}} \tag{2-13}$$

"In literature, a vast amount of kinetic data for the gasification of fossil [62] and biogenic [20] fuels with both CO_2 and H_2O is available. However, the kinetic parameters may vary several orders of magnitude depending on the fuel, the char particle size, the experimental set-up used and the pyrolysis conditions applied. Pyrolysis conditions affect graphitization degree of the carbon matrix [18,63], char morphology [26,27] and dispersion of inorganic ash components [14,64,65]." [57]

Char properties affecting gasification kinetics will be addressed in detail in chapter 2.3.

Additionally, the experimental set-up may have influence on the reaction kinetic data obtained. A pie chart illustrating the percentage of frequently used experimental set-ups for the determination of heterogeneous gasification kinetics can be found in the appendix (see Fig. A.9) [49]. Due to its simple handling, the TGA is most widely used for the determination of gasification kinetics of fossil and biogenic solid fuels. In thermogravimetric analyzers, however, diffusional effects may evoke artefacts due to the limited gas flow through the char sample. Diffusion processes of the reactant gas through the crucible freeboard and the char bed must be taken into consideration in order to verify the kinetic data obtained [66,67]. A schematic drawing of a crucible that is normally used in a TGA showing mass transfer processes during the gasification of biomass char particles with CO_2 limiting the effective reaction rate can be found in the appendix (see Fig. A.10). Nowak et al. [67] conclude that regime I conditions (microkinetics, see chapter 2.2.2) during gasification of spruce bark char with CO_2 in their thermogravimetric device can be

preserved at higher temperatures by decreasing the sample amount, decreasing the crucible's freeboard and increasing the partial pressure of the reactant gas. In brief, the experimental process parameters i.e. sample mass, temperature, gas velocity and reactant partial pressure must be carefully chosen when using TGA in order to determine kinetic data that are truly under chemical control [49]. This is especially the case when investigating biomass chars since they are typically more reactive than coal chars (see appendix A).

"Other experimental concepts such as vertically blown reactors (e.g. fixed-bed reactors) may be more suitable for the determination of gasification kinetics allowing for the application of wider process parameter windows. Here, the reactant gas is forced to flow through the char sample ameliorating mass transport of educt gas to and removal of product gas from the sample." [57]

Examples for lab-scale gasification experiments with biogenic and fossil fuels conducted in fixed-bed reactors can be found in the appendix A.

"In a technical entrained-flow gasifier, CO_2 and H_2O always coexist in the syngas produced. Thus, knowledge about the dominating heterogeneous gasification reaction when both gases are present is required. According to publications investigating the gasification kinetics of char in mixed atmospheres of CO_2 and H_2O, two possible surface reaction mechanisms were proposed. The first mechanism accounts for the existence of active sites that are suitable for both char-CO_2 and char-H_2O reaction [53,68–72]. Thus, CO_2 and H_2O are competing for the same active sites inhibiting each other." [57]

"An alternative reaction mechanism for the gasification of chars in mixtures of CO_2 and H_2O is based on the assumption that the char-CO_2 and the char-H_2O reactions occur at separate active sites [39,73–75]." [57]

Guizani et al. [73] published a short literature review concerning biomass, lignite and coal char gasification in mixed CO_2/H_2O atmospheres including the pyrolysis conditions of the chars investigated as well as the dominating reaction mechanism during mixed atmosphere gasification. The review shows that no conclusive statement is possible whether the two reactions are competing or additive.

2.3 Char properties affecting gasification kinetics

2.3.1 Morphology

It is evident that heterogeneous gas-solid reactions – as it is the case with gasification reactions – take place on the surface of the solid and therefore, the reaction rate depends on the surface area available as well as the adsorption of gaseous reactants [42,76]. As carbonaceous solid fuels are porous particles, the gasification reaction may occur on the outer- and inner surface. In literature, there are several definitions for surface area that are used in order to characterize char particles and interpret their reactivity during gasification reactions.

A first quantitative approximation for the surface area which is available for the chemical reaction is the use of the **total accessible surface area** (TSA) determined by physical adsorption and applying e.g. the Brunauer-Emmett-Teller (BET) [77] or Dubinin-Radushkevich (DR) [78] models. However, TSA only quantifies the surface area and does not consider surface chemistry i.e. carbon active sites C_f or catalytically active ash components. It rather represents the entire sum of surface area of a solid particle taking into account the internal pore structure but excluding inaccessible surfaces (closed pores). Pore sizes in porous materials can be classified into three size ranges, according to the International Union of Pure and Applied Chemistry (IUPAC) [79]: pores with widths not exceeding 2 nm are micropores, mesopores lie between 2 nm and 50 nm whereas macropores exceed widths of 50 nm.

Numerous particle conversion models are based on the mathematical modeling of TSA evolution as a function of particle conversion. The RPM developed by Bhatia and Perlmutter [43] describes growth and collapse of the pore structure of a char particle during conversion. The RPM and its modifications have also been successfully used in some cases concerning biomass char gasification [80–82]. Furthermore, Fatehi & Bai [45] and Singer & Ghoniem [83] propose models accounting for a multimodal pore structure. Experimental values for the variation of morphological properties (specific surface area, pore size distribution and porosity) of biomass chars during gasification can be taken from literature [84–87]. However, the structural parameters needed for these models are very difficult to be determined experimentally.

The **active surface area** (ASA), on the other hand, represents a different concept and is based on the theory that only a small fraction of the TSA, i.e. active sites, take part in the heterogeneous gasification reaction. ASA considers surface chemistry of the char as edge carbon atoms, defects

in the carbon matrix, heteroatoms or mineral components where heterogeneous gasification reactions occur. The approach was originally presented by Laine et al. [88] in 1963 and further developed by Radovic et al. [89,90] and Lizzio et al. [91] and is based on the mechanistic concept of catalytic heterogeneous reactions where the activity of the catalyst is proportional to the ASA. The gasification reaction proceeds via oxygenated surface complexes, so-called carbon-oxygen intermediates (C(O), see Eq. R7). Hence, the ASA is defined as the quantity of these C(O) complexes and was directly correlated with the specific conversion rate of a char during gasification [91]. ASA can be determined by chemisorption experiments using oxygen containing reactive gases such as CO_2, H_2O and O_2. A summary of investigations that followed the approach for the determination of active sites proposed by Laine et al. [88] can be found in literature [92].

The concept of **reactive surface area** (RSA) is an extension of the active site mechanism including the differentiation between carbon-oxygen intermediates C(O) that form either stable or reactive complexes [91]. Reactive complexes are able to chemisorb the reactant gas dissociatively and desorb as carbon monoxide after the reaction occurred. Furthermore, it is assumed that stable complexes cannot be desorbed and thus, do not contribute to the gasification reaction. RSA is usually determined at reaction temperature either using temperature-programmed desorption (TPD) technique [91,93–95] or a transient kinetics (TK) approach [95–98]. Klose & Wölki [94] investigated the gasification reaction of beech wood char and oil palm shell char with CO_2 and H_2O concerning the evolution of RSA as a function of conversion degree using TPD. Their results showed that observed reaction rates were proportional to the experimentally determined RSA.

As reaction rates of heterogeneous gas-solid reactions depend on the surface area available for the reaction, it is generally believed that gasification rates are higher for chars with higher initial surface areas [99]. Based on the various definitions given for different surface areas, it is evident that gasification reactivity depends on quantity (TSA) and quality (ASA, RSA) of the char surface.

Yuan et al. [100] investigated the effects of biomass type and pyrolysis temperature on char morphology and carbon matrix as well as CO_2 gasification kinetics in a TGA. The authors prepared three biomasses i.e. rice straw char (RS char), chinar leaves char (CL char) and pine sawdust char (PS char) in a high-frequency furnace under rapid pyrolysis conditions at 800 °C - 1200 °C. Based on their results, they conclude that gasification rates are affected by surface characteristics and porosity of the char. During rapid pyrolysis of PS, melting and accumulation processes occur leading to the destruction of pore structures, low specific surface area and thus, lower gasification rates of the PS char. On the other hand, the RS and CL chars were able to preserve their initial

morphological structures during the pyrolysis process. Due to the higher porosity and specific surface area of the CL char, higher gasification reactivities were obtained as compared to the RS char. Gasification reactivity of the three biomass chars with CO_2 were observed to be in the order of CL char > RS char > PS char which can be directly correlated with the specific surface areas determined via N_2 adsorption using BET method.

In contrast, there are several publications investigating biomass [81,101] and coal chars [102] that do not observe any tendency between char reactivity and specific surface area or micropore surface area determined by physical adsorption. The results of Wang et al. [81] and Xu et al. [101] indicate that specific surface area does not match well with the gasification activity of the biomass chars investigated. The authors suggest to further analyze the carbon matrix and catalytic activity of the inorganic ash components in order to evaluate gasification reactivity. Jing et al. [102] conducted CO_2 chemisorption experiments of eight different coal rank chars in order to further characterize the quality of the char surface and concluded that this method suits best for the evaluation of gasification reactivity. The amount of chemisorbed CO_2 may be affected by inorganic ash components as well as pore and carbon crystalline structures.

2.3.2 Carbon matrix

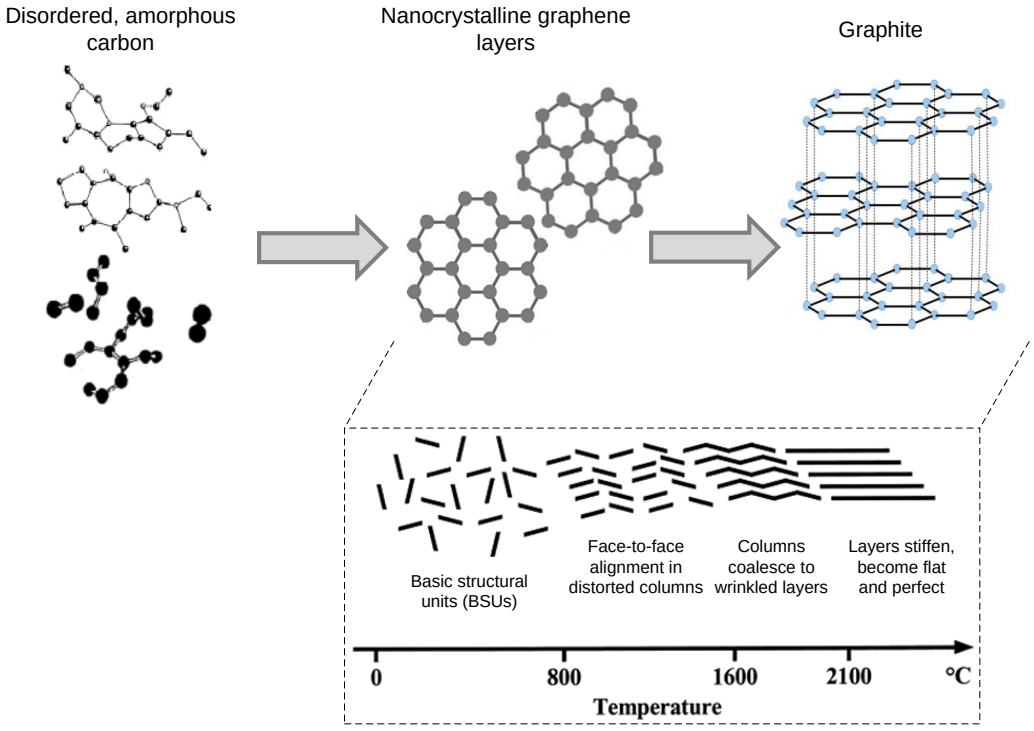

Fig. 2.4. Graphitization process of carbonaceous materials with increasing heat treatment temperature; adapted from [16,103–105].

As already mentioned in chapter 2.1.2, high temperatures during devolatilization in the flame zone of the entrained-flow gasifier evoke structural changes in the char affecting its reactivity. “One reason for the loss of reactivity is the graphitization of the carbon matrix. Graphitization describes the process of increase and arrangement of graphene layers in carbonaceous materials [18]. This process is characterized by formation, growth and order of aromatic clusters and graphite crystals [15,16,106]. In raw solid fuels such as coal or biomass, most of the carbon is available as turbostratic. Turbostratic carbon consists of graphene layers, which are disordered and nonplanar. If these layers are accompanied by other types of carbon bonds (e.g. sp^2- or sp^3-bonds) or even heteroatoms (e.g. H, O, N, S), the present structure is titled as amorphous carbon [106,107].” [108]

In Fig. 2.4, the graphitization process of carbonaceous materials with increasing heat treatment temperature is schematically depicted. “Below pyrolysis temperatures of 500 °C, ordered and/or turbostratic carbon is very low while basic structures are present predominantly. Between 800 °C and 1500 °C, nanocrystalline graphite grows and associates face-to-face in distorted columns. From 1600 °C to 2000 °C, these columns coalesce into distorted wrinkled layers. These layers stiffen and become flat above 2100 °C [15,16,103,109,110]. Many authors have proven that graphitization progresses at higher residence times at high temperatures resulting in a char with low reactivity towards combustion and gasification [22,25,26,107,111]. This is due to the fact, that the number of carbon atoms in an amorphous structure, at defect sites or at the edge of a graphene layer decreases with increasing graphitization. Carbon atoms located in these areas are more reactive than those inside an aromatic cluster [15]. Common methods for the experimental determination of a graphitization degree can be found in literature using X-ray diffraction (XRD) [106,107,111–114] and Raman spectroscopy [63,103,109,112,114,115].” [108]

2.3.3 Catalytically active ash components

Char reactivity is additionally affected by inorganic, ash-forming elements inherent in the fuel [20,54,62,116–120]. Especially the presence of alkaline [80,82,121–131] and alkaline earth [80,82,126–133] metals (AAEM) evoke an increase of char reactivity during gasification with CO_2 and H_2O. Moreover, iron may act as a catalyst accelerating the gasification reactions [128,134]. In contrast, silicon, phosphorous and alumina may inhibit the gasification reactions by binding catalytically active compounds (e.g. potassium) [121,122,134,135].

The most widely accepted theory of catalytic carbon conversion is the oxygen exchange mechanism [120,136]. It consists of a redox cycle involving the carbothermic reduction of a metal carbonate to the elemental metal Me. The proposed reaction steps of the oxygen exchange mechanism for the catalytic Boudouard reaction can be described as follows [120]:

$$Me_2CO_3 + C \rightarrow 2Me + CO + CO_2 \quad \text{(R17)}$$

$$2Me + CO_2 \rightarrow Me_2O + CO \quad \text{(R18)}$$

$$Me_2O + CO_2 \rightarrow Me_2CO_3 \quad \text{(R19)}$$

$$C + CO_2 \rightarrow 2CO \quad \text{(R20)}$$

The sum of reactions R17 – R19 is represented in R20 being the Boudouard reaction. A similar set of steps can be written for H_2O as gaseous reactant:

$$Me_2CO_3 + C \rightarrow 2Me + CO + CO_2 \quad \text{(R21)}$$

$$2Me + 2H_2O \rightarrow 2MeOH + H_2 \quad \text{(R22)}$$

$$2MeOH + CO_2 \rightarrow Me_2CO_3 + H_2O \quad \text{(R23)}$$

$$C + H_2O \rightarrow CO + H_2 \quad \text{(R24)}$$

Again, R24 represents the sum of reactions R21 – R23 being the heterogeneous water-gas gasification reaction.

A similar theory is proposed by Lobo & Carabineiro [54] accounting for the diffusion of carbon through the catalytically active material. Fig. 2.5 (a) shows a schematic illustration of the carbon diffusion process through the catalytically active component (top: solid catalyst particle, bottom: molten catalyst film) [137]. The authors assume that first, carbon has to diffuse through the catalyst material before being converted into product gas at the outer surface of the catalyst. Consequently, the catalyst particles are oxidized by oxygen containing educt gases at the contact area to the surrounding gas phase while in turn being reduced by carbon subsequently diffusing to the outer surface of the catalyst. This process can be described by a redox cycle again.

The continuous consumption of carbon at the contact area between catalyst and carbon support leads to mobility of the catalyst particles [54] (see Fig. 2.5 (b)). Motion of the catalytically active material may change the char morphology by increasing the total and/or active surface area (see chapter 2.3.1) and thus, increasing the conversion rate during gasification. Furthermore, Lobo & Carabineiro [54] state that a change in conversion rate during gasification indicates that the catalytically active component might not be in a state of equilibrium.

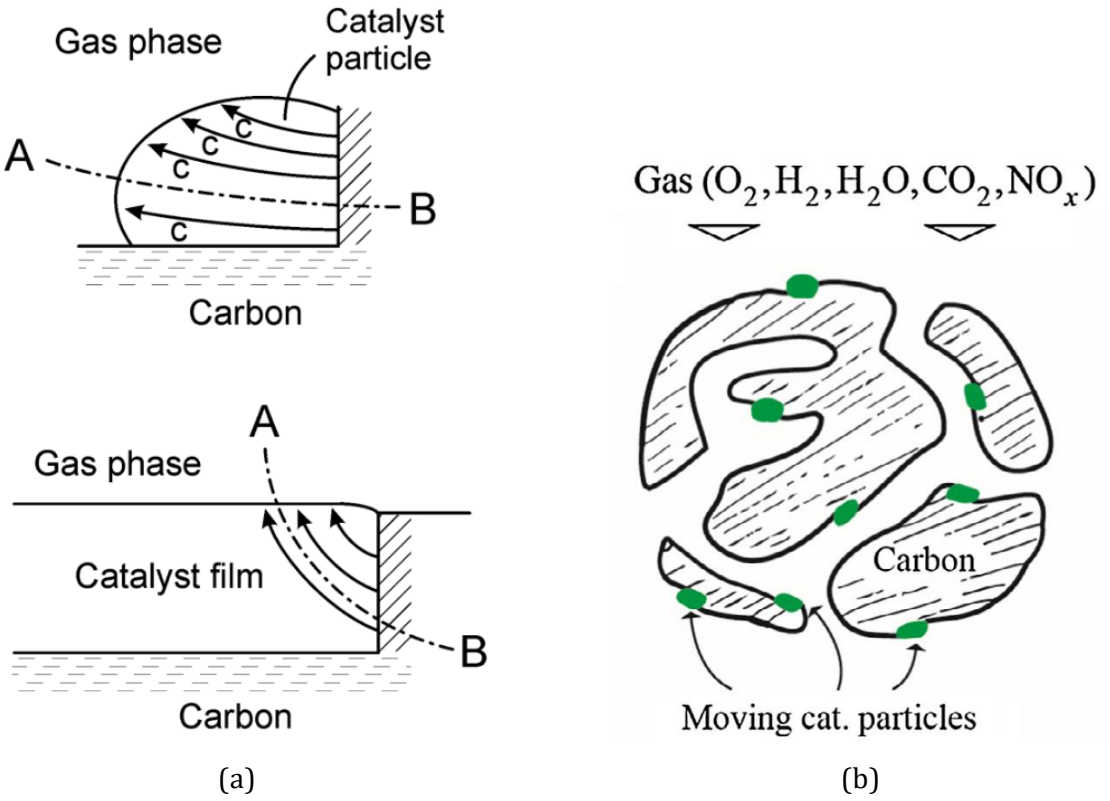

Fig. 2.5. (a) Schematic illustration of the carbon diffusion process through a catalytically active component, top: solid catalyst particle, bottom: molten catalyst film [137]; (b) Movement of catalyst nanoparticles under reaction conditions forming an overall reaction front while consuming carbon [54].

Various ash components exhibit different catalytic activity during char gasification. Lahijani et al. [128] investigated the catalytic influence of alkali (Na, K), alkaline earth (Ca, Mg) and transition (Fe) metal salts on the CO_2 gasification reactivity of biomass char. Fig. 2.6 shows the carbon conversion curves during gasification of pistachio nut shell (PNS) chars impregnated using various metal nitrates (3 wt.-%) with CO_2 at 875 °C in a TGA. The experiments showed a significant increase of char reactivity for the impregnated samples as compared to the raw char that can be deduced from the decreasing total conversion times. Based on their results, the authors were

able to formulate the following order of catalytic activity for the inorganic ash components investigated: Na > Ca > Fe > K > Mg. The authors also investigated the influence of metal salt loading on the char reactivity by varying the $NaNO_3$ content between 3 wt.-% and 7 wt.-%. Here, the highest reactivity was observed during gasification of PNS char impregnated with 5 wt.-% $NaNO_3$ suggesting an optimum for metal salt loading and decreasing char reactivity for higher Na contents.

During gasification with H_2O, however, Zhang et al. [82] report that alkaline metals (K and Na) exhibit much higher catalytic activity than alkaline earth metals (Ca and Mg) and K being the most active species for char gasification. For their experiments, the authors impregnated activated carbon (AC) with KCOOH, NaCOOH, $Ca(COOH)_2$ or $Mg(COOH)_2 \cdot 4H_2O$, respectively.

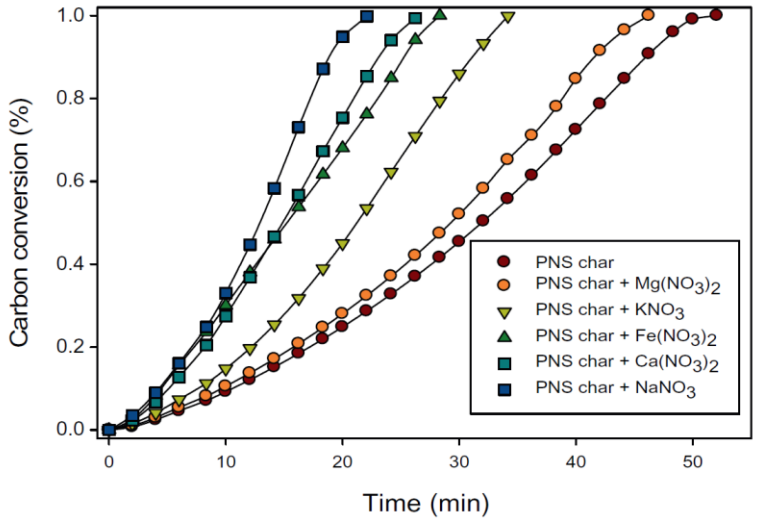

Fig. 2.6. Carbon conversion during gasification of pistachio nut shell (PNS) chars impregnated using various metal nitrates (3 wt.-%) with CO_2 at 875 °C in a TGA [128].

Struis et al. [130] investigated the catalytic activity of different metal elements (Na, K, Ca, Mg, Zn, Pb, Cu) found in the ashes of waste wood and their influence on the resulting carbon conversion curve. For the experiments, the authors impregnated fir wood with the corresponding metal nitrate solutions and pyrolyzed the samples subsequently in a two-step process. Their results indicate a superposition of structural changes in the micropore domain of the char particle as well as catalyst-specific effects during gasification of the impregnated samples with CO_2. Fig. 2.7 (a) shows a comparison of conversion rates (reaction rates as denoted by the authors) during gasification of fir wood chars impregnated with alkaline nitrate salts i.e. $NaNO_3$ and KNO_3. Gasifica-

tion of these samples with CO_2 resulted in a conversion rate maximum at X_C = 0.5 – 0.7. The authors explained this maximum with the accumulation of an oxidic alkali type catalyst (Me_xO_y) which is formed during the early gasification stage. In Fig. 2.7 (b), the conversion rates during gasification of fir wood chars impregnated with alkaline earth metals is depicted. Results show that alkaline earth nitrate salts exhibit a high catalytic activity during the early gasification stage followed by a decreasing conversion rate for the whole carbon conversion range. This phenomenon may be evoked by sintering processes of the resulting alkaline earth metals, as the authors presumed.

"An important parameter to evaluate the catalytic activity of ash forming elements is the dispersion on the char surface [120,138]. Cazorla-Amoros et al. [29] investigated the dispersion and sintering of Ca species on carbon samples during pyrolysis and gasification with CO_2. They found a strong link between Ca dispersion and carbon-CO_2 reactivity and were able to deduce the following findings: first, a high heating rate during pyrolysis resulted in a high calcium dispersion. Second, Ca dispersion decreased with increasing carbon burn-off during gasification with CO_2 suggesting a deactivation mechanism presumably due to sintering processes. Furthermore, results showed the enormous effect of chemical state of calcium ($CaCO_3$ or CaO) on the sintering rate. It was observed that $CaCO_3$ had a much higher mobility on the carbon surface than CaO because of the great difference in their Tammann temperatures." [108]

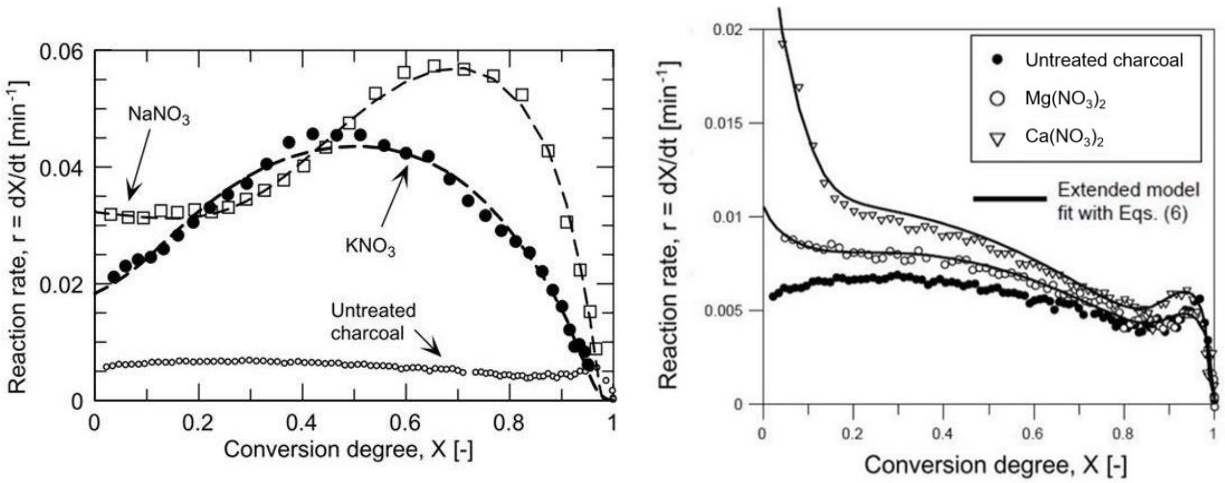

(a) (b)

Fig. 2.7. Comparison of conversion rates during gasification of fir wood chars impregnated with (a) alkaline metals and (b) alkaline earth metals with CO_2 as a function of conversion degree; adapted from [130].

3 Materials and methods

3.1 Fuel characterization

3.1.1 Primary chars

In the frame of this work, two different primary chars (both based on beech wood) were used as precursor for the pyrolysis experiments in the Drop-tube reactor (DTR) (see chapter 3.2). According to the bioliq® process, these chars were generated at moderate temperatures of approx. 500 °C to 600 °C still containing volatiles and heteroatoms i.e. H, O, N to some extent.

The first primary char, called WC500, was produced from bark-less beech wood in a screw pyrolysis reactor (STYX at Institute for Technical Chemistry (ITC), KIT) at 500 °C and a solid material residence time of five minutes. A detailed description of the screw pyrolysis reactor STYX can be found in literature [139,140]. After pyrolysis in the screw reactor, the primary char was milled in a blade granulator. Data from proximate and ultimate analysis are illustrated in the appendix (see table B.1). The primary char contains approx. 26 wt.-% of volatiles, 3 wt.-% of moisture and 2 wt.-% of ash. Furthermore, the organic components consist of approx. 80 wt.-% carbon, 3 wt.-% hydrogen and 17 wt.-% oxygen (by difference). WC500 was predominantly used to produce high temperature secondary chars in the DTR at 1600 °C that consist of almost pure carbon, have practically no volatiles, a minimum amount of heteroatoms and were therefore considered as biogenic model fuels (see chapter 3.1.2).

The other primary char used in the present work is a commercially available beech wood char (Holzkohleverarbeitung Schütte GmbH & Co. KG) referred to as HK06. This char is utilized as feedstock in the bioliq® entrained-flow gasifier and fed into the gasifier as a suspension fuel mixed with pyrolysis oil for research operation. Data from proximate and ultimate analysis can be found in the appendix (see table B.1). As compared to WC500, HK06 has a lower amount of volatile matter (approx. 12 wt.-%) and with almost 90 wt.-% a higher amount of carbon. Total ash content is similar for both chars. In the frame of this work, HK06 was used to study the influence of pyrolysis conditions on the physico-chemical properties i.e. morphology, carbon matrix and catalytically active ash components of the resulting secondary chars [108].

The ash elemental analysis of both primary chars was determined by inductively coupled plasma optical emission spectrometry (ICP-OES) (see table B.2). It can be seen that the inorganic matter composition is similar for both samples since they both originate from beech wood. According to the chemical classification system of biomass ash proposed by Vassilev et al. [141], both chars

can be assigned to type C corresponding to wood and woody biomass with low to medium acid tendency (see appendix A). The main component of both primary char ashes is by far calcium with 36.1 wt.-% for WC500 and 38.2 wt.-% for HK06, respectively. The only major difference between both chars is found in terms of silica being 8 wt.-% for WC500 and 2 wt.-% for HK06. In general, HK06 is slightly depleted in Al and Fe while being enriched in K, Mg and Ca as compared to WC500.

3.1.2 Secondary chars

Secondary chars were generated in a DTR (see chapter 3.2) imitating the process conditions found during the devolatilization step in an entrained-flow gasifier i.e. high temperatures, high heating rates and short residence times. Starting from the primary char WC500 as precursor, two secondary chars referred to as WC1600 and WC1600n were produced in the DTR at 1600 °C and 200 ms residence time. Data from proximate and ultimate analysis of both secondary chars is illustrated in the appendix (see table B.3). It can be seen that both secondary chars originating from WC500 show high amounts of carbon (approx. 97 wt.-%) and a low amount of volatiles (4.6 wt-% and 2.4 wt. % respectively). A higher discrepancy can be observed for the total ash content of both chars. This difference can be traced back to the sample selection of the primary char WC500 prior to the secondary pyrolysis experiments. For the production of WC1600 in the DTR, the fine material of WC500 was directly taken from the container and subsequently sieved into the desired particle fraction (50 – 150 µm). In the fine material, however, inorganic matter usually accumulates due to the lower size of the ash particles (nanometer scale). The production of WC1600 in the DTR was carried out in a previous work [142]. For the generation of WC1600n in the DTR, in contrast, larger WC500 particles (millimeter scale) were taken and milled using an ultra centrifugal mill (ZM 100, Fa. Retsch) before sieving into the desired particle fraction (50 – 150 µm).

Due to the low amount of volatiles and the high fraction of carbon, both secondary chars (WC1600 and WC1600n) were referred to as biogenic model fuels. These chars were primarily used to assess and validate experimental methods for the determination of gasification kinetics in various set-ups [49]. Furthermore, these model fuels allowed for a detailed investigation of char morphology as a function of carbon conversion degree [143].

Two secondary chars referred to as P1400 and P1600 originating from HK06 were used to determine heterogeneous gasification kinetics with CO_2 and H_2O at elevated pressure [57]. Both secondary chars were generated in a DTR (see chapter 3.2) at a residence time of 200 ms and

pyrolysis temperatures of 1400 °C and 1600 °C, respectively. Prior to the pyrolysis experiments, the primary char HK06 was milled (ultra centrifugal mill) and sieved to a particle size fraction of 50 – 150 µm. Data from proximate and ultimate analysis for P1400 and P1600 can be found in the appendix (see table B.3). Again, the carbon amount of both chars was high with approx. 97 wt.-% for P1400 and 99 wt.-% for P1600 while volatile content was relatively low being 2.5 wt.-% and 1.3 wt.-%, respectively. Ash content of both chars was very similar being approx. 2 wt.-%. The gasification experiments were carried out in a pressurized single-particle reactor (see chapter 3.3) at elevated pressure using CO_2, H_2O and its mixture as reactant gases.

Additionally, both chars were part of a systematic study investigating the influence of pyrolysis conditions on the physico-chemical char properties i.e. morphology, carbon matrix and catalytically active ash components [108]. Here, secondary chars were produced from HK06 in a DTR at 200 ms and temperatures varying between 1000 °C and 1600 °C. Furthermore, the effect of calcium dispersion and graphitization degree of the resulting secondary chars on the gasification reaction with CO_2 was studied in a TGA. A detailed characterization of all chars utilized in this experimental campaign can be found in the corresponding reference [108].

The ash elemental analysis of the secondary chars was determined by ICP-OES (see table B.4). Again, calcium constitutes the main component in the ash of the secondary chars presented. Major differences can be observed in the amount of silica being approx. 26 wt.-% for WC1600 and only 9 wt.-% for WC1600n. Both secondary chars originate from the same parent fuel (WC500). However, the sample selection and preparation were different prior to the pyrolysis experiments as explained before in this chapter leading to significant changes in the inorganic matter composition. Due to the high amount of silica and potassium in the ash of WC1600, these elements presumably accumulated in the fine material of the parent fuel. On the contrary, WC1600n is enriched in calcium by approx. 10 wt.-% as compared to WC1600. Both secondary chars originating from HK06 (P1400 and P1600) show a similar low amount of silica of 2.5 wt.-% which is corresponding to the parent fuel. Moreover, a depletion of Mg can be observed from P1400 to P1600 indicating a devolatilization of magnesium at the highest pyrolysis temperature of 1600 °C accompanied by an enrichment of calcium from 35 wt.-% to 39 wt.-%.

3.1.3 Impregnated activated carbon

Commercially available activated carbon (AC) with an ash content < 1wt.-% (Merck CAS 7440-44-0, particle diameter < 100 µm, BET surface area 740 $m^2\ g^{-1}$) was used to investigate the catalytic behavior of calcium and potassium during gasification with CO_2. AC was impregnated with

calcium nitrate and potassium nitrate in a round bottom flask filled with 5 g of the AC sample and the corresponding solution of metal salt in demineralized water. Subsequently, the flask was attached to a vacuum rotary evaporator (Heidolph VV 2000) and lowered into a water bath, which was tempered at 55 °C and rotated with 30 min^{-1}. The pressure was decreased to 170 mbar using a vacuum pump. The liquid was completely evaporated after approx. 4 hours. Eventually, the impregnated chars were dried for 12 h at 105 °C. Calcium, potassium and silica mass fractions were determined by ICP-OES. These values can be found in the appendix (see table B.5) for the raw activated carbon and three impregnated samples AC1Ca, AC2Ca and AC1K.

3.2 Drop-tube reactor

The drop-tube reactor (DTR) was used to generate high-temperature secondary chars originating from primary chars WC500 and HK06 under high heating rates and short residence times (see chapter 3.1). Furthermore, the model fuel WC1600n was partially gasified with CO_2 in the DTR in order to investigate char morphology as a function of carbon conversion degree.

The DTR was designed, constructed and commissioned in the frame of a previous work [142]. A flow sheet of the reactor set-up can be found in the appendix (see Fig. B.1). It consists of an oven with three heating zones (l_{H1} = 200 mm, l_{H2} = 920 mm, l_{H3} = 200 mm) and a maximum temperature of 1700 °C (1650 °C for continuous operation). For the secondary pyrolysis experiments, an alumina oxide reaction tube with a length of 2100 mm and an inner diameter of 20 mm was inserted vertically into the oven. For the partial gasification experiments, a reaction tube with an inner diameter of 40 mm was used. Temperature calibration was conducted with a type B thermocouple, which was introduced from top into the reactor under steady state gas flow but without solid fuel dosing. Axial gas temperature profiles for secondary pyrolysis experiments using HK06 as precursor can be found in the appendix (see Fig. B.2). The product gas concentration was continuously analyzed by infrared photometry and gas chromatography. Further information concerning the DTR as well as the operating conditions during pyrolysis and gasification experiments can be found in literature [108,142–144].

3.3 Pressurized single-particle reactor

In the frame of the present work, a novel pressurized single-particle reactor (pSPR) was designed, constructed and commissioned allowing for the determination of gasification kinetics of biogenic solid fuels with CO_2 and H_2O at elevated pressure. A schematic flow diagram of the reactor set-up is depicted in Fig. 3.1. The gas dosing system consists of mass flow controllers (MFC)

for CO_2 and Ar. Demineralized water is stored in a vessel (V = 1 dm³) and pressurized with 30 bar of helium and can be dosed using a mini CORI-FLOW. Steam is generated in a Controlled Evaporation and Mixing unit (CEM) and led into the reactor together with a carrier gas. The tubular reactor (1200 mm height, 19.5 mm inner diameter) is mounted vertically and can be operated at a pressure of up to 24 bar and a maximum temperature of 1000 °C (900 °C for continuous operation). The pressure is controlled by two back pressure regulators. Product gases are analyzed using infrared photometry and gas chromatography. The reactor was operated in a differential way allowing only for very low changes in the educt gas phase composition during gasification experiments ($\Delta c_{CO_2} < 3\ \%$).

Detailed information concerning the pSPR, the operating conditions and the modeling methods during gasification experiments at elevated pressure can be found in the appendix B and in literature [57,145,146].

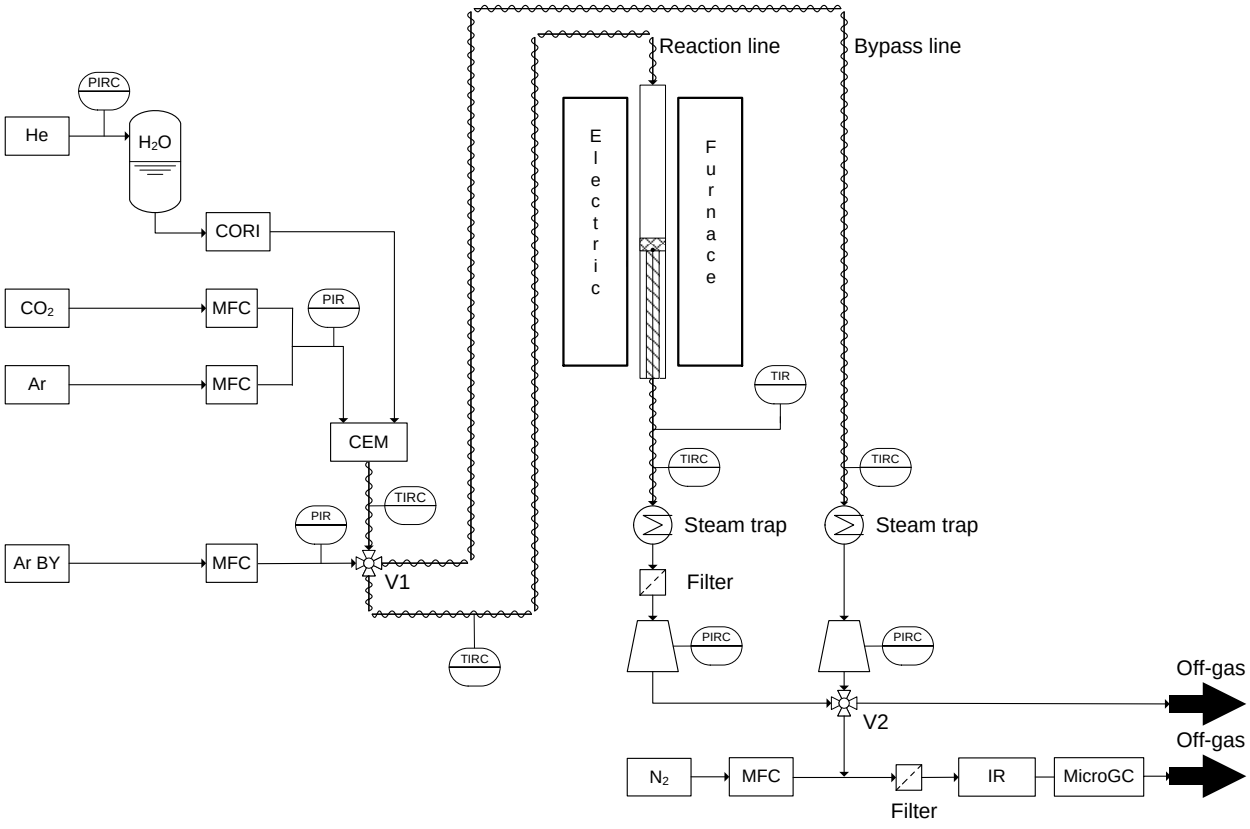

Fig. 3.1. Schematic flow diagram of the single-particle reactor used for pressurized gasification experiments at EBI ceb, KIT [57].

3.4 Pressurized thermogravimetric analyzer

The pressurized thermogravimetric analyzer (pTGA, Rubotherm GmbH) was used to assess and validate experimental methods for the determination of gasification kinetics of WC1600 with CO_2 in various set-ups at atmospheric pressure [49]. Furthermore, the initial conversion rate R_0 of various secondary chars with CO_2 was determined in order to investigate the influence of ash dispersion, graphitization and morphology on the gasification rate [108]. Additionally, kinetic data from the pTGA during gasification of P1400 with CO_2 at elevated pressure was used to validate the results obtained in the pSPR [145]. Besides gasification experiments, the dispersion of CaO particles on the char surface was determined by chemisorption in the TGA [108]. A schematic flow diagram of the set-up can be found in the appendix (see Fig. B.5).

The pTGA consists of a magnetic suspension balance which allows for a continuous recording of the sample mass with an accuracy of ± 10 µg. In the gasification experiments, the total gas flow was varied between 100 – 200 ml min^{-1}. The sample mass of approx. 2 ± 0.1 mg was placed in the ceramic crucible with an inner diameter of 16 mm and a wall height of 10 mm. Prior to the gasification experiment, the reaction chamber was evacuated two times and purged with argon. The char samples were heated up at a constant heating rate of 20 K min^{-1} to the desired reaction temperature followed by 20 min holding time to ensure stable conditions. The initial conversion rate R_0 was determined by a least-square fit in the carbon conversion range between 0.2 and 0.5. This range was chosen in order to minimize the effect of the gas exchange at the start of each gasification segment. Furthermore, char properties were only characterized prior to gasification and may have changed significantly throughout the course of reaction (see chapter 2.3).

The quantification of CaO dispersion was conducted in the pTGA using the temperature-programmed reaction (TPR) technique. In each TPR experiment, a sample mass of 30 ± 0.1 mg and a CO_2 volume flow of 100 ml min^{-1} was used. Prior to the chemisorption segment, the reactor was evacuated and backfilled with argon two times. Subsequently, the char sample was heated to 850 °C in flowing argon to decompose any $CaCO_3$ if present. After cooling and stabilizing at 300 °C, the chemisorption segment started by switching the gas atmosphere from pure argon to a mixture of 90 vol.-% argon and 10 vol.-% CO_2 for 300 min. Detailed information concerning the pTGA set-up, the operating conditions and the modeling methods during gasification and chemisorption experiments can be found in literature [49,108,143,145].

3.5 Chemisorption analyzer

The chemisorption analyzer (BELCAT-II, MicrotracBEL) was used for the determination of active sites during gasification of WC1600 and impregnated activated carbon samples with CO_2 using temperature-programmed desorption (TPD) [147,148]. A schematic drawing of the quartz glass reactor system is presented in the appendix (see Fig. B.6).

The glass reactor consists of two concentric quartz tubes. The reactant gas is introduced through the outer tube and heated up to reaction temperature. The char sample is located between two quartz wool layers in the inner reactor tube (inner diameter of 8 mm). The sample temperature is measured by a type K thermocouple that is in contact in the fixed-bed. Gas species i.e. CO, CO_2 and Ar are continuously monitored by a quadrupole mass spectrometer (MS).

RSA was investigated as a function of carbon conversion degree X_C. The biomass char samples were partially gasified up to carbon conversion degrees of 0.25, 0.50, 0.75 and 0.90. Prior to each gasification segment, the sample was degassed for 1 h at 900 °C in flowing argon and cooled down to gasification temperature. Subsequently, partial gasification up to the desired carbon conversion degree was conducted at 820 °C and atmospheric pressure in a mixture of 80 vol.-% CO_2 and 20 vol.-% argon. A sample mass of 30 mg and a total volume flow of 100 ml min^{-1} were applied to ensure differential operation of the chemisorption analyzer ($\Delta c_{CO_2} < 3$ %). RSA was determined using a two-step procedure: First, total surface complexes (TSC) during the gasification reaction were measured by quenching the char sample to 200 °C in reactant gas atmosphere after reaching the desired carbon conversion degree. After the CO concentration in the off-gas reached baseline level, the gas atmosphere was switched to pure argon. Subsequently, a TPD was performed in flowing argon with a heating rate of 3 K min^{-1} to a final temperature of 900 °C. The desorption of CO and CO_2 was measured in the MS. For the determination of stable surface complexes (SSC), the gas atmosphere was switched to argon at reaction temperature in order to desorb all unstable C(O) complexes. After quenching to 200 °C, the same TPD was performed again. The RSA was calculated by the difference of TSC and stable surface complexes. A detailed description of the experimental and mathematical methods can be found in literature [147,148].

4 Results and discussion

4.1 Evolution of char properties during gasification reaction

In this chapter, evolution of morphology, concentration of catalytically active ash components and number of active sites during heterogeneous gasification of a char particle with CO_2 are analyzed. Furthermore, their influence on char reactivity and the course of gasification reaction as a function of carbon conversion is investigated. The results are presented in detail in two publications [147,148] (Papers **III** & **IV**) as well as one master thesis [143]. Research question 1 is answered within this chapter:

Question 1: *Which biogenic char properties affect heterogeneous gasification reactions predominantly and how do they change upon char gasification?*

4.1.1 Morphology

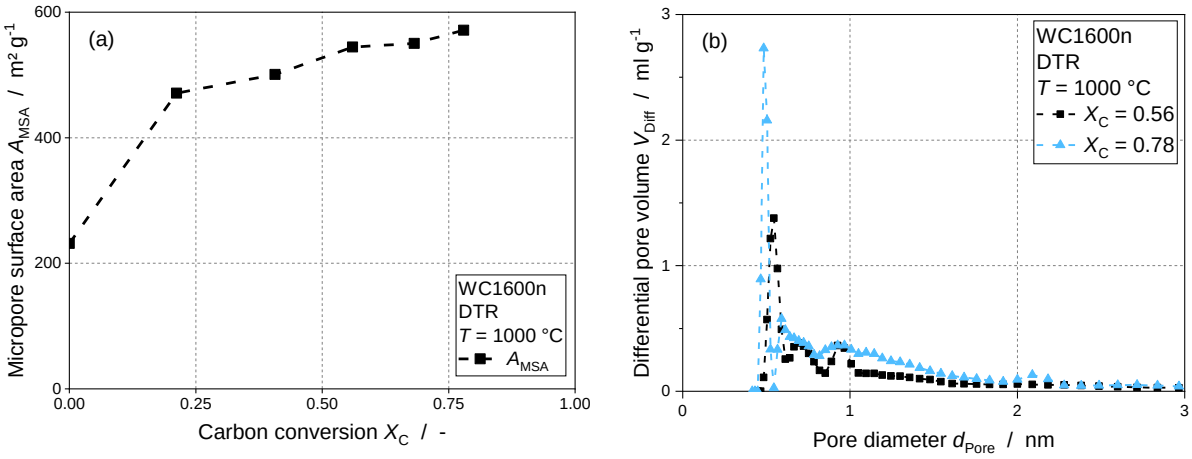

Fig. 4.1. (a) Evolution of micropore surface area A_{MSA} as a function of carbon conversion degree and (b) differential pore volume as a function of pore diameter during gasification of WC1600n at 1000 °C and 1,5 s residence time in the DTR; adapted from [143].

The aim was to analyze char morphology i.e. micropore surface area and pore size distribution during the gasification process in order to characterize the changes as a function of carbon conversion degree. The approach constitutes the production of the model fuel WC1600n under EFG conditions in the DTR. The secondary char consists almost solely of carbon and contains nearly no volatile matter. Subsequently, WC1600n was partially gasified in the DTR at 1000 °C (microkinetic regime I) and a residence time of 1,5 s for several cycles. A final carbon conversion degree of X_C = 0.78 was achieved after 10 cycles. After each gasification cycle, the samples were analyzed in terms of micropore surface area A_{MSA} by physisorption of CO_2 at 0 °C using the DR method. The

micropore surface area A_{MSA} quantifies the TSA that exclusively accounts for micropores (< 2 nm, see chapter 2.3.1). Furthermore, two samples at carbon conversion degrees X_C of 0.56 and 0.78 were analyzed by physisorption of argon at 87 K in order to characterize the pore size distribution using density functional theory (DFT). The latter analyses were conducted by Quantachrome (Odelzhausen, Germany). Fig. 4.1 (a) shows the evolution of micropore surface area A_{MSA} as a function of carbon conversion degree. In general, A_{MSA} increases for increasing carbon conversion degrees. Especially between X_C = 0 and X_C = 0.21, a steep increase of A_{MSA} from 232 $m^2\ g^{-1}$ to 471 $m^2\ g^{-1}$ can be observed. It can be assumed that the gasification reaction with CO_2 in the microkinetic regime predominantly generates micropores. This statement can be verified by the results from the argon physisorption analyses depicted in Fig. 4.1 (b). Increasing the carbon conversion degree from X_C = 0.56 to X_C = 0.78, the differential pore volume increases significantly at approx. 0.5 nm. Additionally, the total pore volume between 0.5 nm and 1.5 nm for the sample at a carbon conversion degree of X_C = 0.78 is higher as compared to the sample at X_C = 0.56. In the appendix (see Fig. C.1), the adsorption isotherms of both samples with argon at 87 K are depicted. It is obvious that the shape of both isotherms can be assigned to type I according to the IUPAC classification system (high microporosity, no mesopores).

In conclusion, micropore surface area increases significantly during gasification of WC1600n with CO_2 in the DTR at 1000 °C. Based on the results reported, the gasification reaction with CO_2 predominantly generates micropores. Here, new surface area is created by the consumption of solid carbon.

4.1.2 Effect of inorganic matter on the conversion rate R_X

The aim was to investigate the effect of catalytically active ash components that are usually present in abundance in biogenic fuels on the char reactivity and the conversion rate as a function of carbon conversion degree. For this purpose, pure activated carbon (AC) (CAS 7440-44-0, Merck) was impregnated with calcium and potassium nitrate salts. Subsequently, the impregnated samples (AC1Ca and AC1K) as well as the raw AC were gasified in the pTGA at 800 °C and atmospheric pressure (80 vol.-% CO_2 and 20 vol. % Ar). Fig. 4.2 shows the raw data as well as the trend lines (moving averages) of the conversion rate R_X as a function of carbon conversion degree for all three samples. The conversion rate of the raw AC sample was very low as compared to the other 2 samples with a mean conversion rate of approx. $4 \cdot 10^{-5}\ s^{-1}$ with a total gasification time of approx. 8 h at the process conditions applied. On the other hand, the addition of calcium or potassium changes the course of the conversion rate upon carbon conversion drastically. During

gasification of AC1Ca, the conversion rate steadily decreases for increasing carbon conversion degrees while total gasification time decreases by a factor of 6 (approx. 80 min) as compared to the raw AC char. The conversion rate of AC1K, on the other hand, shows a maximum at approx. X_C = 0.6 – 0.7 while total gasification was only 20 min. Struis et al. [130] observed similar gasification behavior during gasification experiments of impregnated fir wood samples (see chapter 2.3.3). According to the authors, the high initial conversion rate followed by a decreasing conversion rate for char samples impregnated with calcium salts may be due to sintering processes of the resulting alkaline earth metal oxide reducing the dispersion of the catalytically active ash particles. In contrast, the authors assume that the maximum during gasification of chars impregnated with potassium salts is related to an accumulation of an oxidic alkali type catalyst (Me_xO_y) being formed during the early gasification stage which is predominantly responsible for the catalytic activity.

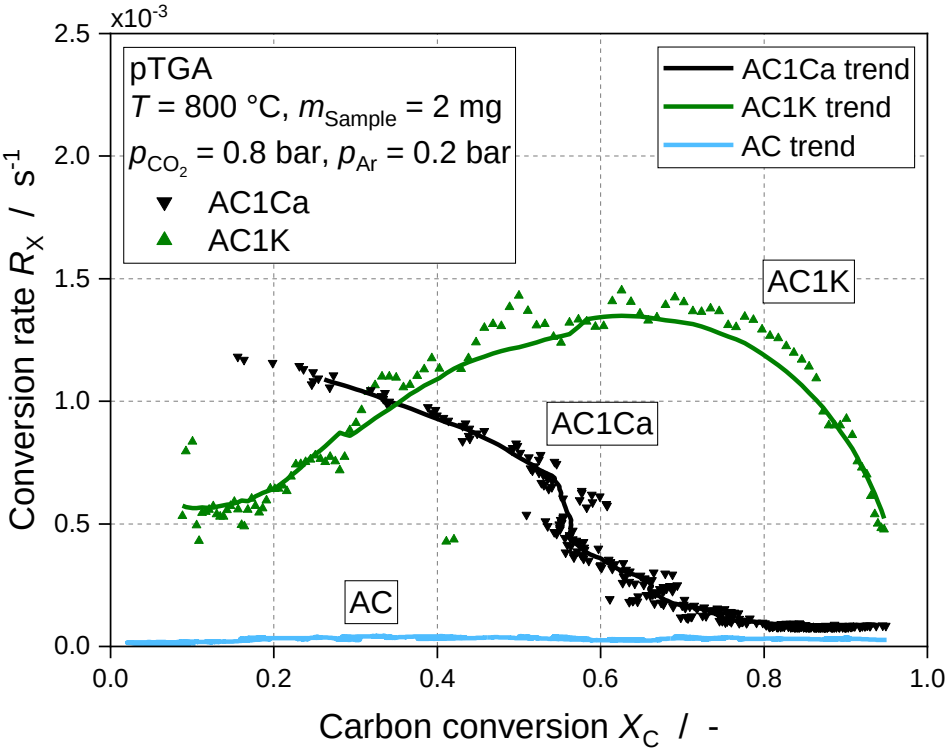

Fig. 4.2. Conversion rate R_X as a function of carbon conversion degree X_C during gasification of raw AC and impregnated AC samples with CO_2 in the pTGA at 800 °C and atmospheric pressure (80 vol.-% CO_2, 20 vol.-% Ar); adapted from [143].

As a result of the impregnation, the surface of the raw AC char has been modified. The influence of the impregnation process on the resulting specific surface area (SSA) was investigated by physisorption of N_2 at 77 K using the BET method. Table 4.1 shows the values obtained for the raw AC and the sample AC2Ca impregnated with calcium nitrate. The results show that due to impregnation, the specific surface area of AC2Ca halves as compared to the raw AC sample. This effect was also reported in literature [121]. Despite the lower SSA, total gasification time of AC2Ca with CO_2 in the pTGA at 800 °C and atmospheric pressure (80 vol.-% CO_2, 20 vol.-% Ar) was approx. 15 min while being 8 h for the raw AC sample (factor 32).

Table 4.1. Specific surface areas of raw AC and impregnated AC2Ca sample determined by physisorption of N_2 at 77 K using BET method [143].

	AC	AC2Ca
Specific surface area A / $m^2\ g^{-1}$	740	340

In conclusion, catalytically active ash components that are usually found in biomass (i.e. calcium and potassium) affect char reactivity and the course of the conversion rate as a function of carbon conversion degree significantly. Their influence on the gasification behavior with CO_2 may be regarded as superior as compared to morphological properties for the process conditions investigated (regime I conditions).

4.1.3 Determination of active sites

Based on Fig. 4.2 and table 4.1 from the previous chapter, the influence of specific or micropore surface area may be of minor significance during gasification of bio-chars with CO_2. Therefore, the aim of the following investigation was to quantitatively determine the amount of active sites and the reactive surface area (RSA) during the gasification of biogenic model fuel (WC1600) using the TPD technique. Total (TSC) and stable (SSC) surface complexes were determined at different carbon conversion degrees based on a two-step approach. According to the reaction mechanism proposed by Lizzio et al. [91], TSC and SSC must originate from oxygenated carbon atoms on the char surface (also noted as carbon–oxygen intermediates). These carbon-oxygen intermediates are bound on the surface of carbonaceous materials in the form of oxygen functional groups, i.e. lactones, carbonyls, anhydrides, phenols, ethers and quinones. During the desorption segment of the TPD experiment, the bonds of these functional groups are destroyed leading to a release of gaseous species such as CO, CO_2 and H_2O.

The experimental two-step approach involves the gasification of the char sample in CO_2 until the desired conversion degree at first. For the determination of TSC, the sample was subsequently quenched in CO_2 followed by a TPD in argon. For the determination of SSC, the sample was quenched in argon followed by a TPD in argon. Desorption of CO and CO_2 was continuously monitored. TSC and SSC were calculated via integration of the CO and CO_2 molar flow rates in the exhaust gas during TPD. Eventually, the RSA was obtained by calculating the difference between TSC and SSC. For further details on the methodology, Papers I & II can be consulted.

Fig. 4.3 shows the TPD spectra for the WC1600 char samples gasified up to X_C = 0.75 in the chemisorption analyzer at 820 °C with 80 vol.-% CO_2 and 20 vol.-% Ar. During TPD, CO_2 and CO desorb from total and stable surface complexes. According to the reaction mechanism proposed by Lizzio et al. [91], TSC should always be higher than SSC. However, this is not the case for CO_2 at approx. 430 °C, since SSC is higher than TSC. Thus, desorbing gases may not only originate from oxygenated surface complexes but also from decomposition of carbonated ash compounds.

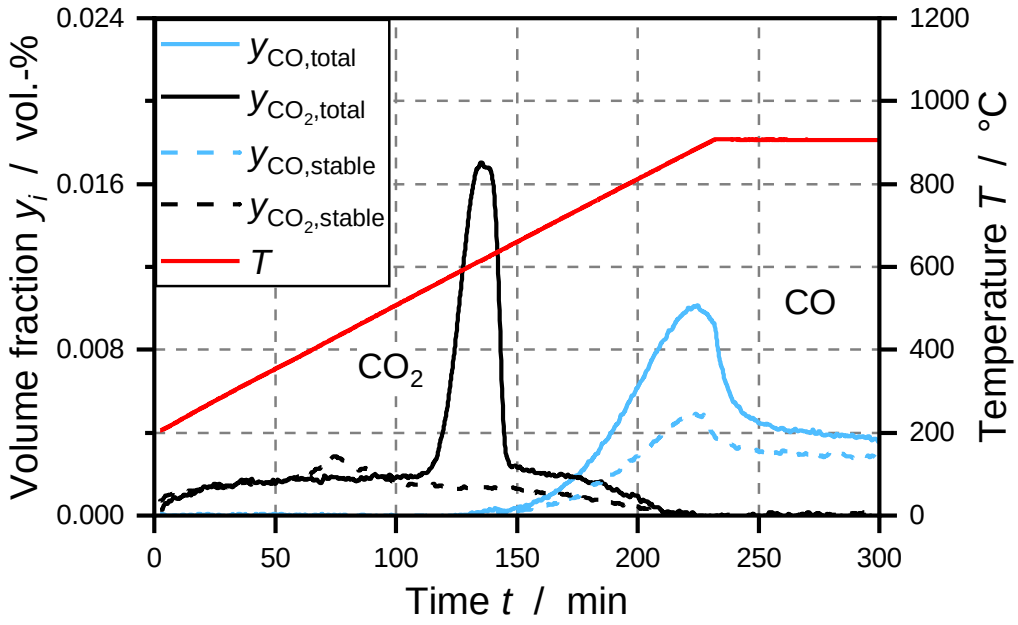

Fig. 4.3. TPD spectra for the WC1600 char samples gasified up to X_C = 0.75; gasification of WC1600 at 820 °C with 80 vol-% CO_2 and 20 vol-% Ar at atmospheric pressure in the chemisorption analyzer; total and stable complexes desorbed as CO_2 and CO; adapted from [147].

In fact, three different types of sites on the char surface can be observed during gasification of WC1600 with CO_2: stable and reactive sites as proposed and defined by Lizzio et al. [91] and additionally catalytically active sites representing the influence of inorganic ash components.

The released amounts of CO_2 and CO can be considered to be a measure of the catalytic influence of inorganic matter during the gasification reaction.

Fig. 4.4 shows the specific conversion rate R_m as a function of reactive plus catalytically active sites for the gasification of WC1600 at 820 °C in 80 vol.-% CO_2. A linear correlation is derived from the experimental data. This indicates that the calculated value $x_{reactive+catalytic}$ is an appropriate measure of the available sites on the char surface participating in the gasification reaction of WC1600 with CO_2. Eq. 4-2 represents an analytical expression for the linear fit of the experimental values reported in Fig. 4.4 implying that the surface concentration of active sites available for the gasification reaction c_{C_f} is proportional to the specific conversion rate during the gasification reaction, as the specific conversion rate constant k depends only on temperature.

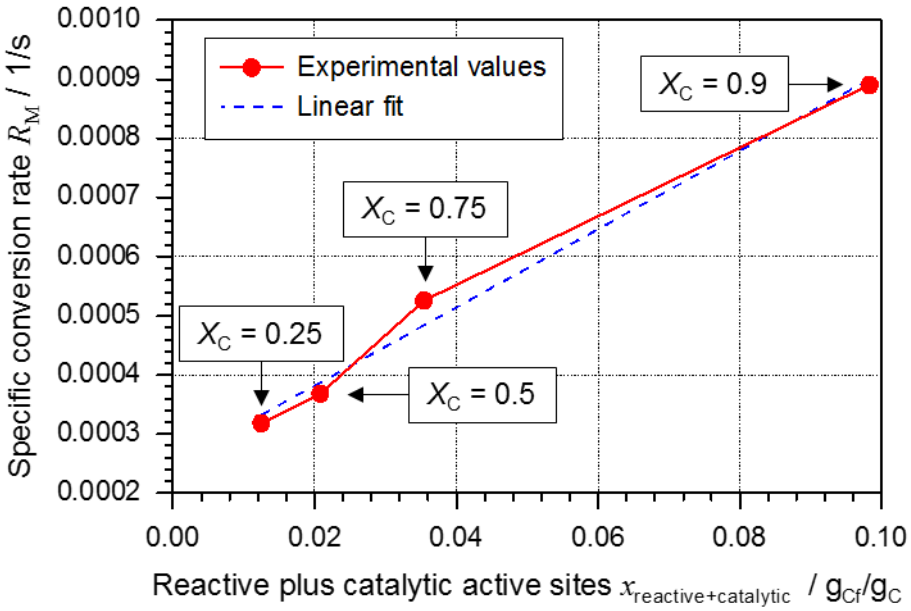

Fig. 4.4. Specific conversion rate as a function of $x_{reactive+catalytic}$ for the gasification of WC1600 at 820 °C in 80 vol-% CO_2 in the chemisorption analyzer; adapted from [148].

$$R_m = \frac{1}{1 - X_C(t)} \frac{dX_C}{dt} = k\, c_{C_f} \tag{4-1}$$

$$R_m = 0.006616\ s^{-1}\, x_{reactive+catalytic} + 0.000249\ s^{-1} \tag{4-2}$$

4.2 High-temperature pyrolysis of biogenic solid fuel

The following chapter outlines the changes in char properties during high-temperature pyrolysis in a DTR. Moreover, the effect of calcium dispersion and graphitization degree on the gasification

reactivity with CO_2 is discussed. The results are presented in detail in the publication Schneider, Walker et al. [108] (Paper **II**). Research question 2 is answered within this chapter:

Question 2: *How are biogenic char properties influenced by secondary pyrolysis during entrained-flow gasification?*

4.2.1 Micropore surface area

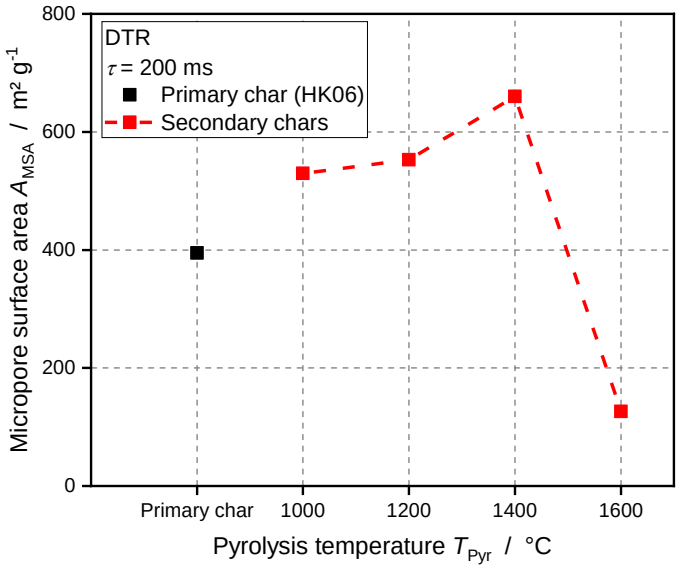

Fig. 4.5. Micropore surface area of primary (HK06) and secondary chars generated in the DTR at 200 ms as a function of pyrolysis temperature determined by physisorption of CO_2 at 0 °C using DR method; adapted from [108].

The aim was to characterize char morphology i.e. micropore surface area of primary and secondary chars as a function of pyrolysis temperature and correlate the values with the initial conversion rate R_0 during gasification with CO_2. For this, pyrolysis experiments of the primary char HK06 were conducted in the DTR between 1000 °C and 1600 °C under high heating rates and a residence time of 200 ms imitating the conditions found during EFG. Micropore surface area was determined by physisorption of CO_2 at 0 °C using the DR method (ASAP 2000, Micromeritics). Results indicate a slight increase of micropore surface area starting from primary char HK06 from approx. 400 $m^2\ g^{-1}$ up to 660 $m^2\ g^{-1}$ at a pyrolysis temperature of 1400 °C (see Fig. 4.5). Due to the high heating rates in the DTR, additional surface area is created by rapid devolatilization (see chapter 2.1). Furthermore, secondary reactions between pyrolysis gases, i.e. CO_2, and the resulting char (Boudouard reaction) may occur that possibly lead to an increase in micropore surface area (see chapter 4.1.1). At 1600 °C, however, the micropore surface area erratically decreases to a value of approx. 126 $m^2\ g^{-1}$. This phenomenon may be explained by the formation of

a molten ash layer on the char surface clogging micropores which was detected using SEM/TEM images. A possible correlation between micropore surface area and initial conversion rate R_0 during gasification with CO_2 in the pTGA could not be established (see chapter 4.2.2).

4.2.2 Initial conversion rate

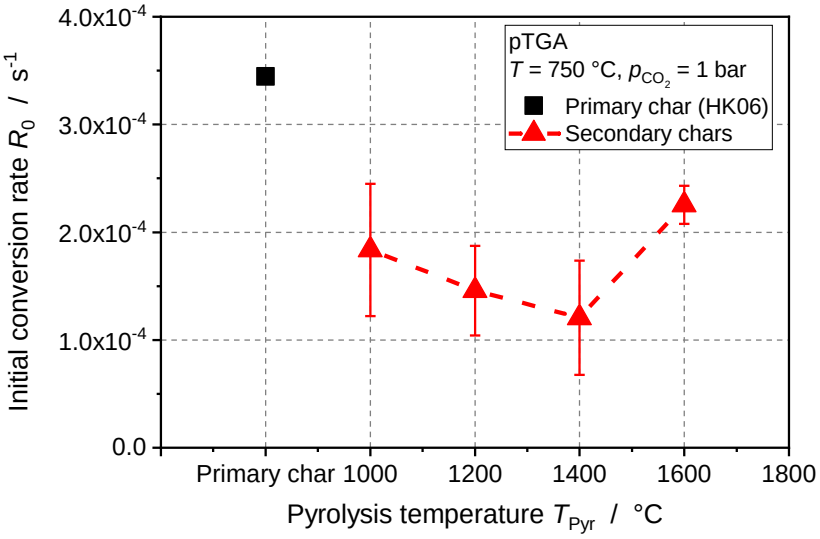

Fig. 4.6. Initial conversion rate R_0 during gasification of primary (HK06) and secondary chars generated in the DTR with CO_2 in pTGA (750 °C, 100 vol.-% CO_2, atmospheric pressure) as a function of pyrolysis temperature; adapted from [108].

The objective was to investigate the influence of pyrolysis temperature during devolatilization of HK06 on the subsequent gasification kinetics with CO_2. The initial conversion rate R_0 was determined for gasification of primary char and secondary chars generated in the DTR at different temperatures. Results show a steady decrease of R_0 between 1000 °C and 1400 °C pyrolysis temperature (see Fig. 4.6). This thermal deactivation is caused by an increasing graphitization degree of the carbon matrix and a decreasing CaO dispersion with increasing pyrolysis temperature due to sintering processes (see chapter 4.2.3). However, a strong increase in initial conversion rate R_0 is encountered for the char produced at 1600 °C which cannot be explained by thermal deactivation due to graphitization. This phenomenon is caused by the formation of a thin CaO layer during pyrolysis which catalyzes the char-CO_2 gasification reaction.

4.2.3 Summary

The aim was to assess the influence of CaO dispersion and graphitization on the gasification reactivity of the secondary chars with CO_2, since the comparison of R_0 with the micropore surface

area was not conclusive. Fig. 4.7 summarizes the evolution of the most important char characteristics i.e. CaO dispersion D_{CaO}, graphitization defined as $L_a\ L_{a,0}^{-1}$ and initial conversion rate R_0 as a function of pyrolysis temperature between 1000 °C and 1600 °C.

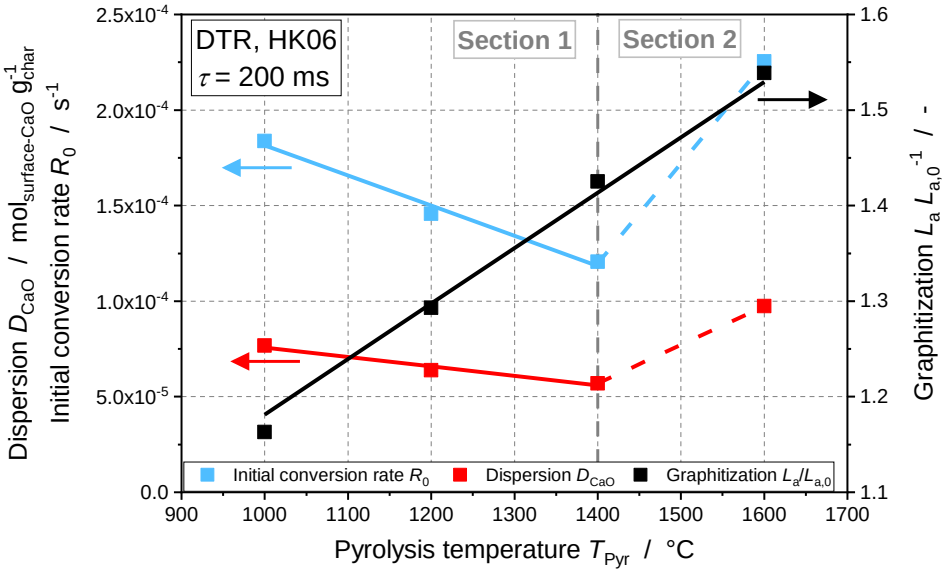

Fig. 4.7. Evolution of CaO dispersion D_{CaO}, initial conversion rate R_0, and graphitization (defined as $L_a\ L_{a,0}^{-1}$) as a function of pyrolysis temperature between 1000 °C and 1600 °C; adapted from [108].

Graphitization is defined as ratio of the radial expansion of graphene layers L_a and the radial expansion of graphene layers of the primary char $L_{a,0}$ and was determined by XRD. The CaO dispersion D_{CaO} was measured via chemisorption in the pTGA. The findings can be divided into two regimes: In section 1, the initial conversion rate R_0 as well as the CaO dispersion D_{CaO} show a linear decrease with increasing pyrolysis temperature. The graphitization degree increases linearly with increasing pyrolysis temperature up to 1600 °C. In section 2, in contrast, the initial conversion rate of the secondary char pyrolyzed at 1600 °C increases significantly despite having the highest graphitization degree. Furthermore, this char exhibits the lowest micropore surface area of all samples investigated (see chapter 4.2.1). Therefore, a strong correlation between initial conversion rate R_0 and calcium dispersion D_{CaO} can be deduced. Calcium dispersion increases drastically at 1600 °C presumably due to the formation of a thin CaO layer selectively catalyzing the gasification reaction with CO_2. The formation of the CaO layer was observed via SEM/TEM images.

4.3 Determination of gasification kinetics

This chapter focusses on the determination of heterogeneous gasification kinetics in various experimental set-ups. First, a valid process window for each system was determined in order to obtain reliable kinetic data at atmospheric pressure. Based on these data, gasification experiments at elevated pressure were performed in a pTGA resulting in diffusional limitations for increasing system pressures. Thus, a novel pressurized single-particle reactor was designed in order to obtain valid gasification kinetics for a wide process window. The results are presented in detail in the publications Stoesser, Schneider et al. [49] and Schneider, Zeller et al. [57] (Papers **V** & **I**) as well as one master thesis [145]. Research questions 3 and 4 are answered within this chapter:

Question 3: *Which experimental set-ups are suitable for the determination of heterogeneous gasification kinetics and which experimental set-up can be applied for the determination of gasification kinetics at elevated pressure?*

Question 4: *What is the dominating reaction mechanism during mixed gasification of biogenic solid fuels in a CO_2/H_2O atmosphere at elevated pressure?*

4.3.1 Experimental systems

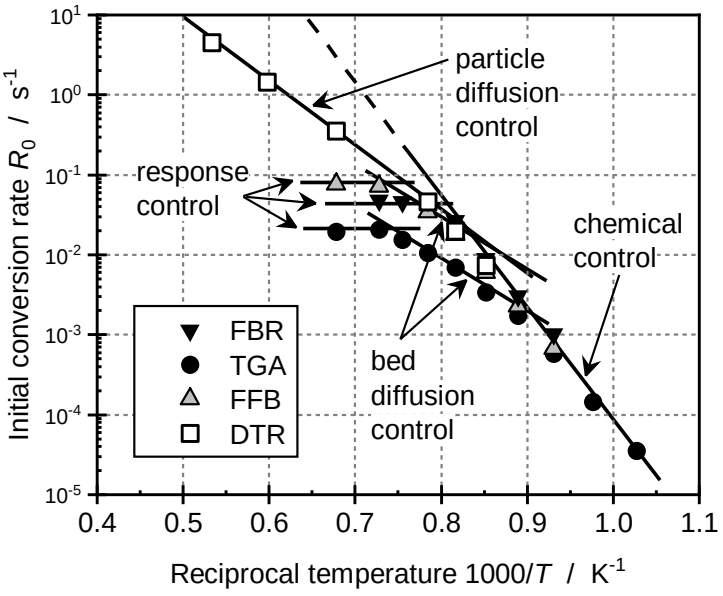

Fig. 4.8. Arrhenius diagram of gasification experiments conducted with WC1600 and $p_{CO_2} = 0.8$ bar (p_{tot} = 1 bar) in four different reaction systems: a thermogravimetric analyzer (TGA), a fluidized-bed reactor (FBR), a free-fall fixed-bed reactor (FFB) and a drop-tube reactor (DTR); adapted from [49].

The objective of this study was to investigate the influence of different experimental systems on the measured gasification rates and identify a valid process window for each of the set-ups. The approach was to conduct gasification experiments with a biogenic model fuel (WC1600) with CO_2 and determine the initial conversion rate R_0 in four different reaction systems: a thermogravimetric analyzer (TGA, operated by Christoph Schneider at EBI ceb), a fluidized-bed reactor (FBR, operated by Thobias Kreitzberg at RWTH Aachen), a free-fall fixed-bed reactor and a drop-tube reactor (FFB & DTR, both operated by Philipp Stoesser at EBI ceb). Temperatures were varied between 700 °C and 1600 °C while residence times from 200 ms to 8 h were investigated at a constant CO_2 partial pressure of 0.8 bar (total pressure of 1 bar).

Four fundamentally different reaction domains were identified of which two were classified as true particle behavior, while the observed initial conversion rates of the other two domains are mainly dominated by the characteristics of the experimental set-up applied (see Fig. 4.8). The domains with true particle behavior were referred to as chemical control (microkinetics) and particle (pore) diffusion control while bed diffusion and response control were induced by the corresponding reaction system. All systems were able to operate under chemical control determining microkinetic initial conversion rates. The obtained activation energy in this reaction domain lies between 229–238 kJ mol^{-1}. At high gasification temperatures, however, only the DTR was able to determine effective initial conversion rates accounting for pore diffusion control. The non-steady systems (FBR, TGA, FFB) showed response control. For the FFB and the TGA, an additional reaction domain referred to as bed diffusion control was observed.

4.3.2 Pressurized thermogravimetric analyzer

Using the results presented in chapter 4.3.1, a valid process window for the gasification experiments in the pTGA (TGA in Fig. 4.8) needed to be identified in order to generate reliable microkinetic data. The atmospheric gasification experiments of WC1600 with CO_2 are depicted in Fig. 4.9. Temperatures were varied between 700 °C and 1200 °C applying a constant CO_2 partial pressure of 0.8 bar (rest Ar). The identification of the microkinetic regime with a corresponding activation energy of 238 kJ mol^{-1} succeeded for temperatures between 700 °C and 850 °C. A second domain with an activation energy of approx. 129 kJ mol^{-1} was observed and referred to as bed diffusion control regime. Here, the activation energy decreases due to either a local depletion of the reactant CO_2 or a local accumulation of the product gas CO, causing an inhibition of the Boudouard reaction. At the highest temperatures between 1150 °C and 1200 °C, the observed

activation energy drastically decreases to approx. 0 kJ mol^{-1}. This domain is referred to as response control and is the result of the non-steady nature of an isothermal, batch-wise TGA experiment, in which the gas flow is switched from inert to reactant gas at a fixed time point. Backmixing throughout the system and crucible volume causes a steady rise of the CO_2 concentration towards the sample rather than a prompt change from pure inert atmosphere to the desired CO_2 concentration. Furthermore, the reactant gas is consumed instantaneously as it reaches the particle bed. Thus, the observed conversion rates at these temperatures rather represent the diffusion rate of CO_2 into the crucible than the microkinetic fuel reactivity.

In conclusion, it is possible to generate reliable microkinetic data (regime I) for the gasification reaction of biogenic chars with CO_2 in the pTGA. However, the valid process window depends on several process conditions i.e. char reactivity, sample mass, gas velocity, total/partial pressure as well as crucible and reactor geometry. Using only one reactor system requires special care to avoid misinterpretation of the data.

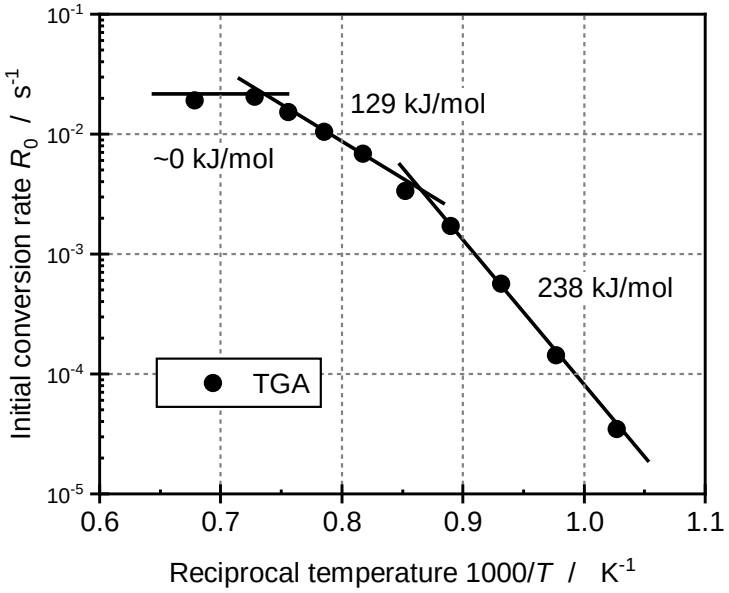

Fig. 4.9. Arrhenius diagram of gasification experiments conducted with WC1600 in the pTGA at $p_{CO_2} = 0.8$ bar and temperatures between 700 °C and 1200 °C; adapted from [49].

Based on the validated gasification kinetics at atmospheric pressure, high-pressure experiments were conducted in the pTGA. Gasification of WC1600 was carried out between 750 °C – 850 °C applying CO_2 partial pressures p_{CO_2} between 0.2 bar and 5 bar. For the experiments with CO_2 partial pressures below 1 bar, the feed was mixed with argon in order to obtain a total pressure

of 1 bar. Fig. 4.10 shows an Arrhenius diagram of all gasification experiments with WC1600 conducted in the pTGA in the microkinetic regime. The reaction rates determined at $p_{CO_2} = 0.8$ bar are validated with three other experimental set-ups (see chapter 4.3.1). For CO_2 partial pressures lower than 0.8 bar, the observed activation energy slightly decreases to approx. 190 kJ mol^{-1}. In contrast, increasing the partial pressure above 1 bar leads to slightly higher activation energies of approx. 260 kJ mol^{-1}. The reaction kinetic data for these experiments applying a power law approach can be found in the appendix (see table C.1). For CO_2 partial pressures of 5 bar, however, the pTGA only gives valid results up to 790 °C. Increasing the temperature above 790 °C did not lead to a significant increase in reaction rate suggesting mass transport limitations in the set-up.

"Especially for highly reactive bio-chars, the process window for the determination of intrinsic reaction rates during gasification is narrow in a TGA. Additionally, when higher pressures are applied in a TGA, even more restrictions may occur. Diffusion coefficients are inversely proportional to pressure ($D_{AB} \sim 1/p$). Furthermore, the maximum gas flow rate of a TGA is usually below 1 l/min at standard ambient temperature and pressure (rather around 50–200 ml/min). Increasing the pressure in a TGA leads to a proportional decrease of gas velocity towards the crucible as the volume flow rate at standard ambient temperature and pressure cannot be further increased. Moreover, high reactant gas volume flows during pressurized TGA experiments lead to a lot of noise in the mass signal." [57]

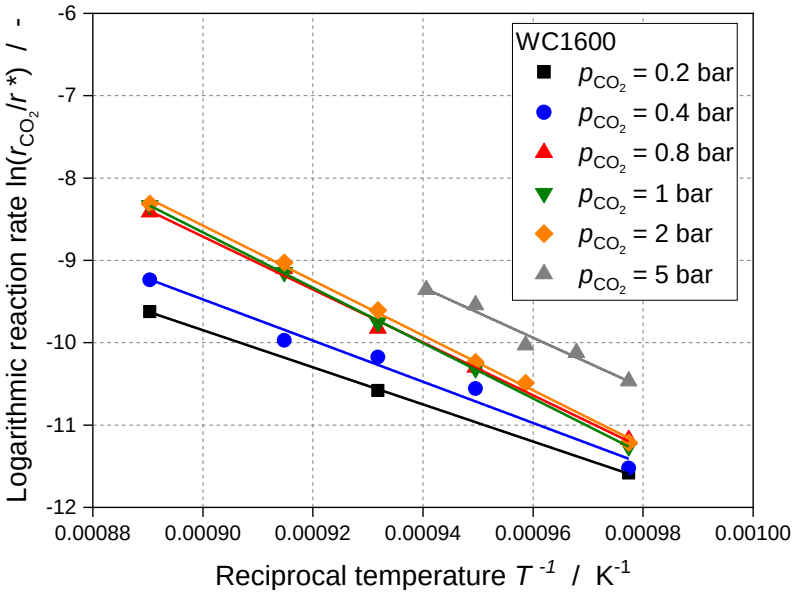

Fig. 4.10. Arrhenius diagram for gasification of WC1600 with CO_2 in pTGA between 750 °C – 850 °C and CO_2 partial pressures up to 5 bar.

4.3.3 Comparison between pTGA and pSPR

Due to the observed limitations for gasification experiments in the pTGA at elevated pressure for biogenic chars, the pressurized single-particle reactor (pSPR) with forced flow-through conditions was designed and built in the frame of this work reducing diffusional effects to a minimum. "The reactant gases flow convectively through the char particles. It was assured that the reactor was operated in a differential way meaning that the reactant gas concentration did not decrease > 3 % along the particle bed. Thus, all char particles were able to get in contact with the desired gas concentration and no concentration gradient was formed. Furthermore, the gas velocity was kept constant at a high level. Consequently, no accumulation of product gas near the char particles occurred as it may happen at the bottom of a TGA crucible. Since the product gas is swept away by the gas flow convectively, re-adsorption of product gases on the char surface is minimized." [57]

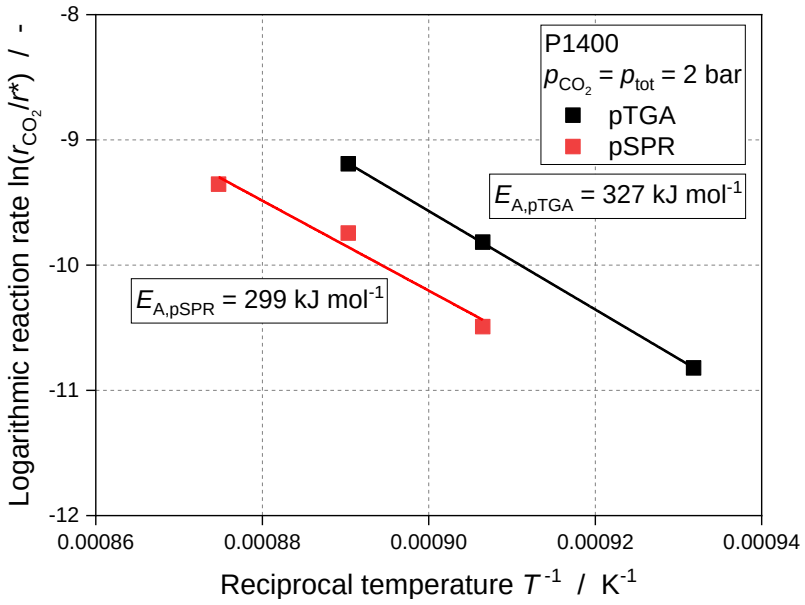

Fig. 4.11. Comparison of reaction rates r_{CO_2} during gasification of P1400 in pTGA and pSPR at $p_{CO_2} = p_{tot} = 2$ bar and temperatures between 800 °C and 870 °C; adapted from [145].

In order to validate the pSPR, gasification experiments were carried out in the pTGA and the pSPR at elevated pressure. Fig. 4.11 shows a comparison between reaction rates r_{CO_2} determined during gasification of P1400 with CO_2 in the pTGA and the pSPR between 800 °C and 870 °C and a CO_2 partial and total pressure of 2 bar. The obtained activation energies in both set-ups are relatively high being approx. 299 kJ mol^{-1} in the pSPR and 327 kJ mol^{-1} in the pTGA suggesting no mass transport limitations. Thus, both set-ups allow for the determination of microkinetics

within the process conditions investigated. The deviations between both activation energies is below 10 %. However, small differences in reaction rates r_{CO_2} from both set-ups were observed which may be traced back to differences in temperature measurement in both setups in the range of 15 K – 20 K.

4.3.4 Determination of gasification kinetics at elevated pressure in pSPR

In this chapter, gasification experiments of P1400 and P1600 with CO_2, H_2O and its mixture at elevated pressure are presented. All experiments have been carried out in the pSPR.

Gasification with CO_2

The objective of this study was to determine kinetic data for the microkinetic regime during pressurized gasification of biogenic chars, which were produced under technical relevant conditions found in entrained flow gasification. For this purpose, secondary chars (P1400 & P1600) were produced in the DTR under high heating rates and short residence times. Subsequently, gasification experiments with CO_2 between p_{CO_2} = 1 bar and 20 bar and temperatures between 830 °C and 870 °C were carried out in the pSPR. Gasification kinetics were modeled using the power law and Langmuir-Hinshelwood (LH) approach. The modeling results and the corresponding kinetic parameters for the power law can be found in Fig. 4.12 and table C.2 while the LH model is illustrated in Fig. 4.13 and table C.3.

Results indicate that "P1600 shows higher reactivity as compared to P1400 for all CO_2 partial pressures and temperatures applied. However, for the highest CO_2 partial pressure applied (20 bar), both chars show similar reactivity. The higher reactivity of P1600 during CO_2 gasification may be explained by the CaO film on the char surface catalyzing the char-CO_2 gasification reaction. A power law approach is suitable to describe gasification kinetics of both chars with CO_2 up to pressures of 20 bar. However, the observed saturation during gasification of P1600 applying high CO_2 partial pressures is better described by a LH approach." [57]

Power law

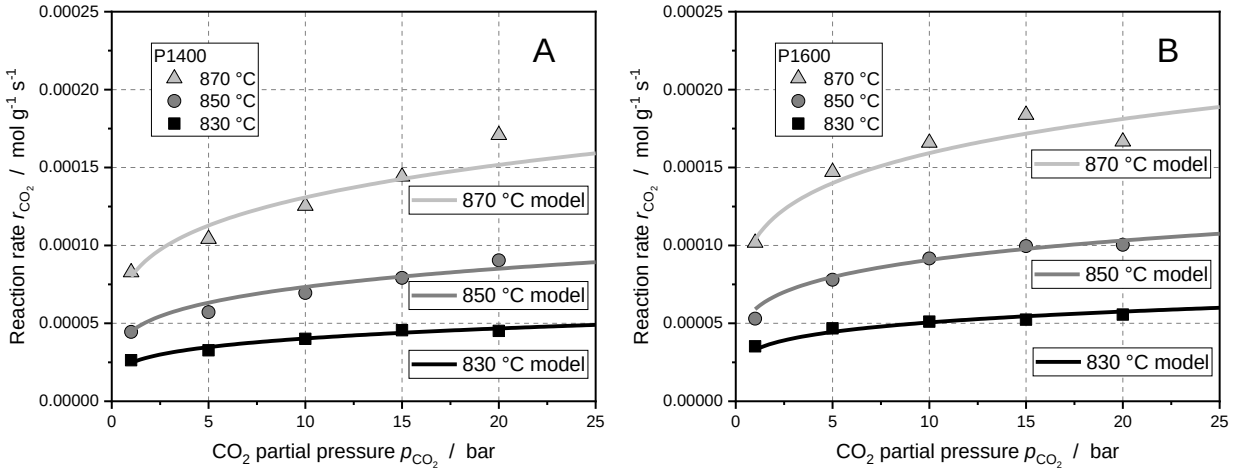

Fig. 4.12. Modeling of the gasification reaction with CO_2 for P1400 (A) and P1600 (B) using power law approach [57].

Langmuir-Hinshelwood

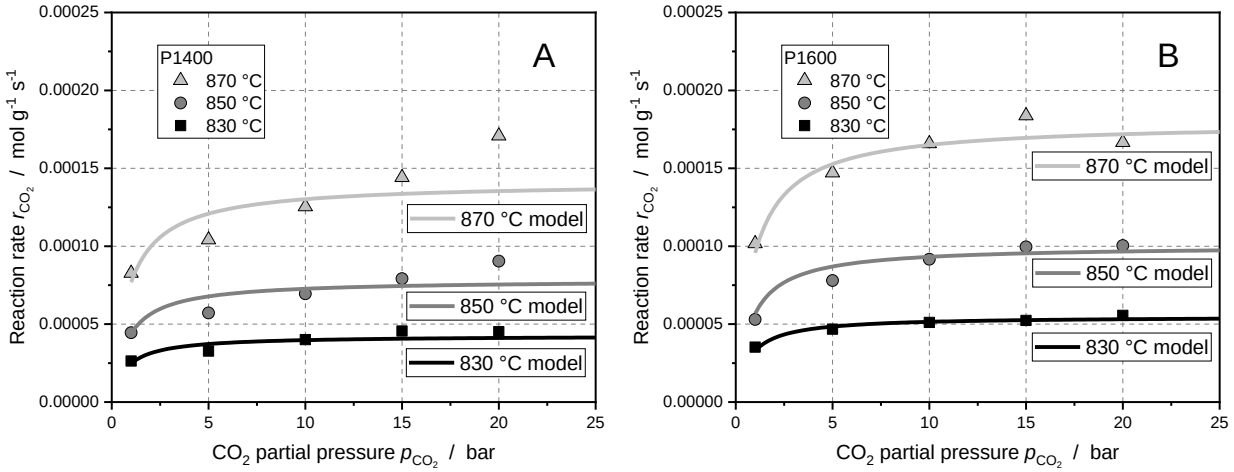

Fig. 4.13. Modeling of the gasification reaction with CO_2 for P1400 (A) and P1600 (B) using an LH approach [57].

Gasification with H_2O

In order to generate kinetic data for the gasification reaction with H_2O at elevated pressure, gasification experiments with P1400 and P1600 were carried out in the pSPR at H_2O partial pressures between 0.2 bar and 5 bar and temperatures between 830 °C and 870 °C. Reaction kinetic modeling was conducted using the power law and LH approach. Since no saturation effects were detected with H_2O under the process conditions applied, the LH approach does not give good

modeling results for both chars (see Fig. C.1 and table C.5 in the appendix). The modeling results and the corresponding parameters for the power law can be found in Fig. 4.14 and table C.4. In contrast to the gasification with CO_2, "P1400 shows higher reactivity towards H_2O as compared to P1600 which is expected from the char specifications reported above. The dominating char properties affecting H_2O reactivity were considered to be constitution of carbon matrix (i.e. graphitization degree) and micropore surface area. The catalytically active CaO film is of minor relevance when gasification is carried out with H_2O. Modeling of pressurized char-H_2O gasification kinetics of both samples was achieved using a power law approach to full satisfaction within the process conditions applied." [57]

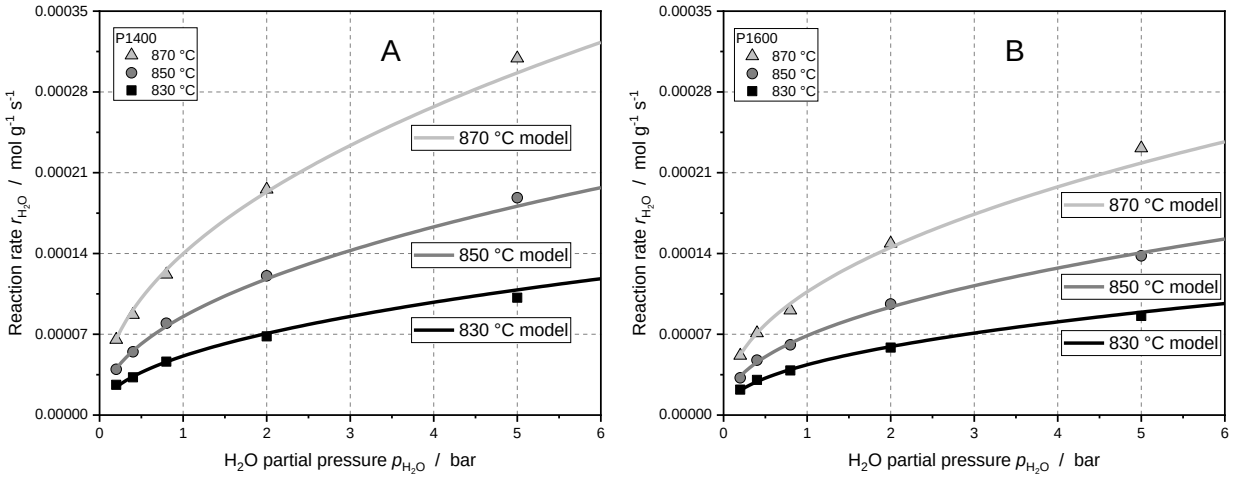

Fig. 4.14. Modeling of the gasification reaction with H_2O for P1400 (A) and P1600 (B) using power law approach [57].

Gasification in mixed CO_2/H_2O atmospheres

The aim was to investigate the dominating reaction mechanism during mixed gasification in CO_2/H_2O containing atmospheres at elevated pressure and to state whether both reactions are additive or inhibitory. For this purpose, gasification experiments were conducted with P1400 and P1600 in mixed CO_2/H_2O atmospheres in the pSPR at 830 °C and reactant gas partial pressure up to $p_{\mathrm{CO_2}} = p_{\mathrm{H_2O}} = 5$ bar.

Fig. 4.15 (A) illustrates the reaction rates r_{mix} as a function of CO_2 partial pressure in the range of 0 bar to 5 bar for H_2O partial pressures of 0.8 and 2 bar, respectively. Total pressure was varied between 5 and 20 bar. The values for $p_{\mathrm{CO_2}}$ = 0 bar correspond to the H_2O gasification experiments reported earlier in this chapter. Additionally, one set of experimental data is reported for $p_{\mathrm{CO_2}}$ = $p_{\mathrm{H_2O}} = 5$ bar. As already discussed, "P1400 shows a higher reactivity during gasification with H_2O

(p_{CO_2} = 0 bar) as compared to P1600. For a CO_2 partial pressure of 0.8 bar, an increase in reaction rate r_{mix} for both chars at both H_2O partial pressure levels (p_{H_2O} = 0.8 bar and 2 bar) is detected. However, P1600 exhibits a stronger increase in reaction rate as compared to P1400 and becomes more reactive than P1400. For p_{H_2O} = 0.8 bar both chars show a similar slope with increasing CO_2 partial pressure i.e. P1600 reactivity remains higher than P1400 reactivity. For p_{H_2O} = 2 bar, P1600 reaction rate r_{mix} remains almost constant for p_{CO_2} > 0.8 bar, whereas P1400 reactivity increases with CO_2 partial pressures at the same slope as for p_{H_2O} = 0.8 bar leading to a slightly higher reactivity at p_{CO_2} = 5 bar. At $p_{CO_2} = p_{H_2O} = 5$ bar, P1400 exhibits a significantly higher reaction rate r_{mix} as compared to P1600, which shows only a small increase in reactivity with increasing H_2O partial pressure from 2 bar to 5 bar.

Increasing the CO_2 partial pressure from 0 bar to 0.8 bar during mixed gasification leads to an increase in reaction rate r_{mix} for both chars which can be expressed by the addition of the single atmosphere reaction rates r_{CO_2} and r_{H_2O}. In Fig. 4.15 (B), the reaction rates r_{H_2O} and r_{CO_2} for single atmosphere gasification experiments at p_{H_2O} = 0.8 bar, 2 bar and p_{CO_2} = 1 bar, 5 bar are shown together with calculated values for r_{mix} using a simple addition of the single atmosphere reaction rates ($r_{mix} = r_{CO_2} + r_{H_2O}$). By this approach, the reaction rates for mixed gasification are reasonably modeled for the low pressure range up to p_{CO_2} = 1 bar and both chars, despite the fact that the experimental values are slightly overestimated for P1400. Thus, no competition between the H_2O and the CO_2 gasification reaction is observed in the low pressure range. Here, a separate active site mechanism might be valid for both chars. The strong increase of P1600 reactivity from p_{CO_2} = 0 bar to p_{CO_2} = 0.8 bar may be explained by the catalytic activity of the CaO film on the char surface selectively increasing the reactivity towards CO_2" [57] (see chapter 4.2).

"At p_{H_2O} = 2 bar, however, the reaction rate r_{mix} of P1600 stagnates for CO_2 partial pressures above 0.8 bar (see Fig. 4.15(A)). The observed trend may be interpreted as saturation of reactant gases on the char surface since P1600 has a distinctly lower surface area as P1400 and – due to a higher graphitization degree – a lower amount of carbon active sites. Thus, morphology and graphitization might become more relevant for higher reactant gas partial pressures while Ca catalysis fades into the background. At high reactant gas partial pressures, a common reactive sites mechanism might be more adequate for P1600. Here, the simple addition of the single atmosphere reaction rates might become invalid. This thesis is fortified by the experimental results

at $p_{CO_2} = p_{H_2O} = 5$ bar, where an inhibition of the P1600 reactivity is clearly visible as compared to P1400." [57]

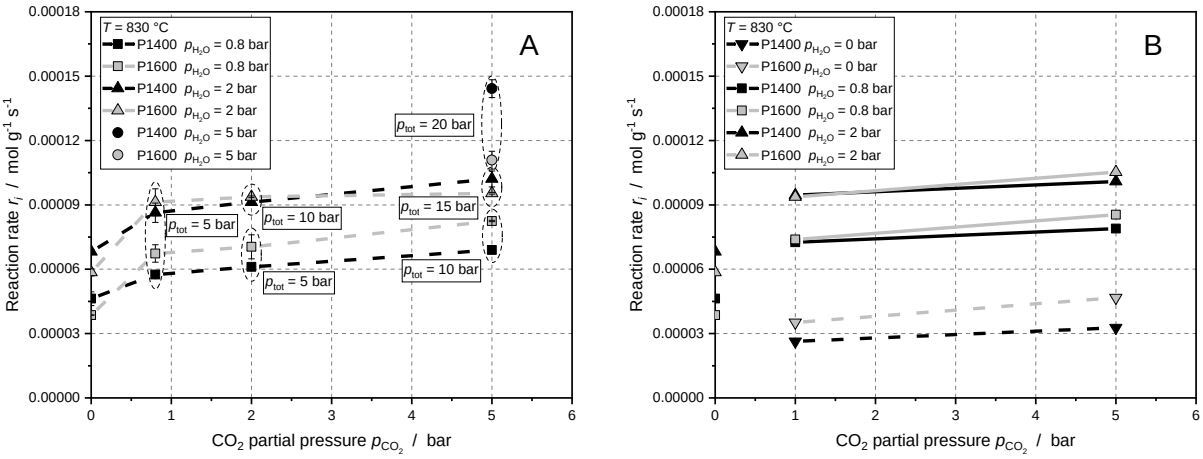

Fig. 4.15. (A) Reaction rates r_{mix} of P1400 and P1600 during mixed gasification at 830 °C for three H_2O partial pressures (p_{H_2O} = 0.8 bar, 2 bar, 5 bar and p_{tot} = 5 – 20 bar) as a function of p_{CO_2} as well as r_{H_2O} at p_{H_2O} = 0.8 bar, 2 bar. (B) Reaction rates r_{H_2O} and r_{CO_2} for single atmosphere gasification experiments at p_{H_2O} = 0.8 bar, 2 bar and p_{CO_2} = 1 bar, 5 bar; r_{mix} calculated as an addition of the single atmosphere reaction rates (symbols with solid line) [57].

Kinetic modeling for gasification in mixed CO_2/H_2O atmospheres

"Experimental results from the previous chapter indicate that – for the chars and process conditions investigated – CO_2 and H_2O gasification occurs rather on separate than on same active sites except for the high pressure experiments with P1600. Therefore, simple approaches were used in order to model mixed gasification via addition of the single atmosphere reaction kinetics with the highest fit quality" [57].

Fig. 4.16 illustrates the measured reaction rates of P1400 (A) and P1600 (B) for CO_2, H_2O and mixed atmosphere gasification together with the corresponding modeling approaches. Results indicate that "the addition of the single atmosphere reaction kinetics gives satisfying results for P1400. The experimental values are slightly overestimated by the addition of the single atmosphere reaction kinetics. However, the conception of a separate carbon active sites reaction mechanism is significantly better represented as compared to the approach of competing active sites.

In contrast to P1400, the addition of both single atmosphere kinetics of P1600 for modeling of mixed gasification gives satisfying results only in the low pressure range. The char with the lower

specific surface area and the higher graphitization degree (P1600) reaches a saturated state earlier when applying higher reactant gas partial pressures. Therefore, the addition of both single atmosphere kinetics becomes invalid and a common active site mechanism might be relevant.

Considering the experimental results for mixed gasification presented in this work, the following conclusions can be drawn:

- Increasing the CO_2 partial pressure leads to higher reactivity for both chars. The reaction rate r_{mix} can be expressed by addition of the single atmosphere reaction rates in the low pressure area suggesting a separate active site mechanism.
- Catalytic activity of CaO increases the reaction rate r_{mix} of P1600 distinctively for lower H_2O and CO_2 partial pressures.
- For higher H_2O and CO_2 partial pressures, P1600 reactivity stagnates due to lower specific surface area and higher graphitization degree i.e. lower amount of carbon active sites. Here, a common active sites mechanism can be assumed." [57]

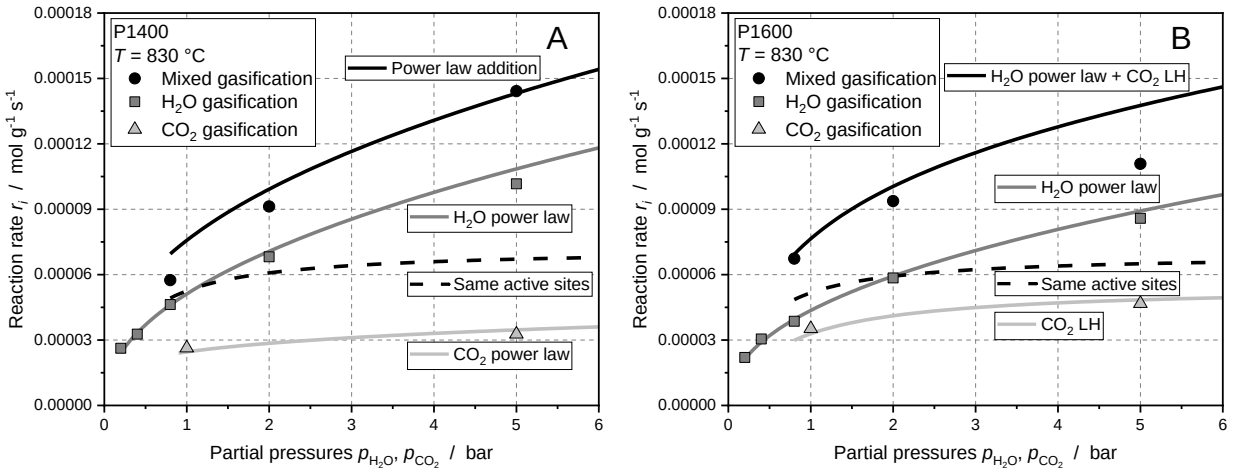

Fig. 4.16. Modeling approaches for the mixed H_2O/CO_2 gasification of P1400 (A) and P1600 (B) using an addition of the single atmosphere reaction kinetics [57].

5 Concluding remarks

The main results of this work are recapitulated by answering the research questions posed in chapter 1.

Question 1: *Which biogenic char properties affect heterogeneous gasification reactions predominantly and how do they change upon char gasification?* (Papers **III** & **IV** and chapter **4.1**)

Gasification experiments with CO_2 using a biogenic model fuel (WC1600n) were conducted in a drop-tube reactor (DTR) in order to produce samples for the determination of micropore surface area A_{MSA} and pore size distribution as a function of carbon conversion. Results indicate that the gasification reaction with CO_2 predominantly takes place in micropores. Furthermore, the influence of morphology and catalytically active ash components on the conversion rate was investigated using activated carbon (AC) impregnated with calcium and potassium. The presence of calcium and potassium on the carbon surface is found to dominate reactivity and course of conversion rate during gasification with CO_2. The determination of active sites during gasification of a biogenic model fuel (WC1600) with CO_2 was carried out in a chemisorption analyzer via temperature-programmed desorption (TPD). A good correlation between reactive surface area (RSA) and specific conversion rate is obtained if catalytically active sites are taken into account in the calculations for RSA.

Question 2: *How are biogenic char properties influenced by secondary pyrolysis during entrained-flow gasification?* (Paper **II** and chapter **4.2**)

Secondary pyrolysis experiments have been conducted in a drop-tube reactor (DTR) with temperatures varying between 1000 °C and 1600 °C. The effect of pyrolysis conditions on initial conversion rate R_0, graphitization and ash dispersion was investigated. "A linear decrease in initial conversion rate R_0 was observed between 1000 °C and 1400 °C. However, a strong increase of R_0 at 1600 °C was encountered. Micropore surface area of the secondary chars showed no correlation with the initial conversion rate R_0 during gasification with CO_2. Graphitization of the carbon matrix was determined using X-ray diffraction and Raman spectroscopy suggesting the growth of aromatic clusters and graphite-like structures for increasing pyrolysis temperatures up to 1600 °C. " [108]

"CaO dispersion D_{CaO} decreases steadily between 1000 °C and 1400 °C whereas a strong increase can be observed at 1600 °C, which is in good accordance with the development of the initial conversion rate R_0 as a function of pyrolysis temperature. SEM/TEM images indicate the formation of a thin CaO layer at 1600 °C that is presumably responsible for the strong increase in initial conversion rate R_0 at this temperature." [108]

Question 3: *Which experimental set-ups are suitable for the determination of heterogeneous gasification kinetics and which experimental set-up can be applied for the determination of gasification kinetics at elevated pressure?* (Papers **I** & **V** and chapter **4.3**)

First, the influence of different experimental systems on the measured gasification rates at atmospheric pressure was investigated in order to identify a valid process window for each of the set-ups. The approach was to conduct gasification experiments with CO_2 using a biogenic model fuel (WC1600) and determine the initial conversion rate R_0 in four different reaction systems: a thermogravimetric analyzer (TGA), a fluidized-bed reactor (FBR), a free-fall fixed-bed reactor (FFB) and a drop-tube reactor (DTR). All systems were able to operate under chemical control determining microkinetic initial conversion rates. At high temperatures, however, only the DTR was able to determine effective initial conversion rates accounting for pore diffusion control while the non-steady systems (FBR, TGA, FFB) showed response control. For the FFB and the TGA, an additional reaction domain referred to as bed diffusion control was observed.

In the case of highly reactive biomass chars, the process window for the determination of microkinetic reaction rates during gasification is narrow in a TGA. Applying higher pressures, even more restrictions may occur as diffusion coefficients are inversely proportional to pressure. Therefore, a pressurized single-particle reactor (pSPR) with forced flow-through conditions reducing system inherent diffusional effects to a minimum was designed and built in the frame of this work. Gasification experiments with CO_2 and H_2O at elevated pressure were carried out in the pSPR using two secondary chars (P1400 and P1600). Modeling of gasification kinetics was successfully conducted using a power law approach for CO_2 and H_2O. However, the observed saturation during gasification of P1600 applying high CO_2 partial pressures is better described by a Langmuir-Hinshelwood (LH) approach.

Question 4: *What is the dominating reaction mechanism during mixed gasification of biogenic solid fuels in a CO_2/H_2O atmosphere at elevated pressure?* (Paper **I** and chapter **4.3**)

Gasification experiments in mixed CO_2/H_2O atmospheres using P1400 and P1600 were conducted in the pSPR. "Increasing the CO_2 partial pressure leads to higher reactivity for both chars. The reaction rate r_{mix} can be expressed by addition of the single atmosphere reaction rates in the low pressure area suggesting a separate active site mechanism. Catalytic activity of CaO increases the reaction rate r_{mix} of P1600 distinctively for lower H_2O and CO_2 partial pressures. For higher H_2O and CO_2 partial pressures, P1600 reactivity stagnates due to lower specific surface area and higher graphitization degree i.e. lower amount of carbon active sites. Here, a common active sites mechanism can be assumed." [57]

Appendix

A Literature review

Gas production from solid feedstock

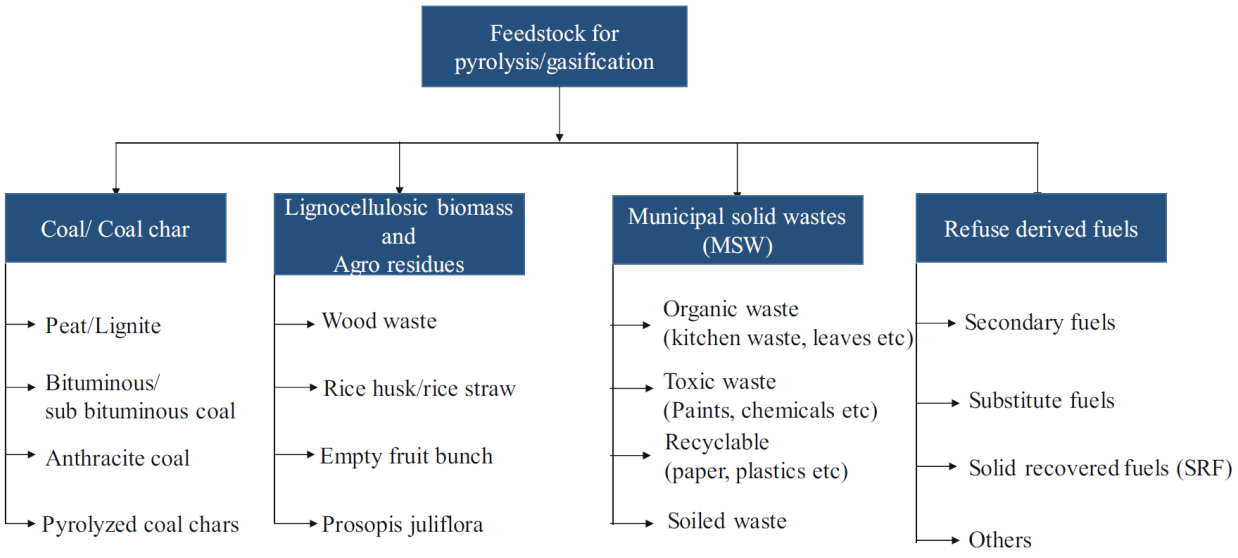

Fig. A.1. Schematic of feedstock classification for gas production [7].

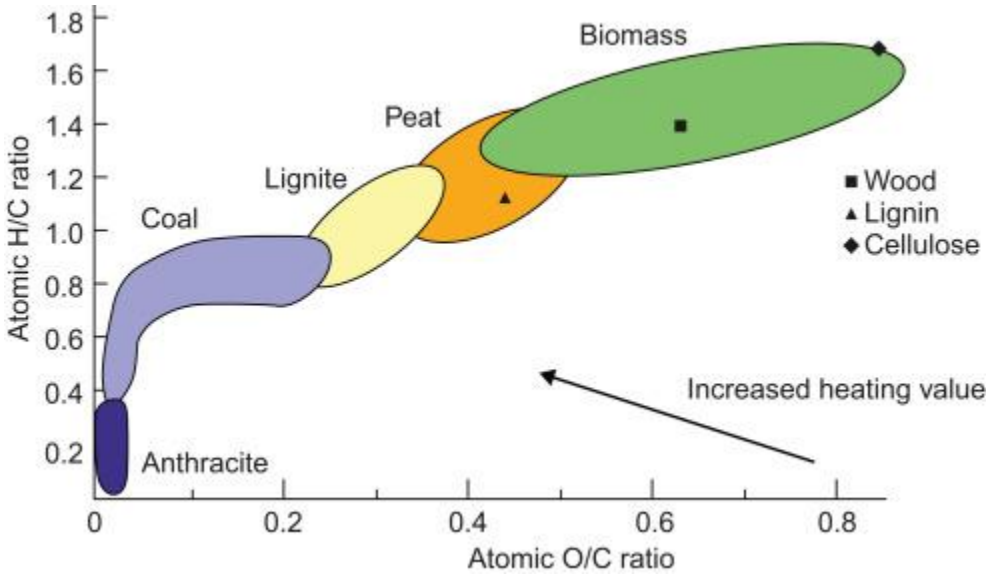

Fig. A.2. Van Krevelen diagram [149].

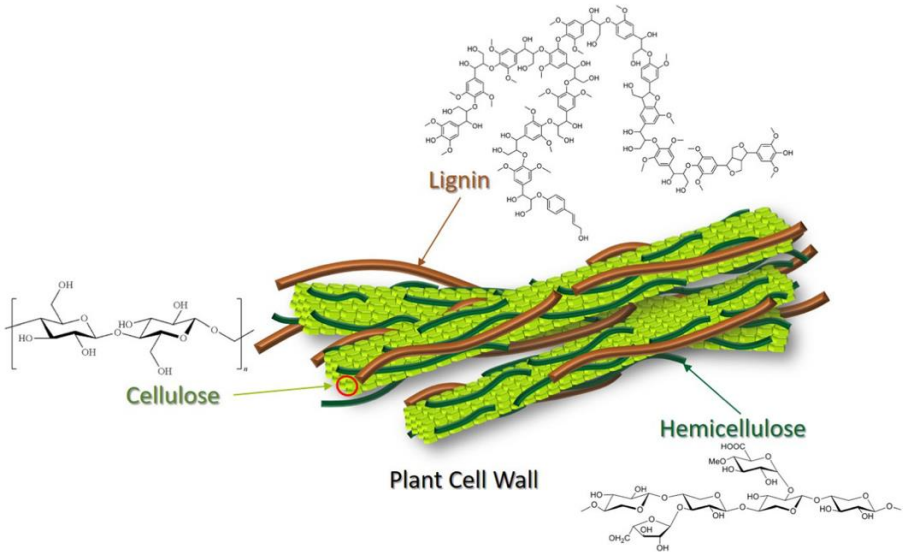

Fig. A.3. Structure of lignocellulosic biomass [150].

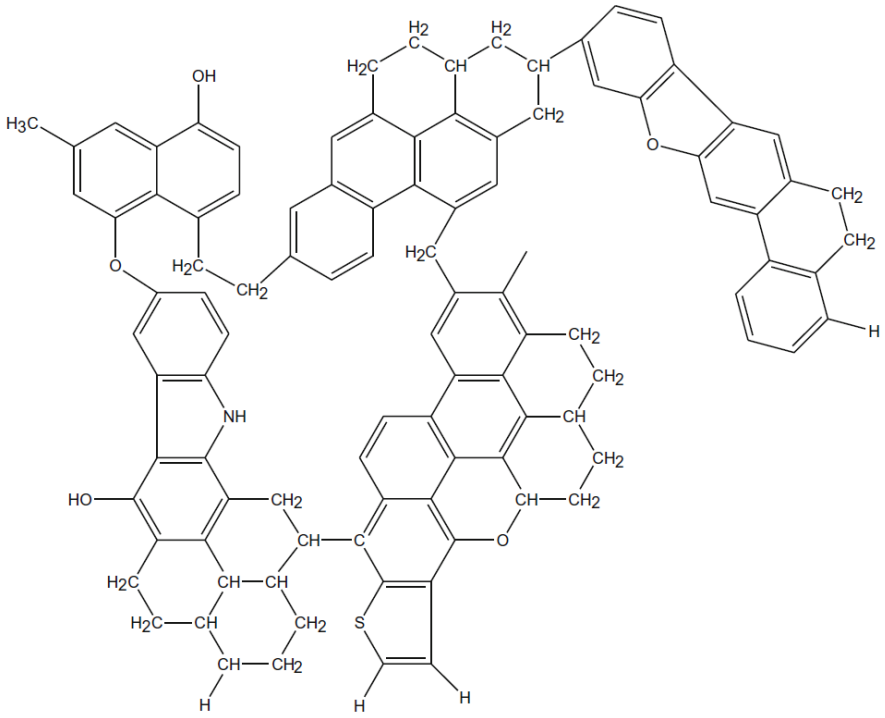

Fig. A.4. Model structure of a bituminous coal [151].

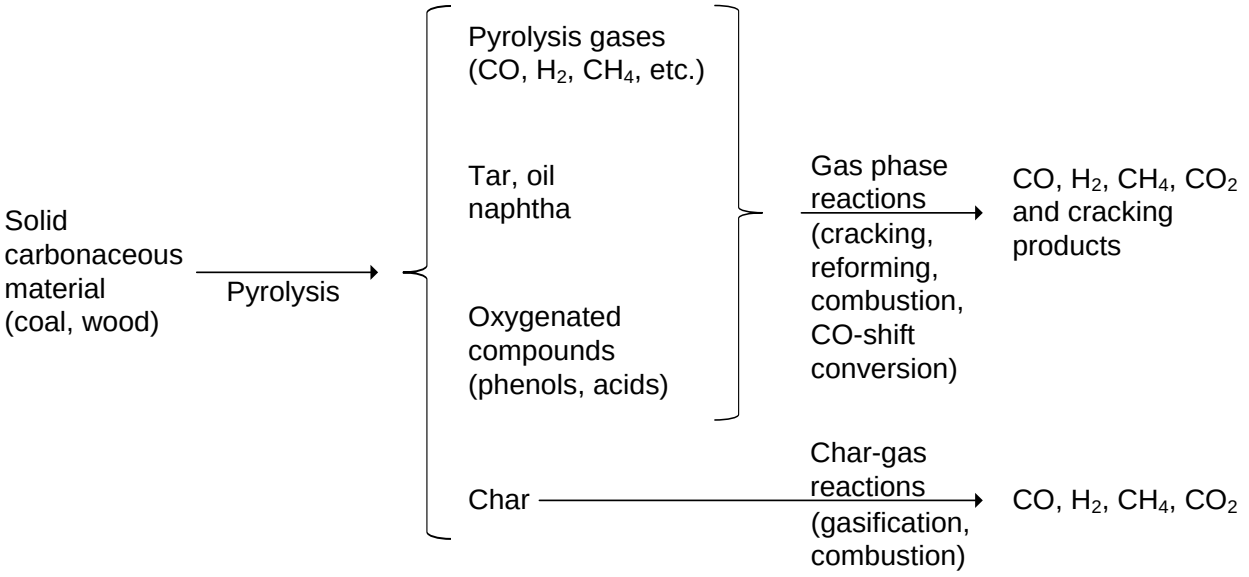

Fig. A.5. Main conversion processes and chemical reactions of solid carbonaceous materials [152].

Pyrolysis of solid fuels

Depending on the biomass component, various temperature regimes for pyrolysis can be assigned. Hemicellulose decomposes at 200 °C – 260 °C followed by cellulose with decomposition temperatures of 240 °C – 350 °C. Lignin exhibits the largest temperature range for decomposition reactions with 280 °C – 500 °C [153,154]. Fig. A.6 shows a differential thermogravimetry (DTG) curve during pyrolysis of beech wood between 423 K and 723 K [155]. Here, the change of solid mass fraction is depicted as a function of pyrolysis temperature. Open circles represent the actual weight loss rate during devolatilization of beech wood while the other curves and symbols are deconvoluted from the original mass loss signal. The first peak at approx. 573 K corresponds to the decomposition of hemicellulose, the global maximum can be assigned to the decomposition of cellulose. Due to the large temperature range for lignin decomposition, no specific peak can be observed (dashed line).

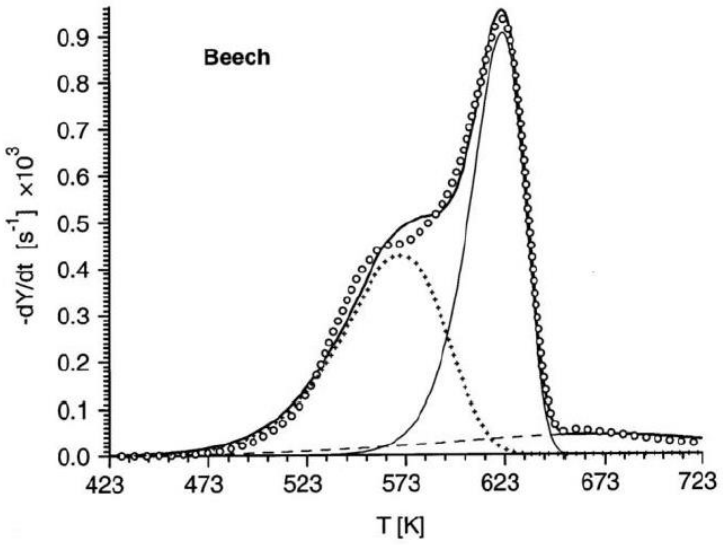

Fig. A.6. Comparison between observed (open circles) and simulated (lines) DTG curves during pyrolysis of beech wood [155].

Influence of pyrolysis pressure on char reactivity

Cetin et al. [28] and Okumura et al. [156] observed a decreasing reactivity of biogenic chars with increasing pyrolysis pressure. Fig. A.7 shows the CO_2 gasification reactivity of radiata pine char generated in a WMR (High HR) as a function of pyrolysis pressure. Results indicate that the char generated at 20 bar reacts approx. three times slower than the atmospheric pressure char. The authors conclude that this effect is evoked by changes in the chemical structure i.e. carbon matrix of the char since the influence of pyrolysis pressure on specific surface area was found to be less significant [28]. The changes in carbon structure due to increasing pyrolysis pressure were also verified using X-ray diffraction (XRD) analysis [26]. On the contrary, Roberts et al. [157] observed an increase in apparent gasification and combustion rates with increasing pyrolysis pressure investigating coal chars that were produced in a pressurized entrained flow reactor. Furthermore, the authors indicate that the micropore surface area of the chars generated at high pressure was higher as compared to the chars produced at atmospheric pressure. It was concluded that the increase in apparent gasification and combustion rates may originate from the augmented surface area as no significant changes in the carbon matrix were detected using XRD analysis [157].

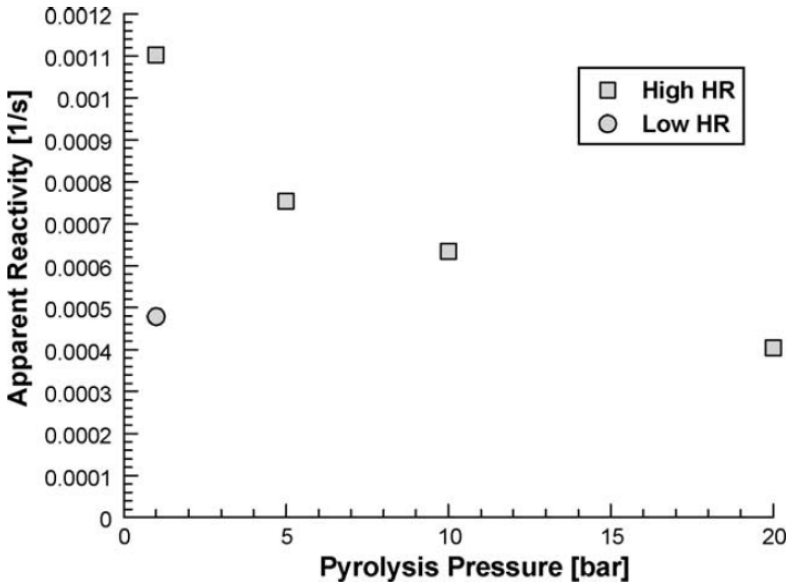

Fig. A.7. Apparent CO_2 reactivity (850 °C, 1 bar) of radiata pine chars produced in a WMR (High HR) and in a tubular reactor (Low HR) as a function of pyrolysis pressure [28].

Heterogeneous gasification of solid fuels

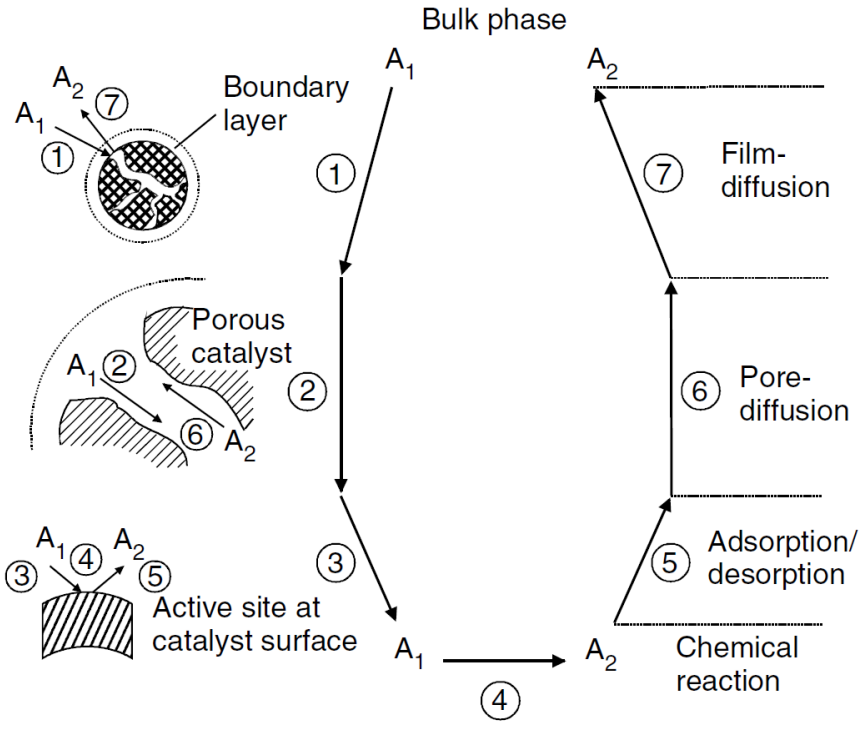

Fig. A.8. Series of steps during a heterogeneous gas-solid reaction $A_1 \rightarrow A_2$ on a porous catalyst [47].

Pore diffusion modeling

By means of dimensionless numbers, it is possible to determine quantitatively whether the reaction rate is affected by mass transport limitations. The Thiele modulus ϕ describes the ratio between microkinetic reaction rate and diffusion rate within a porous particle (see Eq. A-1). Its detailed derivation can be found in literature [158].

$$\phi = l_c \sqrt{\frac{n_i + 1}{2} \frac{k_i(T) c_\infty^{n_i - 1}}{D_{\text{eff}}}} \tag{A-1}$$

Input parameters are the characteristic length of a particle l_c, the reaction order n_i, the Arrhenius rate constant $k_i(T)$, the reactant gas concentration in the bulk phase c_∞ as well as the effective diffusion coefficient D_{eff}. In order to calculate the effective diffusion coefficient for heterogeneous gas-solid reactions, the binary diffusion coefficient D_{AB} as well as the Knudsen diffusion coefficient D_{Kn} need to be taken into account since the mean free path of the reactant gases may be in the same order of magnitude as the pore diameter of the solid fuel. Furthermore, porosity ε and tortuosity τ of the particle have to be considered the calculation of D_{eff} [158].

$$D_{\text{eff}} = \frac{\varepsilon}{\tau} \frac{1}{\frac{1}{D_{\text{AB}}} + \frac{1}{D_{\text{Kn}}}} \tag{A-2}$$

The effectiveness factor η is defined as the ratio of effective reaction rate r_{eff} to true reaction rate determined in the microkinetic regime without mass transport limitation (see Eq. A-3). For a spherical particle and a first order reaction, the following relation between effectiveness factor and Thiele modulus is obtained [159].

$$\eta = \frac{r_{\text{eff}}}{r_i} \tag{A-3}$$

$$\eta = \frac{3}{\phi} \left(\frac{1}{\tanh\phi} - \frac{1}{\phi} \right) \tag{A-4}$$

Usage of different experimental set-ups

Fig. A.9 compares the number of publications reporting the use of different experimental set-ups for the determination of kinetic data in terms of CO_2 gasification. The chart, which is considering experiments for coal and biomass gasification, is based on two review papers by Di Blasi [20] and

Irfan et al. [62]. Here, the majority of experiments were carried out in thermogravimetric systems (62.0 %), followed by fixed-bed reactors (18.5 %) and drop-tube furnaces (DTF).

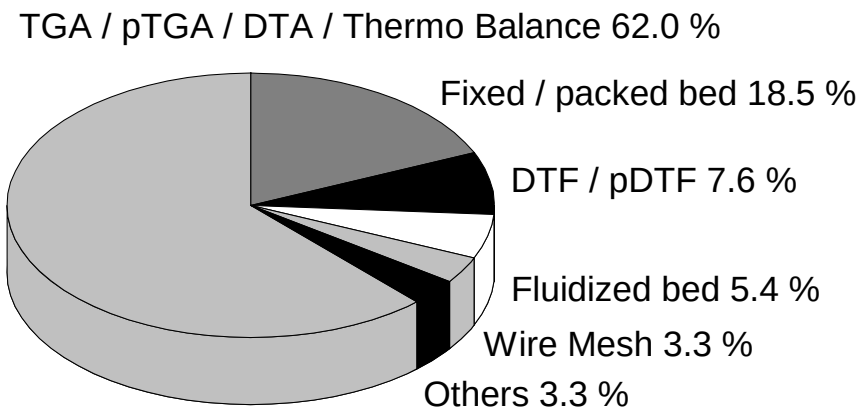

Fig. A.9. Usage of different experimental set-ups for the determination of heterogeneous gasification kinetics with CO_2 [49].

Mass transport processes during gasification of biomass char in TGA

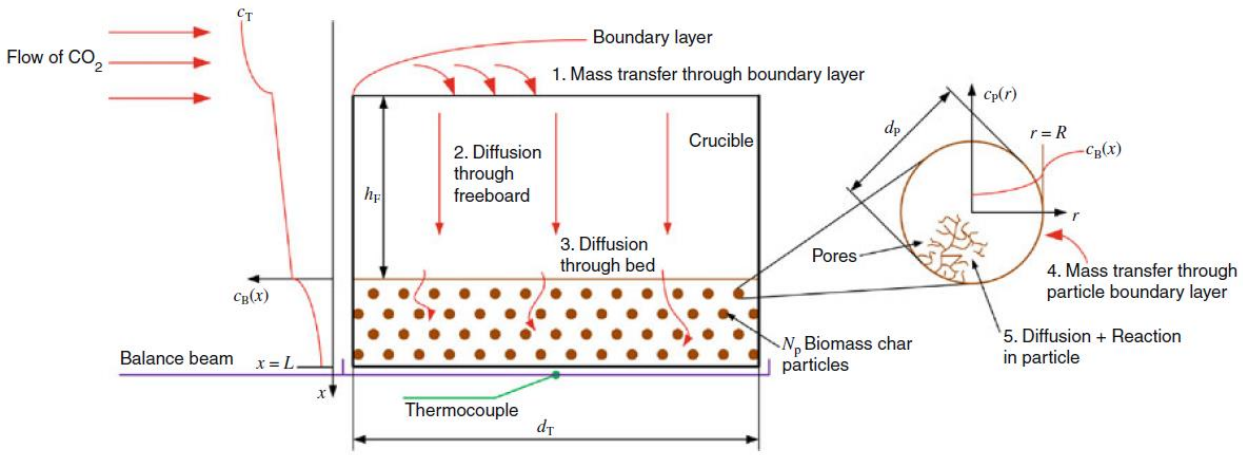

Fig. A.10. Crucible used in a thermogravimetric device including mass transfer processes limiting the effective reaction rate [67].

Nowak et al. [67] aim to model the effective reaction rate that they assume to be kinetically and diffusion controlled considering the following steps (see Fig. A.10):

1. Mass transfer from the free flow of CO_2 through the boundary layer to the surface of the crucible.
2. Diffusion through the freeboard of the crucible.
3. Diffusion through the bed of biomass char particles.
4. Mass transfer through the char particle's boundary layer.
5. Diffusion through the pores of the biomass char particle and reaction at a carbon active site C_f at the char surface.

Usage of fixed-bed reactors for the determination of gasification kinetics

Zhou et al. [134] studied the gasification behavior of German Rhenish brown coal and wheat straw chars with CO_2 in a quartz glass fixed-bed reactor at atmospheric pressure. The authors were able to determine reaction kinetic data for both fuels and highlighted the effect of pyrolysis conditions on the data obtained. Furthermore, Wu & Wang [160] investigated the effect of pressure on the K_2CO_3-catalyzed steam gasification of ash-free coal in a vertically blown reactor at elevated pressure. The experimental set-up was operated as a differential reactor applying steam partial pressures of up to 6 bar and total pressures of 20 bar. The authors state that diffusional effects can be eliminated thoroughly by this type of reactor. Furthermore, kinetic parameters using an nth-order as well as a LH approach were determined.

Mixed gasification in CO_2/H_2O atmosphere

Chen et al. [71] investigated the effect of pyrolysis conditions on the gasification of lignite chars in mixtures of CO_2 and H_2O in a TGA and a fluidized-bed reactor. Two different chars were produced by fast pyrolysis in a drop-tube furnace and by slow pyrolysis using a fixed-bed reactor at 1000 °C. The authors report that the gasification rates in the mixture of CO_2 and H_2O were lower than the sum of the rates of the chars reacting independently with CO_2 and H_2O but higher than the rate of each independent reaction for both chars. Furthermore, their results from TGA and fluidized-bed indicate that the char-H_2O reaction was independent of the char-CO_2 reaction, while the char-CO_2 reaction was inhibited by the char-H_2O reaction.

Li et al. [75] conducted gasification experiments with lignite chars in mixtures of CO_2 and H_2O at elevated pressure using a fixed-bed reactor. Results indicate that the dominating reaction mechanism depends on the total pressure applied. The authors conclude that under low reactant pressures, the reaction mechanism was consistent with the separate reactive site reaction mechanism, while under higher pressure, the common active site reaction mechanism is rather valid.

Char properties affecting gasification kinetics

Morphology

Besides characterizing the initial specific surface area and porosity prior to gasification, a lot of effort is put into describing the evolution of char morphology as a function of conversion degree. Malekshahian & Hill [99] investigated the effect of pyrolysis and CO_2 gasification pressure on the surface area and pore size distribution of petroleum coke using nitrogen and carbon dioxide physisorption. Nitrogen was used for the determination of total surface area while CO_2 adsorption indicated micropore surface area. Fig. A.11 shows the evolution of surface areas measured by N_2 (Fig. A.11 (a)) and CO_2 (Fig. A.11 (b)) as a function of conversion degree during gasification of petcoke with CO_2 at 1173 K and CO_2 pressures between 0.1 – 1.4 MPa. It can be seen that the surface area measured by both N_2 and CO_2 increased with increasing conversion degree, indicating the enlargement of meso-/macropores as well as micropores during gasification. Furthermore, total and micropore surface area increased significantly during gasification at higher CO_2 pressures.

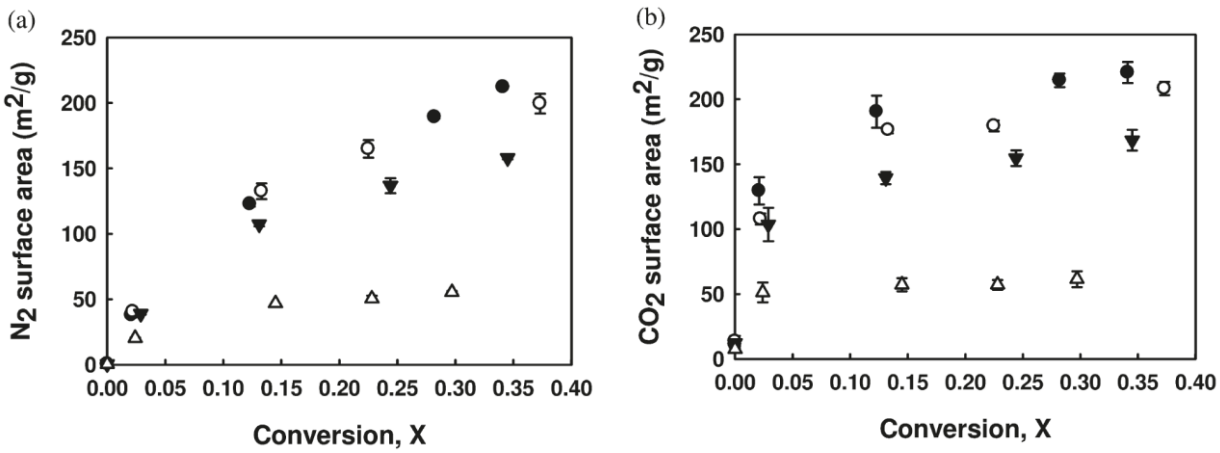

Fig. A.11. Surface area determined by (a) N_2 and (b) CO_2 adsorption as a function of conversion degree during gasification of petcoke with CO_2 at 1173 K and different pressures: Δ 0.1 MPa, ▼ 0.5 MPa, ○ 1.0 MPa, ● 1.4 MPa [99].

Liu et al. [114] characterized coal char samples in terms of morphology at different conversion degrees during pressurized gasification with CO_2. Fig. A.12 shows BET surface area and pore volume determined by N_2 adsorption at 77 K. During gasification with CO_2, the surface area of the char samples were significantly increased from 40 to 380 $m^2\ g^{-1}$ when the carbon conversion increased from 0 to 0.9. A similar trend was observed concerning the pore volume upon char

conversion. For conversion degrees above 0.9, pores started to coalesce and collapse, leading to a disappearance of available surface area for the gasification reaction. The authors conclude that throughout the entire gasification process, variations of surface area and pore structure determine the gasification kinetics of the coal char samples investigated.

Guizani et al. [87] investigated the evolution of chemical, textural and structural properties of biomass chars during atmospheric gasification with CO_2, H_2O and mixed CO_2/H_2O atmospheres. Their results indicate that gasification with H_2O leads to a higher internal char porosity than CO_2 at equivalent conversion levels. Furthermore, SEM images and porosity measurements showed that CO_2 gasification affects the outer particle surface to a higher extent than the particle core which may be related to a lower diffusivity of CO_2 as compared to H_2O. Based on their experimental results, the authors conclude that CO_2 and H_2O follow different pathways. In mixed CO_2/H_2O atmospheres, however, these two molecules do not react independently since several competition and synergy interactions were observed that led to an apparent law of reactivity.

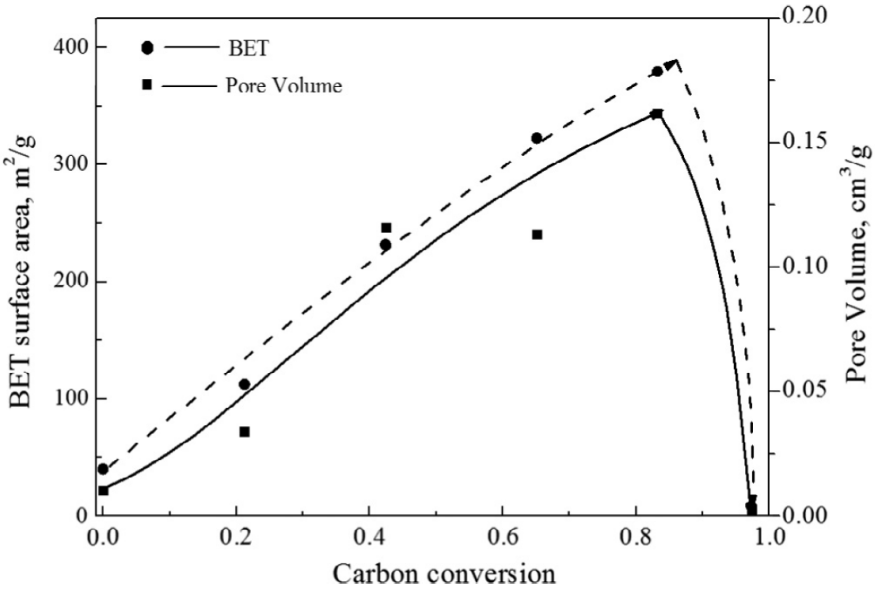

Fig. A.12. Evolution of surface area and pore volume of coal chars during pressurized gasification with CO_2 [114].

Comparison between fossil and biogenic solid fuels

The following chapter gives a brief comparison of properties found in fossil and biogenic solid fuels focusing on their differences and similarities concerning morphology, carbon matrix and catalytically active ash components affecting the heterogeneous gasification reactions.

Morphology

Wang et al. [161] studied the CO_2 gasification kinetics in respect of the physico-chemical properties of biomass and anthracite chars. In Fig. A.13, SEM images of chars originating from biomass ((a) wheat stalk, (b) rice lemma and (c) pine sawdust) and coal ((d) anthracite) are depicted [161]. For the wheat stalk char, a vertical texture with a thin skeleton and a porous structure can be observed. The rice lemma char exhibits an obvious framework structure including large random pores. For the pine sawdust char, the authors state that before milling and sieving, the particles form a honeycomb structure whereas the residual char mainly consists of a slice structure. On the other hand, the anthracite char particles show a non-uniform surface with no significant void spaces. The authors conclude that from the SEM images, higher porosity and surface area for the biomass chars can be deduced. A quantitative analysis of the specific surface areas was conducted using N_2 physisorption using the BET method confirming this statement.

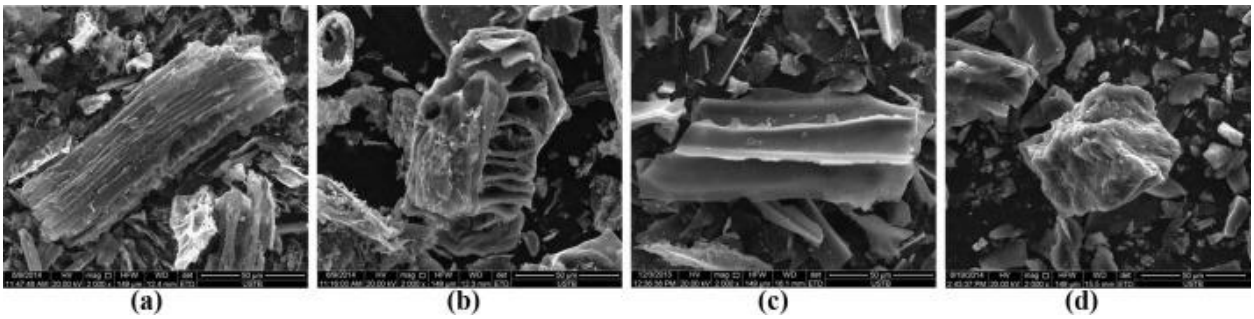

Fig. A.13. SEM images of chars originating from (a) wheat stalk, (b) rice lemma, (c) pine sawdust and (c) anthracite [161].

Borrego et al. [162] characterized biomass chars prepared in a drop tube furnace under high heating rates at 950 °C in atmospheres of nitrogen and carbon dioxide. For their pyrolysis experiments, rice husk, wood chips and forest residues were used as parent fuel. Specific surface area was determined via N_2 adsorption at 77 K using BET as well as CO_2 adsorption at 0 °C using DR. The authors propose that these two methods can be regarded as complementary since CO_2 has difficulties in filling the larger micropores and N_2 exhibits low diffusivity through the small micropores at 77 K [163]. The results of Borrego et al. [162] show values in terms of specific surface area determined via BET (N_2 adsorption at 77 K) for the chars prepared in N_2 atmosphere between 225 $m^2\ g^{-1}$ and 277 $m^2\ g^{-1}$. On the other hand, specific surface area measured using CO_2 adsorption at 0 °C gave approx. doubled values ranging between 490 $m^2\ g^{-1}$ and 552 $m^2\ g^{-1}$. These results indicate that in general, biomass chars pyrolyzed under high heating rates usually have

high specific surface areas. Additionally, due to the high values for specific surface during adsorption measurements using CO_2 at 0 °C applying the DR method, it can be deduced that these chars are highly microporous.

To sum up, the specific surface area of biomass chars is generally higher as compared to fossil-based solid fuels. However, pyrolysis conditions strongly affect char morphology i.e. specific surface area and pore size distribution. Biomass chars generated under high heating rates usually have a high specific surface area and are highly microporous. Since the available surface area might not be a restriction during gasification of highly porous biomass chars, the degree of graphitization as well as catalytically active ash components may predominantly determine char reactivity and the course of reaction. However, pore diffusion limitations might become relevant in case the gasification reaction takes place under regime II conditions (see chapter 2.2.2).

Carbon matrix

Huo et al. [164] characterized the carbon crystalline structure of biomass, coal and petroleum coke chars using XRD. For the coal and coke chars, the authors obtained narrow and sharp patterns for the diffraction peaks as compared to the biomass chars indicating a higher order of crystallinity concerning the former chars. Moreover, the graphitization degree was determined quantitatively by calculating the stacking height of graphene layers L_c and the distance between two graphene layers d_{002}. The highest values for L_c and the lowest values for d_{002} were found in the petroleum coke char. Additionally, the higher the coal rank, the higher was the stacking height of the graphene layers L_c. On the other hand, biomass chars were found to have relatively low stacking heights L_c and a larger distance between the graphene layers d_{002} as compared to the other samples. The authors correlated higher values for L_c (and the smaller the values for d_{002}) with a higher order of the carbon crystalline structure. This trend was in good accordance with the observed gasification reactivity. The lowest CO_2 gasification reactivities were observed for the chars with the highest values for L_c indicating that the chars with the highest graphitization degree are the least reactive.

Wang et al. [161] compared the carbon crystalline structure of biomass and anthracite chars using Raman spectroscopy. From the Raman spectra obtained, the authors formed the intensity ratios of V- and G-Peak (I_V/I_G) and were able to correlate this value with the observed gasification reactivity towards CO_2. Again, the sample with the highest graphitization degree (lowest value for I_V/I_G), i.e. anthracite char, showed the lowest reactivity. Another characterization of biomass

and coal chars concerning the graphitization degree using Raman spectra is conducted by Senneca et al. [63]. Walnut shells (WS) and a high-volatile bituminous Colombian coal (CC) were pyrolyzed in a heated strip reactor (HSR) allowing for high heating rates at temperatures of 1573 K– 2073 K and holding times of 3 s using atmospheres of either N_2 or CO_2. The resulting chars were characterized in terms of reactivity towards oxygen as well as graphitization and morphology. The authors conclude that the loss of reactivity by "thermal annealing" and structural reorganization follow similar pathways for coal and biomass. However, the WS chars developed an even larger degree of structural order upon severe heat treatment as compared to the coal chars.

Kreitzberg et al. [165] investigated thermally induced changes in the carbon crystalline structure and CO_2 gasification reactivity during pyrolysis of biogenic (torrefied poplar wood) and fossil fuels (Rhenish lignite). Experiments were carried out in a small scale fluidized bed reactor. For the assessment of thermal deactivation, heat treatment temperatures were varied between 1023 K and 1173 K and holding times between 0 s and 1800 s. The graphitization process was qualitatively evaluated as a function of heat treatment time at 1073 K using high resolution transmission electron microscopy (HRTEM) and selected area electron diffraction (SAED) patterns. Based on these patterns, the authors deduce that both fuels undergo a structural conversion from purely amorphous carbon to a turbostratic structure. For Rhenish lignite, turbostratic carbon layers with a high degree of ordering were found after 600 s of heat treatment at 1073 K indicating first fully graphitized regions. On the other hand, the structure of the torrefied poplar char showed turbostratic arrangements, but no visible carbon layer formations at 600 s were observed. In fact, the carbon structure of the biomass char at 600 s is comparable to the pattern found for the fossil fuel at 180 s heat treatment time. The authors conclude that the graphitization process of the Rhenish lignite proceeds more rapidly than the torrefied poplar wood particles. This effect was also quantitatively validated by the determination of thermal deactivation rates for both fuels. Despite the higher graphitization degrees of Rhenish lignite chars as compared to the torrefied biomass for the same heat treatment temperatures and holding times, the fossil fuel particles show overall higher reaction rates towards CO_2. Unfortunately, no further information concerning char morphology (specific surface area, pore structure) and ash elemental analysis is given by the authors in order to allow for an explanation of this phenomenon.

In conclusion, coal chars usually show a higher order of the carbon crystalline structure often resulting in a lower reactivity as compared to biomass chars. However, thermal deactivation and

structural reorganization during pyrolysis follow similar pathways for biomass and coal. For high pyrolysis temperatures, biomass chars might even develop higher graphitization degrees as compared to coal chars generated at the same pyrolysis conditions. Since chars with high graphitization degrees still might be more reactive than those with a lower degree of order, a thorough examination of the catalytically active ash components inherent in both, biogenic and fossil fuels, must be considered.

Catalytically active ash components

Due to their different formation processes, biomass and coal may show significantly varying inherent ash contents and compositions. Vassilev et al. [166] did an extensive study on the chemical composition of biomass with special emphasis its ash composition. In order to describe the biomass types investigated, the authors used reference peer-reviewed data for chemical compositions of 86 varieties of biomass. The authors were able to show that the chemical composition of biomass ash components is highly variable due to extremely high variations in total ash content and different genetic types of inorganic matter. The following inorganic species were found to be most abundant in biomass ash (decreasing order of abundance): Ca, K, Si, Mg, Al, S, Fe, P, Cl, Na, Mn, and Ti. Respective chemical data was found and evaluated for 38 solid fossil fuels. In comparison to ash originating from coal, natural biomass ash is highly enriched in Mn > K > P > Cl > Ca > Mg, Na while being depleted in total ash content, Al, Fe, S, Si, and Ti. Fig. A.14 shows a ternary diagram based on a chemical classification system of biomass ash including the aforementioned data of 86 biomass varieties plus algae and 38 solid fossil fuels [141]. Solid points show the mean ash composition of the fuels investigated. The grey area marks all the reference data concerning biomass ash emphasizing its large variety in chemical composition (biomass area). With this classification system, the authors were able to identify four main chemical biomass ash types (S, C, K and CK type). These can be further specified into seven sub-types with high, medium and low acid tendencies. Hence, wood and woody biomass ash can be classified as C type with low to medium acid tendency and a (CaO + MgO + MnO) content above 30 wt. %. For animal biomass ash, both sums of (CaO + MgO + MnO and $K_2O + P_2O_5 + SO_3 + Cl_2O$) are above 30 wt.-% while ($SiO_2 + Al_2O_3 + Fe_2O_3 + Na_2O + TiO_2$) is below 40 wt.-% resulting in a CK type with low acid tendency. Herbaceous and agricultural biomass, grass, straw and residue can be subsumed into K type ashes with low to medium acid tendency and values for ($K_2O + P_2O_5 + SO_3 + Cl_2O$) above 30 wt.-%. Eventually, contaminated biomass ash can be assigned to S type with ($SiO_2 + Al_2O_3 + Fe_2O_3 + Na_2O + TiO_2$) values between 40 and 70 wt.-% being close to solid fossil fuels.

WWB - Wood and woody biomass
HAB - Herbaceous and agricultural biomass
HAG - Herbaceous and agricultural grass
HAS - Herbaceous and agricultural straw
HAR - Herbaceous and agricultural residue
AB - Animal biomass
MB - Mixture of biomass
CB - Contaminated biomass
AVB - All varieties of biomass
P - Peat
L - Lignite
S - Sub-bituminous coal
B - Bituminous coal
A - Algae

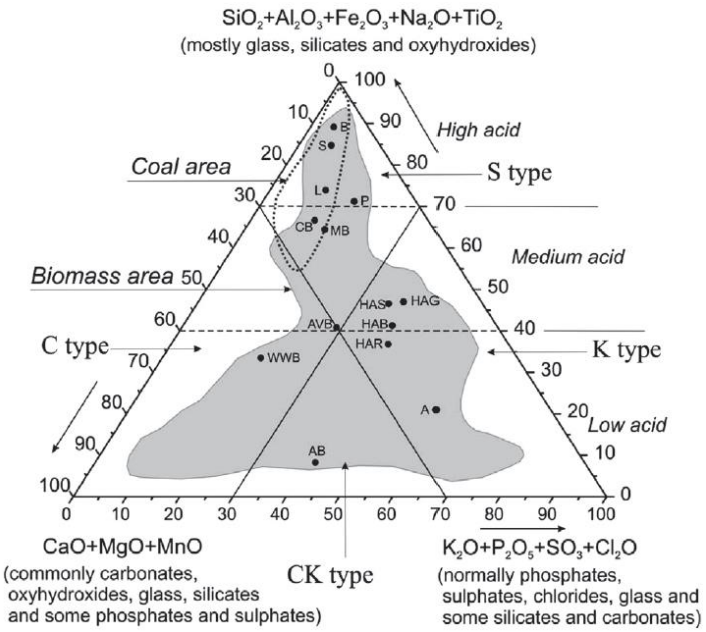

Fig. A.14. Ternary diagram including 86 biomass varieties plus algae and 38 solid fossil fuels in the chemical classification system of biomass ash, wt.-% [141].

The chemical composition of various coal ashes is highlighted with a dashed line (coal area) given mean values for lignite and (sub-)bituminous coals. It can be noted that ash of solid fossil fuels would be solely classified as S type with medium or high acid tendencies including high silica and alumina contents. This phenomenon has strong influence on the gasification behavior of the resulting chars. Since silica and alumina have the tendency to decrease the catalytic activity of potassium [167,168], the catalytic gasification reaction will be less dominating during heterogeneous conversion of coal chars. On the other hand, the most abundant inorganic species found in biomass ashes are calcium and potassium showing strong catalytic activity and increasing the observed gasification reactivity (see chapter 2.3.3).

To sum up, total ash content and ash composition differ significantly between solid biogenic and fossil fuels. Among different biomass types, in addition, the encountered inorganic matter composition may vary strongly. Vassilev et al. [166] presented an overview concerning the chemical composition of many biomass varieties and proposed a classification system for biomass ashes including four major types. The ashes of solid fossil fuels would be assigned to only one type (type S) of this system. Coals usually have high amounts of silica and alumina that may inhibit the catalytic gasification reaction. On the other hand, biogenic fuels are generally rich in calcium and potassium that evidentially catalyze the heterogeneous gasification reaction (see chapter 2.3.3).

B Materials and methods

Primary chars

Table B.1. Proximate and ultimate analysis of the primary chars.

	WC500	HK06
Proximate analysis / wt.-%, ad		
Moisture	2.9	0.9
Ash content	2.0	1.8
Volatiles	26.4	11.8
Ultimate analysis / wt.-%, daf		
C	79.7	89.8
H	3.1	2.6
O (diff)	17.2	7.2
N	< 0.1	0.4

Table B.2. Ash elemental analysis of the primary chars.

	Na	K	Mg	Ca	Al	Si	Fe
				wt.-%			
WC500	0.9	3.2	5.5	36.1	1.2	8.0	1.4
HK06	0.8	4.6	6.0	38.2	0.3	2.0	0.7

Secondary chars

Table B.3. Proximate and ultimate analysis of secondary chars.

	WC1600	WC1600n	P1400	P1600
Proximate analysis / wt.-%, ad				
Moisture	1.1	0.5	0.2	0.0
Ash content	6.6	2.6	1.9	1.6
Volatiles	4.6	2.4	2.5	1.3
Ultimate analysis / wt.-%, daf				
C	97.4	97.2	97.2	99.0
H	< 0.1	< 0.1	0.2	0.2
O (diff)	1.6	2.2	1.9	0.3
N	1.0	0.6	0.7	0.5

Table B.4. Ash elemental analysis of the secondary chars.

	Na	K	Mg	Ca	Al	Si	Fe	P
				wt.-%				
WC1600	0.5	9.1	1.6	30.1	3.5	25.8	2.6	n.a.
WC1600n	0.9	4.4	1.1	39.2	1.3	9.0	1.3	n.a.
P1400	1.0	5.5	5.8	35.3	0.3	2.5	0.8	1.7
P1600	0.8	5.1	1.0	39.1	0.3	2.5	0.8	1.5

Impregnated activated carbon

Table B.5. Mass fractions of raw activated carbon (AC) and two impregnated samples AC1Ca and AC1K determined by ICP-OES.

	Ca	K	Si
		mg g_C^{-1}	
AC	0.8	0.7	2.8
AC1Ca	26.5	0.7	2.8
AC2Ca	57.0	0.7	2.8
AC1K	0.8	25.0	2.8

Drop-tube reactor

Schematic flow diagram

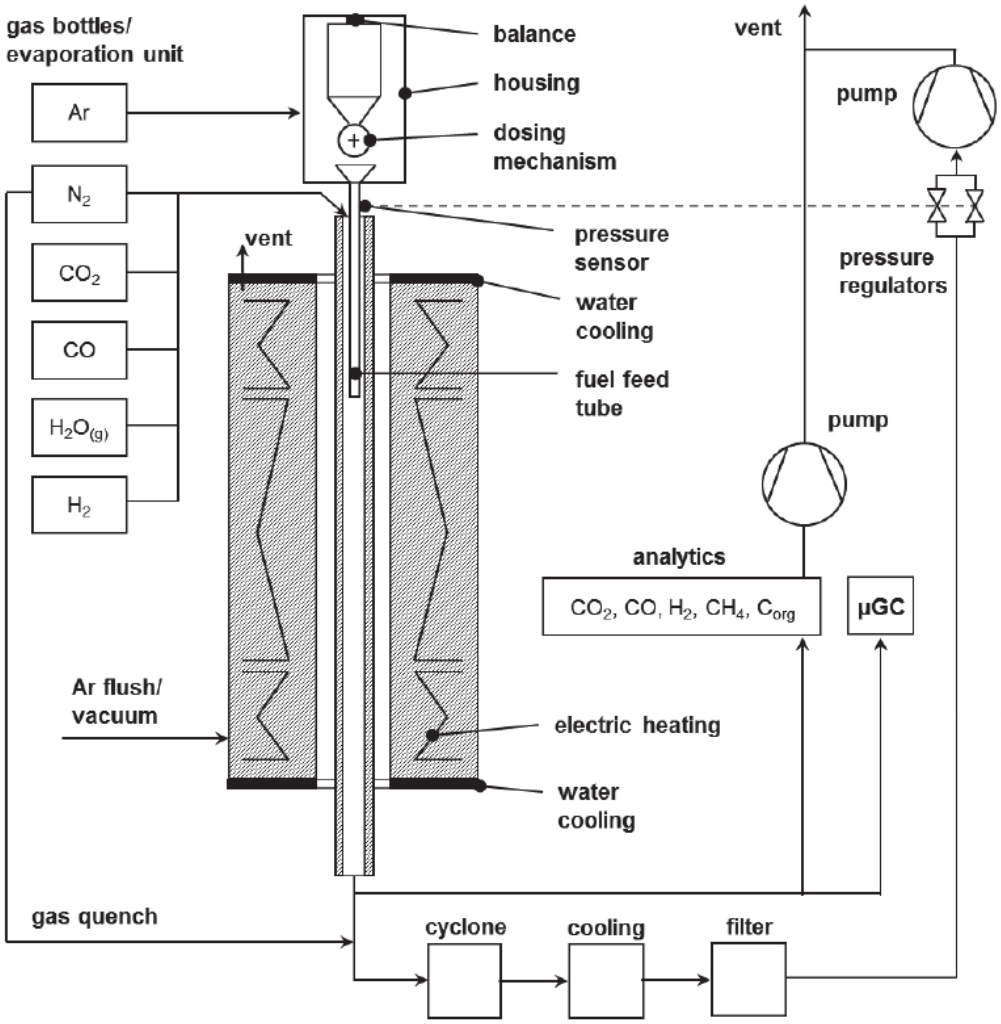

Fig. B.1. Flow sheet of the drop tube reactor set-up at EBI ceb, KIT [142].

Detailed description

"The drop-tube reactor (DTR) consists of an oven (HTM Reetz GmbH) with three heating zones (l_{H1} = 200 mm, l_{H2} = 917 mm, l_{H3} = 200 mm) and a total length of 2000 mm. Each heating zone can be heated to a maximum temperature of 1700 °C. An alumina oxide reaction tube (Aliaxis Deutschland GmbH) with a length of 2100 mm and the inner diameter of 20 mm is inserted vertically in the oven. The temperature calibration was conducted with a type B thermocouple, which was introduced into the reactor from the top under steady-state gas flow. Gas temperature

profiles for the pyrolysis experiments can be found in the supplementary material section. A co-axial alumina oxide pipe (length 810 mm, inner diameter 4 mm) was used to feed Argon (tracer and carrier gas) and the primary char into the reactor. The feeding system consists of a slowly rotating ceramic disc (Pure Feed DP-4, Schenck Process Europe GmbH) enabling stable solid mass flow rates of approx. 1 g min^{-1}. The primary char was mixed with the reaction gas at the beginning of the second heating zone. For the experiments presented in this work, gas velocity in the reactor was adjusted in order to ensure a gas-phase residence time in the isothermal zone of 200 ms using N_2 as core flow. N_2 volume flow was varied between 11.85 l/min and 17.44 l/min while Ar flow was varied between 0.52 l/min and 0.76 l/min leading to an N_2/Ar ratio of approx. 23. Ar flow was adjusted in order to ensure similar gas velocities inside the dosing and the reactor tube. At the outlet of the reactor, the hot reaction gas and secondary char were cooled by an inert gas quench to temperatures below 400 °C. Subsequently, the char samples were separated in a hot gas cyclone and collected in a nitrogen-flushed lock for further analyses. The reactor pressure was controlled by two electrically controlled valves and set to 5 mbar gauge. Product gas was continuously monitored with infrared photometry (URAS, ABB) and micro gas chromatography (490 Micro GC, Agilent Technologies)." [108]

Gas temperature profiles

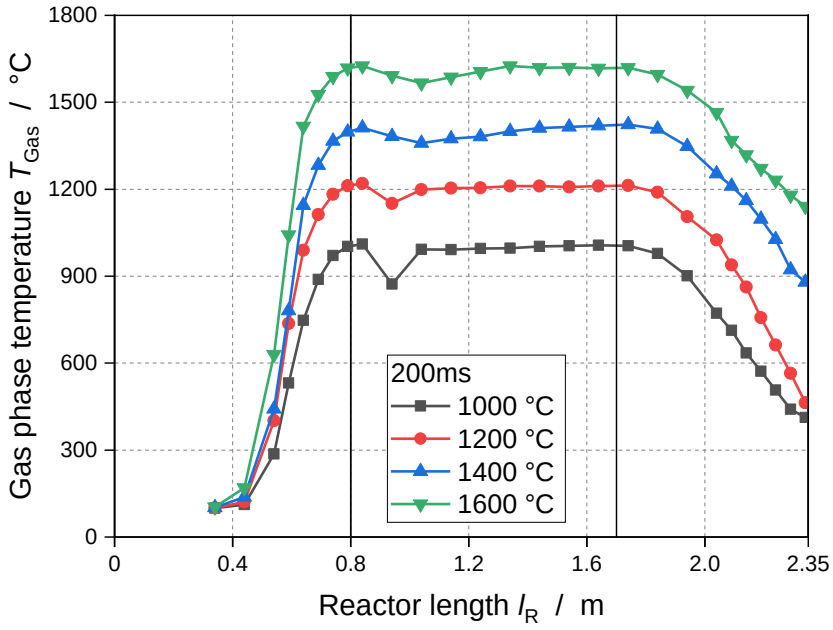

Fig. B.2. Axial gas temperature profiles for the secondary pyrolysis experiments of HK06 between 1000 °C and 1600 °C; steady state gas flow with N_2/Ar at 200 ms isothermal residence time [108].

Pressurized single-particle reactor

Detailed description

"The gas dosing system consists of mass flow controllers (MFC, EL-FLOW, Bronkhorst High-Tech B.V.) for CO_2 and argon allowing for volume flows up to 20 l min^{-1}. Furthermore, one MFC is used for dosing small amounts of nitrogen that is used as a tracer in the analytic strand. Demineralized water is stored in a vessel (V = 1 l) and pressurized with 30 bar helium. Measurement of the liquid water flow is carried out using a *mini CORI-FLOW* (Bronkhorst High-Tech B.V.). Steam is generated in a *Controlled Evaporation and Mixing* unit (CEM, Bronkhorst High-Tech B.V.) and - together with a carrier gas - led to the reaction line. A 4-port 2-position valve (V1, VICI) allows the feed gas mixture which is normally entering the reactor to be switched to the bypass line. With this arrangement, the reactor line including the reactor can be purged with argon. The tubular reactor (1200 mm height, 19.5 mm inner diameter) is mounted vertically and can be operated at a pressure of up to 24 bar. The pressure of reaction and bypass line is controlled by back pressure regulators (EL-PRESS, Bronkhorst High-Tech B.V.). Another 4-port 2-position valve (V2, VICI) after the back pressure regulators allows the product gases to either be analyzed using infrared photometry (IR, URAS, ABB) and micro gas chromatography (490 Micro GC, Agilent Technologies) or directly be sent to the off-gas system.

The char is fed into the reactor batch-wise with a dosing unit that is schematically depicted in Fig. B.3 (A). The central component of this device is a brass cylinder (a) with a cylindrical bore where the char is placed prior to the gasification experiment. This brass cylinder can be removed from the dosing unit in order to fill the bore with char and weigh the sample. When the brass cylinder (a) is inserted into the dosing unit, it is sealed with PTFE foil. The brass cylinder (a) is situated beneath a receiver tank (b) that can be flushed with argon in order to remove oxygen from the dosing unit (valve (d) closed, valves (c) and (e) open). The receiver tank is filled with quartz wool in order to minimize void space with potential accumulation of oxygen. Prior to each gasification experiment, the receiver tank (b) was flushed with argon for at least 10 minutes. Subsequently, the valves (c) and (e) are closed to prevent oxygen from entering the receiver tank (b) and valve (d) is opened. Argon flows down the conus (f) of the dosing unit and serves as a carrier gas for the char. Eventually, the brass cylinder (a) is turned by 180 ° and the char falls out of the dosing unit being carried onto a quartz wool bed inside the reactor by the gas flow.

Fig. B.3 (B) shows the arrangement inside the single-particle reactor during a gasification experiment. The char sample is placed on a quartz wool bed while the feed gas flows top-down. Beneath the quartz wool bed, a quartz glass tube with fused-in quartz frit is located. In order to measure the temperature of the char sample, a type K thermocouple is inserted via a quartz glass capillary tube that is fused into the frit. The end of the quartz glass tube is sealed with a stuffing box packing (not shown in Fig. B.3 (B)), i.e. a ceramic fiber rope that prevents an idle gas flow past the char sample and the quartz glass tube." [57]

Dosing unit and inside arrangement

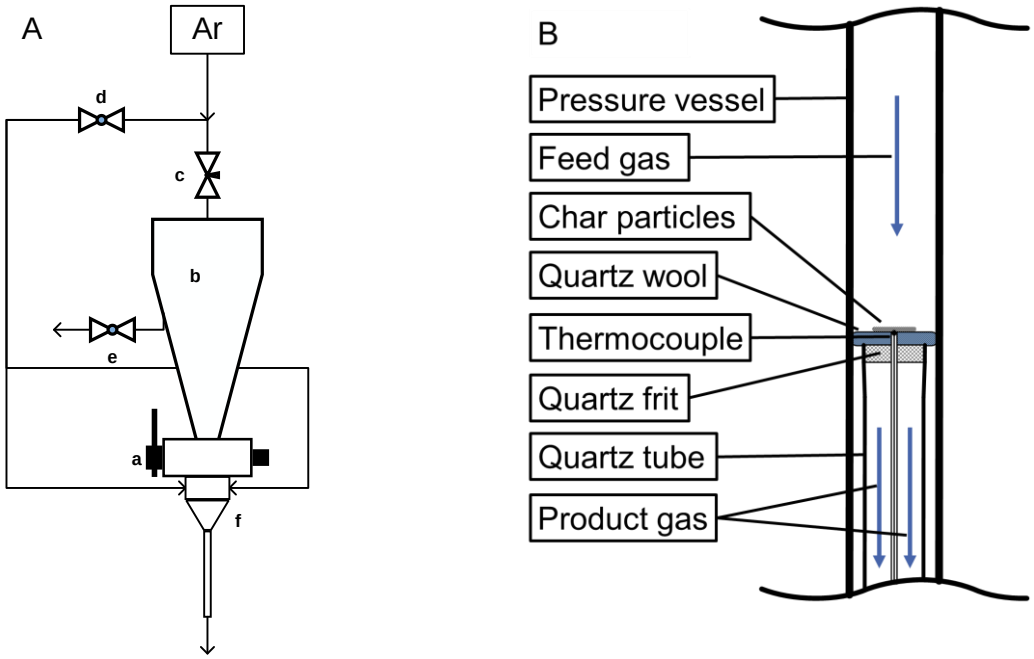

Fig. B.3. Schematic illustration of the dosing unit (A) (a, brass cylinder; b receiver tank; c-e, valves; f conus) and the arrangement inside the single-particle reactor (B) [57].

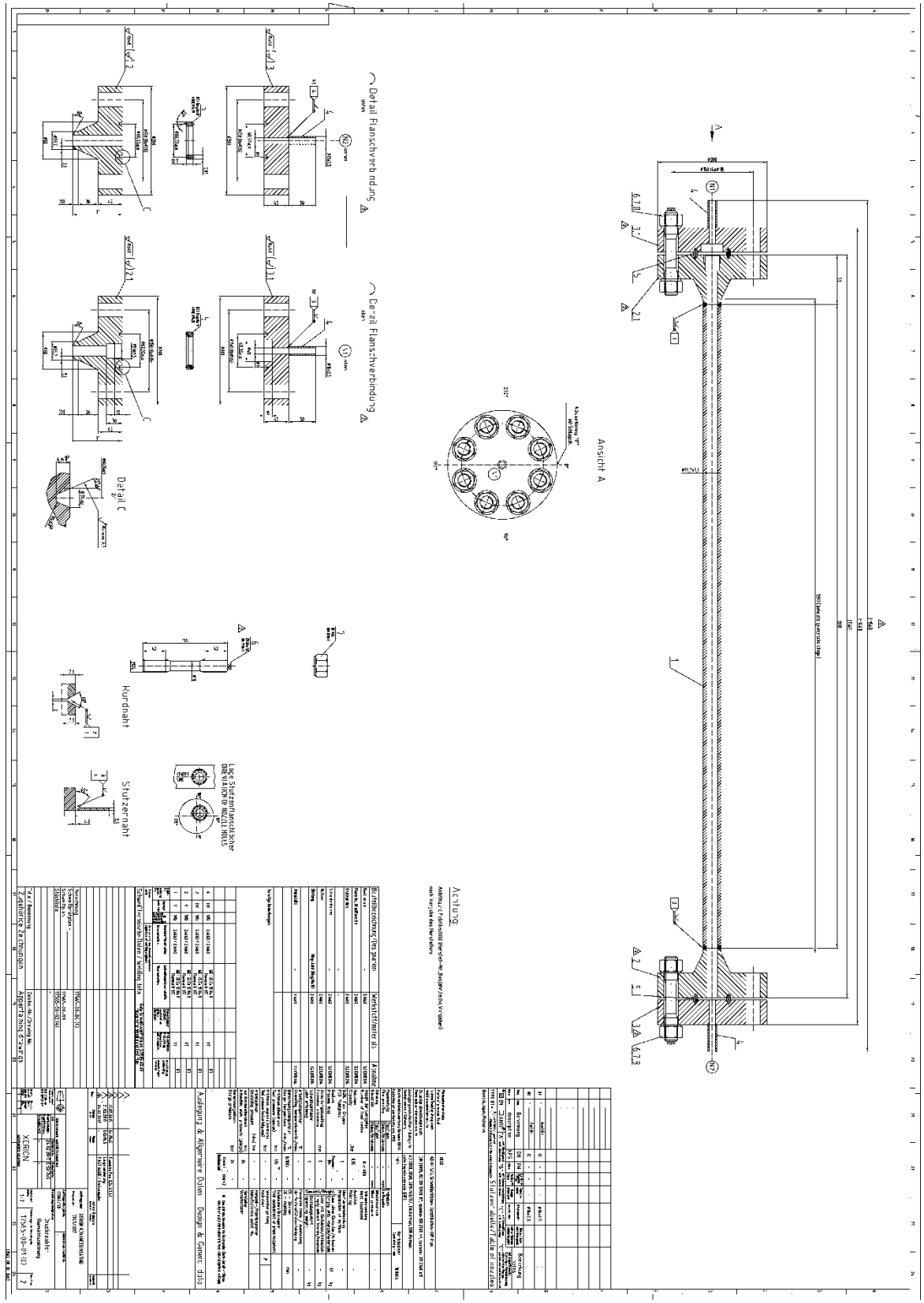

Fig. B.4. Engineering drawing of the high-pressure vessel of the singe-particle reactor [169].

Pressurized thermogravimetric analyzer

Schematic flow diagram

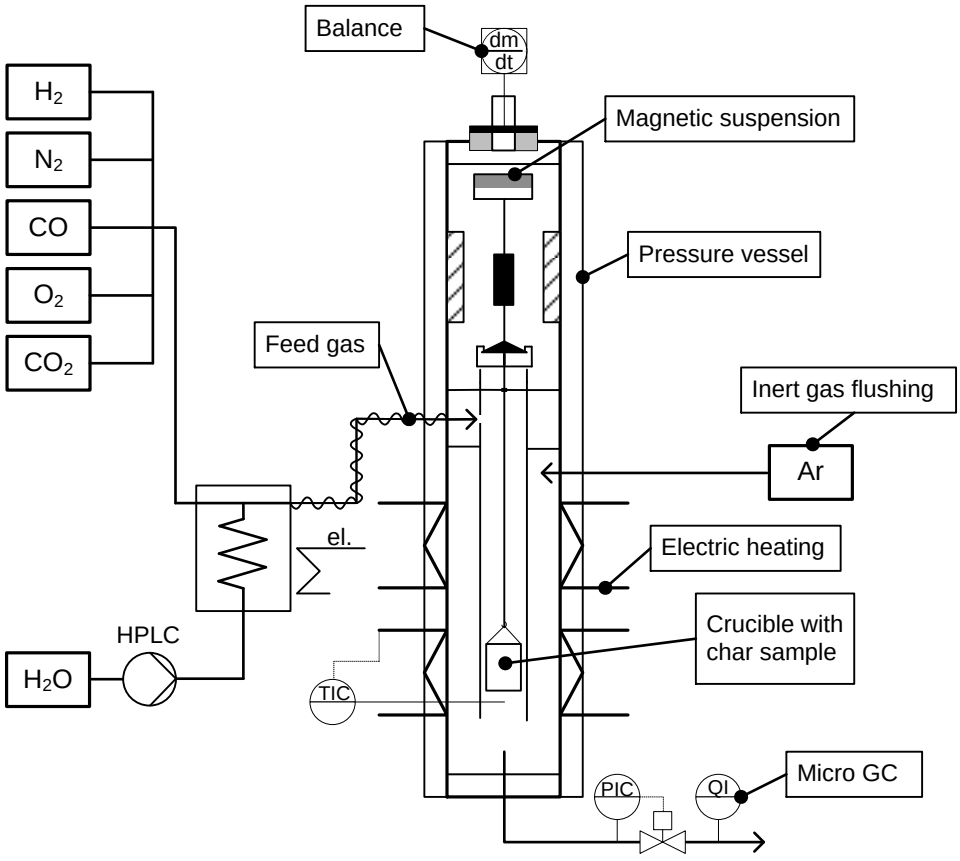

Fig. B.5. Schematic flow diagram of the pressurized thermogravimetric analyzer set-up at EBI ceb, KIT.

Chemisorption analyzer

Schematic drawing of the quartz glass reactor system

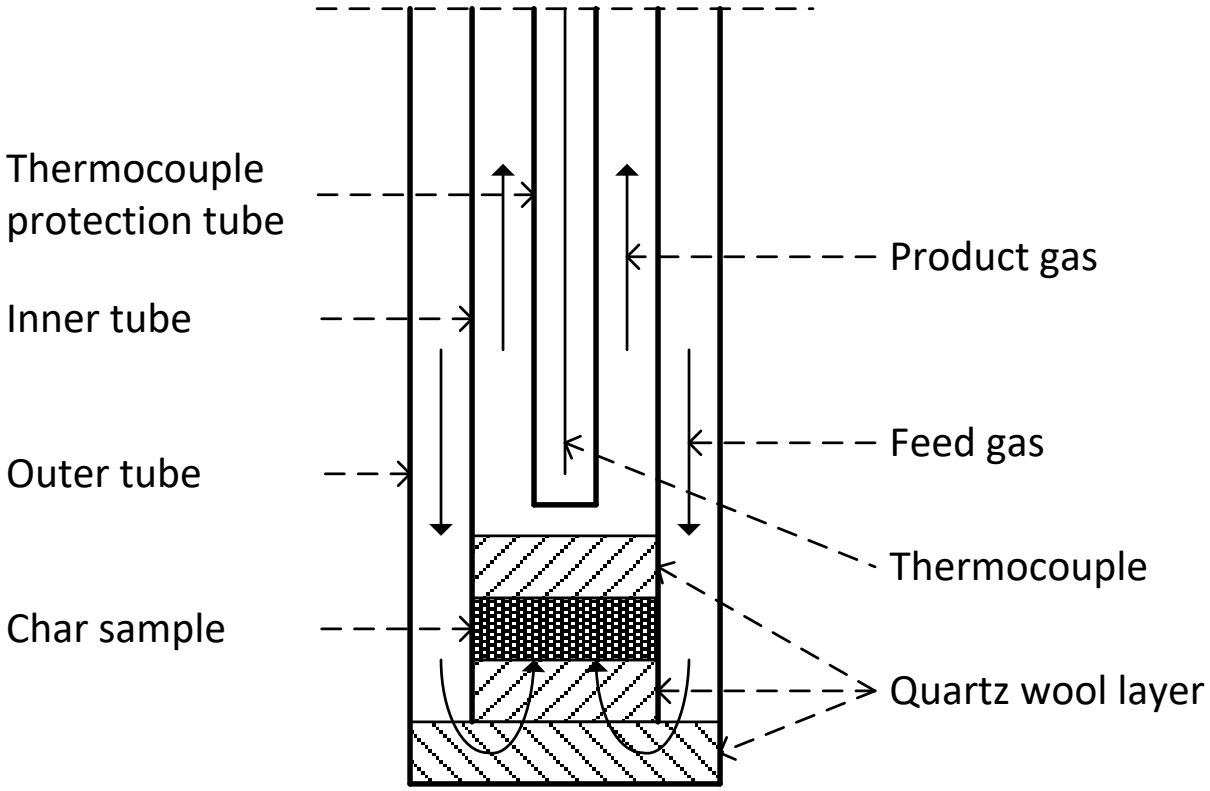

Fig. B.6. Schematic drawing of the quartz glass reactor system of the chemisorption analyzer at EBI ceb, KIT [147].

C Results and discussion

Evolution of char properties during gasification

Adsorption isotherms

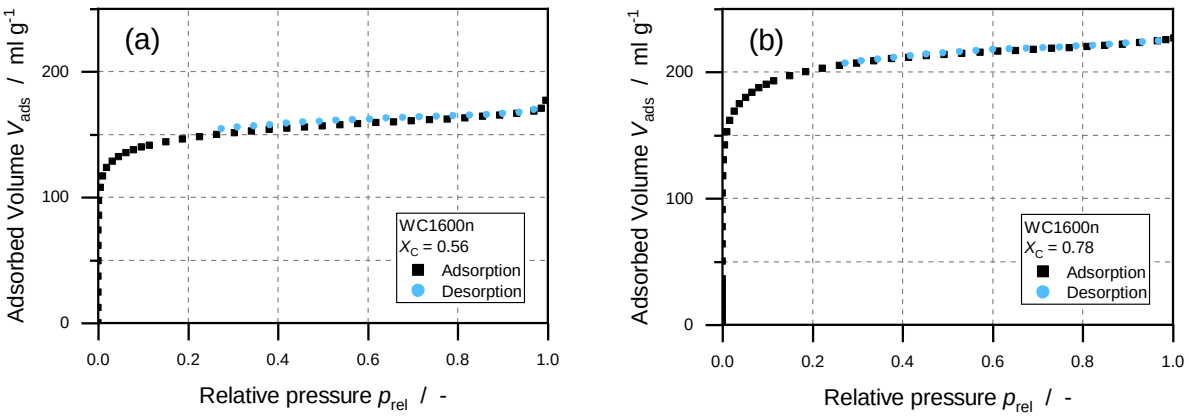

Fig. C.1. Adsorption and desorption isotherms of WC1600n at carbon conversion degrees of (a) X_C = 0.56 and (b) X_C = 0.78; gasification in the DTR at 1000 °C and 1,5 s residence time; adapted from [143].

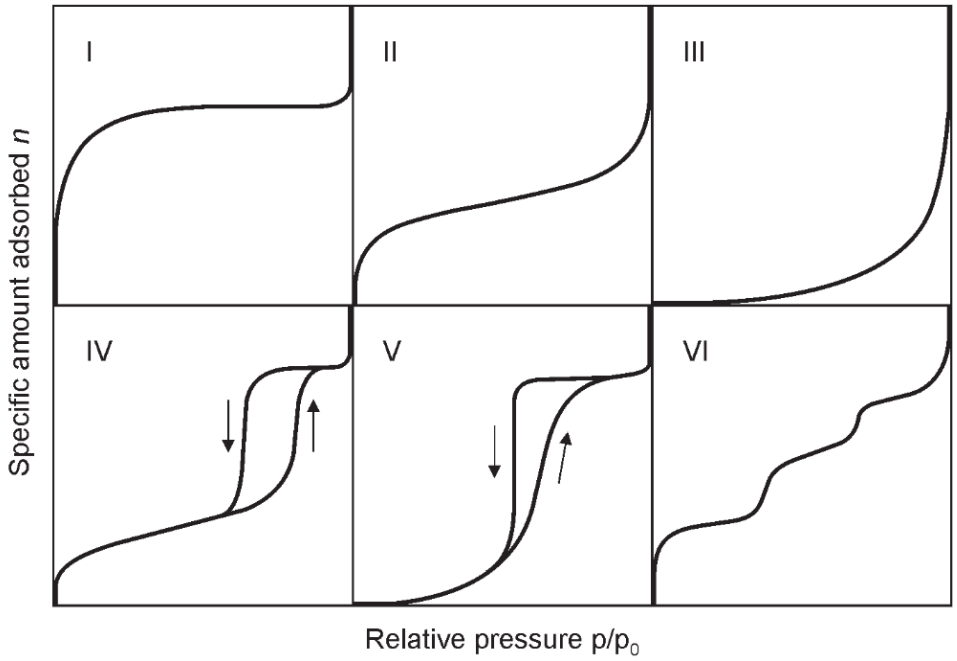

Fig. C.2. Schematic illustration of six adsorption isotherm types [170,171].

Determination of gasification kinetics

Gasification kinetics with CO_2 in pTGA

Table C.1. Kinetic parameters for gasification of WC1600 with CO_2 using power law approach.

		WC1600
k_{0,CO_2}	mol (g s bar^n)$^{-1}$	7.5 10^5
E_{A,CO_2}	kJ mol^{-1}	248.7
n_{CO_2}	-	0.35

Gasification kinetics with CO_2 in pSPR

Table C.2. Kinetic parameters for gasification of P1400 and P1600 with CO_2 using power law approach.

		P1400	P1600
k_{0,CO_2}	mol (g s bar^n)$^{-1}$	1.0163 10^{10}	5.675 10^9
E_{A,CO_2}	kJ mol^{-1}	308.7	300.7
n_{CO_2}	-	0.214	0.186

Table C.3. Kinetic parameters for the gasification of P1400 and P1600 with CO_2 using LH approach.

		P1400	P1600
$k_{0,1}$	mol (g s bar)$^{-1}$	6.80 10^8	2.1 10^7
$k_{0,3}$	mol (g s)$^{-1}$	3.0348 10^{10}	2.6775 10^{10}
$E_{A,1}$	kJ mol^{-1}	275.9	241.0
$E_{A,3}$	kJ mol^{-1}	313.7	310.2

Gasification kinetics with H_2O in pSPR

Table C.4. Reaction kinetic parameters for gasification of P1400 and P1600 with H_2O using power law approach.

		P1400	P1600
k_{0,H_2O}	mol (g s bar^n)$^{-1}$	1.55 10^8	5.7 10^6
E_{A,H_2O}	kJ mol^{-1}	263.6	234.8
n_{H_2O}	-	0.467	0.445

Table C.5. Reaction kinetic parameters for gasification of P1400 and P1600 with H_2O using LH approach.

		P1400	P1600
$k_{0,4}$	mol (g s bar)$^{-1}$	6.7 10^6	1.5 10^6
$k_{0,6}$	mol (g s)$^{-1}$	3.142 10^9	3.0 10^7
$E_{A,4}$	kJ mol^{-1}	225.9	213.5
$E_{A,6}$	kJ mol^{-1}	284.7	243.8

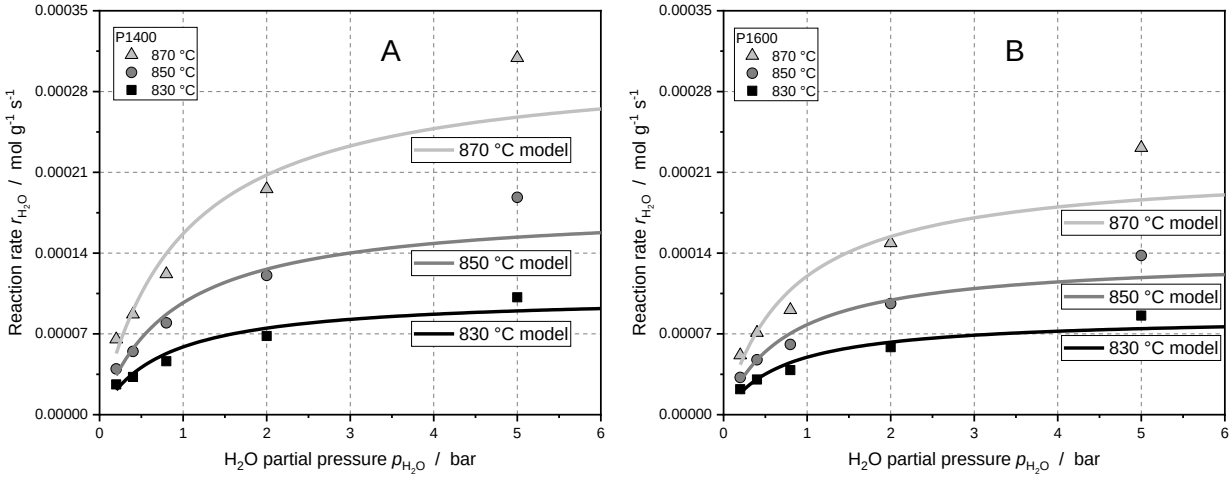

Fig. C.1. Modeling of the gasification reaction with H_2O for P1400 (A) and P1600 (B) using an LH approach [57].

References

[1] European Comission. The European Green Deal - Communication from the Commission to the European Parliament, the European Council, the Council, the European Economic and Social Committee and the Committee of the Regions; 2019.

[2] Eberhard M, Santo U, Michelfelder B, Günther A, Weigand P, Matthes J et al. The bioliq Entrained-Flow Gasifier - A Model for the German Energiewende. ChemBioEng Reviews 2020;7(4):106–18. doi:10.1002/cben.202000006.

[3] Jakobs T, Djordjevic N, Fleck S, Mancini M, Weber R, Kolb T. Gasification of high viscous slurry R&D on atomization and numerical simulation. Applied Energy 2012;93:449–56. doi:10.1016/j.apenergy.2011.12.026.

[4] Fleck S, Santo U, Hotz C, Jakobs T, Eckel G, Mancini M et al. Entrained flow gasification Part 1: Gasification of glycol in an atmospheric-pressure experimental rig. Fuel 2018;217:306–19. doi:10.1016/j.fuel.2017.12.077.

[5] Watter H. Nachhaltige Energiesysteme: Grundlagen, Systemtechnik und Anwendungsbeispiele aus der Praxis mit 45 Tabellen. 1st ed. Wiesbaden: Vieweg+Teubner Verlag / GWV Fachverlage GmbH Wiesbaden; 2009.

[6] Higman C, van der Burgt M. Gasification. Boston: Elsevier/Gulf Professional Pub; 2003.

[7] De S, Agarwal AK, Moholkar VS, Thallada B (eds.). Coal and Biomass Gasification: Recent Advances and Future Challenges. Singapore: Springer; 2018.

[8] Di Blasi C. Modeling chemical and physical processes of wood and biomass pyrolysis. Progress in Energy and Combustion Science 2008;34(1):47–90. doi:10.1016/j.pecs.2006.12.001.

[9] Niksa S, Kerstein AR. FLASHCHAIN theory for rapid coal devolatilization kinetics. 1. Formulation. Energy Fuels 1991;5(5):647–65. doi:10.1021/ef00029a006.

[10] Solomon PR, Hamblen DG, Carangelo RM, Serio MA, Deshpande GV. General model of coal devolatilization. Energy Fuels 1988;2(4):405–22. doi:10.1021/ef00010a006.

[11] Fletcher TH, Kerstein AR, Pugmire RJ, Solum MS, Grant DM. Chemical percolation model for devolatilization. 3. Direct use of carbon-13 NMR data to predict effects of coal type. Energy Fuels 1992;6(4):414–31. doi:10.1021/ef00034a011.

[12] Fletcher TH. Review of 30 Years of Research Using the Chemical Percolation Devolatilization Model. Energy Fuels 2019;33(12):12123–53. doi:10.1021/acs.energyfuels.9b02826.

[13] Hurt R, Sun J-K, Lunden M. A Kinetic Model of Carbon Burnout in Pulverized Coal Combustion. Combustion and Flame 1998;113(1):181–97. doi:10.1016/S0010-2180(97)00240-X.

[14] Radovic LR, Steczko K, Walker PL, Jenkins RG. Combined effects of inorganic constituents and pyrolysis conditions on the gasification reactivity of coal chars. Fuel Processing Technology 1985;10(3):311–26. doi:10.1016/0378-3820(85)90038-4.

[15] Russell NV, Gibbins JR, Man CK, Williamson J. Coal Char Thermal Deactivation under Pulverized Fuel Combustion Conditions. Energy Fuels 2000;14(4):883–8. doi:10.1021/ef990241w.

[16] Russell NV, Gibbins JR, Williamson J. Structural ordering in high temperature coal chars and the effect on reactivity. Fuel 1999;78(7):803–7. doi:10.1016/S0016-2361(98)00210-5.

[17] Salatino P, Senneca O, Masi S. Assessment of Thermodeactivation during Gasification of a Bituminous Coal Char. Energy Fuels 1999;13(6):1154–9. doi:10.1021/ef9900334.

[18] Senneca O, Salatino P, Masi S. Microstructural changes and loss of gasification reactivity of chars upon heat treatment. Fuel 1998;77(13):1483–93. doi:10.1016/S0016-2361(98)00056-8.

[19] Kreitzberg T, Bormann C, Pielsticker S, Hatzfeld O, Kneer R. Thermal deactivation of biogenic and fossil fuels: Experimental investigation and modeling approaches. Energy Procedia 2019;158:2025–30. doi:10.1016/j.egypro.2019.01.468.

[20] Di Blasi C. Combustion and gasification rates of lignocellulosic chars. Progress in Energy and Combustion Science 2009;35(2):121–40. doi:10.1016/j.pecs.2008.08.001.

[21] Zanzi R, Sjöström K, Björnbom E. Rapid high-temperature pyrolysis of biomass in a free-fall reactor. Fuel 1996;75(5):545–50. doi:10.1016/0016-2361(95)00304-5.

[22] Morin M, Pécate S, Hémati M, Kara Y. Pyrolysis of biomass in a batch fluidized bed reactor: Effect of the pyrolysis conditions and the nature of the biomass on the physicochemical properties and the reactivity of char. Journal of Analytical and Applied Pyrolysis 2016;122:511–23. doi:10.1016/j.jaap.2016.10.002.

[23] Feng B, Jensen A, Bhatia SK, Dam-Johansen K. Activation Energy Distribution of Thermal Annealing of a Bituminous Coal. Energy Fuels 2003;17(2):399–404. doi:10.1021/ef020108v.

[24] Zhuo Y. Conversion of coal particles in pyrolysis and gasification: Comparison of conversions in a pilot-scale gasifier and bench-scale test equipment. Fuel 2000;79(7):793–802. doi:10.1016/S0016-2361(99)00194-5.

[25] Lu L, Kong C, Sahajwalla V, Harris D. Char structural ordering during pyrolysis and combustion and its influence on char reactivity. Fuel 2002;81(9):1215–25. doi:10.1016/S0016-2361(02)00035-2.

[26] Cetin E, Moghtaderi B, Gupta R, Wall TF. Influence of pyrolysis conditions on the structure and gasification reactivity of biomass chars. Fuel 2004;83(16):2139–50. doi:10.1016/j.fuel.2004.05.008.

[27] Tremel A, Spliethoff H. Gasification kinetics during entrained flow gasification – Part I; Devolatilisation and char deactivation. Fuel 2013;103:663–71. doi:10.1016/j.fuel.2012.09.014.

[28] Cetin E, Gupta R, Moghtaderi B. Effect of pyrolysis pressure and heating rate on radiata pine char structure and apparent gasification reactivity. Fuel 2005;84(10):1328–34. doi:10.1016/j.fuel.2004.07.016.

[29] Cazorla-Amoros D, Linares-Solano A, Salinas-Martinez de Lecea C, Yamashita H, Kyotani T, Tomita A et al. XAFS and thermogravimetry study of the sintering of calcium supported on carbon. Energy Fuels 1993;7(1):139–45.

[30] Rocca PAD, Cerrella EG, Bonelli PR, Cukierman AL. Pyrolysis of hardwoods residues: On kinetics and chars characterization. Biomass and Bioenergy 1999;16(1):79–88. doi:10.1016/S0961-9534(98)00067-1.

[31] Fushimi C, Araki K, Yamaguchi Y, Tsutsumi A. Effect of Heating Rate on Steam Gasification of Biomass. 1. Reactivity of Char. Ind. Eng. Chem. Res. 2003;42(17):3922–8. doi:10.1021/ie030056c.

[32] Guerrero M, Ruiz MP, Alzueta MU, Bilbao R, Millera A. Pyrolysis of eucalyptus at different heating rates: Studies of char characterization and oxidative reactivity. Journal of Analytical and Applied Pyrolysis 2005;74(1):307–14. doi:10.1016/j.jaap.2004.12.008.

[33] Kurosaki F, Ishimaru K, Hata T, Bronsveld P, Kobayashi E, Imamura Y. Microstructure of wood charcoal prepared by flash heating. Carbon 2003;41(15):3057–62. doi:10.1016/S0008-6223(03)00434-2.

[34] Biagini E, Fantozzi C, Tognotti L. Characterization of devolatilization of secondary fuels in different conditions. Combustion Science and Technology 2004;176(5-6):685–703. doi:10.1080/00102200490428008.

[35] Kaltschmitt M, Hartmann H, Hofbauer H (eds.). Energie aus Biomasse: Grundlagen, Techniken und Verfahren. 2nd ed. Berlin: Springer; 2009.

[36] Emig G, Klemm E. Chemische Reaktionstechnik. 6th ed. Berlin: Springer; 2017.

[37] Ollero P, Serrera A, Arjona R, Alcantarilla S. The CO_2 gasification kinetics of olive residue. Biomass and Bioenergy 2003;24(2):151–61. doi:10.1016/S0961-9534(02)00091-0.

[38] Risnes H, Sørensen LH, Hustad JE. CO_2 Reactivity of Chars from Wheat, Spruce and Coal. In: Bridgwater AV, editor. Progress in Thermochemical Biomass Conversion. Oxford, UK: Blackwell Science Ltd; 2001, p. 61–72.

[39] Everson RC, Neomagus HWJP, Kasaini H, Njapha D. Reaction kinetics of pulverized coal-chars derived from inertinite-rich coal discards: Gasification with carbon dioxide and steam. Fuel 2006;85(7-8):1076–82. doi:10.1016/j.fuel.2005.10.016.

[40] Levenspiel O. The chemical reactor omnibook. 5th ed. Corvallis, Or.: OSU Book Stores Inc; 1996.

[41] Ishida M, Wen CY. Comparison of zone-reaction model and unreacted-core shrinking model in solid—gas reactions—I isothermal analysis. Chemical Engineering Science 1971;26(7):1031–41. doi:10.1016/0009-2509(71)80017-9.

[42] Wen CY. Noncatalytic heterogeneous solid-fluid reaction models. Industrial & Engineering Chemistry 1968;60(9):34–54.

[43] Bhatia SK, Perlmutter DD. A random pore model for fluid-solid reactions: I. Isothermal, kinetic control. AIChE J. 1980;26(3):379–86. doi:10.1002/aic.690260308.

[44] Fatehi H, Bai X-S. Effect of Pore Size on the Gasification of Biomass Char. Energy Procedia 2015;75:779–85. doi:10.1016/j.egypro.2015.07.514.

[45] Fatehi H, Bai X-S. Structural evolution of biomass char and its effect on the gasification rate. Applied Energy 2017;185:998–1006. doi:10.1016/j.apenergy.2015.12.093.

[46] Tang J, Wu X, Wang J. Kinetic study of steam gasification of two mineralogically different lignite chars: An active site/intermediate model. Fuel 2015;141:46–55. doi:10.1016/j.fuel.2014.10.028.

[47] Dittmeyer R, Emig G. Simultaneous heat and mass transfer and chemical reaction. Handbook of Heterogeneous Catalysis: Online 2008:1727–84.

[48] Rossberg M, Wicke E. Transportvorgänge und Oberflächenreaktionen bei der Verbrennung graphitischen Kohlenstoffs. Chemie Ingenieur Technik 1956;28(3):181–9. doi:10.1002/cite.330280309.

[49] Stoesser P, Schneider C, Kreitzberg T, Kneer R, Kolb T. On the influence of different experimental systems on measured heterogeneous gasification kinetics. Applied Energy 2018;211:582–9. doi:10.1016/j.apenergy.2017.11.037.

[50] Huo W, Zhou Z, Wang F, Yu G. Mechanism analysis and experimental verification of pore diffusion on coke and coal char gasification with CO_2. Chemical Engineering Journal 2014;244:227–33. doi:10.1016/j.cej.2014.01.069.

[51] Krzack S, Gutte H, Meyer B (eds.). Stoffliche Nutzung von Braunkohle. Berlin, Heidelberg: Springer Berlin Heidelberg; 2018.

[52] Bai J, Li W, Li C-z, Bai Z, Li B. Influences of minerals transformation on the reactivity of high temperature char gasification. Fuel Processing Technology 2010;91(4):404–9. doi:10.1016/j.fuproc.2009.05.017.

[53] Liu G-S, Niksa S. Coal conversion submodels for design applications at elevated pressures. Part II. Char gasification. Progress in Energy and Combustion Science 2004;30(6):679–717. doi:10.1016/j.pecs.2004.08.001.

[54] Lobo LS, Carabineiro SAC. Kinetics and mechanism of catalytic carbon gasification. Fuel 2016;183:457–69. doi:10.1016/j.fuel.2016.06.115.

[55] Wang Y-L, Zhu S-H, Gao M-Q, Yang Z-R, Yan L-J, Bai Y-H et al. A study of char gasification in H_2O and CO_2 mixtures: Role of inherent minerals in the coal. Fuel Processing Technology 2016;141:9–15. doi:10.1016/j.fuproc.2015.06.001.

[56] Laurendeau NM. Heterogeneous kinetics of coal char gasification and combustion. Progress in Energy and Combustion Science 1978;4(4):221–70. doi:10.1016/0360-1285(78)90008-4.

[57] Schneider C, Zeller M, Böhm D, Kolb T. Influence of pressure on the gasification kinetics of two high-temperature beech wood chars with CO_2, H_2O and its mixture. Fuel 2021;299(3):120523. doi:10.1016/j.fuel.2021.120523.

[58] Blackwood JD, Ingeme AJ. The Reaction of Carbon with Carbon Dioxide at High Pressure. Aust. J. Chem. 1960;13(2):194. doi:10.1071/CH9600194.

[59] Roberts DG, Harris DJ. A Kinetic Analysis of Coal Char Gasification Reactions at High Pressures. Energy Fuels 2006;20(6):2314–20. doi:10.1021/ef060270o.

[60] Hüttinger KJ, Merdes WF. The carbon-steam reaction at elevated pressure: Formations of product gases and hydrogen inhibitions. Carbon 1992;30(6):883–94. doi:10.1016/0008-6223(92)90011-K.

[61] Barrio M, Gøbel B, Risnes H, Henriksen U, Hustad JE, Sørensen LH. Steam gasification of wood char and the effect of hydrogen inhibition on the chemical kinetics. Progress in thermochemical biomass conversion 2001;1:32–46.

[62] Irfan MF, Usman MR, Kusakabe K. Coal gasification in CO_2 atmosphere and its kinetics since 1948: A brief review. Energy 2011;36(1):12–40. doi:10.1016/j.energy.2010.10.034.

[63] Senneca O, Apicella B, Russo C, Cerciello F, Salatino P, Heuer S et al. Pyrolysis and Thermal Annealing of Coal and Biomass in CO_2-Rich Atmospheres. Energy Fuels 2018;32(10):10701–8. doi:10.1021/acs.energyfuels.8b02417.

[64] Cazorla-Amoros D, Linares-Solano A, Salinas-Martinez de Lecea C, Nomura M, Yamashita H, Tomita A. Local structure of calcium species dispersed on carbon: Influence of the metal loading procedure and its evolution during pyrolysis. Energy Fuels 1993;7(5):625–31. doi:10.1021/ef00041a010.

[65] Wang L, Moilanen A, Lehtinen J, Konttinen J, Matas BG. Release of Potassium During Devolatilization of Spruce Bark. Energy Procedia 2017;105:1295–301. doi:10.1016/j.egypro.2017.03.463.

[66] Ollero P. Diffusional effects in TGA gasification experiments for kinetic determination. Fuel 2002;81(15):1989–2000. doi:10.1016/S0016-2361(02)00126-6.

[67] Nowak B, Karlström O, Backman P, Brink A, Zevenhoven M, Voglsam S et al. Mass transfer limitation in thermogravimetry of biomass gasification. J Therm Anal Calorim 2013;111(1):183–92. doi:10.1007/s10973-012-2400-9.

[68] Roberts DG, Harris DJ. Char gasification in mixtures of CO_2 and H_2O: Competition and inhibition. Fuel 2007;86(17-18):2672–8. doi:10.1016/j.fuel.2007.03.019.

[69] Goyal A, Zabransky RF, Rehmat A. Gasification kinetics of Western Kentucky bituminous coal char. Ind. Eng. Chem. Res. 1989;28(12):1767–78. doi:10.1021/ie00096a006.

[70] Mühlen H-J, van Heek KH, Jüntgen H. Kinetic studies of steam gasification of char in the presence of H_2, CO_2 and CO. Fuel 1985;64(7):944–9. doi:10.1016/0016-2361(85)90149-8.

[71] Chen C, Wang J, Liu W, Zhang S, Yin J, Luo G et al. Effect of pyrolysis conditions on the char gasification with mixtures of CO_2 and H_2O. Proceedings of the Combustion Institute 2013;34(2):2453–60. doi:10.1016/j.proci.2012.07.068.

[72] Chen C, Zhang S, Xu K, Luo G, Yao H. Experimental and Modeling Study of Char Gasification with Mixtures of CO_2 and H_2O. Energy Fuels 2015;30(3):1628–35. doi:10.1021/acs.energyfuels.5b02294.

[73] Guizani C, Escudero Sanz FJ, Salvador S. Influence of temperature and particle size on the single and mixed atmosphere gasification of biomass char with H_2O and CO_2. Fuel Processing Technology 2015;134:175–88. doi:10.1016/j.fuproc.2015.01.031.

[74] Huang Z, Zhang J, Zhao Y, Zhang H, Yue G, Suda T et al. Kinetic studies of char gasification by steam and CO_2 in the presence of H_2 and CO. Fuel Processing Technology 2010;91(8):843–7. doi:10.1016/j.fuproc.2009.12.020.

[75] Li F, Yan Q, Huang J, Zhao J, Fang Y, Wang J. Lignite-char gasification mechanism in mixed atmospheres of steam and CO_2 at different pressures. Fuel Processing Technology 2015;138:555–63. doi:10.1016/j.fuproc.2015.06.035.

[76] Smith KL, Smoot LD, Fletcher TH, Pugmire RJ. The Structure and Reaction Processes of Coal. Boston, MA: Springer; 1994.

[77] Brunauer S, Emmett PH, Teller E. Adsorption of Gases in Multimolecular Layers. J. Am. Chem. Soc. 1938;60(2):309–19. doi:10.1021/ja01269a023.

[78] Dubinin MM, Zaverina ED, Radushkevich LV. Sorption and structure of active carbons. I. Adsorption of organic vapors. Zhurnal Fizicheskoi Khimii 1947;21(3):151–62.

[79] Gold Book, Compendium of chemical terminology. International Union of Pure and Applied Chemistry 2014(Version 2.3.3).

[80] Duman G, Uddin MA, Yanik J. The effect of char properties on gasification reactivity. Fuel Processing Technology 2014;118:75–81. doi:10.1016/j.fuproc.2013.08.006.

[81] Wang G, Zhang J, Shao J, Liu Z, Wang H, Li X et al. Experimental and modeling studies on CO_2 gasification of biomass chars. Energy 2016;114:143–54. doi:10.1016/j.energy.2016.08.002.

[82] Zhang Y, Ashizawa M, Kajitani S, Miura K. Proposal of a semi-empirical kinetic model to reconcile with gasification reactivity profiles of biomass chars. Fuel 2008;87(4):475–81. doi:10.1016/j.fuel.2007.04.026.

[83] Singer SL, Ghoniem AF. An Adaptive Random Pore Model for Multimodal Pore Structure Evolution with Application to Char Gasification. Energy Fuels 2011;25(4):1423–37. doi:10.1021/ef101532u.

[84] Bouraoui Z, Jeguirim M, Guizani C, Limousy L, Dupont C, Gadiou R. Thermogravimetric study on the influence of structural, textural and chemical properties of biomass chars on CO_2 gasification reactivity. Energy 2015;88:703–10. doi:10.1016/j.energy.2015.05.100.

[85] Fu P, Hu S, Xiang J, Yi W, Bai X, Sun L et al. Evolution of char structure during steam gasification of the chars produced from rapid pyrolysis of rice husk. Bioresource Technology 2012;114:691–7. doi:10.1016/j.biortech.2012.03.072.

[86] Gómez A, Klose W, Rincón S. Thermogravimetrische Untersuchungen zur Entwicklung des Porensystems bei der einstufigen Teilvergasung von Biomasse. Chemie Ingenieur Technik 2008;80(5):631–9. doi:10.1002/cite.200700159.

[87] Guizani C, Jeguirim M, Gadiou R, Escudero Sanz FJ, Salvador S. Biomass char gasification by H_2O, CO_2 and their mixture: Evolution of chemical, textural and structural properties of the chars. Energy 2016;112:133–45. doi:10.1016/j.energy.2016.06.065.

[88] Laine NR, Vastola FJ, Walker PL. The Importance of Active Surface Area in the Carbon-Oxygen Reaction. J. Phys. Chem. 1963;67(10):2030–4. doi:10.1021/j100804a016.

[89] Radovic LR. Importance of carbon active sites in coal char gasification—8 years later. Carbon 1991;29(6):809–11. doi:10.1016/0008-6223(91)90020-J.

[90] Radović LR, Walker PL, Jenkins RG. Importance of carbon active sites in the gasification of coal chars. Fuel 1983;62(7):849–56. doi:10.1016/0016-2361(83)90041-8.

[91] Lizzio AA, Jiang H, Radovic LR. On the kinetics of carbon (Char) gasification: Reconciling models with experiments. Carbon 1990;28(1):7–19. doi:10.1016/0008-6223(90)90087-F.

[92] Wölki M. Über die wahre Reaktionsgeschwindigkeit der Vergasung von Biomassepyrolysat mit Kohlendioxid und Wasserdampf: Kassel University Press; 2005.

[93] Lizzio A, Radovic LR. Temperature-programmed desorption studies of coal char gasification. Prepr. Pap.(Am. Chem. Soc., Div. Fuel Chem.) 1989:102–11.

[94] Klose W, Wölki M. On the intrinsic reaction rate of biomass char gasification with carbon dioxide and steam. Fuel 2005;84(7):885–92. doi:10.1016/j.fuel.2004.11.016.

[95] Kyotani T, Yamada H, Yamashita H, Tomita A, Radovic LR. Use of transient kinetics and temperature-programmed desorption to predict carbon/char reactivity: The case of copper-catalyzed gasification of coal char in oxygen. Energy Fuels 1992;6(6):865–7. doi:10.1021/ef00036a027.

[96] Freund H. Gasification of carbon by CO_2: A transient kinetics experiment. Fuel 1986;65(1):63–6. doi:10.1016/0016-2361(86)90143-2.

[97] Radovic LR, Jiang H, Lizzio AA. A transient kinetics study of char gasification in carbon dioxide and oxygen. Energy Fuels 1991;5(1):68–74. doi:10.1021/ef00025a011.

[98] Kapteijn F, Meijer R, Moulijn JA, Cazorla-Amóros D. On why do different carbons show different gasification rates: A transient isotopic CO_2 gasification study. Carbon 1994;32(7):1223–31. doi:10.1016/0008-6223(94)90106-6.

[99] Malekshahian M, Hill JM. Effect of Pyrolysis and CO_2 Gasification Pressure on the Surface Area and Pore Size Distribution of Petroleum Coke. Energy Fuels 2011;25(11):5250–6. doi:10.1021/ef201231w.

[100] Yuan S, Chen X-l, Li J, Wang F-c. CO_2 Gasification Kinetics of Biomass Char Derived from High-Temperature Rapid Pyrolysis. Energy Fuels 2011;25(5):2314–21. doi:10.1021/ef200051z.

[101] Xu R-s, Zhang J-l, Wang G-w, Zuo H-b, Zhang P-c, Shao J-g. Gasification behaviors and kinetic study on biomass chars in CO_2 condition. Chemical Engineering Research and Design 2016;107:34–42. doi:10.1016/j.cherd.2015.10.014.

[102] Jing X, Wang Z, Zhang Q, Yu Z, Li C, Huang J et al. Evaluation of CO_2 Gasification Reactivity of Different Coal Rank Chars by Physicochemical Properties. Energy Fuels 2013;27(12):7287–93. doi:10.1021/ef401639v.

[103] Ferrari AC, Robertson J. Raman spectroscopy of amorphous, nanostructured, diamond-like carbon, and nanodiamond. Philosophical transactions. Series A, Mathematical, physical, and engineering sciences 2004;362(1824):2477–512. doi:10.1098/rsta.2004.1452.

[104] Bielefelder Informationssystem (BIS), Universität Bielefeld. eKVV - Das elektronische, kommentierte Vorlesungsverzeichnis im Internet: Graphen-Platten. [December 10, 2020]; Available from: http://ekvv.uni-bielefeld.de/bilddb/bild?id=71998.

[105] Laboratoire de Physique et Modélisation des Milieux Condensés. Graphite structure. [December 10, 2020]; Available from: http://lpmmc.grenoble.cnrs.fr/spip.php?article407.

[106] Ishimaru K, Hata T, Bronsveld P, Nishizawa T, Imamura Y. Characterization of sp^2- and sp^3-bonded carbon in wood charcoal. J Wood Sci 2007;53(5):442–8. doi:10.1007/s10086-007-0879-7.

[107] Lu L, Sahajwalla V, Kong C, Harris D. Quantitative X-ray diffraction analysis and its application to various coals. Carbon 2001;39(12):1821–33. doi:10.1016/S0008-6223(00)00318-3.

[108] Schneider C, Walker S, Phounglamcheik A, Umeki K, Kolb T. Effect of calcium dispersion and graphitization during high-temperature pyrolysis of beech wood char on the gasification rate with CO_2. Fuel 2021;283(3):118826. doi:10.1016/j.fuel.2020.118826.

[109] Ferrari AC, Robertson J. Interpretation of Raman spectra of disordered and amorphous carbon. Phys. Rev. B 2000;61(20):14095–107. doi:10.1103/PhysRevB.61.14095.

[110] Oberlin A. Carbonization and graphitization. Carbon 1984;22(6):521–41. doi:10.1016/0008-6223(84)90086-1.

[111] Septien S, Valin S, Peyrot M, Dupont C, Salvador S. Characterization of char and soot from millimetric wood particles pyrolysis in a drop tube reactor between 800°C and 1400°C. Fuel 2014;121:216–24. doi:10.1016/j.fuel.2013.12.026.

[112] Guerrero M, Ruiz MP, Millera Á, Alzueta MU, Bilbao R. Characterization of Biomass Chars Formed under Different Devolatilization Conditions: Differences between Rice Husk and Eucalyptus. Energy Fuels 2008;22(2):1275–84. doi:10.1021/ef7005589.

[113] Trubetskaya A, Jensen PA, Jensen AD, Steibel M, Spliethoff H, Glarborg P et al. Comparison of high temperature chars of wheat straw and rice husk with respect to chemistry, morphology and reactivity. Biomass and Bioenergy 2016;86:76–87. doi:10.1016/j.biombioe.2016.01.017.

[114] Liu L, Cao Y, Liu Q. Kinetics studies and structure characteristics of coal char under pressurized CO_2 gasification conditions. Fuel 2015;146:103–10. doi:10.1016/j.fuel.2015.01.002.

[115] Guizani C, Jeguirim M, Valin S, Peyrot M, Salvador S. The Heat Treatment Severity Index: A new metric correlated to the properties of biochars obtained from entrained flow pyrolysis of biomass. Fuel 2019;244:61–8. doi:10.1016/j.fuel.2019.01.170.

[116] Baker RTK, Chludzinski JJ. Catalytic gasification of graphite by calcium and nickel-calcium. Carbon 1985;23(6):635–44. doi:10.1016/0008-6223(85)90223-4.

[117] Huang Y, Yin X, Wu C, Wang C, Xie J, Zhou Z et al. Effects of metal catalysts on CO_2 gasification reactivity of biomass char. Biotechnology advances 2009;27(5):568–72. doi:10.1016/j.biotechadv.2009.04.013.

[118] Lobo LS. Intrinsic kinetics in carbon gasification: Understanding linearity, "nanoworms" and alloy catalysts. Applied Catalysis B: Environmental 2014;148-149:136–43. doi:10.1016/j.apcatb.2013.09.048.

[119] Mahinpey N, Gomez A. Review of gasification fundamentals and new findings: Reactors, feedstock, and kinetic studies. Chemical Engineering Science 2016;148:14–31. doi:10.1016/j.ces.2016.03.037.

[120] Wood BJ, Sancier KM. The Mechanism of the Catalytic Gasification of Coal Char: A Critical Review. Catalysis Reviews 2006;26(2):233–79. doi:10.1080/01614948408078065.

[121] Bouraoui Z, Dupont C, Jeguirim M, Limousy L, Gadiou R. CO_2 gasification of woody biomass chars: The influence of K and Si on char reactivity. Comptes Rendus Chimie 2016;19(4):457–65. doi:10.1016/j.crci.2015.08.012.

[122] Dupont C, Jacob S, Marrakchy KO, Hognon C, Grateau M, Labalette F et al. How inorganic elements of biomass influence char steam gasification kinetics. Energy 2016;109:430–5. doi:10.1016/j.energy.2016.04.094.

[123] Kapteijn F, Abbel G, Moulijn JA. CO_2 gasification of carbon catalysed by alkali metals. Fuel 1984;63(8):1036–42. doi:10.1016/0016-2361(84)90184-4.

[124] Kirtania K, Axelsson J, Matsakas L, Christakopoulos P, Umeki K, Furusjö E. Kinetic study of catalytic gasification of wood char impregnated with different alkali salts. Energy 2017;118:1055–65. doi:10.1016/j.energy.2016.10.134.

[125] Kopyscinski J, Habibi R, Mims CA, Hill JM. K_2CO_3-Catalyzed CO_2 Gasification of Ash-Free Coal: Kinetic Study. Energy Fuels 2013;27(8):4875–83. doi:10.1021/ef400552q.

[126] Aho A, DeMartini N, Pranovich A, Krogell J, Kumar N, Eränen K et al. Pyrolysis of pine and gasification of pine chars--influence of organically bound metals. Bioresource Technology 2013;128:22–9. doi:10.1016/j.biortech.2012.10.093.

[127] Kramb J, Gómez-Barea A, DeMartini N, Romar H, Doddapaneni TRKC, Konttinen J. The effects of calcium and potassium on CO_2 gasification of birch wood in a fluidized bed. Fuel 2017;196:398–407. doi:10.1016/j.fuel.2017.01.101.

[128] Lahijani P, Zainal ZA, Mohamed AR, Mohammadi M. CO_2 gasification reactivity of biomass char: Catalytic influence of alkali, alkaline earth and transition metal salts. Bioresource Technology 2013;144:288–95. doi:10.1016/j.biortech.2013.06.059.

[129] Mitsuoka K, Hayashi S, Amano H, Kayahara K, Sasaoaka E, Uddin MA. Gasification of woody biomass char with CO_2: The catalytic effects of K and Ca species on char gasification reactivity. Fuel Processing Technology 2011;92(1):26–31. doi:10.1016/j.fuproc.2010.08.015.

[130] P. W. J. Struis R, Scala C von, Stucki S, Prins R. Gasification reactivity of charcoal with CO_2. Part II: Metal catalysis as a function of conversion. Chemical Engineering Science 2002;57(17):3593–602. doi:10.1016/S0009-2509(02)00255-5.

[131] Zhang Y, Hara S, Kajitani S, Ashizawa M. Modeling of catalytic gasification kinetics of coal char and carbon. Fuel 2010;89(1):152–7. doi:10.1016/j.fuel.2009.06.004.

[132] Kapteijn F, Porre H, Moulijn JA. CO_2 gasification of activated carbon catalyzed by earth alkaline elements. AIChE J. 1986;32(4):691–5. doi:10.1002/aic.690320421.

[133] Kuznetsov PN, Kolesnikova SM, Kuznetsova LI. Steam Gasification of Different Brown Coals Catalysed by the Naturally Occurring Calcium Species. IJCCE 2013;02(01):1–11. doi:10.4236/ijcce.2013.21001.

[134] Zhou L, Zhang G, Schurz M, Steffen K, Meyer B. Kinetic study on CO_2 gasification of brown coal and biomass chars: Reaction order. Fuel 2016;173:311–9. doi:10.1016/j.fuel.2016.01.042.

[135] Hognon C, Dupont C, Grateau M, Delrue F. Comparison of steam gasification reactivity of algal and lignocellulosic biomass: Influence of inorganic elements. Bioresource Technology 2014;164:347–53. doi:10.1016/j.biortech.2014.04.111.

[136] McKee DW. Mechanisms of the alkali metal catalysed gasification of carbon. Fuel 1983;62(2):170–5. doi:10.1016/0016-2361(83)90192-8.

[137] Lobo LS. Catalytic Carbon Gasification: Review of Observed Kinetics and Proposed Mechanisms or Models - Highlighting Carbon Bulk Diffusion. Catalysis Reviews 2013;55(2):210–54. doi:10.1080/01614940.2013.780557.

[138] Argyle M, Bartholomew C. Heterogeneous Catalyst Deactivation and Regeneration: A Review. Catalysts 2015;5(1):145–269. doi:10.3390/catal5010145.

[139] Tomasi Morgano M. Screw pyrolysis of biogenic feedstock with integrated hot gas filtration. Stuttgart; 2019.

[140] Tomasi Morgano M, Leibold H, Richter F, Seifert H. Screw pyrolysis with integrated sequential hot gas filtration. Journal of Analytical and Applied Pyrolysis 2015;113(No. 2):216–24. doi:10.1016/j.jaap.2014.12.019.

[141] Vassilev SV, Baxter D, Vassileva CG. An overview of the behaviour of biomass during combustion: Part II. Ash fusion and ash formation mechanisms of biomass types. Fuel 2014;117(3):152–83. doi:10.1016/j.fuel.2013.09.024.

[142] Stoesser P. Investigation of solid-phase processes during the conversion of biogenic slurry in entrained-flow gasifiers. München: Dr. Hut; 2020.

[143] Dubil K. Betrachtungen zum Partikelabbrand während der Vergasung unter Berücksichtigung der Entwicklung der Reaktivität. Karlsruhe; 2017.

[144] Schneider M. Untersuchungen zur Pyrolysekinetik eines biogenen Festbrennstoffes im Fallrohrreaktor. Karlsruhe; 2018.

[145] Zeller M. Untersuchungen zur intrinsischen Reaktionsgeschwindigkeit biogener Festbrennstoffe im Festbettreaktor bei erhöhtem Druck. Karlsruhe; 2019.

[146] Böhm D. Bestimmung der Vergasungsgeschwindigkeit biogener Festbrennstoffe mit H_2O im Einzelpartikelreaktor bei erhöhtem Druck. Karlsruhe; 2020.

[147] Schneider C, Rincón Prat S, Kolb T. Determination of active sites during gasification of biomass char with CO_2 using temperature-programmed desorption. Part 1: Methodology & desorption spectra. Fuel 2020;267(4):116726. doi:10.1016/j.fuel.2019.116726.

[148] Rincón Prat S, Schneider C, Kolb T. Determination of active sites during gasification of biomass char with CO_2 using temperature-programmed desorption. Part 2: Influence of ash components. Fuel 2020;267(2):117179. doi:10.1016/j.fuel.2020.117179.

[149] Basu P. Chapter 3 - Biomass Characteristics. In: Basu P, editor. Biomass Gasification, Pyrolysis and Torrefaction (Third Edition): Academic Press; 2018, p. 49–91.

[150] Jensen CU, Rodriguez Guerrero JK, Karatzos S, Olofsson G, Iversen SB. Fundamentals of Hydrofaction™: Renewable crude oil from woody biomass. Biomass Conv. Bioref. 2017;7(4):495–509. doi:10.1007/s13399-017-0248-8.

[151] Heredy LA, Wender I. Model structure for a bituminous coal. Am. Chem. Soc., Div. Fuel Chem., Prepr; (United States) 1980;25:4.

[152] Reimert R, Marschner F, Renner H ‐ J, Boll W, Supp E, Brejc M et al. Gas Production, 2. Processes. Ullmann's Encyclopedia of Industrial Chemistry 2011. doi:10.1002/14356007.o12_o01.

[153] Mohan D, Pittman CU, Steele PH. Pyrolysis of Wood/Biomass for Bio‐oil: A Critical Review. Energy Fuels 2006;20(3):848–89. doi:10.1021/ef0502397.

[154] Radmanesh R, Courbariaux Y, Chaouki J, Guy C. A unified lumped approach in kinetic modeling of biomass pyrolysis. Fuel 2006;85(9):1211–20. doi:10.1016/j.fuel.2005.11.021.

[155] Grønli MG, Várhegyi G, Di Blasi C. Thermogravimetric Analysis and Devolatilization Kinetics of Wood. Ind. Eng. Chem. Res. 2002;41(17):4201–8. doi:10.1021/ie0201157.

[156] Okumura Y, Hanaoka T, Sakanishi K. Effect of pyrolysis conditions on gasification reactivity of woody biomass-derived char. Proceedings of the Combustion Institute 2009;32(2):2013–20. doi:10.1016/j.proci.2008.06.024.

[157] Roberts DG, Harris DJ, Wall TF. On the effects of high pressure and heating rate during coal pyrolysis on char gasification reactivity. Energy Fuels 2003;17(4):887–95.

[158] Baerns M, Hofmann H, Renken A. Chemische Reaktionstechnik: Mit 41 Tabellen. 3rd ed. Stuttgart: Thieme Verl; 1999.

[159] Thiele EW. Relation between catalytic activity and size of particle. Industrial & Engineering Chemistry 1939;31(7):916–20.

[160] Wu X, Wang J. K_2CO_3-catalyzed steam gasification of ash-free coal char in a pressurized and vertically blown reactor. Influence of pressure on gasification rate and gas composition. Fuel Processing Technology 2017;159:9–18. doi:10.1016/j.fuproc.2017.01.001.

[161] Wang G, Zhang J, Hou X, Shao J, Geng W. Study on CO_2 gasification properties and kinetics of biomass chars and anthracite char. Bioresource Technology 2015;177:66–73. doi:10.1016/j.biortech.2014.11.063.

[162] Borrego AG, Garavaglia L, Kalkreuth WD. Characteristics of high heating rate biomass chars prepared under N_2 and CO_2 atmospheres. International Journal of Coal Geology 2009;77(3-4):409–15. doi:10.1016/j.coal.2008.06.004.

[163] Jagiello J, Thommes M. Comparison of DFT characterization methods based on N_2, Ar, CO_2, and H_2 adsorption applied to carbons with various pore size distributions. Carbon 2004;42(7):1227–32. doi:10.1016/j.carbon.2004.01.022.

[164] Huo W, Zhou Z, Chen X, Dai Z, Yu G. Study on CO_2 gasification reactivity and physical characteristics of biomass, petroleum coke and coal chars. Bioresource Technology 2014;159:143–9. doi:10.1016/j.biortech.2014.02.117.

[165] Kreitzberg T, Wirch N, Bormann C, Pielsticker S, Hatzfeld O, Mayer J et al. Thermally induced changes in microstructure and reactivity of biogenic and fossil fuel particles. Applied Energy 2019;254(3):113607. doi:10.1016/j.apenergy.2019.113607.

[166] Vassilev SV, Baxter D, Andersen LK, Vassileva CG. An overview of the chemical composition of biomass. Fuel 2010;89(5):913–33. doi:10.1016/j.fuel.2009.10.022.

[167] Kajita M, Kimura T, Norinaga K, Li C-z, Hayashi J-i. Catalytic and Noncatalytic Mechanisms in Steam Gasification of Char from the Pyrolysis of Biomass. Energy Fuels 2010;24(1):108–16. doi:10.1021/ef900513a.

[168] Kannan MP, Richards GN. Gasification of biomass chars in carbon dioxide: Dependence of gasification rate on the indigenous metal content. Fuel 1990;69(6):747–53. doi:10.1016/0016-2361(90)90041-N.

[169] TRT (S&A) Ingenieurbüro GmbH. Engineering Drawing; 2017.

[170] Sing KSW, Everett DH, Haul RAW, Moscou L, Pierotti RA, Rouquérol J et al. Reporting physisorption data for gas/solid systems with special reference to the determination of surface area and porosity (Recommendations 1984). Pure and Applied Chemistry 1985;57(4):603–19. doi:10.1351/pac198557040603.

[171] Klobes P, Munro RG. Porosity and specific surface area measurements for solid materials. National Institute of Standards and Technology (NIST) Recommended Practice Guide 2006(Special Publication 960-17).

Publications

Publication list

I. Schneider, C., Zeller, M., Böhm, D., Kolb, T. Influence of pressure on the gasification kinetics of two high-temperature beech wood chars with CO_2, H_2O and its mixture. *Fuel*, 2021, 299(3). https://doi.org/10.1016/j.fuel.2021.120523.

II. Schneider, C., Walker, S., Phounglamcheik, A., Umeki, K., Kolb, T. Effect of calcium dispersion and graphitization during high-temperature pyrolysis of beech wood char on the gasification rate with CO_2. *Fuel,* 2021, 283(3). https://doi.org/10.1016/j.fuel.2020.118826.

III. Rincón Prat, S., Schneider, C., Kolb, T. Determination of active sites during gasification of biomass char with CO_2 using temperature-programmed desorption. Part 2. Influence of ash components. *Fuel,* 2020, 267(2). https://doi.org/10.1016/j.fuel.2020.117179.

IV. Schneider, C., Rincón Prat, S., Kolb, T. Determination of active sites during gasification of biomass char with CO_2 using temperature-programmed desorption. Part 1. Methodology & desorption spectra. *Fuel,* 2020, 267(4). https://doi.org/10.1016/j.fuel.2019.116726.

V. Stoesser, P., Schneider, C., Kreitzberg, T., Kneer, R., Kolb, T. On the influence of different experimental systems on measured heterogeneous gasification kinetics. *Applied Energy,* 2018, 211, 582-589. https://doi.org/10.1016/j.apenergy.2017.11.037.

Verification of the contribution from the co-authors

Title: **Influence of pressure on the gasification kinetics of two high-temperature beech wood chars with CO_2, H_2O and its mixture**

Journal: Fuel

Authors: Christoph Schneider, Michael Zeller, Daniel Böhm, Thomas Kolb

Position in the dissertation:

The content of this paper has been included in Chapters 2, 3 and 4.

Contribution of Christoph Schneider: Conceptualization, char generation and all gasification experiments: methodology, validation, data evaluation; writing - original draft, editing - final version, visualization, supervision of students.

Contribution of Michael Zeller: Based on results from master thesis - gasification experiments with CO_2: contribution to methodology, experimental procedure, data evaluation.

Contribution of Daniel Böhm: Based on results from master thesis - gasification experiments with H_2O and mix: contribution to methodology, experimental procedure, data evaluation.

Contribution of Thomas Kolb: Supervision of research, resources, concept of paper, review & editing.

Signature of the authors:

Author	*Date*	*Signature*
Christoph Schneider		
Michael Zeller		
Daniel Böhm		
Thomas Kolb		

Title: **Effect of calcium dispersion and graphitization during high-temperature pyrolysis of beech wood char on the gasification rate with CO_2**

Journal: Fuel

Authors: Christoph Schneider, Stella Walker, Aekjuthon Phounglamcheik, Kentaro Umeki, Thomas Kolb

Position in the dissertation:

The content of this paper has been included in Chapters 3 and 4.

Contribution of Christoph Schneider: Conceptualization, char generation and characterization: methodology, validation, data evaluation; writing - original draft, editing - final version, visualization, supervision of student.

Contribution of Stella Walker: Based on results from master thesis – char characterization: contribution to methodology, experimental procedure, data evaluation.

Contribution of Aekjuthon Phounglamcheik: Char characterization: contribution to methodology, experimental procedure.

Contribution of Kentaro Umeki: Supervision of research, resources, review & editing.

Contribution of Thomas Kolb: Supervision of research, resources, concept of paper, review & editing.

Signature of the authors:

Author	*Date*	*Signature*
Christoph Schneider		
Stella Walker		
Aekjuthon Phounglamcheik		
Kentaro Umeki		
Thomas Kolb		

Title: **Determination of active sites during gasification of biomass char with CO_2 using temperature-programmed desorption. Part 2: Influence of ash components**

Journal: Fuel

Authors: Sonia Rincón Prat, Christoph Schneider, Thomas Kolb

Position in the dissertation:

The content of this paper has been included in Chapter 4.

Contribution of Sonia Rincón Prat: Conceptualization, TPD experiments: experimental procedure, data evaluation; writing - original draft, editing - final version, visualization.

Contribution of Christoph Schneider: TPD experiments: methodology, data evaluation; writing - original draft, review & editing.

Contribution of Thomas Kolb: Supervision of research, resources, concept of paper, review & editing.

Signature of the authors:

Author	*Date*	*Signature*
Sonia Rincón Prat		
Christoph Schneider		
Thomas Kolb		

Title: **Determination of active sites during gasification of biomass char with CO_2 using temperature-programmed desorption. Part 1: Methodology & desorption spectra**

Journal: Fuel

Authors: Christoph Schneider, Sonia Rincón Prat, Thomas Kolb

Position in the dissertation:

The content of this paper has been included in Chapters 3 and 4.

Contribution of Christoph Schneider: Conceptualization, TPD experiments: methodology, validation, experimental procedure, data evaluation; writing - original draft, editing - final version, visualization.

Contribution of Sonia Rincón Prat: TPD experiments: experimental procedure, data evaluation; writing - original draft, review & editing.

Contribution of Thomas Kolb: Supervision of research, resources, concept of paper, review & editing.

Signature of the authors:

Author	*Date*	*Signature*
Christoph Schneider		
Sonia Rincón Prat		
Thomas Kolb		

Title: **On the influence of different experimental systems on measured heterogeneous gasification kinetics**

Journal: Applied Energy

Authors: Philipp Stoesser, Christoph Schneider, Thobias Kreitzberg, Reinhold Kneer, Thomas Kolb

Position in the dissertation:

The content of this paper has been included in Chapter 4.

Contribution of Philipp Stoesser: Conceptualization, drop-tube reactor and free-fall fixed-bed reactor experiments: methodology, validation, experimental procedure, data evaluation, writing - original draft; editing - final version, visualization.

Contribution of Christoph Schneider: TGA experiments: methodology, validation, experimental procedure, data evaluation, writing - original draft, visualization.

Contribution of Thobias Kreitzberg: Fluidized-bed experiments: methodology, validation, experimental procedure, data evaluation, writing - original draft, visualization.

Contribution of Reinhold Kneer: Supervision of research Thobias Kreitzberg, resources, review & editing.

Contribution of Thomas Kolb: Supervision of research Philipp Stoesser & Christoph Schneider, resources, concept of paper, review & editing.

Signature of the authors:

Author	*Date*	*Signature*
Philipp Stoesser		
Christoph Schneider		
Thobias Kreitzberg		
Reinhold Kneer		
Thomas Kolb		

Fuel 299 (2021) 120523

Contents lists available at ScienceDirect

Fuel

journal homepage: www.elsevier.com/locate/fuel

Full Length Article

Influence of pressure on the gasification kinetics of two high-temperature beech wood chars with CO_2, H_2O and its mixture

Christoph Schneider [a,*], Michael Zeller [b], Daniel Böhm [a], Thomas Kolb [a,b]

[a] Karlsruhe Institute of Technology, Engler-Bunte-Institute, Fuel Technology, EBI-ceb, Engler-Bunte-Ring 3, 76131 Karlsruhe, Germany
[b] Karlsruhe Institute of Technology, Institute for Technical Chemistry, ITC, Hermann-von-Helmholtz-Platz 1, 76344 Eggenstein-Leopoldshafen, Germany

ARTICLE INFO

Keywords:
Biomass char
Gasification kinetics
CO_2/H_2O partial pressure
Total pressure
Single-particle reactor
Forced flow-through conditions

ABSTRACT

This paper presents experimental data and modeling approaches to describe the influence of CO_2 and H_2O partial pressure as well as absolute pressure on the gasification kinetics of two different beech wood chars. The chars were produced at 1400 °C (P1400) and 1600 °C (P1600) at high-heating rates and short residence times in a drop-tube reactor. The gasification experiments were conducted in a single-particle reactor with forced flow-through conditions reducing diffusional effects to a minimum. The interpretation of the experimentally determined reaction rates during gasification with CO_2, H_2O and its mixture is based on the char properties (graphitization, ash dispersion and morphology) presented in a previous publication.

During gasification with CO_2, P1600 shows higher reactivity as compared to P1400 for all CO_2 partial pressures and temperatures applied. The higher reactivity of P1600 during CO_2 gasification may be explained by a CaO film on the char surface catalyzing the char-CO_2 gasification reaction. On the other hand, P1400 shows higher reactivity towards H_2O which may be evoked by the lower graphitization degree and higher specific surface area. Reaction kinetic modeling for single atmosphere gasification was successfully carried out using a power law approach. The Langmuir-Hinshelwood model, however, only gave good results where a possible saturation of the char surface at high pressure was observed.

Increasing the CO_2 partial pressure during gasification in mixed CO_2/H_2O atmospheres leads to higher reactivity for both chars. The reaction rate r_{mix} can be expressed by addition of the single atmosphere reaction rates in the low pressure area suggesting a separate active site mechanism. Catalytic activity of CaO increases the P1600 reactivity distinctively for lower H_2O and CO_2 partial pressures. For higher H_2O and CO_2 partial pressures, P1600 reactivity stagnates due to lower specific surface area and higher graphitization degree. Here, a common active sites mechanism can be assumed.

1. Introduction

The use of low-grade biogenic and fossil fuels in high-pressure entrained-flow gasification (EFG) allows for the production of high-quality synthesis gas that can be converted into fuels and chemicals or used for power generation via integrated gasification combined cycle (IGCC) systems. In the near future, EFG can play an important role in satisfying the demand for basic chemicals and power [1,2]. In EFG, the fuel is converted via thermal and thermo-chemical processes i.e. drying, pyrolysis under high heating rates as well as the subsequent heterogeneous gasification reactions of the resulting char in a CO_2– and H_2O-rich atmosphere. For the achievement of a high cold gas efficiency, a complete char conversion is desired. Since the heterogeneous reactions are considered as the rate-limiting step for complete fuel conversion, the knowledge of the gasification kinetics is essential for the design of entrained-flow gasifiers [3].

The heterogeneous gasification of char particles is controlled by process parameters, i.e. temperature, partial pressure of the reactant gas and process pressure as well as the chemical and physical properties of the char. Char properties affecting the conversion rate during gasification mainly include surface area and porosity, graphitization of the carbon matrix and inorganic ash components [4–8]. Generally, the heterogeneous char gasification reactions with CO_2 and H_2O can be described by an oxygen exchange mechanism [9]. In the case of CO_2 gasification, the following reaction mechanism presented in (R1)–(R3) is widely accepted [9,10].

* Corresponding author.
E-mail address: ch.schneider@kit.edu (C. Schneider).

https://doi.org/10.1016/j.fuel.2021.120523
Received 20 November 2020; Received in revised form 16 February 2021; Accepted 18 February 2021

$$C_f + CO_2 \xrightarrow{k_1} C(O) + CO \quad (R1)$$

$$C(O) + CO \xrightarrow{k_2} C_f + CO_2 \quad (R2)$$

$$C(O) \xrightarrow{k_3} CO \quad (R3)$$

Here, C_f represents an active site on the char surface and C(O) a carbon oxygen intermediate while $k_{1\text{-}3}$ are Arrhenius rate constants. As can be seen from (R2), the presence of CO exerts an inhibitory effect by lowering the concentration of the C(O) carbon oxygen intermediate. If a steady-state assumption is applied and the rate of reaction is described by the rate of desorption of the carbon oxygen intermediate (R3), the following Langmuir-Hinshelwood (LH) approach can be used [9].

$$r_{CO_2}(T, p_{CO_2}, p_{CO}) = \frac{k_1 p_{CO_2}}{1 + \frac{k_2}{k_3} p_{CO} + \frac{k_1}{k_3} p_{CO_2}} \quad (1)$$

For low CO concentrations, the inhibitory effect of CO is negligible and CO partial pressure p_{CO} can be set to zero [11]. Furthermore, a simplified global kinetic model can also be applied (see Eq. (2)).

$$r_{CO_2}(T, p_{CO_2}) = k_{0,CO_2} \exp\left(-\frac{E_{A,CO_2}}{R_U T}\right) p_{CO_2}^{n_{CO_2}} \quad (2)$$

Here, k_{0,CO_2} represents the pre-exponential factor, E_{A,CO_2} the activation energy, R_U the universal gas constant, T the reaction temperature and n_{CO_2} the reaction order towards CO_2 partial pressure.

The reaction of carbon with steam proceeds similarly to the Boudouard reaction but has more possible inhibition steps as summarized by Hüttinger & Merdes [12].

$$C_f + H_2O \xrightarrow{k_4} C(O) + H_2 \quad (R4)$$

$$C(O) + H_2 \xrightarrow{k_5} C_f + H_2O \quad (R5)$$

$$C(O) \xrightarrow{k_6} CO \quad (R6)$$

$$C_f + H_2 \xrightarrow{k_7} C(H_2) \quad (R7)$$

$$C(H_2) \xrightarrow{k_8} C_f + H_2 \quad (R8)$$

$$C_f + \frac{1}{2} H_2 \xrightarrow{k_9} C(H) \quad (R9)$$

$$C(H) \xrightarrow{k_{10}} C_f + \frac{1}{2} H_2 \quad (R10)$$

Basically, the reaction steps can be subsumed into two main processes: the oxygen exchange mechanism (see (R4)–(R6)) and possible hydrogen inhibition reactions (see (R7) to (R10)). Again, $k_{4\text{-}10}$ are Arrhenius rate constants while C(H) and $C(H_2)$ represent carbon hydrogen intermediates. Hydrogen not only inhibits the reaction by lowering the amount of C(O) carbon oxygen intermediates (see (R5)) but also by direct adsorption on carbon active sites C_f associatively (see (R7)) or dissociatively (see (R9)). However, the experimental data presented within this work was obtained in a simplified system containing very low amounts of product gases. Thus, this paper focusses on the oxygen exchange mechanism (see (R4)–(R6)) while inhibitory effects via adsorption of H_2 were not explicitly investigated leading to a simplified rate expression (see Eq. (3)). This approach is also consistent with previous experimental studies where kinetic data for the carbon steam reaction is determined [11,13].

$$r_{H_2O}(T, p_{H_2O}, p_{H_2}) = \frac{k_4 p_{H_2O}}{1 + \frac{k_5}{k_6} p_{H_2} + \frac{k_4}{k_6} p_{H_2O}} \quad (3)$$

Again, for low H_2 concentrations, the inhibitory effect of H_2 is negligible and H_2 partial pressure p_{H_2} can be set to zero [11]. Thus, a simplified global kinetic model is applicable as well (see Eq. (4)).

$$r_{H_2O}(T, p_{H_2O}) = k_{0,H_2O} \exp\left(-\frac{E_{A,H_2O}}{R_U T}\right) p_{H_2O}^{n_{H_2O}} \quad (4)$$

k_{0,H_2O} represents the pre-exponential factor, E_{A,H_2O} the activation energy and n_{H_2O} is the reaction order towards H_2O partial pressure for the carbon steam reaction.

In a technical entrained-flow gasifier, CO_2 and H_2O always coexist in the syngas produced. Thus, knowledge about the dominating heterogeneous gasification reaction when both gases are present is required. According to publications investigating the gasification kinetics of char in mixed atmospheres of CO_2 and H_2O, two possible surface reaction mechanisms were proposed.

The first mechanism accounts for the existence of active sites that are suitable for both char-CO_2 and char-H_2O reaction [4,14–18]. Thus, CO_2 and H_2O are competing for the same active sites inhibiting each other. Roberts & Harris [14] investigated the gasification of three Australian bituminous coal chars in mixtures of CO_2 and H_2O in a thermogravimetric analyzer (TGA) at elevated pressure up to 50 bar. Their data indicate that the gasification rate in a mixture of CO_2 and H_2O did not add up to the sum of the two pure-gas reaction rates. Thus, they proposed a kinetic equation to interpret their experimental data based on the assumption that both reactions compete for the same active sites. Chen et al. [17] investigated the effect of pyrolysis conditions on char gasification with mixtures of CO_2 and H_2O in a TGA and a fluidized-bed reactor using two differently pyrolyzed lignite chars (fast and slow pyrolysis). The authors report that the char gasification rates in the mixture of CO_2 and H_2O were lower than the sum of the rates of the char reacting independently with CO_2 and H_2O. However, the reaction rates in the mixed atmospheres were higher than the rate of each independent reaction for both the fast pyrolysis and slow pyrolysis char gasification. Furthermore, their results from TGA and fluidized-bed indicate that the char-H_2O reaction was independent of the char-CO_2 reaction, while the char-CO_2 reaction was inhibited by the char-H_2O reaction.

An alternative reaction mechanism for the gasification of chars in mixtures of CO_2 and H_2O is based on the assumption that the char-CO_2 and the char-H_2O reactions occur at separate active sites [19–23]. Guizani et al. prepared beech wood chars at low [21] and high heating rate [23] and found that the beech wood char reactivity is fairly represented by this additive approach for temperatures up to 900 °C and relatively low reactant partial pressures. Gasification experiments in mixtures of CO_2 and H_2O at elevated pressure using a fixed-bed reactor were carried out by Li et al. [22]. Their results indicate that the dominating reaction mechanism depends on the total pressure applied. They conclude that under low reactant pressures, the reaction mechanism was consistent with the separate reactive site reaction mechanism, while under higher pressure, the common active site reaction mechanism is rather valid. A short literature review concerning biomass, lignite and coal char gasification in mixed atmospheres is conducted by Guizani et al. [21], the quintessence being that no conclusive statement is possible whether the two reactions are competing or additive.

In literature, a vast amount of kinetic data for the gasification of fossil [24] and biogenic [25] fuels with both CO_2 and H_2O is available. However, the kinetic parameters may vary several orders of magnitude depending on the fuel, the char particle size, the experimental set-up used and the pyrolysis conditions applied. Pyrolysis conditions affect graphitization degree of the carbon matrix [26,27], char morphology [28,29] and dispersion of inorganic ash components [30,31]. In a previous publication [32], the authors were able to show an effect of both ash dispersion and graphitization on the gasification rate with CO_2. The investigated beech wood char samples were pyrolyzed in a drop-tube reactor under high heating rates, short residence times and temperatures between 1000 °C and 1600 °C in order to imitate the process conditions found in technical entrained-flow gasifiers. Due to thermal stress during pyrolysis, an increasing graphitization of the carbon matrix

leads to a decrease in initial conversion rate R_0 during gasification with CO_2. However, a thin layer of CaO that formed on the char surface at a pyrolysis temperature of 1600 °C was found to significantly increase the conversion rate of the char-CO_2 reaction.

Furthermore, the experimental set-up may have impact on the kinetic data obtained. The thermogravimetric analyzer (TGA) is most widely used for the determination of gasification kinetics of fossil and biogenic solid fuels [24,25]. However, diffusional effects due to the limited gas flow through the char sample may evoke artefacts. These artefacts would lead to observed reaction rates that are not truly intrinsic but rather a superposition of diffusion processes and the chemical reaction. Diffusion of the reactant gas through the crucible freeboard and the char bed must be taken into consideration in order to verify the kinetic data obtained [33,34]. Therefore, the experimental process parameters i.e. sample mass, temperature, gas velocity and reactant partial pressure must be carefully chosen when using TGA in order to determine kinetic data that are truly intrinsic [35]. It is important to conduct intrinsic gasification experiments in a TGA at relatively low temperatures in order to ensure that the diffusion processes are always faster than the actual gasification reaction. Especially for highly reactive bio-chars, the process window for the determination of intrinsic reaction rates during gasification is narrow in a TGA. Additionally, when higher pressures are applied in a TGA, even more restrictions may occur. Diffusion coefficients are inversely proportional to pressure ($D_{AB} \sim 1/p$). Furthermore, the maximum gas flow rate of a TGA is usually below 1 l/min at standard ambient temperature and pressure (rather around 50–200 ml/min). Increasing the pressure in a TGA leads to a proportional decrease of gas velocity towards the crucible as the volume flow rate at standard ambient temperature and pressure cannot be further increased. Moreover, high reactant gas volume flows during pressurized TGA experiments lead to a lot of noise in the mass signal.

Other experimental concepts such as vertically blown reactors (e.g. fixed-bed reactors) may be more suitable for the determination of gasification kinetics allowing for the application of wider process parameter windows. Here, the reactant gas is forced to flow through the char sample ameliorating mass transport of educt gas to and removal of product gas from the sample. Wu & Wang [36] investigated the effect of pressure on the K_2CO_3-catalyzed steam gasification of ash-free coal in a vertically blown reactor. The experimental set-up was operated as a differential reactor applying steam partial pressures of up to 6 bar and total pressures of 20 bar. The authors state that diffusional effects can be eliminated thoroughly by this type of reactor. Furthermore, kinetic parameters using an nth-order and a LH approach were determined.

From literature review it becomes obvious that kinetic data for pressurized gasification of biogenic char generated under typical EFG conditions (high heating rate, short residence time and high temperature) is rather scarce. For the determination of gasification kinetics at elevated pressure, a TGA is often used where the elimination of diffusional effects is difficult to be achieved, especially for highly reactive biogenic chars. Furthermore, gasification kinetics for bio-chars using CO_2, H_2O and its mixture at elevated pressure has not been investigated extensively to the best of our knowledge. Concerning the dominating reaction mechanism during gasification of bio-chars in mixtures of CO_2 and H_2O, no conclusive statement about the interdependence of the two reactions was found in literature.

The aim of this work is to determine the influence of pressure on the gasification kinetics for two beech wood chars that were produced under inert conditions at 1400 °C and 1600 °C at high-heating rates and short residence times in a drop-tube reactor imitating the conditions found during EFG. These chars exhibited different reactivities towards CO_2 due to distinct differences in morphology, graphitization and catalytic influence of ash components arising from their various pyrolysis temperatures [32]. The gasification experiments presented in this work are conducted in a single-particle reactor with forced flow-through conditions reducing diffusional effects to a minimum. The reactant gases flow convectively through the char particles. It was assured that the reactor was operated in a differential way meaning that the reactant gas concentration did not decrease >3 vol-% along the particle bed. Thus, all char particles were able to get in contact with the desired gas concentration and no concentration gradient was formed. Furthermore, the gas velocity was kept constant at a high level. Consequently, no accumulation of product gas near the char particles occurred as it may happen at the bottom of a TGA crucible. Since the product gas is swept away by the gas flow convectively, re-adsorption of product gases on the char surface is minimized. Product gas re-adsorption could possibly inhibit the gasification reaction leading to observed reaction rates that are not truly intrinsic. The interpretation of the experimentally determined reaction rates during gasification with CO_2, H_2O and its mixture is based on the char properties (graphitization, ash dispersion and morphology) presented in a previous publication [32]. Kinetic parameters for the gasification of both beech wood chars (P1400 and P1600) with CO_2 and H_2O at elevated pressure are derived using an nth-order as well as a LH approach. Moreover, gasification experiments in a mixture of CO_2 and H_2O are carried out in order to further clarify the dominating reaction mechanism during gasification of biomass chars in CO_2/H_2O containing atmospheres. A possible approach for the reaction kinetic modeling in mixtures of CO_2 and H_2O is presented for both bio-chars.

2. Materials and methods

2.1. Fuel

Commercially available primary beech wood char (Holzkohleverarbeitung Schütte GmbH & Co. KG) was purchased and used as precursor for the secondary pyrolysis experiments in the drop-tube reactor since the same char is utilized in the bioliq® EFG for research operation. The feedstock which is fed into the entrained flow gasifier of the bioliq® process is a suspension fuel consisting of bio-char and pyrolysis oil. The primary char is produced under mild conditions at an estimated pyrolysis temperature of 500–600 °C. Table 1 shows the proximate/ultimate analysis and the micropore surface area of the primary char. It still contains approx. 12 wt-% of volatiles and consists of 1.8 wt-% ash and 85.5 wt-% fixed carbon. Furthermore, the organic components consist of approx. 90 wt-% carbon, 3 wt-% hydrogen and 7 wt–% oxygen (by difference). The micropore surface area was determined with CO_2 at 0 °C and constitutes 394.6 $m^2\ g^{-1}$. For secondary pyrolysis in the drop-tube reactor, the primary char was sieved to a particle fraction of 50–150 µm.

The determination of kinetic parameters was carried out using two secondary chars produced at 1400 °C and 1600 °C in a drop-tube reactor with a residence time of 200 ms. Prior to the analyses and gasification experiments, the secondary chars were sieved to a particle fraction of 50–100 µm. Table 2 shows proximate/ultimate analysis and the micropore surface area of the secondary chars P1400 and P1600. Both chars consist almost of pure carbon with values for fixed carbon of 95.4 wt-% for P1400 and 97.1 wt-% for P1600. Total ash content of both chars is similar, whereas volatile content of P1400 being 2.5% is almost double as compared to P1600. Both chars differ significantly in micropore

Table 1
Properties of primary char.

Proximate analysis / wt.-%, ad	
Moisture	0.9
Ash content	1.8
Volatiles	11.8
Fixed carbon	85.5
Ultimate analysis / wt.-%, daf	
C	89.8
H	2.6
O (diff)	7.2
N	0.4
Micropore surface area / $m^2\ g^{-1}$	394.6

Table 2
Properties of secondary chars P1400 and P1600.

	P1400	P1600
Proximate analysis / wt.-%, ad		
Moisture	0.2	0.0
Ash content	1.9	1.6
Volatiles	2.5	1.3
Fixed carbon	95.4	97.1
Ultimate analysis / wt.-%, daf		
C	97.2	99.0
H	0.2	0.2
O (diff)	1.9	0.3
N	0.7	0.5
Micropore surface area / $m^2\ g^{-1}$	660.0	126.4

surface area with values of 660.0 $m^2\ g^{-1}$ for P1400 and 126.4 $m^2\ g^{-1}$ for P1600 that can be traced back to a collapse of micropore structure at 1600 °C.

Table 3 shows the ash elemental analysis for both secondary chars determined by inductively coupled plasma optical emission spectrometry (ICP-OES). The main ash component of these beech wood chars is calcium with values between 35.30 wt-% and 39.10 wt-%. A decrease of magnesium content from 1400 °C to 1600 °C can be observed being only 1 wt-% at 1600 °C. For the secondary chars, K/Si ratios are 2.2 and 2.1, respectively while K/(Si + P) ratios have a value of 1.3 being comparatively low (P content of primary char was not determined). Thus, a deactivation of K by Si and P can be assumed [37,38].

In order to gain a better understanding for the experimental results presented in this work, a key figure from our previous publication [32] is shown. In Fig. 1, the most important char characteristics being the initial conversion rate R_0 during gasification with CO_2, CaO dispersion D_{CaO} and graphitization defined as $L_a\ L_{a,0}^{-1}$ are summed up in one graph. Quantification of the CaO dispersion was carried out in a TGA using temperature-programmed reaction (TPR) and chemisorption of CO_2 on CaO at 300 °C. At 300 °C, CO_2 reacts with the CaO atoms on the surface of ash particles forming $CaCO_3$. Increasing the temperature would lead to the carbonization of bulk CaO due to diffusion of CO_2 into the ash particle [39]. Thus, chemisorption of CO_2 at 300 °C can be used to determine the outer surface of CaO particles in the bio-char ash giving a value for the dispersion of CaO particles in mole surface CaO per gram char. The radial expansion of graphene layers of the secondary chars L_a as well as the radial expansion of graphene layers of the primary char $L_{a,0}$ was determined using X-ray diffraction (XRD) and Scherrer equation. Further information about the analyses and methods for char characterization can be found in our previous publication [32]. Concerning the gasification experiments with CO_2, Fig. 1 shows a linear decrease in initial conversion rate R_0 for chars produced at pyrolysis temperatures between 1000 °C and 1400 °C. However, a strong increase of R_0 at a pyrolysis temperature of 1600 °C was encountered. Micropore surface area of the secondary chars showed no correlation with the initial conversion rate R_0 during gasification with CO_2. Graphitization of the carbon matrix suggested the growth of aromatic clusters and graphite-like structures for increasing pyrolysis temperatures up to 1600 °C. Furthermore, CaO dispersion decreased steadily between 1000 °C and 1400 °C whereas a strong increase can be observed at 1600 °C, which is in good accordance with the development of the initial conversion rate R_0 as a function of pyrolysis temperature. Furthermore, SEM/TEM images indicate the formation of a thin CaO layer at 1600 °C that is presumably responsible for the strong increase in initial conversion rate R_0 during gasification with CO_2 (not shown in this work).

Table 3
Ash elemental analysis of primary and secondary chars.

Element	Primary char	P1400C_200ms wt.-%	P1600C_200ms
Ca	38.20	35.30	39.10
K	4.62	5.48	5.05
Mg	6.03	5.80	1.03
Si	2.01	2.51	2.45
P	n. a.	1.73	1.52
Na	0.82	0.96	0.84
Fe	0.74	0.84	0.83
Al	0.25	0.28	0.31

2.2. Pressurized single-particle reactor

Gasification experiments were conducted in a pressurized single-particle reactor that was operated in a differential way allowing only for very low changes in the educt gas phase composition. A schematic flow diagram of the reactor system is shown in Fig. 2. The gas dosing system consists of mass flow controllers (MFC, EL-FLOW, Bronkhorst High-Tech B.V.) for CO_2 and argon allowing for volume flows up to 20 l min^{-1}. Furthermore, one MFC is used for dosing small amounts of nitrogen that is used as a tracer in the analytic strand. Demineralized water is stored in a vessel ($V = 1$ l) and pressurized with 30 bar helium. Measurement of the liquid water flow is carried out using a *mini CORI-FLOW* (Bronkhorst High-Tech B.V.). Steam is generated in a *Controlled Evaporation and Mixing* unit (CEM, Bronkhorst High-Tech B.V.) and - together with a carrier gas - led to the reaction line. A 4-port 2-position valve (V1, VICI) allows the feed gas mixture which is normally entering the reactor to be switched to the bypass line. With this arrangement, the reactor line including the reactor can be purged with argon. The tubular reactor (1200 mm height, 19.5 mm inner diameter) is mounted vertically and can be operated at a pressure of up to 24 bar. The pressure of reaction and bypass line is controlled by back pressure regulators (EL-PRESS, Bronkhorst High-Tech B.V.). Another 4-port 2-position valve (V2, VICI) after the back pressure regulators allows the product gases to either be analyzed using infrared photometry (IR, URAS, ABB) and micro gas chromatography (490 Micro GC, Agilent Technologies) or directly be sent to the off-gas system.

The char is fed into the reactor batch-wise with a dosing unit that is schematically depicted in Fig. 3A. The central component of this device is a brass cylinder (a) with a cylindrical bore where the char is placed prior to the gasification experiment. This brass cylinder can be removed from the dosing unit in order to fill the bore with char and weigh the sample. When the brass cylinder (a) is inserted into the dosing unit, it is sealed with PTFE foil. The brass cylinder (a) is situated beneath a receiver tank (b) that can be flushed with argon in order to remove oxygen from the dosing unit (valve (d) closed, valves (c) and (e) open). The receiver tank is filled with quartz wool in order to minimize void space with potential accumulation of oxygen. Prior to each gasification experiment, the receiver tank (b) was flushed with argon for at least 10 min. Subsequently, the valves (c) and (e) are closed to prevent oxygen from entering the receiver tank (b) and valve (d) is opened. Argon flows down the conus (f) of the dosing unit and serves as a carrier gas for the char. Eventually, the brass cylinder (a) is turned by 180° and the char falls out of the dosing unit being carried onto a quartz wool bed inside the reactor by the gas flow.

Fig. 3B shows the arrangement inside the single-particle reactor during a gasification experiment. The char sample is placed on a quartz wool bed while the feed gas flows top-down. Beneath the quartz wool bed, a quartz glass tube with fused-in quartz frit is located. In order to measure the temperature of the char sample, a type K thermocouple is inserted via a quartz glass capillary tube that is fused into the frit. The end of the quartz glass tube is sealed with a stuffing box packing (not shown in Fig. 3B), i.e. a ceramic fiber rope that prevents an idle gas flow past the char sample and the quartz glass tube.

Prior to each gasification experiment, the desired reaction temperature was set by means of the type K thermocouple within the quartz glass capillary in the single-particle reactor under constant argon flow and atmospheric pressure using the electric furnace. Reaction temperatures were varied between 810 °C and 870 °C. During gasification stage

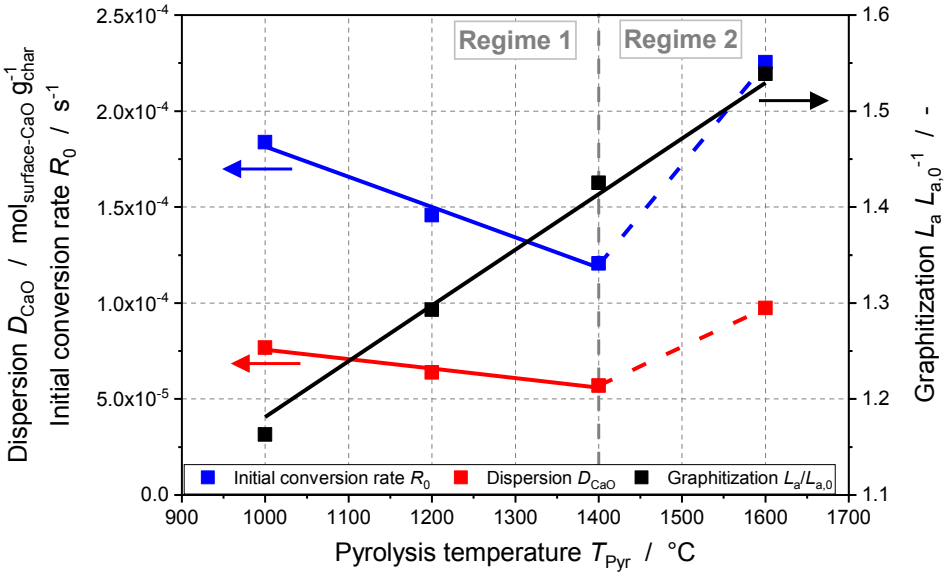

Fig. 1. Summary of the most important experimental results (CaO dispersion D_{CaO}, initial conversion rate R_0 and graphitization degree L_a $L_{a,0}^{-1}$) for the secondary chars pyrolyzed between 1000 °C and 1600 °C [32].

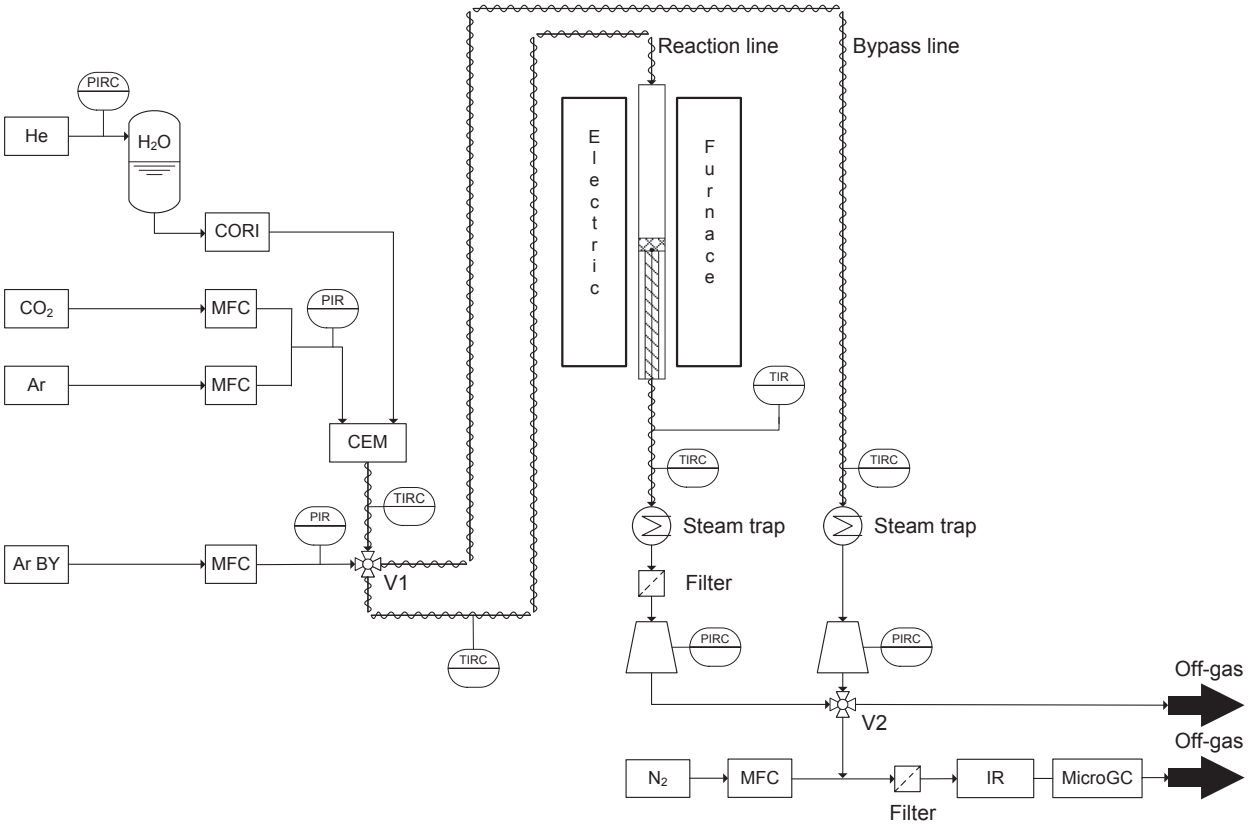

Fig. 2. Schematic flow diagram of the single-particle reactor used for pressurized gasification experiments.

of the experiments, the temperature deviations detected where within ± 1 K. Subsequently, the char sample was filled into the bore of the brass cylinder and the dosing unit was mounted on top of the reactor after being flushed with argon. For the experiments in CO_2 atmosphere, a sample amount of 50 mg was chosen while the experiments in H_2O and mixed CO_2/H_2O atmospheres were carried out using 20 mg. The sample mass was determined in preliminary studies in order to eliminate diffusional effects and ensure the differential operation of the reactor maintaining a concentration deviation of the educts below 3 vol-%. After directing the argon flow through the cone of the dosing unit, the brass

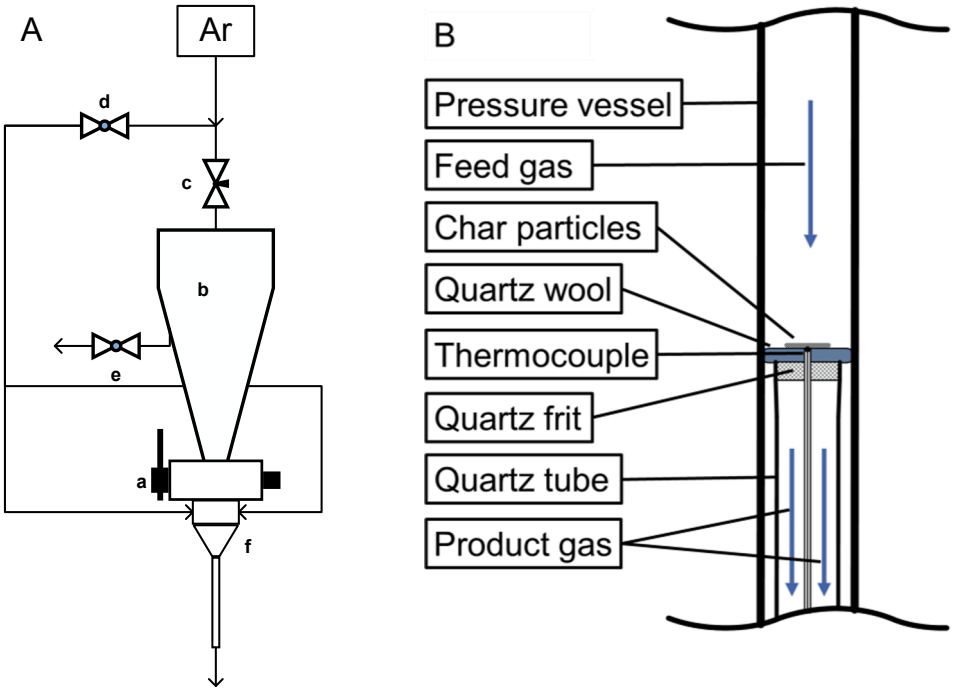

Fig. 3. Schematic illustration of the dosing unit (A) (a, brass cylinder; b receiver tank; c-e, valves; f conus) and the arrangement inside the single-particle reactor (B).

cylinder was turned by 180° and the char sample fell onto the quartz wool bed. Immediately after, a slight increase in the CO concentration was observed via IR in the order of few ppm due to partial combustion of char with oxygen that was still adsorbed on the char surface. After few seconds, the CO signal reached baseline level again. The calculated amount of fixed carbon being combusted in this step was estimated to be approx. 3.2% for P1400 and 0.6% for P1600 accounting for a worst case where the whole micropore surface area is occupied with air (21% oxygen and 79% nitrogen). For the calculation, it was assumed that the edge carbon atoms lie in the (1 0 0) plane and each carbon atom occupies an area of $8.3{\cdot}10^{-20}$ m^2 [40].

At this stage of the experiment, argon flows through both lines (reaction and bypass) with 1 l min^{-1} at atmospheric pressure. Before the gasification started, valve V1 was set to position B, at which the reactant gases are led to the bypass line and argon (Ar BY) flows through the reaction line. Subsequently, the reactant gas composition was adjusted in the bypass line and the desired system pressure was set in both lines using the back pressure regulators. The total volumetric flow rate of the reactant gases was adapted for each experiment in order to maintain a constant superficial linear gas velocity of 21 cm s^{-1} for the CO_2 and 10.5 cm s^{-1} for the H_2O and mixed atmosphere gasification experiments at reaction conditions. These values were determined in preliminary studies and also depend on the chosen sample amounts in order to eliminate diffusional effects and operate the reactor differentially. The reactant gas composition was checked using gas phase analytics (IR and MicroGC) setting valve V2 to position B. Immediately after the gas phase analysis, valve V2 was switched back to position A. To begin the gasification experiment, valve V1 was set to position A as well. The change in product gas concentration was monitored online via IR and the MicroGC took samples every 3 min. All further data evaluation is based on the MicroGC measurements. A gasification experiment was terminated when the measured volume fraction of the product gases was in the range of a low two-digit ppm value and did not change for at least two MicroGC measurements. An overview of all experiments conducted for single atmosphere and mixed gasification process conditions can be found in Tables 4–6.

Table 4
Process conditions during CO_2 gasification of P1400 and P1600.

v_{gas} cm s^{-1}	m_{sample} mg	T °C	p_{tot} bar	p_{CO_2} bar
21	50	830	1	1
		850	5	5
		870	10	10
			15	15
			20	5
				10
				15
				20

Table 5
Process conditions during H_2O gasification of P1400 and P1600.

				P1400	P1600
v_{gas} cm s^{-1}	m_{sample} mg	T °C	p_{tot} bar	p_{H_2O} bar	p_{H_2O} bar
10.5	20	830	1	0.2	0.2
		850		0.4	
		870	2	0.4	0.4
				0.8	0.8
			5	0.8	
				2	2
			10	2	
				5	5

2.3. Determination of carbon conversion X_C

A common definition for carbon conversion X_C can be written as follows:

$$X_C(t) = \frac{m_{C,0} - m_C(t)}{m_{C,0}} \tag{5}$$

$$m_{C,0} = m_{char} x_{C_{fix}} \tag{6}$$

Here, $m_{C,0}$ represents the initial mass of fixed carbon, $m_C(t)$ is the

Table 6
Process conditions during mixed gasification of P1400 and P1600.

v_{gas} cm s^{-1}	m_{sample} mg	T °C	p_{tot} bar	p_{H_2O} bar	p_{CO_2} bar
10.5	20	810	5	0.8	0.8
		830			
		850			
		830	5	0.8	2
				2	0.8
			10	0.8	5
				2	2
			15	2	5
			20	5	5

remaining carbon mass at a certain time t, with m_{char} being the char mass and $x_{C_{fix}}$ being the fixed carbon mass fraction of the char sample. However, the single-particle reactor used in this work does not allow for the measurement of discrete mass signals. In fact, the carbon conversion X_C was determined using a carbon balance and gas phase analysis (see Sections 2.3.1–2.3.3). The carbon mass balance leads to the following differential equation for a fractional carbon conversion dX_C:

$$\frac{dX_C}{dt} = \frac{M_C}{m_{C,gasif}} \dot{n}_{C,out}(t) \tag{7}$$

$\dot{n}_{C,out}(t)$ is the time dependent molar flow rate of carbon containing gasification product gases, M_C the carbon molar mass and $m_{C,gasif}$ the total mass of gasified carbon. The gasification product gases considered for $\dot{n}_{C,out}(t)$ differed for each gasification experiment, i.e. CO_2, H_2O and mixed CO_2/H_2O atmospheres. During CO_2 gasification, only CO was taken into account (see Section 2.3.1) while during H_2O gasification, CO and CO_2 had to be considered due to water–gas shift reaction (see Section 2.3.2). Based on an approach from Chen et al. [17] for mixed CO_2/H_2O gasification, the volume fraction of hydrogen produced was taken into account for $\dot{n}_{C,out}(t)$ during mixed gasification experiments (see Section 2.3.3).

The gasified mass of carbon $m_{C,gasif}$ can be calculated via integration of the molar flow rate of carbon containing gasification product gases $\dot{n}_{C,out}(t)$ from $t = 0$ to the end of the experiment at t_{end} and the carbon molar mass M_C.

$$m_{C,gasif} = M_C \int_0^{t_{end}} \dot{n}_{C,out}(t)dt \tag{8}$$

The molar flow rate $\dot{n}_{out}$ of all permanent gases exiting the reactor and being detected in gas phase analytics was calculated using the nitrogen reference flow $\dot{V}_{N_2}$, the nitrogen volume fraction $y_{N_2}(t)$ and the molar volume $V = 22{,}414$ l mol^{-1}. In the frame of this work, molar and volume fractions were considered to be equal (ideal gas), since gas phase analytics were operated at atmospheric pressure.

$$\dot{n}_{out}(t) = \frac{\dot{V}_{N_2}}{y_{N_2}(t)V} \tag{9}$$

For the subsequent determination of the initial conversion rate R_0 and reaction rate r_i (see Section 2.4), the carbon conversion X_C was always based on the gasified mass of carbon $m_{C,gasif}$ calculated from gas phase data as described above. A comparison of $m_{C,gasif}$ with the value of the initially weighed out carbon mass $m_{C,0}$ was conducted for each experiment allowing for an evaluation of the methodological approach.

2.3.1. Gasification with CO_2

During experiments with CO_2, the only gasification product gas considered for $\dot{n}_{C,out}(t)$ was CO. In this case, the gasified mass of carbon $m_{C,gasif,CO_2}$ is calculated using the CO molar fraction y_{CO} taking into account the stoichiometry of the Boudouard reaction.

$$m_{C,gasif,CO_2} = \frac{M_C}{2} \int_0^{t_{end}} y_{CO}(t)\dot{n}_{out}(t)dt \tag{10}$$

$$X_{C,gasif,CO_2}(t) = \frac{\int_0^t y_{CO}(t)\dot{n}_{out}(t)dt}{\int_0^{t_{end}} y_{CO}(t)\dot{n}_{out}(t)dt} \tag{11}$$

Based on this approach, the carbon conversion X_C always reaches the value 1 at the end of an experiment as the carbon balance is carried out for the gas phase. Comparing the initially weighed out amount of carbon $m_{C,0}$ with $m_{C,gasif,CO_2}$, the carbon mass balance was closed between 78% and 98% for the gasification experiments with CO_2.

2.3.2. Gasification with H_2O

The carbon containing product gases during gasification with H_2O included not only CO but also CO_2. Since CO can be converted to CO_2 via water–gas shift (WGS) reaction in the presence of H_2O, both gases were considered as a measure for the amount of carbon gasified. Due to the low amount of methane (two orders of magnitude lower than the other product gases) found in the product gas, CH_4 was neglected in the carbon balance. The error in carbon balance was estimated to be approx. 0.5%. The mass balance based on the initially weighed out amount of carbon $m_{C,0}$ was closed between 66% and 93% for the gasification experiments with H_2O.

$$m_{C,gasif,H_2O} = M_C \int_0^{t_{end}} (y_{CO}(t) + y_{CO_2})\dot{n}_{out}(t)dt \tag{12}$$

$$X_{C,gasif,H_2O}(t) = \frac{\int_0^t (y_{CO}(t) + y_{CO_2})\dot{n}_{out}(t)dt}{\int_0^{t_{end}} (y_{CO}(t) + y_{CO_2})\dot{n}_{out}(t)dt} \tag{13}$$

2.3.3. Gasification in mixed CO_2/H_2O atmospheres

For the gasification in mixed CO_2/H_2O atmospheres, another approach had to be taken since it is difficult to distinguish between CO_2 from the feed gas and CO_2 formed due to WGS reaction converting CO in the presence of H_2O. According to Chen et al. [17], the following reactions need to be taken into account during mixed gasification (methane formation being neglected).

a $C + CO_2 \rightleftharpoons 2CO$ (R11)

b $C + H_2O \rightleftharpoons H_2 + CO$ (R12)

c $CO + H_2O \rightleftharpoons CO_2 + H_2$ (R13)

Introducing global reaction rates a, b and c (in mol s^{-1}) for (R11)–(R13), the following expressions can be written for the molar flow rates of the gasification product gases involved. The consumption of carbon is considered in Eq. (17).

$$\dot{n}_{CO} = 2a + b - c \tag{14}$$

$$\dot{n}_{H_2} = b + c \tag{15}$$

$$\dot{n}_{CO_2} = -a + c \tag{16}$$

$$-\dot{n}_C = a + b \tag{17}$$

From Eqs. (14), (15) and (17), the carbon consumption $\dot{n}_C$ can be rewritten as the molar flow rate of carbon containing gasification product gases $\dot{n}_{C,out,mix}(t)$ during mixed CO_2/H_2O atmosphere gasification using CO and H_2 molar fractions. The mass balance based on the weighed out amount of carbon $m_{C,0}$ was closed between 57% and 75% for the gasification experiments in mixed CO_2/H_2O atmospheres. A possible source of error for the lower balance closures during H_2O and mixed H_2O/CO_2 gasification is the absorption of CO_2 in the condensing water after the reactor. The CO_2 containing water is extracted from the system in the steam trap that is operated at reaction pressure. Thus, the higher the reaction pressure, the more CO_2 was solved in the water and

removed from the system. This reduces the total molar flow rate $\dot{n}_{out}$ and the CO_2 concentration prior to gas phase analysis and therefore worsens the carbon balance. Another reason is that for balancing purposes, only permanent gases were taken into account. The steam trap is operated at 5 °C. A complete removal of water from the product gas is technically hard to achieve without increasing the delay time of the whole plant dramatically. Thus, the product gas still contains water to a small extent, which corresponds to the dew point concentration at 5 °C. This amount of water was neglected in the carbon balance calculations.

Concerning the gasification in mixed H_2O/CO_2 atmospheres, more Micro GC calibration points for hydrogen in the low ppm area (<5000 ppm) could have further minimized errors and ameliorated the carbon balance.

$$-\dot{n}_C = a + b = \frac{\dot{n}_{CO} + \dot{n}_{H_2}}{2} = \dot{n}_{C,out,mix}(t) = \frac{y_{CO}(t) + y_{H_2}(t)}{2}\dot{n}_{out}(t) \tag{18}$$

$$m_{C,gasif,mix} = M_C \int_0^{t_{end}} \left(\frac{y_{CO}(t) + y_{H_2}(t)}{2}\dot{n}_{out}(t) \right) dt \tag{19}$$

$$X_{C,gasif,mix}(t) = \frac{\int_0^t \left(\frac{y_{CO}(t)+y_{H_2}(t)}{2}\dot{n}_{out}(t) \right) dt}{\int_0^{t_{end}} \left(\frac{y_{CO}(t)+y_{H_2}(t)}{2}\dot{n}_{out}(t) \right) dt} \tag{20}$$

2.4. Determination of reaction rate r_i

Carbon conversion $X_C(t)$ was determined using gas phase analytics and the equations presented in Section 2.3. The conversion rate R_X can be calculated via carbon balance as presented in Eq. (21).

$$R_X = \frac{dX_C}{dt} = \frac{M_C}{m_{C,gasif}}\dot{n}_{C,out}(t) \tag{21}$$

Furthermore, R_X is defined by a rate coefficient $R(T,p)$ and a structural term $F(X)$ [25]:

$$R_X = \frac{dX_C}{dt} = R(T,p)F(X_C) \tag{22}$$

In the frame of this work, the Uniform Conversion Model (UCM) was used to model the conversion process resulting in a structural term of $F(X_C) = 1 - X_C$ [41] and the following expression:

$$R_X = \frac{dX_C}{dt} = R_0(1 - X_C) \tag{23}$$

$$R_0 = \left.\frac{dX_C}{dt}\right|_{X_C=0} \tag{24}$$

$$X_C(t) = 1 - \exp(-R_0 t) \tag{25}$$

R_0 is defined as the initial conversion rate, which was determined by a least-square fit in the carbon conversion range between 20% and 50% (see Fig. 4). In the frame of this work, the focus was to determine the initial conversion rate R_0 by fitting the carbon conversion curve between 20% and 50% using the idealized particle conversion model UCM. The UCM treats the fuel particle as a homogeneous body where the gasification reaction occurs uniformly. However, reactivity of the char might highly change in the course of the reaction due to changes in morphology, ash dispersion and graphitization throughout carbon conversion. Therefore, it was decided to use an early stage of gasification for the determination of a characteristic value of R_0 in order to be able to interpret the results based on the char properties analyzed prior to gasification. The carbon conversion range between 20% and 50% was chosen in order to minimize the effects of gas switch at the start of each experiment. Furthermore, the char properties for higher conversion degrees may have changed and were not characterized. Every gasification experiment was repeated two to three times.

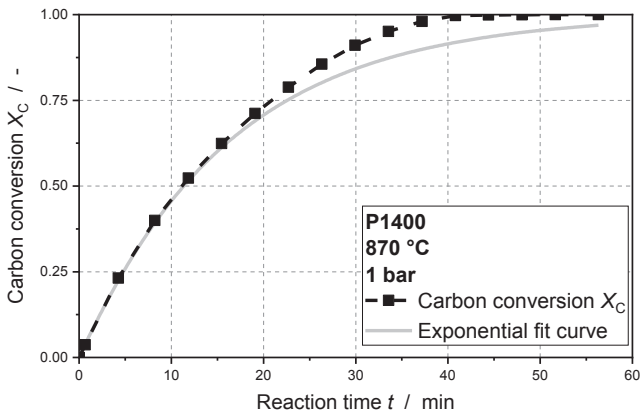

Fig. 4. Carbon conversion X_C and exponential fit curve for the determination of the initial conversion rate R_0 during gasification of P1400 with CO_2 at 870 °C and 1 bar in the single-particle reactor.

Eventually, the reaction rate r_i ($i = CO_2, H_2O$, mix) is calculated using the initial conversion rate R_0 and the molar mass of carbon M_C. All further reaction kinetic parameters were calculated using the experimentally determined reaction rates r_i.

$$r_i = \frac{R_0}{M_C} \tag{26}$$

3. Results and discussion

3.1. Gasification experiments with CO_2

3.1.1. Raw data evaluation

Fig. 5 shows the CO volume fractions y_{CO} and carbon conversion curves $X_{C,gasif,CO_2}$ during gasification of P1400 and P1600 with CO_2 at 830 °C and a total pressure of 1 bar. Carbon conversion $X_{C,gasif,CO_2}$ was calculated using Eq. (11). Both char samples show decreasing CO signals, however, P1600 starts with a higher volume fraction of approx. 0.8 vol-% and decreases faster than the sample P1400. Therefore, the atmospheric gasification experiment with P1600 at 830 °C is already terminated after 100 min whereas the gasification of P1400 lasts approx. 20 min longer. The high starting value and steep decrease of y_{CO} for P1600 leads to a faster increase of carbon conversion $X_{C,gasif,CO_2}$ and thus, to a higher initial conversion rate R_0. Furthermore, the decreasing course of y_{CO}, which was especially pronounced during gasification of P1600, is an indication for Ca catalyzed gasification reaction. Another indication for Ca catalysis during CO_2 gasification may be a decreasing course of conversion rate R_X which is directly correlated with the CO volume fraction y_{CO} as presented in Eqs. (10) and (21). Struis et al. [42] investigated the catalytic activity of different metal elements (Na, K, Ca, Mg, Zn, Pb, Cu) found in waste wood ashes. They observed a high catalytic activity of alkaline earth nitrate salts during the early gasification stage followed by decreasing reaction rate for the whole carbon conversion range. The authors presumed that this decrease arises from sintering of the resulting alkaline earth metal oxides lowering their dispersion on the char surface. Another correlation between char-CO_2 reactivity and CaO dispersion was found by Cazorla-Amoros et al. [43]. The authors investigated the dispersion and sintering of Ca species on carbon samples during pyrolysis and gasification with CO_2. Their results indicated that Ca dispersion decreased with increasing carbon conversion during gasification with CO_2 suggesting a deactivation mechanism presumably due to sintering processes. As expected from the results of our previous work [32], the higher initial conversion rate R_0 of P1600

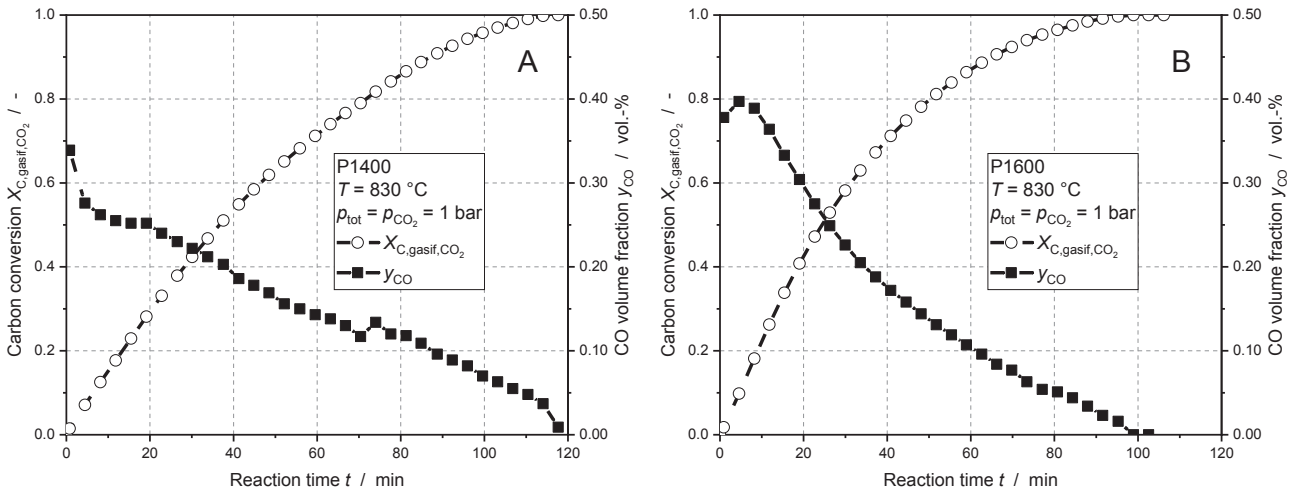

Fig. 5. CO volume fraction y_{CO} and carbon conversion $X_{C,gasif,CO_2}$ during gasification of P1400 (A) and P1600 (B) in CO_2 at 830 °C and 1 bar total pressure.

during gasification with CO_2 was observed for all CO_2 partial pressures and temperatures investigated due to the formation of a thin CaO layer catalyzing the gasification reaction (also see Figs. 7 and 8).

For $p_{CO_2} = 20$ bar, however, both chars showed similar reaction rates (see Fig. 8). Here, the total gasification time of both chars was similar and amounted to approx. 60 min (see Fig. 6). Furthermore, CO volume fractions y_{CO} were in the range of 0.02 for P1400 and 0.03 for P1600, respectively. In comparison to the experiments at lower pressure, a CO volume fraction plateau was obtained for the first 20 min of gasification. This plateau also effects the shape of the carbon conversion curve X_C becoming more linear and may be interpreted as some sort of saturation of the char surface for this CO_2 partial pressure and the corresponding char.

3.1.2. *Influence of temperature*

Arrhenius plots for the gasification of P1400 and P1600 with CO_2 partial pressures between 1 bar and 20 bar and temperatures between 830 °C and 870 °C are depicted in Fig. 7. For P1400, an increase of temperature and CO_2 partial pressure leads to an increase in reaction rate. The slope of the lines for a constant partial pressure are almost parallel suggesting no diffusion limitations during the kinetic measurements. Furthermore, the mean activation energy of the P1400 gasification experiments with CO_2 was 310.8 kJ mol^{-1} being rather at the upper limit of the activation energies presented in literature for biogenic char-CO_2 gasification [25]. The high values for the activation energies obtained may also be an indication for the absence of diffusional effects, i.e. the determination of true microkinetics. For P1600, small differences in the Arrhenius plot can be observed compared to P1400. The mean activation energy of the P1600 gasification experiments with CO_2 was slightly lower and accounted for 301.1 kJ mol^{-1}. The large difference in reaction rate r_{CO_2} between the 1 bar and the 5 bar experiments becomes apparent. During gasification of P1600, a slight increase of p_{CO_2} in the low pressure area induces a high increase in char-CO_2 reaction rate. Furthermore, a saturation for the high pressure area can be observed. An increase of p_{CO_2} from 10 bar to 15 bar only marginally increases the reaction rate. Additionally, the increase of p_{CO_2} from 15 bar to 20 bar does not lead to a further increase in reaction rate. It can be assumed that a saturation of the char surface is achieved starting at $p_{CO_2} = 15$ bar for the sample P1600. The lower specific surface area (micropores) of P1600 with 126.4 m^2 g^{-1} in comparison to the sample P1400 with 660.0 m^2 g^{-1} may be a reason for the saturation of the char surface at higher CO_2 partial pressures.

Fig. 8 shows an Arrhenius plot of P1400 and P1600 for 1 bar, 10 bar and 20 bar CO_2 partial pressure to facilitate a direct comparison between both char samples. Once again, it is remarkable that the reactions rates r_{CO_2} of P1600 are higher than the rates of P1400 for one constant pressure despite the higher graphitization degree and the lower micropore surface area of P1600. Higher char-CO_2 reaction rates of P1600 compared to P1400 were determined for all reaction conditions investigated. At the highest pressure of 20 bar, however, both chars showed

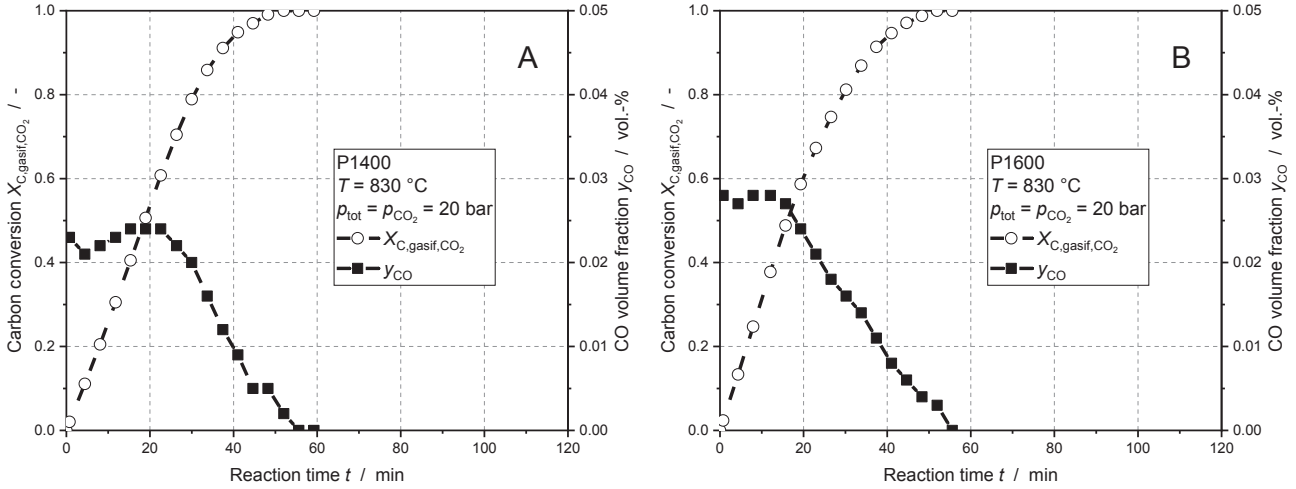

Fig. 6. CO volume fraction y_{CO} and carbon conversion $X_{C,gasif,CO_2}$ during gasification of P1400 (A) and P1600 (B) in CO_2 at 830 °C and 20 bar total pressure.

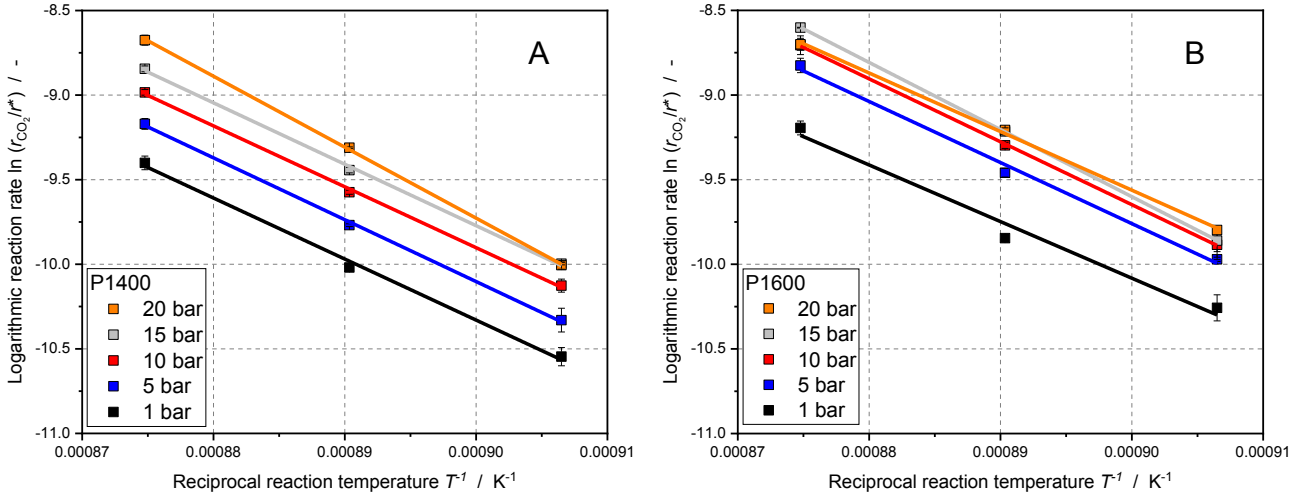

Fig. 7. Arrhenius plots for the gasification of P1400 (A) and P1600 (B) in CO_2 (p_{CO_2} = 1–20 bar and T = 830–870 °C).

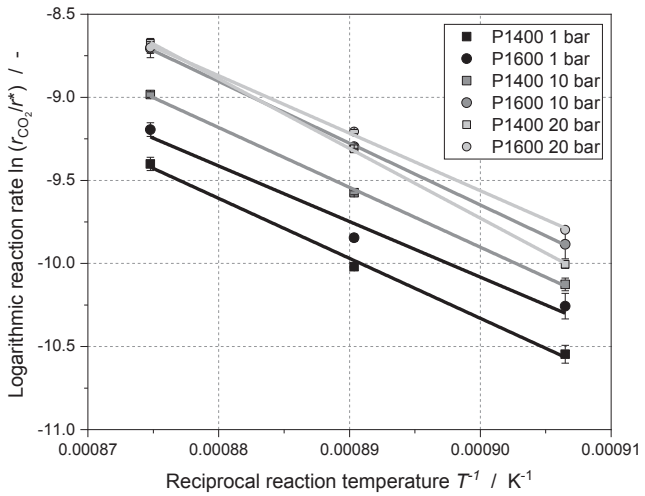

Fig. 8. Arrhenius plot for the gasification of P1400 and P1600 in CO_2 (p_{CO_2} = 1 bar, 10 bar, 20 bar and T = 830–870 °C).

similar reaction rates towards CO_2.

3.1.3. *Influence of total pressure and CO_2 partial pressure*

In Fig. 9, the char-CO_2 reaction rates are depicted as a function of CO_2 partial pressure. Experiments were conducted either with varying total pressure ($p_{tot} = p_{CO_2}$, dark symbols) or with constant total pressure of 20 bar for varying CO_2 partial pressures between 5 bar and 15 bar (open symbols). Results indicate that the influence of total pressure may be negligible as the experiments with a constant total pressure are mostly within the standard deviation of the experiments where CO_2 partial pressure equals total pressure. Slight differences between both experimental approaches may have arisen from the rather high dilution of product gases at a total pressure of 20 bar. Thus, the important parameter was considered to be CO_2 partial pressure or CO_2 concentration, respectively. Therefore, only the experiments where CO_2 partial pressure equals total pressure were taken for modeling purposes (see Section 3.1.4). Concerning the comparison between both chars, following observations can be made: CO_2 reaction rate r_{CO_2} of P1400 increases almost linearly with increasing CO_2 partial pressure showing no signs of saturation at high pressures. On the contrary, the CO_2 reaction rate of P1600 increases strongly between 1 bar and 5 bar and forms a plateau at higher pressures as could also be seen in the Arrhenius plot (see Fig. 7).

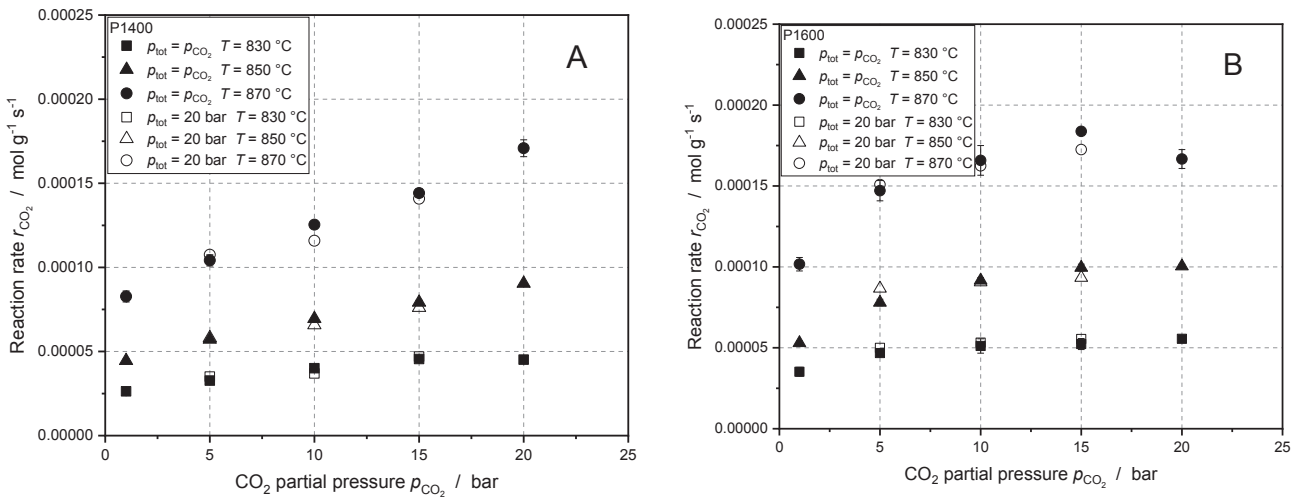

Fig. 9. Influence of total and CO_2 partial pressure on reaction rate r_{CO_2} during gasification of P1400 (A) and P1600 (B) (T = 830–870 °C, diluting gas: argon).

3.1.4. Reaction kinetic modeling

Power law. Fig. 10 shows the experimentally determined reaction rates r_{CO_2} of P1400 and P1600 modeled with a power law approach (see Eq. (2)). The corresponding model parameters k_{0,CO_2}, E_{A,CO_2} and n_{CO_2} can be taken from Table 7. Results indicate that basically, power law is a suitable approach for modeling pressurized char-CO_2 gasification of both samples. However, the specific characteristics of each char that are induced by its pre-gasification history and origin are rather poorly represented i.e. the linear increase of r_{CO_2} with increasing CO_2 partial pressure during gasification of P1400 cannot be adequately described using a power law approach. In addition, the reaction rates at 20 bar are rather underestimated. Concerning the sample P1600, a saturation at CO_2 partial pressures of 10 bar and above was determined. Again, the power law approach is not able to describe this phenomenon for very high pressures and overestimates the values at $p_{CO_2} = 20$ bar. All experimental values determined during pressurized gasification of P1400 and P1600 with CO_2 can be modeled within a deviation of ± 20% using the power law approach.

In order to compare the kinetic parameters determined in this work with similar studies, a discussion based on the values reported in literature is conducted for CO_2 and H_2O gasification, respectively. Fermoso et al. [44] investigated the gasification reaction of pine wood chars with CO_2 that were pyrolyzed in a drop tube reactor at 1000 °C and 1400 °C. The gasification experiments were conducted in a TGA at elevated pressure. During high-pressure experiments, the activation energies obtained (144 kJ mol^{-1}–164 kJ mol^{-1}) were rather low as compared to the activation energies determined at atmospheric pressure (184 kJ mol^{-1}–246 kJ mol^{-1}). This might be an indication for artefacts (e.g. diffusional limitations) evoked by the experimental methodology due to a limited gas flow (75 cm^3 min^{-1}) in the TGA resulting in a low gas velocity during high-pressure experiments. Besides, several particle conversion models were used i.e. the volumetric model, the grain model and the random pore model. No significant differences in the calculated activation energies were observed using these three models.

Another work was published by Cetin et al. [45] concerning pyrolysis and gasification of different biomass types (pine, eucalyptus and bagasse). Pyrolysis was carried out at 950 °C in a wire-mesh reactor at high heating rates (500 K s^{-1}) while pressurized gasification experiments were conducted in a TGA. Their results indicate that the kinetic parameters obtained are strongly dependent on the biomass type investigated. The determined activation energies range between 198 kJ mol^{-1} for bagasse chars and 238 kJ mol^{-1} for pine wood chars.

Gasification experiments with CO_2 in a fixed-bed reactor using different coal chars have been carried out by Li et al. [46]. The coals (lignite, sub-bituminous coal, anthracite) were pyrolyzed at 900 °C for 30 min prior to gasification. The shrinking core model was used to describe the particle conversion during gasification while relatively low activation energies ranging between 120 kJ mol^{-1} and 209 kJ mol^{-1} were obtained. Furthermore, the reaction orders n during CO_2 gasification (0.264–0.312) were similar to the ones presented in this work. The authors were able to show an effect of coal rank on the activation energies determined: the higher the coal rank of the chars, the higher the activation energy obtained. This effect might be caused due to higher degrees of graphitization for increasing coal ranks. Since the beech wood chars investigated in the frame of this work also exhibit a high degree of graphitization (see Section 2.1) due to pyrolysis at very high temperatures, this might be an explanation for the relatively high activation obtained during CO_2 gasification.

Table 7
Kinetic parameters for gasification of P1400 and P1600 with CO_2 using power law approach.

		P1400	P1600
k_{0,CO_2}	mol (g s bar^n)$^{-1}$	1.0163·10^{10}	5.675·10^9
E_{A,CO_2}	kJ mol^{-1}	308.7	300.7
n_{CO_2}	–	0.214	0.186

Atmospheric gasification experiments with chars originating from beech wood were conducted by Guizani et al. [23]. Reaction kinetic parameters were obtained during gasification of beech wood chars that were pyrolyzed at 850 °C–950 °C with a heating rate of approx. 100 K s^{-1}. The pyrolysis step was carried out *in-situ* in a TGA directly before initiating the gasification process. The authors used the char reactivity at a carbon conversion degree of 50% for their kinetic modeling approach. The activation energy was determined to be 154 kJ mol^{-1} being relatively low as compared to the present work. However, this discrepancy may be again explained by differences in the char properties i.e. different graphitization degree due to varying pyrolysis conditions.

Langmuir-Hinshelwood. Fig. 11 shows the CO_2 reaction rates r_{CO_2} of P1400 and P1600 modeled with an LH approach (see Eq. (1)). Model parameters $k_{0,1}$, $k_{0,3}$, $E_{A,1}$ and $E_{A,3}$ can be taken from Table 8. The linear increase of r_{CO_2} with increasing CO_2 partial pressure during gasification of P1400 is even poorer described with the LH approach than with power law. The low pressure area up to 10 bar is overestimated while the high pressure values are underestimated. In terms of parity plot, one point was out of the 20% interval and 4 points were close to the 20% deviation. On the other hand, the saturation of P1600 for high CO_2

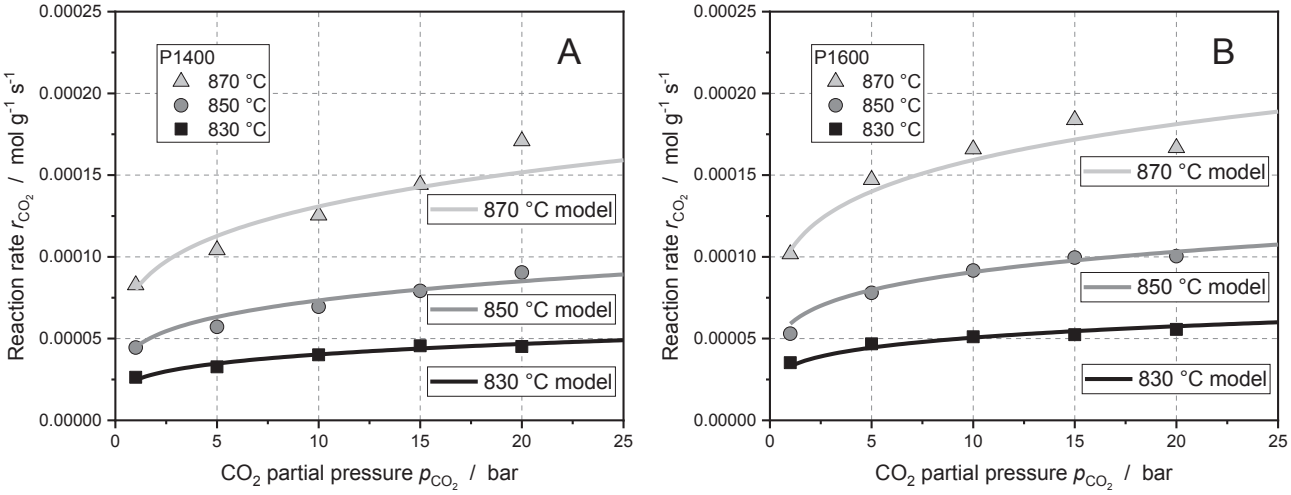

Fig. 10. Modeling of the gasification reaction with CO_2 for P1400 (A) and P1600 (B) using power law approach.

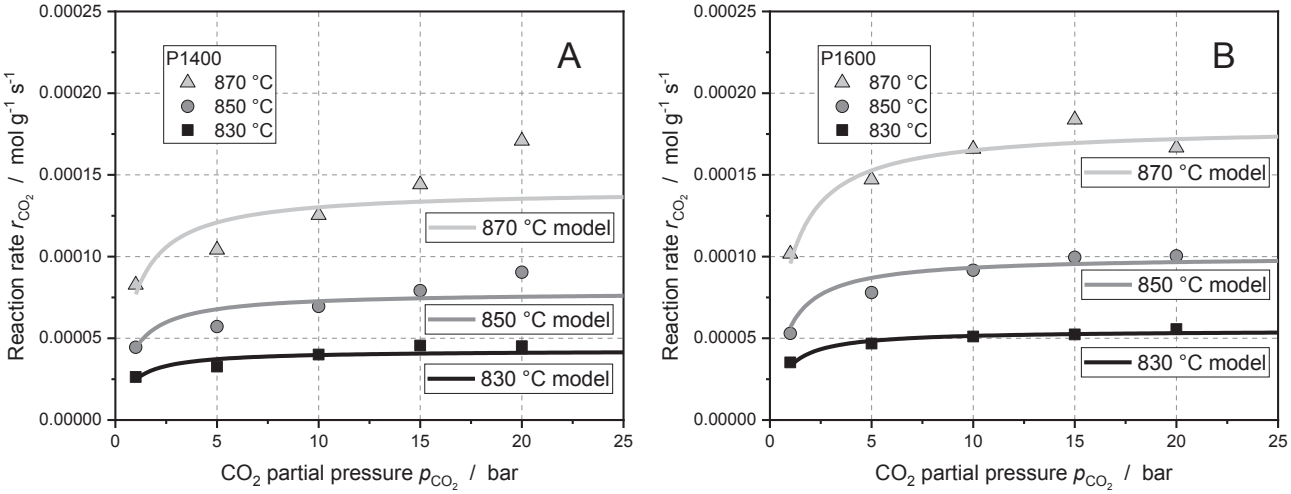

Fig. 11. Modeling of the gasification reaction with CO_2 for P1400 (A) and P1600 (B) using an LH approach.

Table 8
Kinetic parameters for the gasification of P1400 and P1600 with CO_2 using LH approach.

		P1400	P1600
$k_{0,1}$	mol (g s bar)$^{-1}$	$6.80 \cdot 10^{8}$	$2.1 \cdot 10^{7}$
$k_{0,3}$	mol (g s)$^{-1}$	$3.0348 \cdot 10^{10}$	$2.6775 \cdot 10^{10}$
$E_{A,1}$	kJ mol^{-1}	275.9	241.0
$E_{A,3}$	kJ mol^{-1}	313.7	310.2

partial pressures can be modeled precisely using LH approach. Almost all values for P1600 lie within 10% parity. The LH approach describes pressurized gasification of P1600 with CO_2 to full satisfaction.

In summary, it can be stated that the power law approach is suitable to describe gasification kinetics of both chars with CO_2 up to a total pressure of 20 bar. However, the saturation during gasification of P1600 applying high pressures ($p_{CO_2} > 10$ bar) cannot be modeled adequately. Here, the LH approach gives good results, whereas the linear increase of r_{CO_2} with increasing CO_2 partial pressure during gasification of P1400 is described very poorly using the LH approach.

3.2. Gasification experiments with H_2O

3.2.1. Raw data evaluation

Fig. 12 shows the CO and CO_2 volume fractions and carbon conversion curves during gasification of P1400 and P1600 at 830 °C in a mixture of H_2O and Ar. The total pressure was 2 bar while the partial pressure of H_2O was 0.4 bar (rest Ar). The carbon conversion $X_{C,gasif,H_2O}$ is calculated using Eq. (13). In general, H_2O gasification reaction was much faster compared to CO_2 gasification, as can also be seen in literature [25]. Even at H_2O partial pressures of only 0.4 bar and a gasification temperature of 830 °C, carbon conversion $X_{C,gasif,H_2O}$ reached approx. 0.8 within the first 60 min for both char samples. Furthermore, the course of product gas concentrations was rather constant up to a carbon conversion of 0.8 leading to a more linear conversion curve compared to gasification with CO_2. During H_2O gasification of P1400, CO_2 and CO volume fractions were similar at the beginning of the experiment. Both gas concentrations were diverging from each other up to 40 min gasification time. Here, namely at approx. 0.7 carbon conversion, an increase of y_{CO_2} was observed and followed by a steep decrease in both y_{CO} and y_{CO_2}. This decrease was always encountered during gasification with H_2O at a certain carbon conversion degree (mostly between 0.7 and 0.8) depending on the sample and the process conditions applied. The gasification process with H_2O should be considered as finished at this stage of the experiment. The course of the

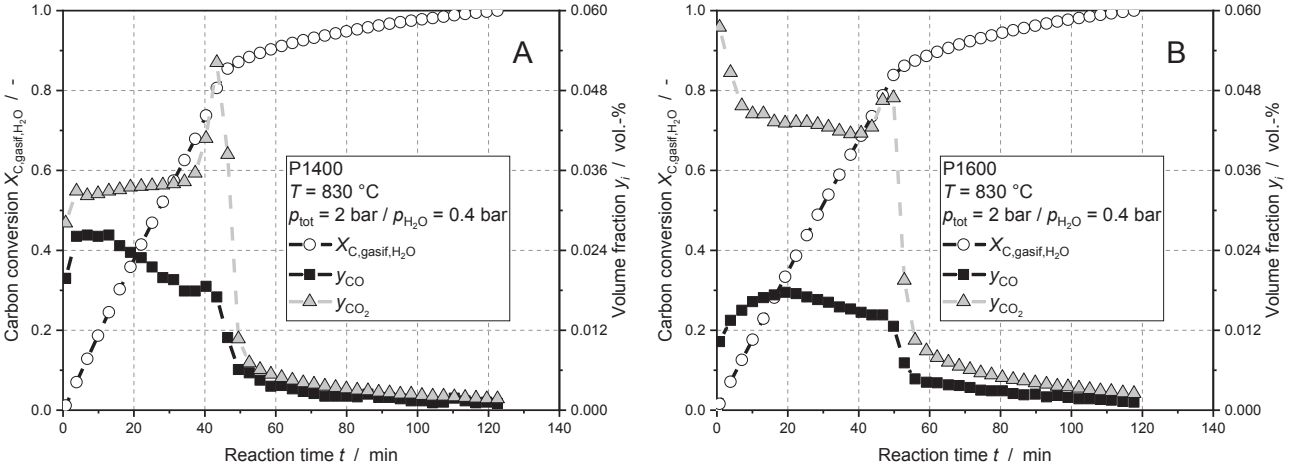

Fig. 12. CO volume fraction y_{CO}, CO_2 volume fraction y_{CO_2} and carbon conversion $X_{C,gasif,H_2O}$ during gasification of P1400 (A) and P1600 (B) with H_2O at 830 °C ($p_{H_2O} = 0.4$ bar, $p_{tot} = 2$ bar, diluting gas: argon).

product gas concentration may be caused by fragmentation of the char particles and back-mixing effects in the exhaust-gas line of the experimental set-up. Since H_2O gasification was much faster than CO_2, the volume fractions of the product gases decreased erratically from a higher level compared to CO_2 gasification where a steady decrease of CO concentration was observed. However, for the determination of initial conversion rates R_0, the experimental and methodological approach should deliver reasonable and reliable data.

Concerning gasification of P1600, again, at around 0.8 carbon conversion, a steep decrease in product gas concentration was observed suggesting that gasification was mainly terminated. Furthermore, CO_2 volume fraction was approx. 4 times the value of y_{CO}. Therefore, it was essential to consider all carbon containing product gases in order to determine a valid initial conversion rate R_0 because of possible changes in product gas concentration due to water–gas shift equilibrium. The existing set-up did not allow to measure the temperature profile of the lower part of the reactor. Therefore, slight differences in product gas concentration could occur because gas temperature at the exit of the reactor may have varied. For future experiments, the simple type K thermocouple recording char temperature will be substituted by a multipoint thermocouple that allows for the recording of a temperature profile in the lower part of the reactor including gas exit temperature.

3.2.2. Influence of temperature

Fig. 13 shows Arrhenius plots for the gasification of P1400 and P1600 with H_2O partial pressures between 0.2 bar and 5 bar and temperatures between 830 °C and 870 °C. Argon was used as carrier gas and H_2O volume fraction was set between 0.2 and 0.5 in the feed gas·H_2O Arrhenius plots can be subsumed since similar trends were observed for both char samples. As for gasification with CO_2, reactions rates r_{H_2O} increase with increasing temperature and reactant gas partial pressure. From the Arrhenius plots, no saturation at the highest pressures investigated can be deduced. The mean activation energy of the P1400 gasification experiments with H_2O was 263.6 kJ mol^{-1} being lower than activation energies for biogenic char-CO_2 gasification which is consistent with literature data [25]. The mean activation energy of the P1600 gasification experiments was slightly lower compared to P1400 and amounted to 234.8 kJ mol^{-1}. Both values for E_{A,H_2O} are also situated in the upper range of activation energies for biogenic char-H_2O gasification reported in literature [25]. Again, this may be an indication for the absence of diffusional effects and the determination of true microkinetics.

Fig. 14 shows an Arrhenius plot of P1400 and P1600 for H_2O partial pressures of 0.2 bar, 0.8 bar and 5 bar to facilitate the direct comparison between both char samples. It becomes apparent that P1400 shows

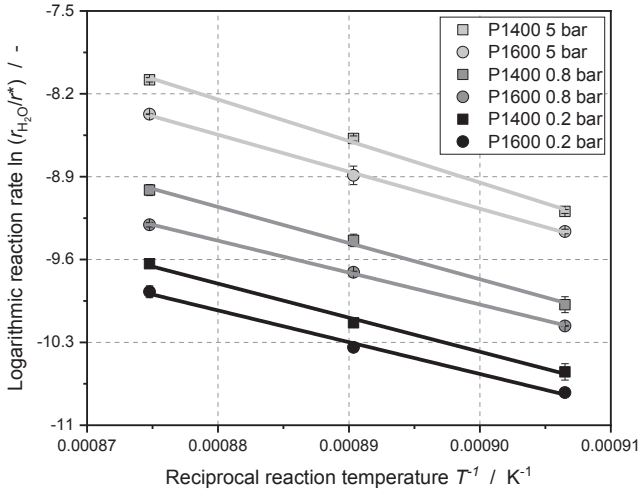

Fig. 14. Arrhenius plot for the gasification of P1400 and P1600 with H_2O (p_{H_2O} = 0.2 bar, 0.8 bar, 5 bar and T = 830–870 °C, diluting gas: argon).

higher reactivity towards H_2O than P1600 which is contrary to the results of CO_2 gasification. However, this finding is what would normally be expected from literature taking into account the higher pyrolysis temperatures of P1600 inducing thermal deactivation due to higher degrees of graphitization and lower micropore surface area. Therefore, it can be stated that the catalytically active CaO film being responsible for the higher initial conversion rates R_0 of P1600 during gasification with CO_2 is of minor significance when gasification is carried out with H_2O. Thus, the dominating char properties affecting H_2O reactivity were considered to be constitution of carbon matrix (i.e. graphitization degree) and micropore surface area.

3.2.3. Influence of total pressure and H_2O partial pressure

Fig. 15 shows an Arrhenius plot illustrating the influence of total pressure during H_2O gasification experiments. Gasification was conducted with P1400 using three different H_2O partial pressures (0.4 bar, 0.8 bar and 2 bar) and varying total pressures (1 bar, 2 bar, 5 bar and 10 bar). Results indicate that very similar reaction rates and activation energies were obtained using two different total pressures. Experiments with p_{H_2O} = 0.8 bar and total pressures of 2 bar and 5 bar, respectively deviated slightly more from each other. Generally, two reasons for possible deviations using different total pressures were identified. First, errors may arise due to higher dilution of product gases at high pressures. Since superficial linear gas velocity was constant during

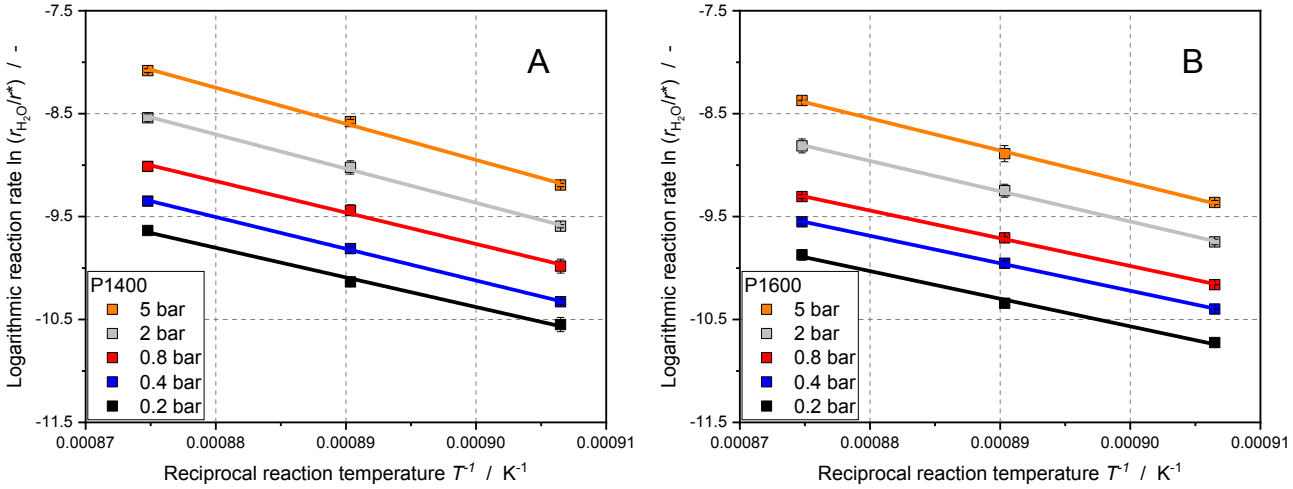

Fig. 13. Arrhenius plots for the gasification of P1400 (A) and P1600 (B) with H_2O (p_{H_2O} = 0.2–5 bar, y_{H_2O}= 0.2–0.5 and T = 830–870 °C, diluting gas: argon).

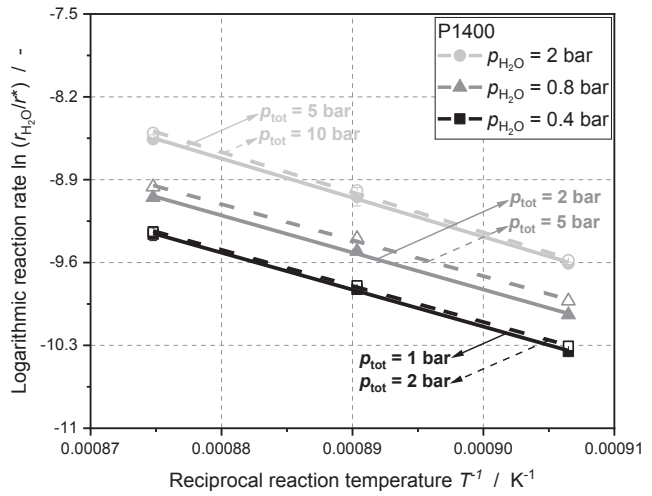

Fig. 15. Influence of total pressure on reaction rate r_{H_2O} during gasification of P1400 with H_2O (T = 830–870 °C, diluting gas: argon).

experiments, volumetric flow rates increased with increasing total pressure. Therefore, product gas concentrations were lower and more difficult to detect using the MicroGC during high pressure experiments. Another possible cause for deviations in the reaction rate determined may originate from absorption of product gases in the condensing water of the steam trap. The three most abundant product gases identified during H_2O gasification were H_2, CO and CO_2. H_2 and CO have relatively low solubility in water compared to CO_2 and may be negligible [47]. Furthermore, CO_2 volume fractions were found to be higher than CO in the exhaust gas suggesting that water–gas shift reaction took place to a certain extent. Increasing the total pressure would lead to significant absorption of CO_2 in water [48] resulting in removal of carbon from the system worsening carbon balance closure. Both phenomena would lead to a shorter reaction time und thus, higher reaction rates applying higher total pressures which is exactly what can be seen in Fig. 15. Consequently, reaction kinetic measurements with H_2O were conducted using rather low total pressures while keeping H_2O volume fractions y_{H_2O} between 0.4 and 0.5 during the experiments above atmospheric pressure.

Fig. 16 shows the reaction rates r_{H_2O} of P1400 and P1600 as a function of H_2O partial pressure. It can be concluded that P1400 exhibits higher reaction rates for all process conditions investigated during H_2O gasification presumably due to lower specific surface area and higher graphitization degree of P1600. Furthermore, no saturation at higher pressures was observed for both chars and the course of experimental data can be well described using a root function. Reaction kinetic modeling of H_2O gasification is presented in Section 3.2.4.

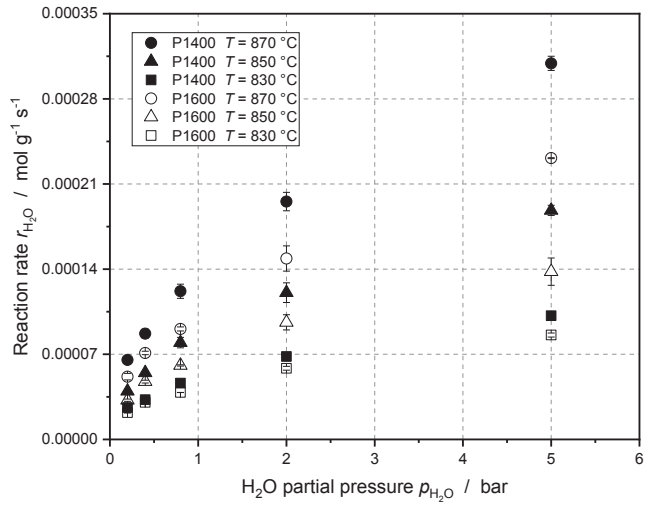

Fig. 16. Influence of H_2O partial pressure on reaction rate r_{H_2O} during gasification of P1400 and P1600 (T = 830–870 °C, diluting gas: argon).

3.2.4. Reaction kinetic modeling

Power law. Fig. 17 shows the experimentally determined reaction rates r_{H_2O} of P1400 and P1600 modeled with a power law approach (see Eq. (4)). The corresponding model parameters k_{0,H_2O}, E_{A,H_2O} and n_{H_2O} can be taken from Table 9. Results indicate that power law is a very suitable method for modeling pressurized char-H_2O gasification of both samples within the process conditions presented in this work. The quality of the power law model was again tested in a parity plot giving a very high goodness of fit. All experimental values determined during pressurized gasification of P1400 and P1600 with H_2O were at least within a deviation of ± 10% using the power law approach.

LH approach does not give good modeling results for both chars since saturation effects were not detected under the process conditions applied. Therefore, LH diagrams and the corresponding model parameters are not shown here but can be found in the supplementary data section.

Again, a comparison with kinetic parameters found in literature is conducted. Li et al. [46] investigated different coals (lignite, subbituminous coal, anthracite) in terms of reactivity towards CO_2 and H_2O in a fixed-bed reactor (cf. Section 3.1.4). For gasification with H_2O, the activation energies obtained with the shrinking core model were relatively low ranging between 114 kJ mol^{-1} and 138 kJ mol^{-1} as compared to the present work. The trend observed during CO_2 gasification concerning higher activation energies for higher rank coals is still valid for H_2O gasification. Furthermore, the reaction orders n during H_2O gasification (0.428–0.493) were similar to the ones presented in this work. The effect of coal rank on activation energy during gasification of different coal chars with H_2O in a fixed-bed reactor was also observed by Yan et al. [49].

Guizani et al. [23] obtained a relatively low activation energy of 139 kJ mol^{-1} during atmospheric gasification of beech wood char with H_2O (cf. Section 3.1.4) as compared to the present work. Again, the rather mild pyrolysis conditions may be an explanation for this discrepancy.

Roberts & Harris [50] and Matsuoka et al. [51] investigated the pressurized gasification reaction of various coal chars with H_2O and obtained activation energies in the range of 221 kJ mol^{-1} to 235 kJ mol^{-1} and 250 kJ mol^{-1}, respectively, both using the uniform conversion model. These activation energies are very similar to the ones presented in this work. Roberts & Harris [50] produced coal chars at 1100 °C with a residence time of 3 h and a low heating rate of 10 K min^{-1} and conducted the subsequent gasification experiments in a pressurized TGA. Matsuoka et al. [51] generated coal chars at 900 °C in a bubbling fluidized bed reactor where the gasification experiments with H_2O were conducted as well.

3.3. Gasification experiments in mixed H_2O/CO_2 atmospheres

3.3.1. Raw data evaluation

Fig. 18 shows the CO and H_2 volume fractions and carbon conversion curves during gasification of P1400 and P1600 at 830 °C in a mixture of CO_2, H_2O and argon. Total pressure was 5 bar while partial pressures of CO_2 and H_2O were 0.8 bar, respectively (rest argon). The carbon conversion $X_{C,gasif,mix}$ was calculated using Eq. (20). The main characteristics of the product gas concentrations during mixed gasification appear to be a superposition of both single atmosphere gasification experiments. First, H_2 and CO volume fractions decrease steadily up to carbon conversion degrees of approx. 0.8. Especially, the decrease of the product

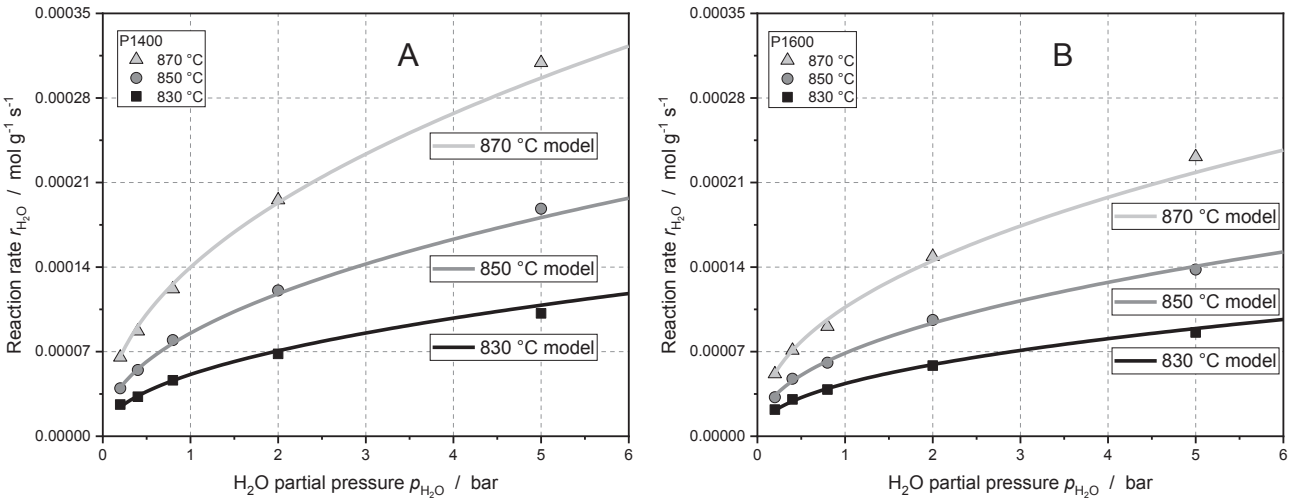

Fig. 17. Modeling of the gasification reaction with H_2O for P1400 (A) and P1600 (B) using power law approach.

Table 9
Reaction kinetic parameters for gasification of P1400 and P1600 with H_2O using power law approach.

		P1400	P1600
k_{0,H_2O}	mol (g s bar^n)$^{-1}$	$1.55 \cdot 10^8$	$5.7 \cdot 10^6$
E_{A,H_2O}	kJ mol^{-1}	263.6	234.8
n_{H_2O}	–	0.467	0.445

gas concentration during P1600 gasification with a steep slope reminds of the course of CO during single CO_2 gasification (see Fig. 5). This may be an indication that Ca catalysis is again dominating CO_2 gasification during mixed experiments [42,43]. The steady decrease in product gas concentration up to $X_{C,gasif,mix} = 0.8$ also leads to a less linear and more exponential shape of the carbon conversion curve of P1600. Second, the strong decrease at $X_{C,gasif,mix} = 0.8$ conversion degree is a characteristic of H_2O gasification experiments and may be caused by particle fragmentation and/or back-mixing effects in the experimental set-up.

3.3.2. *Influence of temperature and CO_2 partial pressure*

Fig. 19 shows an Arrhenius plot for mixed gasification of P1400 and P1600 using CO_2 and H_2O partial pressures of 0.8 bar, respectively. Total pressure was constant at 5 bar while reaction temperatures were varied between 810 °C and 850 °C. During mixed gasification at $p_{H_2O} = p_{CO_2} = 0.8$ bar and a total pressure of 5 bar, P1600 showed a higher reactivity than P1400 within the temperature range investigated. Activation energies for these conditions can be taken from Table 10, being very similar to the values determined for single H_2O gasification at $p_{H_2O} = 0.8$ bar. According to Ergun [52], the strongly temperature dependent desorption of the C(O) surface complex (see Eqs. (R3) and (R6)) is the rate limiting step during heterogeneous gasification reaction. Thus, one possible explanation for the similar activation energies during mixed and pure H_2O gasification could be that the desorption rate of the C(O) complex originating from CO_2 gasification (see Eq. (R3)) is significantly lower than desorption of the C(O) complex from H_2O reaction (see Eq. (R6)). This would also indicate that CO_2 and H_2O gasification reaction takes place at different carbon active sites C_f for the bio-chars and process conditions investigated.

Fig. 20A shows the reaction rates r_{mix} as a function of CO_2 partial pressure in the range of 0 bar to 5 bar for H_2O partial pressures of 0.8 and 2 bar, respectively. In addition, one set of experimental data is reported for $p_{CO_2} = p_{H_2O} = 5$ bar. Temperature was constant at 830 °C for all experiments. Total pressure varied between 5 and 20 bar, however, the effect of total pressure on reactivity can be neglected, as shown in Sections 3.1.3 and 3.2.3. The values for $p_{CO_2} = 0$ bar correspond to the H_2O gasification experiments reported in Section 3.2.

As already shown in Section 3.2, P1400 shows a higher reactivity

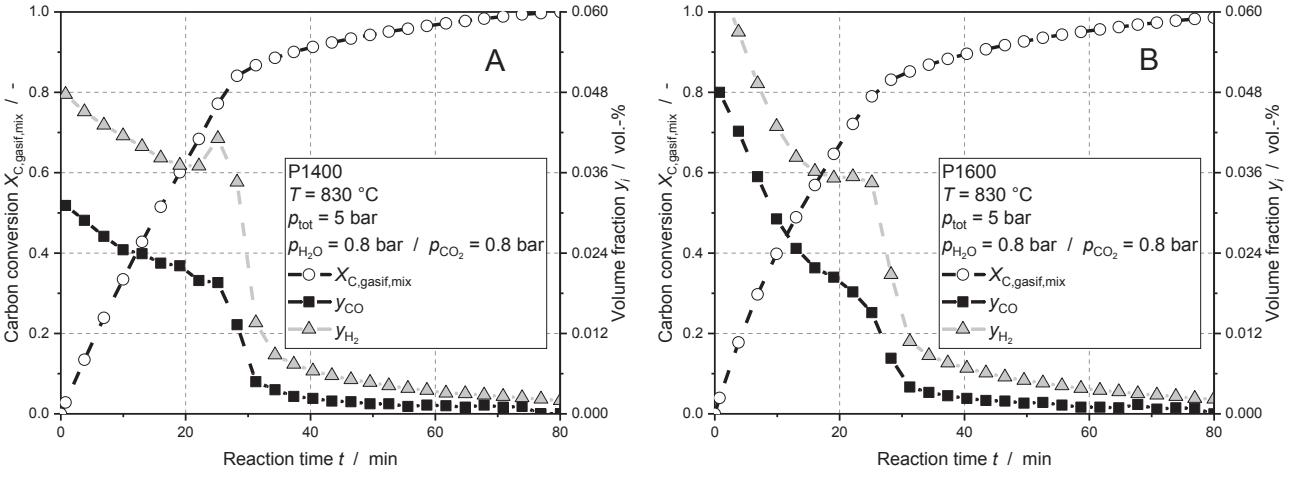

Fig. 18. CO volume fraction y_{CO}, H_2 volume fraction y_{H_2} and carbon conversion $X_{C,gasif,mix}$ during mixed gasification of P1400 (A) and P1600 (B) with H_2O and CO_2 at 830 °C ($p_{H_2O} = p_{CO_2} = 0.8$ bar, $p_{tot} = 5$ bar, diluting gas: argon).

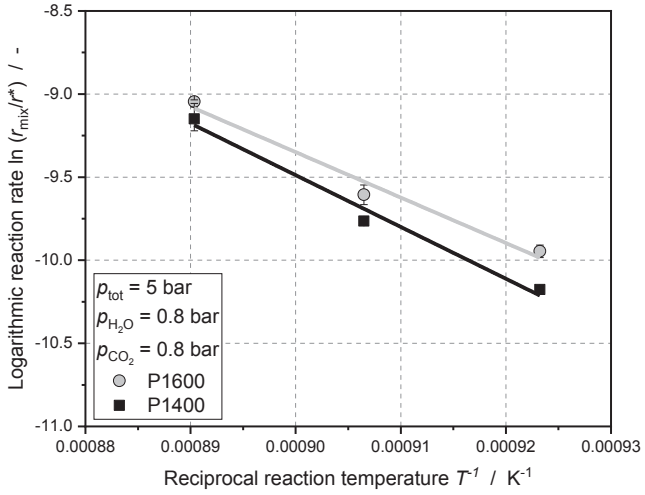

Fig. 19. Arrhenius plot for the gasification of P1400 and P1600 in a mixture of H_2O and CO_2 ($p_{H_2O} = p_{CO_2} = 0.8$ bar, $p_{tot} = 5$ bar and $T = 810–850$ °C, diluting gas: argon).

Table 10
Activation energies for mixed as well as pure H_2O and CO_2 gasification (both for $p_{H_2O} = 0.8$ bar) of P1400 and P1600.

		P1400	P1600
$E_{A,mix}$	kJ mol^{-1}	259.1	227.3
E_{A,H_2O}	kJ mol^{-1}	263.6	234.8
E_{A,CO_2}	kJ mol^{-1}	308.7	300.7

during gasification with H_2O ($p_{CO_2} = 0$ bar) as compared to P1600. For a CO_2 partial pressure of 0.8 bar, an increase in reaction rate r_{mix} for both chars at both H_2O partial pressure levels ($p_{H_2O} = 0.8$ bar and 2 bar) is detected. However, P1600 exhibits a stronger increase in reaction rate as compared to P1400 and becomes more reactive than P1400. For $p_{H_2O} = 0.8$ bar, both chars show a similar slope with increasing CO_2 partial pressure i.e. P1600 reactivity remains higher than P1400 reactivity. For $p_{H_2O} = 2$ bar, P1600 reaction rate r_{mix} remains almost constant for $p_{CO_2} > 0.8$ bar, whereas P1400 reactivity increases with CO_2 partial pressures at the same slope as for $p_{H_2O} = 0.8$ bar leading to a slightly higher reactivity at $p_{CO_2} = 5$ bar. At $p_{CO_2} = p_{H_2O} = 5$ bar, P1400 exhibits a significantly higher reaction rate r_{mix} as compared to P1600, which shows only a small increase in reactivity with increasing H_2O partial pressure from 2 bar to 5 bar.

Increasing the CO_2 partial pressure from 0 bar to 0.8 bar during mixed gasification leads to an increase in reaction rate r_{mix} for both chars which can be expressed by the addition of the single atmosphere reaction rates r_{CO_2} and r_{H_2O}. In Fig. 20B, the reaction rates r_{H_2O} and r_{CO_2} for single atmosphere gasification experiments at $p_{H_2O} = 0.8$ bar, 2 bar and $p_{CO_2} = 1$ bar, 5 bar are shown together with calculated values for r_{mix} using a simple addition of the single atmosphere reaction rates ($r_{mix} = r_{CO_2} + r_{H_2O}$). By this approach, the reaction rates for mixed gasification are reasonably modeled for the low pressure range up to $p_{CO_2} = 1$ bar and both chars, despite the fact that the experimental values are slightly overestimated for P1400. Thus, no competition between the H_2O and the CO_2 gasification reaction is observed in the low pressure range. Here, a separate active site mechanism might be valid for both chars. The strong increase of P1600 reactivity from $p_{CO_2} = 0$ bar to $p_{CO_2} = 0.8$ bar may be explained by the catalytic activity of the CaO film on the char surface selectively increasing the reactivity towards CO_2 (see Section 3.1).

At $p_{H_2O} = 2$ bar, however, the reaction rate r_{mix} of P1600 stagnates for CO_2 partial pressures above 0.8 bar (see Fig. 20A). The observed trend may be interpreted as saturation of reactant gases on the char surface since P1600 has a distinctly lower surface area as P1400 and – due to a higher graphitization degree – a lower amount of carbon active sites. Thus, morphology and graphitization might become more relevant for higher reactant gas partial pressures while Ca catalysis fades into the background. At high reactant gas partial pressures, a common reactive sites mechanism might be more adequate for P1600. Here, the simple addition of the single atmosphere reaction rates might become invalid. This thesis is fortified by the experimental results at $p_{CO_2} = p_{H_2O} = 5$ bar, where an inhibition of the P1600 reactivity is clearly visible as compared to P1400.

3.3.3. Reaction kinetic modeling

Experimental results from the previous chapter indicate that – for the chars and process conditions investigated – CO_2 and H_2O gasification occurs rather on separate than on same active sites except for the high pressure experiments with P1600. Therefore, simple approaches were used in order to model mixed gasification via addition of the single atmosphere reaction kinetics with the highest fit quality (see Sections 3.1.4 and 3.2.4). For pressurized CO_2 gasification, the power law approach was most suitable for P1400 while LH represented the

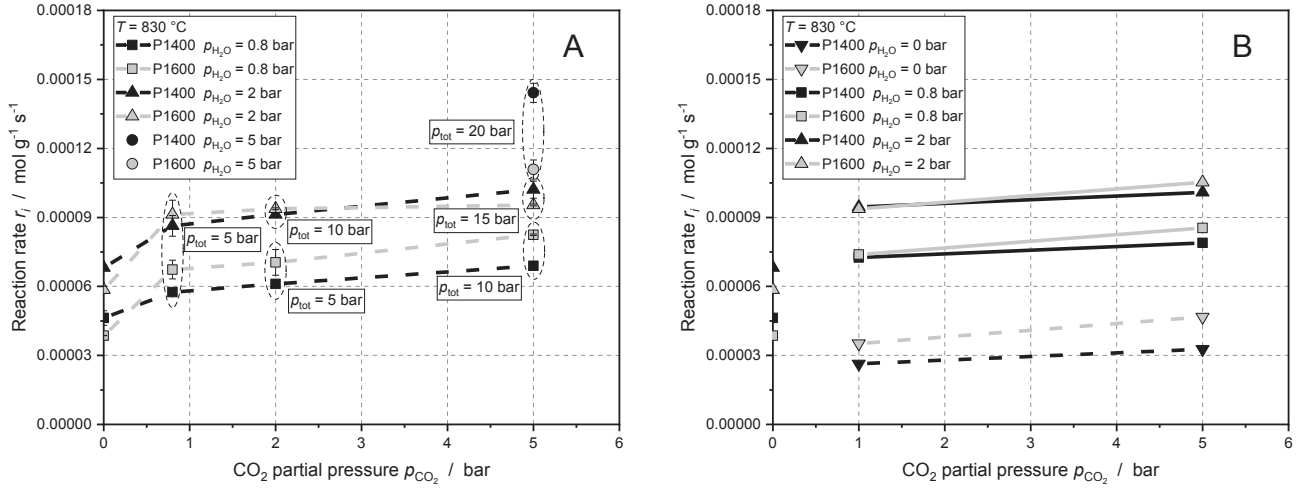

Fig. 20. (A) Reaction rates r_{mix} of P1400 and P1600 during mixed gasification at 830 °C for three H_2O partial pressures ($p_{H_2O} = 0.8$ bar, 2 bar, 5 bar and $p_{tot} = 5 – 20$ bar) as a function of p_{CO_2} as well as r_{H_2O} at $p_{H_2O} = 0.8$ bar, 2 bar. (B) Reaction rates r_{H_2O} and r_{CO_2} for single atmosphere gasification experiments at $p_{H_2O} = 0.8$ bar, 2 bar and $p_{CO_2} = 1$ bar, 5 bar; r_{mix} plotted as a simple addition of the single atmosphere reaction rates (symbols with solid line).

characteristics of P1600 very well especially in the high pressure range. In terms of H_2O gasification, both chars could be sufficiently modeled using the power law approach taking into account the lower reactant gas partial pressures investigated.

Fig. 21A shows the experimental reaction rates of P1400 for CO_2, H_2O and mixed atmosphere gasification together with the corresponding modeling approaches. Promoting a better understanding of the diagram, it is necessary to illustrate the reading of the axis of abscissae: Concerning mixed atmosphere gasification (black dots), both reactant gases had the same partial pressure i.e. $p_{H_2O} = p_{CO_2} = 0.8$ bar, 2 bar and 5 bar. The black line represents the model for mixed atmosphere gasification of P1400 calculated by an addition of both single atmosphere power laws. The remaining experimental values (grey boxes and triangles) are the reaction rates for single atmosphere gasification with the corresponding H_2O or CO_2 partial pressures, respectively.

The simple addition of the single atmosphere reaction kinetics gives a satisfying modeling of the mixed atmosphere gasification reaction for P1400 (see Fig. 21A). The experimental values are rather overestimated by the addition of the single atmosphere reaction kinetics. However, the conception of a separate carbon active sites reaction mechanism is significantly better represented as compared to the approach of same active sites, which is calculated according to the following LH based approach [53]:

$$r_{mix}\left(T, p_{H_2O}, p_{CO_2}\right) = \frac{k_1 p_{CO_2} + k_4 p_{H_2O}}{1 + \frac{k_1}{k_3} p_{CO_2} + \frac{k_4}{k_6} p_{H_2O}} \quad (27)$$

These findings correspond well with the results of Chen et al. [17] who gasified two lignite chars in mixed CO_2/H_2O atmospheres using TGA and fluidized bed. They reported that the gasification rate in CO_2/H_2O mixtures was lower than the sum of both rates but higher than the rate of each independent gasification reaction. Furthermore, the authors stated that char-H_2O reaction was independent from char-CO_2 reaction, what could also be observed for the experiments in the present work (see Section 3.3.2).

Fig. 21B shows the corresponding diagram for mixed atmosphere gasification of P1600. Here, the model approach is conducted using the addition of CO_2 LH kinetics and H_2O power law, since these approaches gave the best quality of fit for the char sample. In contrast to P1400, the addition of both single atmosphere kinetics only gives a satisfying modeling for reactant gas partial pressures up to $p_{H_2O} = p_{CO_2} = 2$ bar. It was already depicted in Fig. 20A (see Section 3.3.2) that the char surface of P1600 reaches a state of saturation applying high pressures resulting in a stagnation of r_{mix}. This phenomenon can also be seen in Fig. 21B at $p_{H_2O} = p_{CO_2} = 5$ bar where the addition of both single atmosphere kinetics becomes invalid and a saturation of the char surface can be assumed. These results also correspond well with the results of Li et al. [22] who gasified lignite with H_2O, CO_2 and its mixtures in a pressurized fixed bed reactor which is similar to the system used in this work. The authors reported that the separate active sites mechanism is valid for relatively low pressures. Moreover, their results indicate that the common active site mechanism becomes relevant applying higher reactant gas partial pressures.

Considering the results presented in this work, this thesis can be expanded in terms of high pressures and specific surface area and graphitization degree. For bio-chars with a rather low specific surface area and fewer carbon active sites – as it is the case for P1600 – a separate active site reaction mechanism is only valid in the low pressure range (up to $p_{H_2O} = p_{CO_2} = 2$ bar in the present work). In contrast to P1400, the char surface of P1600 shows a saturation applying high pressures where a common active site mechanism can be assumed. However, more mixed atmosphere experiments need to be conducted – especially in the high reactant gas partial pressure area – in order to further verify this thesis.

4. Summary and conclusions

The objective of the present work was to investigate the influence of pressure on the gasification kinetics for two beech wood chars that were produced at 1400 °C and 1600 °C at high-heating rates and short residence times in a drop-tube reactor. The gasification experiments presented in this work were conducted in a single-particle reactor with forced flow-through conditions reducing diffusional effects to a minimum. The interpretation of the experimentally determined reaction rates during gasification with CO_2, H_2O and its mixture is based on the char properties (graphitization, ash dispersion and morphology) presented in a previous publication [32]. Kinetic parameters for the gasification of both beech wood chars (P1400 and P1600) with CO_2 and H_2O at elevated pressure were derived using an nth-order and a Langmuir-Hinshelwood (LH) approach. Furthermore, gasification experiments in a mixture of CO_2 and H_2O were carried out in order to further clarify the dominating reaction mechanism during gasification of biomass chars in CO_2/H_2O containing atmospheres. A possible approach for the reaction kinetic modeling in mixtures of CO_2 and H_2O is presented for both biochars.

Dominating char properties affecting gasification reactivity with CO_2 and H_2O were found to be (i) specific surface area, (ii) graphitization degree and (iii) dispersion of catalytic ash components. Due to the higher pyrolysis temperature of P1600, this char showed a higher graphitization degree (lower amount of carbon active sites) and a lower specific surface area as compared to P1400. Furthermore, a thin

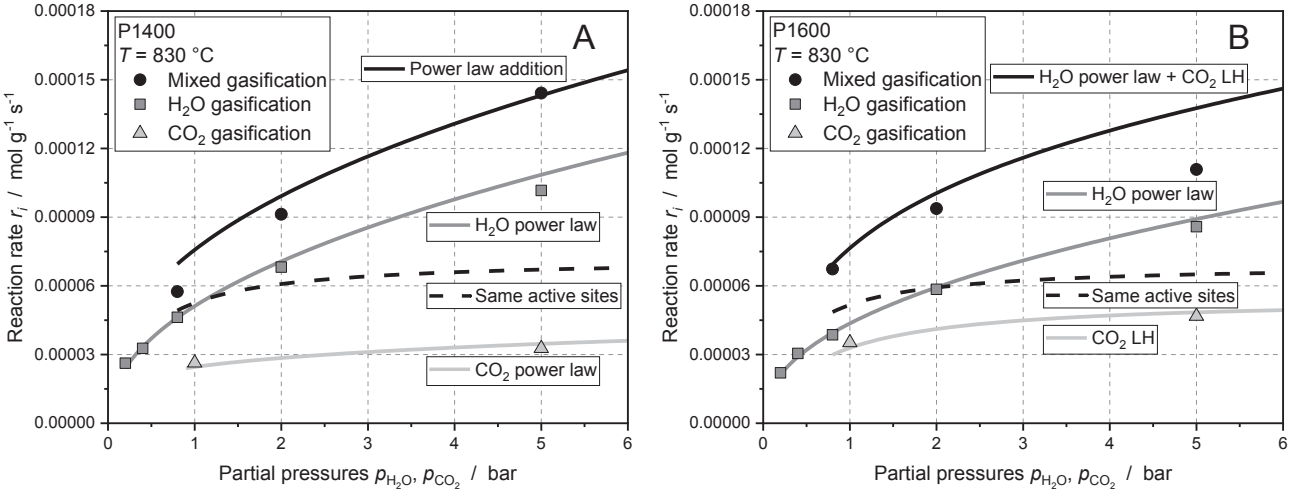

Fig. 21. Modeling approaches for the mixed H_2O/CO_2 gasification of P1400 (A) and P1600 (B) using an addition of the single atmosphere reaction kinetics.

catalytically active CaO layer formed on the surface of P1600 leading to an increased reactivity towards CO_2 [32].

4.1. Gasification with CO_2

P1600 shows higher reactivity as compared to P1400 for all CO_2 partial pressures and temperatures applied. However, for the highest CO_2 partial pressure applied (20 bar), both chars show similar reactivity. The higher reactivity of P1600 during CO_2 gasification may be explained by the CaO film on the char surface catalyzing the char-CO_2 gasification reaction [32]. A power law approach is suitable to describe gasification kinetics of both chars with CO_2 up to pressures of 20 bar. However, the observed saturation during gasification of P1600 applying high CO_2 partial pressures is better described by a LH approach.

4.2. Gasification with H_2O

P1400 shows higher reactivity towards H_2O as compared to P1600 which is expected from the char specifications reported above. The dominating char properties affecting H_2O reactivity were considered to be constitution of carbon matrix (i.e. graphitization degree) and micropore surface area. The catalytically active CaO film is of minor relevance when gasification is carried out with H_2O. Modeling of pressurized char-H_2O gasification kinetics of both samples was achieved using a power law approach to full satisfaction within the process conditions applied.

4.3. Gasification in mixed CO_2/H_2O atmosphere

Increasing the CO_2 partial pressure from 0 bar to 0.8 bar during mixed gasification leads to an increase in reaction rate r_{mix} for both chars which can be expressed by the addition of the single atmosphere reaction rates r_{CO_2} and r_{H_2O}. Thus, no competition between the H_2O and the CO_2 gasification reaction is observed in this low pressure range. Here, a separate active site mechanism might be valid for both chars. The strong increase of P1600 reactivity from $p_{CO_2} = 0$ bar to $p_{CO_2} = 0.8$ bar may be explained by the catalytic activity of the CaO film on the char surface selectively increasing the reactivity towards CO_2. At $p_{H_2O} = 2$ bar, the reaction rate r_{mix} of P1600 stagnates for CO_2 partial pressures above 0.8 bar. The observed trend may be interpreted as saturation of reactant gases on the char surface since P1600 has a distinctly lower surface area as P1400 and – due to a higher graphitization degree – a lower amount of carbon active sites. Thus, morphology and graphitization might become more relevant for higher reactant gas partial pressures while Ca catalysis fades into the background. At high reactant gas partial pressures, a common reactive sites mechanism might be more adequate for P1600. This thesis is fortified by the experimental results at $p_{CO_2} = p_{H_2O} = 5$ bar, where an inhibition of the P1600 reactivity is clearly visible as compared to P1400.

Concerning a possible modeling approach for mixed gasification, the addition of the single atmosphere reaction kinetics gives satisfying results for P1400. The experimental values are slightly overestimated by the addition of the single atmosphere reaction kinetics. However, the conception of a separate carbon active sites reaction mechanism is significantly better represented as compared to the approach of competing active sites.

In contrast to P1400, the addition of both single atmosphere kinetics of P1600 for modeling of mixed gasification gives satisfying results only in the low pressure range. The char with the lower specific surface area and the higher graphitization degree (P1600) reaches a saturated state earlier when applying higher reactant gas partial pressures. Therefore, the addition of both single atmosphere kinetics becomes invalid and a common active site mechanism might be relevant.

Considering the experimental results for mixed gasification presented in this work, the following conclusions can be drawn:

- Increasing the CO_2 partial pressure during mixed gasification leads to higher reactivity for both chars. The reaction rate r_{mix} can be expressed by addition of the single atmosphere reaction rates in the low pressure area suggesting a separate active site mechanism.
- Catalytic activity of CaO increases the reaction rate r_{mix} of P1600 distinctively for lower H_2O and CO_2 partial pressures.
- For higher H_2O and CO_2 partial pressures, P1600 reactivity stagnates due to lower specific surface area and higher graphitization degree i. e. lower amount of carbon active sites. Here, a common active sites mechanism can be assumed.

5. Glossary

Symbol	Description	Unit
a, b, c	Global reaction rates for mixed CO_2/H_2O gasification	mol s^{-1}
D_{AB}	Binary diffusion coefficient	m^2 s^{-1}
D_{CaO}	Dispersion of superficial calcium oxide	mol g^{-1}
$\frac{dX}{dt}$	Conversion rate	s^{-1}
E_A	Activation energy	kJ mol^{-1}
$F(X_C)$	Structural term	–
k_0	Pre-exponential factor	s^{-1} bar^{-n}
L_a	Radial expansion of graphene layers	m
$L_{a,0}$	Radial expansion of graphene layers of primary char	m
k_j	Arrhenius rate coefficient	Various
M_C	Molar mass of carbon	g mol^{-1}
$m_{C,gasif}$	Gasified mass of carbon	g
$m_{C,0}$	Initial mass of fixed carbon	g
$m_C(t)$	Remaining carbon mass at a certain time t	g
m_{char}	Char mass	g
m_{Sample}	Sample mass	g
n	Reaction order	–
$\dot{n}$	Molar flow rate	mol s^{-1}
$\dot{n}_{C,out}$	Molar flow rate of carbon containing gasification product gases	mol s^{-1}
$\dot{n}_{out}$	Molar flow rate of gasification product gases	mol s^{-1}
p	System pressure	bar
p_i	Partial pressure of component i	bar
p_{tot}	Total pressure	bar
$R(T,p)$	Chemical rate coefficient	s^{-1}
R_0	Initial conversion rate	s^{-1}
R_U	Universal gas constant	J mol^{-1} K^{-1}
R_X	Conversion rate	s^{-1}
r^*	Dummy reaction rate ($r^* = 1$ mol g^{-1} s^{-1})	mol g^{-1} s^{-1}
r_i	Reaction rate ($i = CO_2$, H_2O, mix)	mol g^{-1} s^{-1}
T	Temperature	K
t	Time	s
v_{gas}	Superficial linear gas velocity	m s^{-1}
V	Volume	m^3
$\dot{V}$	Volume flow rate	m^3 s^{-1}
V	Molar volume	m^3 mol^{-1}
Xc	Carbon conversion	–
$x_{C,fix}$	Mass fraction of fixed carbon	–
y_i	Volume fraction of component i	–
y_i	Molar fraction of component i	–

Subscripts	Description
C	Carbon
C,fix	Fixed Carbon
CO	Carbon monoxide molecule
CO_2	Concerning CO_2 gasification
end	End of experiment
f	Fixed carbon (in chemical reaction equation)
gasif	Gasified
H_2	Hydrogen molecule
H_2O	Concerning H_2O gasification
i	Control variable
j	Control variable
mix	Concerning mixed gasification in CO_2/H_2O atmosphere
N_2	Nitrogen molecule
surface-CaO	Superficial calcium oxide

Abbreviations	Description
ad	Air-dried
BY	Bypass
CEM	Controlled evaporation and mixing unit
CORI	Coriolis flow controller
daf	Dry ash free
DFG	Deutsche Forschungsgemeinschaft
diff	Determined by difference
EMR	Energy, materials and resources
EFG	Entrained-flow gasification
Eq.	Equation
Fig.	Figure
GC	Gas chromatograph
HGF	Helmholtz-Gemeinschaft Deutscher Forschungszentren
ICP-OES	Inductively coupled plasma optical emission spectrometry
IGCC	Integrated Gasification Combined Cycle
IR	Infrared spectroscopy
KIT	Karlsruhe Institute of Technology
LH	Langmuir-Hinshelwood
MFC	Mass flow controller
P1400, P1600	Chars produced at 1400 °C and 1600 °C
ppm	Parts per million
PTFE	Polytetrafluoroethylene
SEM	Scanning electron microscope
TEM	Transmission electron microscope
TGA	Thermogravimetric analyzer
TPR	Temperature-programmed reaction
UCM	Uniform Conversion Model
vol.	Volume
WGS	Water-gas shift reaction
wt.	Weight
XRD	X-ray diffraction

CRediT authorship contribution statement

Christoph Schneider: Conceptualization, Methodology, Validation, Investigation, Data curation, Writing - original draft, Visualization, Supervision, Project administration. **Michael Zeller:** Methodology, Validation, Investigation, Data curation, Writing - review & editing, Visualization. **Daniel Böhm:** Methodology, Validation, Investigation, Data curation, Writing - review & editing, Visualization. **Thomas Kolb:** Resources, Writing - review & editing, Supervision.

Declaration of Competing Interest

The authors declare that they have no known competing financial interests or personal relationships that could have appeared to influence the work reported in this paper.

Acknowledgments

The authors gratefully acknowledge the financial support by the Deutsche Forschungsgemeinschaft (DFG) (121384/22-1) and the Helmholtz Association of German Research Centers (HGF), within the research program Energy Efficiency, Materials and Resources (EMR). The present work contributes to the Helmholtz Virtual Institute for Gasification Technology - HVIGasTech (VH-VI-429, http: //www.hvi-gastech.org/).

Appendix A. Supplementary data

Supplementary data associated with this article can be found, in the online version, at https://doi.org/10.1016/j.fuel.2021.120523.

References

[1] Dahmen N, Abeln J, Eberhard M, Kolb T, Leibold H, Sauer J, et al. The bioliq process for producing synthetic transportation fuels. WIREs Energy Environ 2017;6 (3). https://doi.org/10.1002/wene.236.
[2] Higman C, others. State of the gasification industry-the updated worldwide gasification database. In: Gasification Technology Conference, Colorado Springs; 2013.
[3] Kolb T, Aigner M, Kneer R, Müller M, Weber R, Djordjevic N. Tackling the challenges in modelling entrained-flow gasification of low-grade feedstock. J Energy Inst 2016;89(4):485–503. https://doi.org/10.1016/j.joei.2015.07.007.
[4] Liu G-S, Niksa S. Coal conversion submodels for design applications at elevated pressures. Part II. Char gasification. Prog Energy Combust Sci 2004;30(6):679–717. https://doi.org/10.1016/j.pecs.2004.08.001.
[5] Lu L. Char structural ordering during pyrolysis and combustion and its influence on char reactivity. Fuel 2002;81(9):1215–25. https://doi.org/10.1016/S0016-2361(02)00035-2.
[6] Lobo LS, Carabineiro SAC. Kinetics and mechanism of catalytic carbon gasification. Fuel 2016;183:457–69. https://doi.org/10.1016/j.fuel.2016.06.115.
[7] Bai J, Li W, Li C-z, Bai Z, Li B. Influences of minerals transformation on the reactivity of high temperature char gasification. Fuel Process Technol 2010;91(4): 404–9. https://doi.org/10.1016/j.fuproc.2009.05.017.
[8] Wang Y-L, Zhu S-H, Gao M-Q, Yang Z-R, Yan L-J, Bai Y-H, et al. A study of char gasification in H2O and CO2 mixtures: Role of inherent minerals in the coal. Fuel Process Technol 2016;141:9–15. https://doi.org/10.1016/j.fuproc.2015.06.001.
[9] Laurendeau NM. Heterogeneous kinetics of coal char gasification and combustion. Prog Energy Combust Sci 1978;4(4):221–70. https://doi.org/10.1016/0360-1285(78)90008-4.
[10] Blackwood JD, Ingeme AJ. The reaction of carbon with carbon dioxide at high pressure. Aust J Chem 1960;13(2):194. https://doi.org/10.1071/CH9600194.
[11] Roberts DG, Harris DJ. A kinetic analysis of coal char gasification reactions at high pressures. Energy Fuels 2006;20(6):2314–20. https://doi.org/10.1021/ef060270o.
[12] Hüttinger KJ, Merdes WF. The carbon-steam reaction at elevated pressure: Formations of product gases and hydrogen inhibitions. Carbon 1992;30(6):883–94. https://doi.org/10.1016/0008-6223(92)90011-K.
[13] Barrio M, Gøbel B, Risnes H, Henriksen UB, Hustad JE, Sørensen LH. Steam gasification of wood char and the effect of hydrogen inhibition on the chemical kinetics. In: Conference on progress in thermochemical biomass conversion; 2000.
[14] Roberts DG, Harris DJ. Char gasification in mixtures of CO2 and H2O: Competition and inhibition. Fuel ;86(17–18):2672–8. https://doi.org/10.1016/j.fuel.2007.03.019.
[15] Goyal A, Zabransky RF, Rehmat A. Gasification kinetics of Western Kentucky bituminous coal char. Ind Eng Chem Res 1989;28(12):1767–78. https://doi.org/10.1021/ie00096a006.
[16] Mühlen H-J, van Heek KH, Jüntgen H. Kinetic studies of steam gasification of char in the presence of H2, CO2 and CO. Fuel 1985;64(7):944–9. https://doi.org/10.1016/0016-2361(85)90149-8.
[17] Chen C, Wang J, Liu W, Zhang S, Yin J, Luo G et al. Effect of pyrolysis conditions on the char gasification with mixtures of CO2 and H2O. Proceedings of the Combustion Institute 2013;34(2):2453–60. doi:10.1016/j.proci.2012.07.068.
[18] Chen C, Zhang S, Xu K, Luo G, Yao H. Experimental and Modeling Study of Char Gasification with Mixtures of CO2 and H2O. Energy Fuels 2015;30(3):1628–35. https://doi.org/10.1021/acs.energyfuels.5b02294.
[19] Huang Z, Zhang J, Zhao Y, Zhang H, Yue G, Suda T, et al. Kinetic studies of char gasification by steam and CO2 in the presence of H2 and CO. Fuel Process Technol 2010;91(8):843–7. https://doi.org/10.1016/j.fuproc.2009.12.020.
[20] Everson RC, Neomagus HWJP, Kasaini H, Njapha D. Reaction kinetics of pulverized coal-chars derived from inertinite-rich coal discards: Gasification with carbon dioxide and steam. Fuel 2006;85(7–8):1076–82. https://doi.org/10.1016/j.fuel.2005.10.016.
[21] Guizani C, Escudero Sanz FJ, Salvador S. Influence of temperature and particle size on the single and mixed atmosphere gasification of biomass char with H2O and CO2. Fuel Process Technol 2015;134:175–88. https://doi.org/10.1016/j.fuproc.2015.01.031.
[22] Li F, Yan Q, Huang J, Zhao J, Fang Y, Wang J. Lignite-char gasification mechanism in mixed atmospheres of steam and CO2 at different pressures. Fuel Process Technol 2015;138:555–63. https://doi.org/10.1016/j.fuproc.2015.06.035.
[23] Guizani C, Escudero Sanz FJ, Salvador S. The gasification reactivity of high-heating-rate chars in single and mixed atmospheres of H2O and CO2. Fuel 2013; 108:812–23. https://doi.org/10.1016/j.fuel.2013.02.027.
[24] Irfan MF, Usman MR, Kusakabe K. Coal gasification in CO2 atmosphere and its kinetics since 1948: A brief review. Energy 2011;36(1):12–40. https://doi.org/10.1016/j.energy.2010.10.034.
[25] Di Blasi C. Combustion and gasification rates of lignocellulosic chars. Prog Energy Combust Sci 2009;35(2):121–40. https://doi.org/10.1016/j.pecs.2008.08.001.
[26] Senneca O, Salatino P, Masi S. Microstructural changes and loss of gasification reactivity of chars upon heat treatment. Fuel 1998;77(13):1483–93. https://doi.org/10.1016/S0016-2361(98)00056-8.
[27] Senneca O, Apicella B, Russo C, Cerciello F, Salatino P, Heuer S, et al. Pyrolysis and thermal annealing of coal and biomass in CO2-rich atmospheres. Energy Fuels 2018;32(10):10701–8. https://doi.org/10.1021/acs.energyfuels.8b02417.
[28] Tremel A, Spliethoff H. Gasification kinetics during entrained flow gasification – Part I Devolatilisation and char deactivation. Fuel 2013;103:663–71. https://doi.org/10.1016/j.fuel.2012.09.014.

[29] Cetin E, Moghtaderi B, Gupta R, Wall TF. Influence of pyrolysis conditions on the structure and gasification reactivity of biomass chars. Fuel 2004;83(16):2139–50. https://doi.org/10.1016/j.fuel.2004.05.008.
[30] Radovic LR, Steczko K, Walker PL, Jenkins RG. Combined effects of inorganic constituents and pyrolysis conditions on the gasification reactivity of coal chars. Fuel Process Technol 1985;10(3):311–26. https://doi.org/10.1016/0378-3820(85)90038-4.
[31] Cazorla-Amoros D, Linares-Solano A, Salinas-Martinez de Lecea C, Nomura M, Yamashita H, Tomita A. Local structure of calcium species dispersed on carbon: Influence of the metal loading procedure and its evolution during pyrolysis. Energy Fuels 1993;7(5):625–31. https://doi.org/10.1021/ef00041a010.
[32] Schneider C, Walker S, Phounglamcheik A, Umeki K, Kolb T. Effect of calcium dispersion and graphitization during high-temperature pyrolysis of beech wood char on the gasification rate with CO2. Fuel 2021;283. https://doi.org/10.1016/j.fuel.2020.118826.
[33] Ollero P. Diffusional effects in TGA gasification experiments for kinetic determination. Fuel 2002;81(15):1989–2000. https://doi.org/10.1016/S0016-2361(02)00126-6.
[34] Nowak B, Karlström O, Backman P, Brink A, Zevenhoven M, Voglsam S, et al. Mass transfer limitation in thermogravimetry of biomass gasification. J Therm Anal Calorim 2013;111(1):183–92. https://doi.org/10.1007/s10973-012-2400-9.
[35] Stoesser P, Schneider C, Kreitzberg T, Kneer R, Kolb T. On the influence of different experimental systems on measured heterogeneous gasification kinetics. Appl Energy 2018;211:582–9. https://doi.org/10.1016/j.apenergy.2017.11.037.
[36] Wu X, Wang J. K2CO3-catalyzed steam gasification of ash-free coal char in a pressurized and vertically blown reactor. Influence of pressure on gasification rate and gas composition. Fuel Process Technol 2017;159:9–18. https://doi.org/10.1016/j.fuproc.2017.01.001.
[37] Bouraoui Z, Dupont C, Jeguirim M, Limousy L, Gadiou R. CO2 gasification of woody biomass chars: the influence of K and Si on char reactivity. C R Chim 2016;19(4):457–65. https://doi.org/10.1016/j.crci.2015.08.012.
[38] Dupont C, Nocquet T, Da Costa JA, Verne-Tournon C. Kinetic modelling of steam gasification of various woody biomass chars: influence of inorganic elements. Bioresour Technol 2011;102(20):9743–8. https://doi.org/10.1016/j.biortech.2011.07.016.
[39] Linares-Solano A, Almela-Alarcón M, Lecea CS-Md. CO2 chemisorption to characterize calcium catalysts in carbon gasification reactions. J Catal 1990;125(2):401–10. https://doi.org/10.1016/0021-9517(90)90313-9.
[40] Laine NR, Vastola FJ, Walker Jr PL. The importance of active surface area in the carbon-oxygen reaction. J Phys Chem 1963;67(10):2030–4.
[41] Levenspiel O. The chemical reactor omnibook. 5th ed. Corvallis, Or: OSU Book Stores Inc; 1996.
[42] P. W. J. Struis R, Scala C von, Stucki S, Prins R. Gasification reactivity of charcoal with CO2. Part II: Metal catalysis as a function of conversion. Chemical Engineering Science 2002;57(17):3593–602. doi:10.1016/S0009-2509(02)00255-5.
[43] Cazorla-Amoros D, Linares-Solano A, Salinas-Martinez de Lecea C, Yamashita H, Kyotani T, Tomita A, et al. XAFS and thermogravimetry study of the sintering of calcium supported on carbon. Energy Fuels 1993;7(1):139–45.
[44] Fermoso J, Stevanov C, Moghtaderi B, Arias B, Pevida C, Plaza MG, et al. High-pressure gasification reactivity of biomass chars produced at different temperatures. J Anal Appl Pyrol 2009;85(1–2):287–93. https://doi.org/10.1016/j.jaap.2008.09.017.
[45] Cetin E, Moghtaderi B, Gupta R, Wall TF. Biomass gasification kinetics: influences of pressure and char structure. Combust Sci Technol 2006;177(4):765–91. https://doi.org/10.1080/00102200590917266.
[46] Li C, Zhao J, Fang Y, Wang Y. Effect of pressure on gasification reactivity of three Chinese coals with different ranks. Front Chem Eng China 2010;4(4):385–93. https://doi.org/10.1007/s11705-010-0501-1.
[47] Sander R. Compilation of Henry's law constants (version 4.0) for water as solvent. Atmos Chem Phys 2015;15(8):4399–981.
[48] Elstner M. Physikalische Chemie I: Thermodynamik und Kinetik. Berlin, Heidelberg: Springer Spektrum; 2017.
[49] Yan Q, Huang J, Zhao J, Li C, Xia L, Fang Y. Investigation into the kinetics of pressurized steam gasification of chars with different coal ranks. J Therm Anal Calorim 2014;116(1):519–27. https://doi.org/10.1007/s10973-013-3492-6.
[50] Roberts DG, Harris DJ. Char Gasification with O2, CO2, and H2O: effects of pressure on intrinsic reaction kinetics. Energy Fuels 2000;14(2):483–9. https://doi.org/10.1021/ef9901894.
[51] Matsuoka K, Kajiwara D, Kuramoto K, Sharma A, Suzuki Y. Factors affecting steam gasification rate of low rank coal char in a pressurized fluidized bed. Fuel Process Technol 2009;90(7–8):895–900. https://doi.org/10.1016/j.fuproc.2009.04.001.
[52] Ergun S. Kinetics of the reactions of carbon dioxide and steam with coke. US Government Printing Office 1962.
[53] Wang Y, Bell DA. Competition between H2O and CO2 during the gasification of Powder River Basin coal. Fuel 2017;187:94–102. https://doi.org/10.1016/j.fuel.2016.08.109.

Fuel 283 (2021) 118826

Contents lists available at ScienceDirect

Fuel

journal homepage: www.elsevier.com/locate/fuel

Full Length Article

Effect of calcium dispersion and graphitization during high-temperature pyrolysis of beech wood char on the gasification rate with CO_2

Christoph Schneider[a,*], Stella Walker[a], Aekjuthon Phounglamcheik[b], Kentaro Umeki[b], Thomas Kolb[a,c]

[a] Karlsruhe Institute of Technology, Engler-Bunte-Institute, Fuel Technology, EBI ceb, Engler-Bunte-Ring 1, 76131 Karlsruhe, Germany
[b] Luleå University of Technology, Department of Engineering Sciences and Mathematics, Division of Energy Science, 97187 Luleå, Sweden
[c] Karlsruhe Institute of Technology, Institute for Technical Chemistry, ITC vgt, Hermann-von-Helmholtz-Platz 1, 76344 Eggenstein-Leopoldshafen, Germany

ARTICLE INFO

Keywords:
Biomass char
Pyrolysis
Gasification
Graphitization
Ash dispersion

ABSTRACT

This paper presents thermal deactivation of beech wood chars during secondary pyrolysis in a drop-tube reactor. Pyrolysis temperature was varied between 1000 °C and 1600 °C at a constant residence time of 200 ms. The effect of pyrolysis conditions on initial conversion rate R_0 during gasification, graphitization of the carbon matrix and ash morphology was investigated. Gasification experiments for the determination of R_0 were conducted in a thermogravimetric analyzer using pure CO_2 at 750 °C and isothermal conditions. A linear decrease in initial conversion rate R_0 was observed between 1000 °C and 1400 °C. However, a strong increase of R_0 at 1600 °C was encountered. Micropore surface area of the secondary chars showed no correlation with the initial conversion rate R_0 during gasification with CO_2. Graphitization of the carbon matrix was determined using X-ray diffraction and Raman spectroscopy suggesting the growth of aromatic clusters and graphite-like structures for increasing pyrolysis temperatures up to 1600 °C. Furthermore, CaO dispersion was analyzed quantitatively and qualitatively using temperature-programmed reaction at 300 °C as well as SEM/TEM. CaO dispersion D_{CaO} decreases steadily between 1000 °C and 1400 °C whereas a strong increase can be observed at 1600 °C, which is in good accordance with the development of the initial conversion rate R_0 as a function of pyrolysis temperature. SEM/TEM images indicate the formation of a thin CaO layer at 1600 °C that is presumably responsible for the strong increase in initial conversion rate R_0 at this temperature. When excluding the catalytic activity of CaO via formation of the ratio $R_0\ D_{CaO}{}^{-1}$, increasing graphitization degree has a linear negative influence on char reactivity at pyrolysis temperatures between 1000 °C and 1400 °C.

1. Introduction

The use of low-grade biogenic and fossil fuels in high-pressure entrained-flow gasification (EFG) allows for the production of high-quality synthesis gas, which can be converted into fuels and chemicals or used for power generation via integrated gasification combined cycle (IGCC) systems. In the near future, EFG will play an important role in satisfying the demand for basic chemicals and power [1,2]. In EFG, the fuel is converted via thermal and thermo-chemical processes i.e. drying and pyrolysis under high heating rates as well as the subsequent heterogeneous gasification reactions of the resulting char in a CO_2- and H_2O-rich atmosphere. For the achievement of high cold gas efficiencies, a complete char conversion is desired. Since the heterogeneous reactions are considered as the rate-limiting step for complete fuel conversion, the knowledge of the gasification kinetics is essential for the design of entrained-flow gasifiers [3].

2. Literature review

During the pyrolysis step in the flame zone of the entrained-flow gasifier, the char undergoes various changes concerning chemical and physical properties of both carbon matrix and inorganic ash components. In this context, high temperatures and long residence times typically lead to a loss of reactivity in the subsequent gasification process. This effect is called thermal deactivation or “thermal annealing” and can be the consequence of thermal stress during pyrolysis and gasification of fossil [4–9] or biomass-based solid fuels [10–12].

One reason for the loss of reactivity is the graphitization of the carbon matrix. Graphitization describes the process of increase and arrangement of graphene layers in carbonaceous materials [6]. This process is characterized by formation, growth and order of aromatic clusters and graphite crystals [8,9,13]. In raw solid fuels such as coal or

* Corresponding author.
E-mail address: ch.schneider@kit.edu (C. Schneider).

https://doi.org/10.1016/j.fuel.2020.118826
Received 26 March 2020; Received in revised form 1 June 2020; Accepted 23 July 2020

biomass, most of the carbon is available as turbostratic. Turbostratic carbon consists of graphene layers, which are disordered and non-planar. If these layers are accompanied by other types of carbon bonds (e.g. sp^2- or sp^3-bonds) or even heteroatoms (e.g. H, O, N, S), the present structure is titled as amorphous carbon [13,14].

During pyrolysis of solid biogenic fuels, cracking reactions occur and lead to condensation, polymerization and the formation of aromatic carbon clusters [12,15]. Below pyrolysis temperatures of 500 °C, ordered and/or turbostratic carbon is very low while basic structures are present predominantly. Between 800 °C and 1500 °C, nanocrystalline graphite grows and associates face-to-face in distorted columns. From 1600 °C to 2000 °C, these columns coalesce into distorted wrinkled layers. These layers stiffen and become flat above 2100 °C [8,9,16–18]. Many authors have proven that graphitization progresses at higher residence times at high temperatures resulting in a char with low reactivity towards combustion and gasification [14,19–22]. This is due to the fact, that the number of carbon atoms in an amorphous structure, at defect sites or at the edge of a graphene layer decreases with increasing graphitization. Carbon atoms located in these areas are more reactive than those inside an aromatic cluster [9]. Common methods for the experimental determination of a graphitization degree can be found in literature using X-ray diffraction (XRD) [13,14,23,24] and Raman spectroscopy [17,18,23,25,26].

Another aspect affecting char reactivity is the influence of inorganic, ash-forming elements in the fuel [12,27–33]. Especially alkali [34–46] and alkaline earth metals [39–49] evoke an increase of char reactivity during gasification with CO_2 and H_2O. Struis et al. [44] investigated the catalytic activity of major metal species (Na, K, Ca, Mg, Zn, Pb, Cu) found with waste wood during the gasification of nitrate salt impregnated charcoal with CO_2. Results indicated a superposition of structural changes in the charcoal micropore domain and catalyst-specific effects during gasification of the impregnated char samples. Gasification of the samples impregnated with alkali nitrate salts resulted in a reaction rate maximum at a carbon conversion degree of $X_C = 0.5 - 0.7$. The authors explained this maximum with an accumulation of an oxidic alkali type catalyst (M_xO_y) being formed during the early gasification stage. Furthermore, alkaline earth nitrate salts exhibited a high catalytic activity during the early gasification stage. However, a decreasing reaction rate for the whole carbon conversion range was observed, likely due to sintering of the resulting alkaline earth metal oxide, as the authors presumed. In contrast, silicon and phosphorous may inhibit the gasification reaction by binding catalytically active compounds such as potassium [34,35,50].

An important parameter to evaluate the catalytic activity of ash forming elements is the dispersion on the char surface [31,51]. Cazorla-Amoros et al. [52] investigated the dispersion and sintering of Ca species on carbon samples during pyrolysis and gasification with CO_2. They found a strong link between Ca dispersion and carbon-CO_2 reactivity and were able to deduce the following findings: first, a high heating rate during pyrolysis resulted in a high calcium dispersion. Second, Ca dispersion decreased with increasing carbon burn-off during gasification with CO_2 suggesting a deactivation mechanism presumably due to sintering processes. Furthermore, results showed the enormous effect of chemical state of calcium ($CaCO_3$ or CaO) on the sintering rate. It was observed that $CaCO_3$ had a much higher mobility on the carbon surface than CaO because of the great difference in their Tammann temperatures (see Eq. (2)).

The dispersion is normally used for the characterization of a catalyst in order to either determine the number of catalyst particles on a support material or the number of active sites in relation to the carrier mass or available surface area [53]. Depending on the experimental method, various definitions for the catalyst dispersion may be appropriate. Established methods for the determination of dispersion are e.g. chemisorption, XRD as well as scanning (SEM) and transmission (TEM) electron microscopes [51,53–56]. If chemisorption is used for the determination of dispersion, it is convenient to define the dispersion as the number of active sites (species B) per mass or specific surface area of the carrier material (species A) in $mol_B\ g_A^{-1}$ or $mol_B\ m_A^{-2}$ [57,58].

In the frame of the present work, catalytic activity of ash forming elements is discussed based on an analogy with synthesized catalysts. Deactivation of synthesized catalysts may occur due to poisoning of active sites or a decrease in the catalytically active surface area hence a lower dispersion of catalytically active particles. If this lower dispersion is thermally driven, the decrease in catalytically active surface area can be attributed to sintering processes [51,53]. For sintering processes and particle migration, three temperatures are relevant: melting temperature T_{melt}, Hüttig temperature $T_{Hü}$ and Tammann temperature T_{Ta}. Detachment and migration of metal atoms are enabled starting at Hüttig temperature $T_{Hü}$. Reaching Tammann temperature T_{Ta}, entire particle migration over the support surface, accompanied by particle collision and coalescence may occur [51,59]. Following estimations for these two temperatures can be found in the literature [51,52]:

$$T_{Hü} = 0.3 T_{melt} \quad (1)$$

$$T_{Ta} = 0.5 T_{melt} \quad (2)$$

Recent studies concerning thermal deactivation of biomass chars during pyrolysis mainly focus on the change of carbonaceous structures. Guizani et al. [60] investigated the influence of entrained flow pyrolysis conditions on biomass char properties. Temperatures of 500 °C–1400 °C were applied. Morphology of the resulting chars was highly modified at high temperature with loss of the initial wood cell structure, sintering and macropore formation. Char reactivity determined by oxidation with O_2 decreased significantly with increasing pyrolysis temperature. Furthermore, Raman analyses showed that the carbonaceous structures ordered with increasing temperature. The authors developed several correlations between char reactivity and the oxygen-to-carbon-ratio as well as parameters deduced from Raman spectroscopy i.e. total Raman area and intensity ratio I_V/I_D. In 2019, Guizani et al. [25] developed the heat treatment severity index (HTSI) taking into account reactor temperature and residence time of a biomass particle during pyrolysis under entrained-flow conditions. Again, several correlations between the HTSI and physicochemical char properties were formed. Senneca et al. [26] investigated coal and biomass pyrolysis in N_2 and CO_2 atmosphere. They reported a remarkable degree of structural order being developed by the biomass chars upon severe heat treatment. This structural order was determined by Raman spectroscopy.

Other authors also couple the change in ash composition, formation and sintering of ash particles to thermal deactivation processes of biomass chars during pyrolysis. Trubetskaya et al. [24] pyrolyzed wheat straw and rice husk in an entrained-flow reactor at high temperatures and heating rates and investigated the effect of inorganic matter on char morphology. They reported that the silicon compounds were dispersed throughout the turbostratic structure of rice husk char in an amorphous phase with a low melting temperature leading to the formation of a glassy shell covering the carbonaceous char matrix and preserving the char particle shape and size. However, the effect of the silicon oxides on char reactivity with respect to oxidation in O_2 was less pronounced. Strandberg et al. [61] found that during pyrolysis of wheat straw, which is rich in Si and K, a molten ash layer is encapsulating the char. During the subsequent gasification process, this ash layer inhibits the gasification reaction and forms a diffusion barrier preventing carbon oxidation.

The objective of this study is to investigate the thermal deactivation of beech wood char during pyrolysis in a drop-tube reactor under high heating rates. The vast majority of previous research work focuses on the increasing graphitization during pyrolysis of solid fuels in order to explain thermal deactivation of the char produced. Only few publications investigate the dispersion of catalytically active ash components of chars at very high pyrolysis temperatures and its influence on the subsequent gasification reaction. This work aims to estimate the influence of both graphitization and inorganic dispersion on thermal

deactivation. Especially, it presents the dispersion of calcium species on the biomass char surface for pyrolysis temperatures up to 1600 °C where literature data is very limited. Thermal deactivation was quantified by gasification experiments with CO_2 in a thermogravimetric analyzer. Furthermore, graphitization was determined using XRD and Raman spectroscopy while inorganic dispersion was investigated using chemisorption, SEM and TEM.

3. Materials and methods

3.1. Fuel

Commercially available primary char (Holzkohleverarbeitung Schütte GmbH & Co. KG) was purchased and used as precursor since the same char is utilized in the bioliq ® EFG for research operation. It is produced under mild conditions at an estimated pyrolysis temperature of 500 °C to 600 °C. Table 1 shows the proximate and ultimate analysis of the primary char. It still contains approx. 12 wt% of volatiles and consists of 1.8 wt% ash and 85.5 wt% fixed carbon. Furthermore, the organic components consist of approx. 90 wt% carbon, 3 wt% hydrogen and 7 wt% oxygen (by difference). For secondary pyrolysis in the drop-tube reactor, the primary char was sieved to a particle fraction of 50–150 µm.

3.2. Drop-tube reactor

The drop-tube reactor (DTR) consists of an oven (HTM Reetz GmbH) with three heating zones (l_{H1} = 200 mm, l_{H2} = 917 mm, l_{H3} = 200 mm) and a total length of 2000 mm. Each heating zone can be heated to a maximum temperature of 1700 °C. An alumina oxide reaction tube (Aliaxis Deutschland GmbH) with a length of 2100 mm and the inner diameter of 20 mm is inserted vertically in the oven. The temperature calibration was conducted with a type B thermocouple, which was introduced into the reactor from the top under steady-state gas flow. Gas temperature profiles for the pyrolysis experiments can be found in the supplementary material section. A coaxial alumina oxide pipe (length 810 mm, inner diameter 4 mm) was used to feed argon (tracer and carrier gas) and the primary char into the reactor. The feeding system consists of a slowly rotating ceramic disc (Pure Feed DP-4, Schenck Process Europe GmbH) enabling stable solid mass flow rates of approx. 1 g min^{-1}. The primary char was mixed with the reaction gas at the beginning of the second heating zone. For the experiments presented in this work, gas velocity in the reactor was adjusted in order to ensure a gas-phase residence time in the isothermal zone of 200 ms using N_2 as core flow. N_2 volume flow was varied between 11.85 l min^{-1} and 17.44 l min^{-1} while Ar flow was varied between 0.52 l min^{-1} and 0.76 l min^{-1} leading to an N_2/Ar ratio of approx. 23. Ar flow was adjusted in order to ensure similar gas velocities inside the dosing and the reactor tube. At the outlet of the reactor, the hot reaction gas and secondary char were cooled by an inert gas quench to temperatures below 400 °C. Subsequently, the char samples were separated in a hot gas cyclone and collected in a nitrogen-flushed lock for further analyses. The reactor pressure was controlled by two electrically controlled valves and set to 5 mbar gauge. Product gas was continuously monitored with infrared photometry (URAS, ABB) and micro gas chromatography (490 Micro GC, Agilent Technologies). Further information concerning the drop-tube reactor and the operating conditions can be found in literature [62,63]. Before each pyrolysis experiment, the primary char was dried for at least 12 h at 105 °C. In order to remove oxygen from the char surface, the fuel was set under vacuum and flushed with nitrogen five times. For secondary pyrolysis experiments, temperatures in the isothermal zone of the reactor were varied between 1000 °C and 1600 °C. All experiments and analyses were carried out at Engler-Bunte-Institute (EBI ceb), Karlsruhe Institute of Technology (KIT) if not denoted specifically.

Table 1
Properties of primary char.

Proximate analysis/wt%, ad	
Moisture	0.9
Ash content	1.8
Volatiles	11.8
Fixed carbon	85.5
Ultimate analysis/wt%, daf	
C	89.8
H	2.6
O (diff)	7.2
N	0.4

3.3. Chemical analyses

Proximate analysis for the determination of moisture, volatiles and ash was conducted in accordance with DIN 51718, DIN 51719 and DIN 51720. Ultimate analysis for the determination of C/H/N/S was carried out in a vario Macro Cube (elementar) according to DIN 15104. Elemental composition of ash was analyzed by inductively coupled plasma optical emission spectrometry (ICP-OES) at the Institute for Applied Materials - Applied Materials Physics (IAM-AWP, KIT). Prior to ICP-OES, the char samples were incinerated at 815 °C followed by acid pressure digestion in a DAB-2 pressure vessel (Berghof) using a mixture of HNO_3, HCl and HF at 350 °C for 12 h. The hydrofluoric acid is later complexed with H_3BO_3 at 180 °C for 2 h.

3.4. Determination of initial conversion rate R_0

Determination of initial conversion rate R_0 of the char samples with CO_2 was carried out in a thermogravimetric analyzer (pTGA, Rubotherm GmbH). The pTGA consists of a magnetic suspension balance that allows for continuous recording of the sample mass with an accuracy of ± 10 µg. In the gasification experiments, a total gas flow of 100 ml min^{-1} was set. A sample mass of approx. 2 ± 0.1 mg was placed in a ceramic crucible (inner diameter 16 mm, height of wall 10 mm). After evacuating the pressure vessel to ensure an oxygen-free atmosphere, the reaction chamber was purged with argon. The fuel samples were heated up at a constant heating rate of 20 °C min^{-1} to the reaction temperature of 750 °C followed by 20 min holding time to ensure stable conditions. The samples were then gasified in 100% CO_2 at atmospheric pressure until the complete conversion of the fuel was reached.

Char conversion $X(t)$ was determined using the discrete mass signals $m(t)$, the initial mass m_0 and the remaining mass of ash m_{ash}:

$$X(t) = \frac{m_0 - m(t)}{m_0 - m_{ash}} \tag{3}$$

$$R_m = -\frac{1}{m(t) - m_{ash}}\frac{dm}{dt} = \frac{1}{1 - X(t)}\frac{dX}{dt} \tag{4}$$

R_m is the specific conversion rate and can be calculated as presented in Eq. (4). Furthermore, R_X is defined as the conversion rate described by a rate coefficient $R(T,p)$ and a structural term $F(X)$:

$$R_X = \frac{dX}{dt} = R(T, p)F(X) \tag{5}$$

In the frame of this work, the Uniform Conversion Model (UCM) was used to model the char conversion process resulting in a structural term of $F(X) = 1 - X$. Thus, the following expression is obtained:

$$R_X = \frac{dX}{dt} = R_0(1 - X) \tag{6}$$

$$R_0 = \left.\frac{dX}{dt}\right|_{X=0} \tag{7}$$

R_0 is defined as the initial conversion rate, which was determined by

a least-square fit in the char conversion range between 20% and 50%. This range was chosen in order to minimize the effects of gas exchange in the pTGA at the start of each experiment. Furthermore, the char properties for higher conversion degrees may have changed and were not characterized anymore. Gasification experiments were repeated three times.

3.5. Micropore surface area

Micropore surface area of the char samples was determined in a physisorption analyzer (ASAP 2020, Micromeritics) using CO_2 at 0 °C. For each adsorption experiment, relative pressure ranges from $1{\cdot}10^{-5}$ to 0.035 were applied. Prior to adsorption, the char samples were heated to 180 °C for 12 h. Data evaluation was carried out based on the Dubinin-Radushkevich method (DR) for micropores in activated carbon.

3.6. Graphitization

X-ray diffraction (XRD) was carried out at Luleå University of Technology using an Empyrean (Malvern Panalytical) diffractometer. Char samples were placed in an alumina sample holder and analyzed in a range of $10^\circ \leq 2\theta \leq 90^\circ$, a step size of 0.0065652° and a step duration time of 99.45 s. The chosen step size enables the detection of graphite, carbon nanocrystals and amorphous carbon. Furthermore, inorganic species like crystalline calcium carbonate were visible. Cu Kα radiation ($\lambda = 1.542$ Å) was used as an X-ray source.

XRD analysis was conducted using the full-width at half maximum (FWHM) of the characteristic carbon peaks at approx. $2\theta = 24^\circ$ and $2\theta = 44^\circ$. The first maximum ($23^\circ - 24^\circ$) can be attributed to the (0 0 2)-Peak, the second (44°) to the (1 0 0)-Peak. The (0 0 2)-Peak represents the reflection at stacked graphene layers whereas the (1 0 0)-Peak originates from reflection at aromatic ring structures within the graphene layers. Furthermore, narrow peaks represent crystalline structures [19,64,65].

Scherrer equation (Eq. (8)) allows for the quantification of graphitization in terms of growth of nanosized carbon crystals:

$$L_i = \frac{K_i \lambda}{B_i \cos(\theta_i)} \quad i = a, c \tag{8}$$

Here, L_i stands for calculated sizes of the nanosized carbon crystals and can be determined using the ratio of X-ray wavelength λ and a structural constant K_i divided by the value for FWHM B_i and the cosine of the reflection angle θ_i. The indices a and c indicate two different sizes of the nanosized carbon crystals: L_a describes the radial expansion of the carbon crystal ((1 0 0)-Peak) while L_c stands for the stacking height of the graphene layers ((0 0 2)-Peak). Values for the structural constants $K_a = 1.84$ and $K_c = 0.89$ are taken from literature [14,20,22,23,64,65]. As a measure for increasing graphitization, the ratio $L_a\ {L_{a,0}}^{-1}$ was formed. Here, $L_{a,0}$ describes the radial expansion of nanosized carbon crystals of the primary char.

The distance between two graphene layers d is calculated using Bragg equation for $n = 1$:

$$2d\sin(\theta_c) = n\lambda \tag{9}$$

Raman spectroscopy was carried out at Luleå University of Technology using a Senterra II (Bruker) microscope. 30 measurements (co-additions) at 3 s were conducted per char particle with green laser ($\lambda_{Laser} = 532$ nm) and low power of 0.2 mW in order to minimize structural changes in the carbon matrix. Three different particles per char sample were analyzed using this approach. During Raman measurements, two intensity maxima were encountered at Raman shifts of approx. 1355 cm^{-1} and 1575 cm^{-1} representing the D- and the G-Peak, respectively. While the G-Peak originates from the vibration within aromatic clusters of nanosized carbon crystals, the D-Peak can be attributed to defects in the graphite crystal or boundary areas of graphene layers [17,18,66]. Furthermore, a valley peak (V-Peak) is located between D- and G-Peak, which can be traced back to amorphous, sp^2-hybridized carbon [13,26,67]. The evaluation of Raman spectra was carried out using the intensity ratios of D- and G-Peak (I_D/I_G) as well as V-and D-Peak (I_V/I_D). Beforehand, the intensities were normalized to the maximum intensity of the G-Peak.

3.7. Ash dispersion

Quantification of ash dispersion was carried out in the pTGA (see chapter 3.4) using temperature-programmed reaction (TPR). In the frame of this work, ash dispersion is determined by chemisorption of CO_2 on CaO at 300 °C, as the element Ca is most abundant in the ash of the char samples and known to catalyze the gasification reaction (see chapter 2). At 300 °C, CO_2 reacts with CaO atoms at the surface of ash particles forming $CaCO_3$. Increasing the temperature would lead to a carbonization of bulk CaO due to diffusion of CO_2 into the ash particle [58]. Thus, chemisorption of CO_2 at 300 °C can be used to determine the outer surface of CaO particles in the biomass ash giving a value for the dispersion of CaO particles. This approach is based on the assumption that no other compound in the ash interacts with CO_2 at this temperature.

In each TPR experiment, 30 ± 0.1 mg of char sample and a CO_2 volume flow of 100 ml min^{-1} was used. Prior to the chemisorption segment, the pTGA was evacuated and backfilled with Argon. Subsequently, the sample was heated to 850 °C in order desorb gases and decompose any $CaCO_3$ if present. Melting, Hüttig and Tamman temperature of CaO are shown in Table 2. In the following segment, the sample was cooled to 300 °C and stabilized in Argon. Chemisorption started switching the gas atmosphere from pure Argon to a mixture of 90 vol-% Ar and 10 vol-% CO_2 and lasted for 300 min.

The chemisorbed mass of CO_2 was calculated as difference between the mass signals after and before the chemisorption segment (average values of the last 30 mass signals of stabilizing segment m_{Stab} and chemisorption segment m_{Chem}, Eq. (10)). Assuming an equimolar stoichiometry for the reaction of surface CaO with CO_2, the molar amount of surface CaO can be directly calculated (Eq. (11)). The dispersion D_{CaO} of surface CaO is then based on the weighed out amount of char m_{Char} in $mol_{surface\text{-}CaO}\ {g_{char}}^{-1}$ (Eq. (12)).

$$m_{CO_2} = m_{Chem} - m_{Stab} \tag{10}$$

$$n_{CO_2} = \frac{m_{CO_2}}{M_{CO_2}} = n_{CaO} \tag{11}$$

$$D_{CaO} = \frac{n_{CaO}}{m_{char}} \tag{12}$$

Scanning electron microscope (SEM) images were taken at Laboratory for Electron Microscopy (LEM, KIT) using a LEO 1530 (Zeiss) with an accelerating voltage of $U = 5$ keV. Prior to SEM analysis, the char sample was positioned on a conductive adhesive tape and coated with a 5 nm layer of platinum (Leica EM ACE600). Four different magnifications (400x, 4000x, 20 000x and 100 000x) were used for each char sample.

Transmission electron microscopy (TEM) was also conducted at LEM (KIT) using a FEI Osiris ChemiSTEM microscope coupled with Quantax system (Bruker) as energy dispersive X-ray (EDX) detector and an accelerating voltage of $U = 200$ keV. The char samples were

Table 2
Melting, Hüttig and Tammann temperature of CaO.

Material	T_{melt} °C	$T_{Hü}$ °C	T_{Ta} °C
CaO	2613 [68]	784	1307

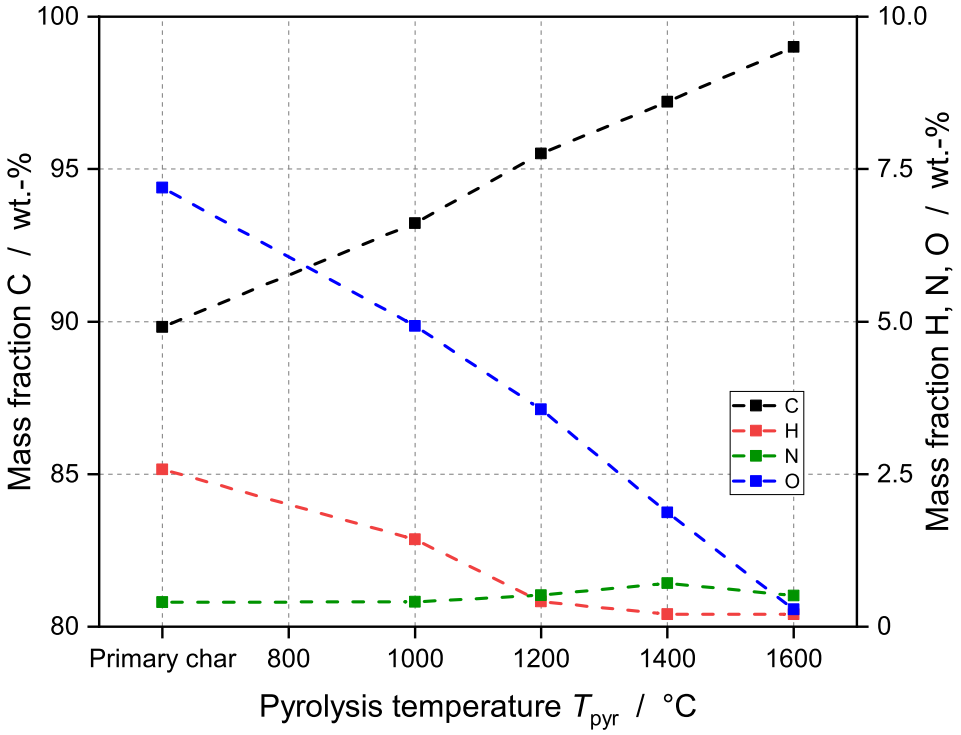

Fig. 1. Chemical composition of primary and secondary chars as a function of pyrolysis temperature. Secondary pyrolysis was carried out in a DTR applying N_2 atmosphere and 200 ms residence time.

dispersed in ethanol and the droplets placed on copper wire with a mesh size of 400 µm.

4. Results and discussion

4.1. Chemical analyses

Fig. 1 shows the chemical composition of primary and secondary chars as a function of pyrolysis temperature. The primary char contains approx. 90 wt% carbon. A steady increase of carbon from 90 wt% to 99 wt% and steady decrease of oxygen from 7.2 wt% to almost zero at 1600 °C can be observed. At 1600 °C, the char consists almost of pure carbon. Nitrogen remains constant at a low level while hydrogen decreases from 2.5 wt% to approx. 0 wt% at 1200 °C.

Table 3 shows the ash elemental analysis of primary and secondary chars determined using ICP-OES. As can be seen from the table, the main ash component of this beech wood char is calcium. The calcium content remains almost constant at approx. 39 wt% with increasing pyrolysis temperature. A slight decrease of approx. 4 wt% at 1400 °C can be observed. Potassium halves at 1000 °C and 1200 °C and increases to approx. 5 wt% at 1400 °C and 1600 °C. Magnesium decreases from 1400 °C being only 1 wt% at 1600 °C. Silicon is between 2 and 3 wt% while phosphorous remains almost constant during secondary pyrolysis (P content of primary char was not determined). K/Si ratios range from 0.83 to 2.30 while K/(Si + P) ratios range from 0.51 to 1.29 being very low in total (not shown in table 3). Thus, deactivation of K by Si and P can be assumed [34,69].

4.2. Determination of initial conversion rate R_0

Gasification experiments of the char samples with CO_2 at 750 °C in a pTGA are discussed in this chapter. Fig. 2 shows the conversion curves during gasification for the primary beech wood char as well as the secondary chars with different pyrolysis history. As can be seen from Fig. 2 A, the primary char was completely gasified within 100 min. Samples pyrolyzed at 1000 °C and 1600 °C were gasified after approx. 150 min (see Fig. 2 B & D). The longest conversion time with approx. 200 min is observed for the sample pyrolyzed at 1400 °C (see Fig. 2 C). The different pyrolysis conditions also affect the shape of the conversion curves (see Fig. 2, orange curves are approximated with 6th-degree polynomial method except Fig. 2 C). In particular, the different shapes of the conversion curves become striking for the sample P1400C_200ms. Here, a constant conversion rate between 20% and 80% conversion degree can be observed. Therefore, the conversion rate $\frac{dX}{dt}$ was set constant in order to make the calculated initial conversion rate R_0 comparable to the other samples.

Table 3
Ash elemental analysis of primary and secondary chars.

Element	Primary char	P1000C_200ms	P1200C_200ms	P1400C_200ms	P1600C_200ms
wt%					
Ca	38.20	39.00	39.50	35.30	39.10
K	4.62	2.54	2.61	5.48	5.05
Mg	6.03	7.13	7.08	5.8	1.03
Si	2.01	3.05	2.97	2.51	2.45
P	n. a.	1.95	1.99	1.73	1.52
Na	0.82	0.76	0.76	0.96	0.84
Fe	0.74	1.05	0.82	0.84	0.83
Al	0.25	0.34	0.29	0.28	0.31

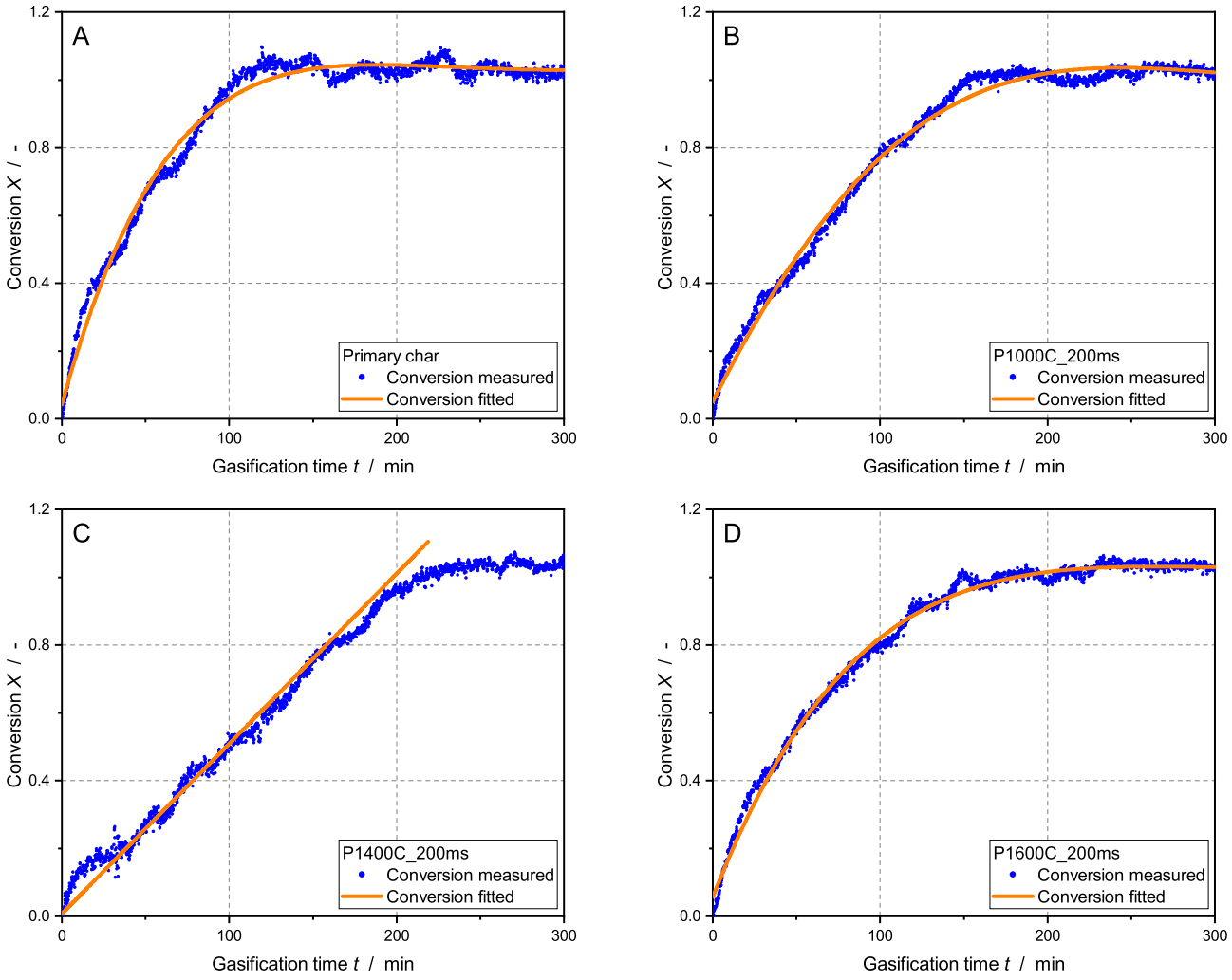

Fig. 2. Measured and fitted conversion curves during gasification in CO_2 for beech wood chars with different secondary pyrolysis history (pTGA, 750 °C, atmospheric pressure, 100% CO_2).

From the fitted conversion curves in Fig. 2 (orange), the conversion rates $\frac{dX}{dt}$ were calculated (see Fig. 3). As stated above, the conversion rate of P1400C_200ms is set to be constant in the conversion range considered. All other samples show a decreasing conversion rate for higher conversion degrees which may be an indication of a calcium catalyzed gasification reaction [44,70].

Fig. 4 shows the initial conversion rate R_0 during gasification of different beech wood chars with CO_2 as a function of pyrolysis temperature. The primary char has the highest initial conversion rate R_0 among the chars investigated. Due to thermal deactivation during secondary pyrolysis, the initial conversion rates decrease between 1000 °C and 1400 °C almost linearly. However, a strong increase in the initial conversion rate at 1600 °C is observed that cannot be explained by thermal deactivation due to graphitization of the carbon matrix. Thus, other effects also influence the initial conversation rate of gasification with CO_2.

4.3. Micropore surface area

Micropore surface area determined via physisorption of CO_2 at 0 °C using Dubinin-Radushkevich is depicted in Fig. 5. The primary char shows a micropore surface area of approx. 395 $m^2\ g^{-1}$. A slight increase at pyrolysis temperatures of 1000 °C and 1200 °C is observed. Due to devolatilization at high heating rates during pyrolysis, micropore surface area is generated additionally. Increasing the pyrolysis

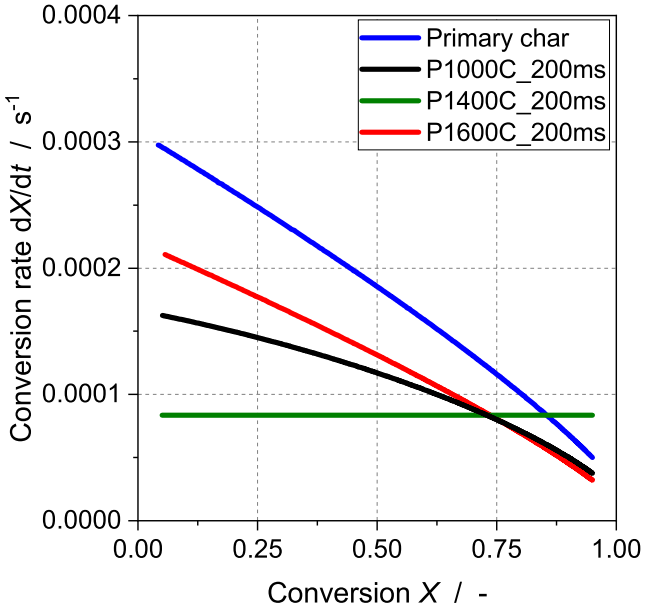

Fig. 3. Calculated conversion rates during gasification of different beech wood chars with CO_2 in pTGA (750 °C, atmospheric pressure, 100% CO_2).

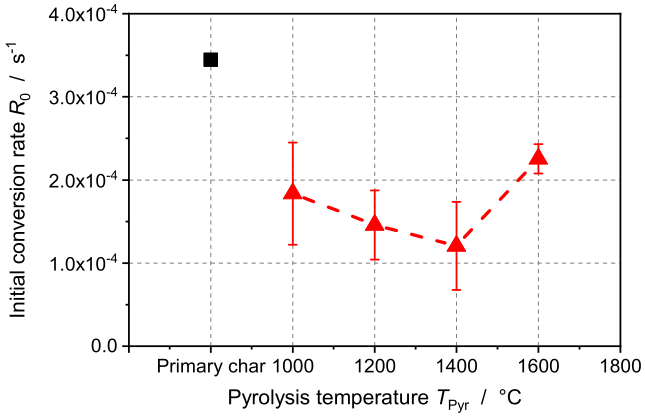

Fig. 4. Initial conversion rate R_0 during gasification of different beech wood chars with CO_2 in pTGA (750 °C, atmospheric pressure, 100% CO_2) as a function pyrolysis temperature.

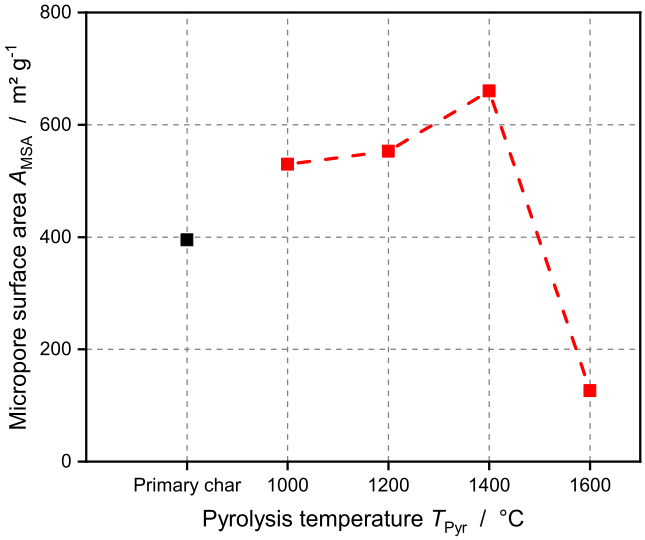

Fig. 5. Micropore surface area via physisorption of CO_2 at 0 °C using Dubinin-Radushkevich as a function of pyrolysis temperature.

temperature leads to an even higher micropore surface area at 1400 °C which may be attributed not only to devolatilization especially at high heating rates but also secondary reactions of the pyrolysis products with the char i.e. Boudouard reaction of released CO_2 with carbon forming carbon monoxide. This hypothesis was further supported by complementary gas-phase measurements showing no CO_2 in the off-gas starting at pyrolysis temperatures of 1400 °C and higher. At 1600 °C, micropore surface area collapses to approx. 126 m^2 g^{-1} which may be explained by ash fusion since melting of mineral matter could change the micropore structure and lead to a blocking of micropores [71,72]. This hypothesis is also supported by SEM/TEM images that show the formation of a thin ash layer on the char surface at 1600 °C (see chapter 4.5). Furthermore, no correlation between initial conversion rate and evolution of micropore surface area can be deduced.

4.4. Graphitization

XRD spectra of primary and secondary chars are depicted in Fig. 6. The intensity maxima for all samples are encountered at reflection angles 2θ of 23°–24° and 44°. The first maximum (23°–24°) can be attributed to the (002)-Peak, the second (44°) to the (100)-Peak (see chapter 3.6). The (002)-Peak represents the reflection from stacked graphene layers whereas the (100)-Peak originates from reflection from aromatic ring structures within the graphene layers. Furthermore, narrow peaks represent highly crystalline structures [19,20,22,23,64,65]. Both peaks grow with increasing pyrolysis temperature. In particular, the (100)-Peak becomes more prominent for the secondary chars compared to primary char. Thus, the radial growth of graphene layers with increasing pyrolysis temperature is shown. From the evolution of the (002)-Peak, it can be concluded that the primary char already contains structured carbon to a certain degree. However, the amount of nanocrystals consisting of aromatic ring structures increases with increasing pyrolysis temperature. Another narrow peak can be observed for the primary char at approx. 29°. This peak is characteristic for crystalline calcium carbonate that is still present in the primary char [23]. During secondary pyrolysis, which is carried out above the decomposition temperature of calcium carbonate (700 – 825 °C), the calcium carbonate is decomposed.

Quantitative evaluation of the (002)- and (100)-Peak is carried out using Bragg's Law ($n = 1$) and Scherrer-Equation in order to calculate the mean distance between graphene layers d, stacking height L_c and radial expansion L_a (see chapter 3.6). Radial expansion L_a increases significantly with increasing pyrolysis temperature while distance d and stacking height L_c remain almost constant (see Fig. 7). By forming the ratio of L_c and d, the number of graphene planes per stack unit can be calculated. The stack units consist of 4 planes, each plane with a distance of $d = 3.87 \pm 0{,}03$ Å apart. This value is – as expected – higher than the plane distance for pure graphite ($d_{graphite} = 3.354$ Å) [73]. Pure graphite is obtained at temperatures higher than 2100 °C [8,9].

To sum up the results of XRD analysis, the radii of parallel arranged aromatic ring structures increase with increasing secondary pyrolysis temperature. Furthermore, the order of stacks and stack height were found to be constant. An increase of both order of stacks and stack height would only be expected for temperatures higher than 1600 °C [9].

Raman spectroscopy results are depicted in Fig. 8 and complementary to XRD findings as they indicate the existence of aromatic clusters. All spectra show peaks at 1355 cm^{-1} (D-Peak) and 1575 cm^{-1} (G-Peak). The intensity of the D-Peak of secondary chars increases with increasing pyrolysis temperature indicating the growth of aromatic clusters and graphite crystals [17,66]. Moreover, the D-Peak of the primary char consists of two shoulders. The first shoulder at approx. 1200 cm^{-1} originates from non-crystallite, sp^3-hybridized carbon structures. The shape of the D-Peak becomes narrower with increasing pyrolysis temperature. The narrowing suggests a growing order of the carbon matrix during pyrolysis since non-crystallite carbon is released as volatiles or condensates/polymerizes into larger molecules such as aromatic clusters [12,74]. Ratios of intensity maxima I_D/I_G and I_V/I_D are shown in Fig. 9 as a function of pyrolysis temperature. Again, an increase in D-Peak intensity can be observed compared to the G-Peak and the Valley for temperatures up to 1400 °C. Furthermore, a stagnation of both ratios between 1400 °C and 1600 °C can be seen.

In summary, Raman spectra are complementary to the XRD results indicating the growth of aromatic clusters and graphite crystals in biomass char due to thermal stress during secondary pyrolysis.

4.5. Ash dispersion

Dispersion of CaO was determined by TPR with CO_2 in a pTGA at 300 °C (see chapter 3.7). TPR experiments of the primary char were not carried out since the method applied would have changed the char's initial ash morphology and composition. From XRD results, it is known that the primary char still contains crystalline $CaCO_3$, which would have been decomposed to CaO in the heating segment prior to TPR. Concerning the secondary chars, CaO dispersion decreases steadily from 1000 °C to 1400 °C (see Fig. 10), which is in accordance with the development of initial conversion rate as a function of pyrolysis temperature. The decrease may be explained by sintering of CaO particles upon heat treatment. The size distribution of ash nanoparticles is depicted in Fig. 14. A strong increase of CaO dispersion at 1600 °C

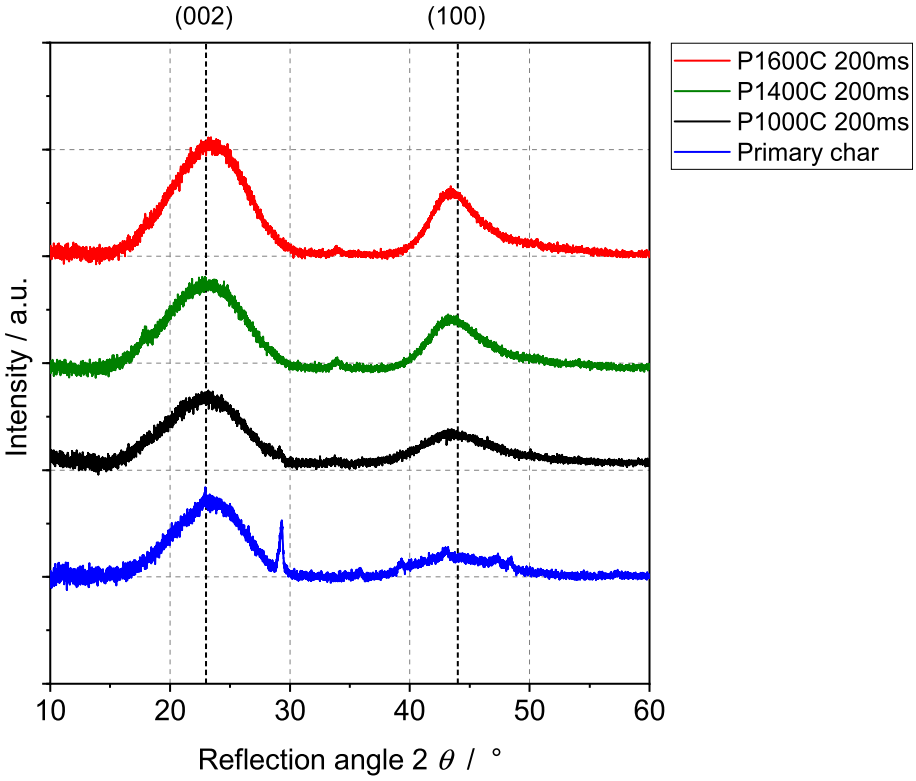

Fig. 6. XRD spectra of primary and secondary chars.

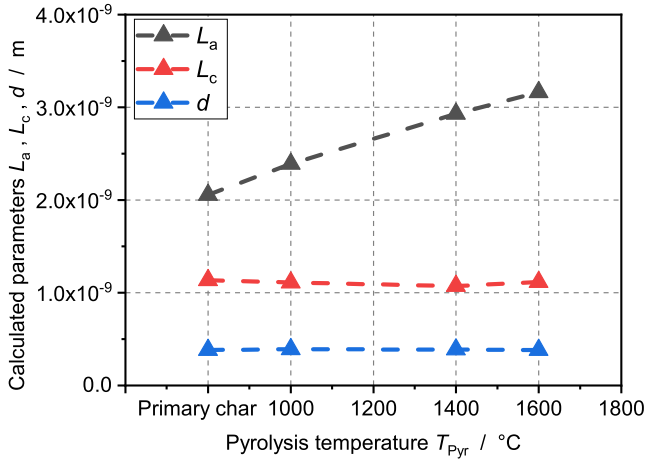

Fig. 7. Radial expansion L_a, stacking height L_c and distance between graphene layers d as a function of pyrolysis temperature.

correlating with increasing initial conversion rate at 1600 °C can be observed. This increase may be traced back to the formation of a thin CaO film on the char surface, which can be seen from SEM/TEM images in Figs. 11–13. The film connects catalytically active ash components to a multitude of carbon atoms on the char surface resulting in an increased initial conversion rate during gasification with CO_2 at 750 °C.

For qualitative evaluation of ash transformation upon heat treatment, SEM images with 20,000× and 100,000× magnification were taken. Fig. 11 shows SEM images of the primary and secondary chars with 20,000× magnification. The visible ash nanoparticles of primary char and P1000C_200ms are very similar. Larger particles are up to 1 µm and clearly distinguishable from the carbon underground. At 1400 °C, droplet-like nanoparticles have formed. However, the large ash particles of approx. 1 µm are still present. The transition between char surface and ash nanoparticles becomes more and more fluent with increasing temperature. For the sample P1600C_200ms, no distinction between char surface and ash nanoparticles can be made anymore suggesting the formation of a thin ash film on the carbon surface. Fig. 12 shows SEM images of two secondary char samples i.e. P1400C_200 ms and P1600C_200ms with 100,000× magnification. Ash nanoparticles of P1600C_200 ms are larger than those of P1400C_200ms. As can be seen from Fig. 14, sintering of ash nanoparticles occurs at higher temperatures. Furthermore, a droplet-like shape of ash particles becomes apparent for P1400C_200ms while for P1600C_200ms, a sharp boundary between carbon surface and ash particles cannot be drawn anymore. SEM images have shown that pyrolysis temperature has an immense impact on ash particle morphology and dispersion.

Complementary to SEM images, TEM analyses were carried out (see Fig. 13). TEM analyses were coupled with EDX in order to visualize the elements calcium (red) potassium (blue) and silicon (yellow) that are most abundant in the chars investigated. In Fig. 13, the TEM images of secondary char samples P1400C_200ms and P1600C_200ms are shown. Ca compounds undergo massive transformation due to heat treatment: On the one hand, sintering of nanoparticles takes place (see Fig. 14). On the other hand, Ca is again highly dispersed at a pyrolysis temperature of 1600 °C forming a catalytically active thin film on the carbon surface. Furthermore, all samples were found to have highly dispersed potassium and silicon compounds combined with oxygen irrespective of heat treatment. A fine dispersion of K and Si during pyrolysis supports

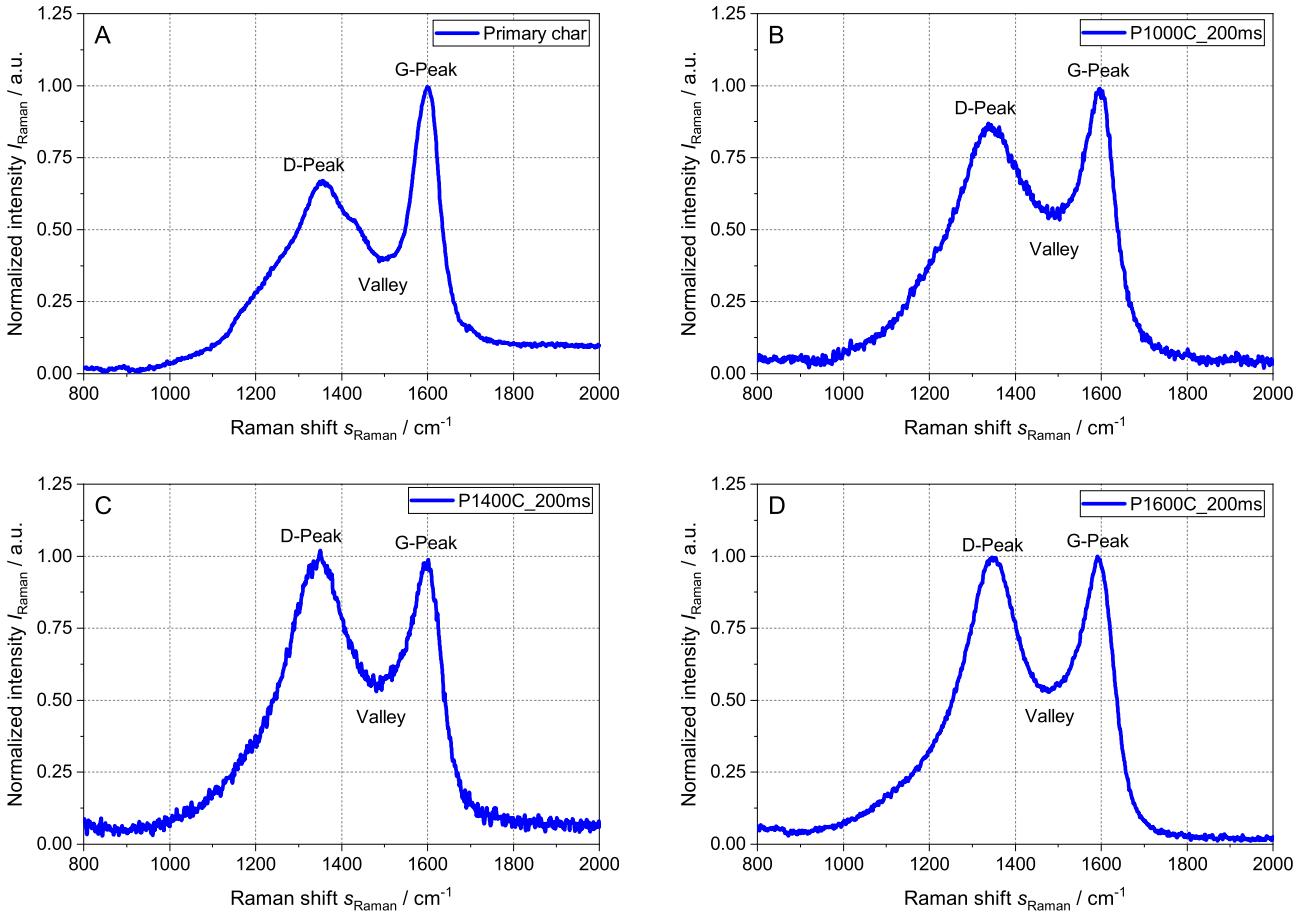

Fig. 8. Raman spectra of primary and secondary chars.

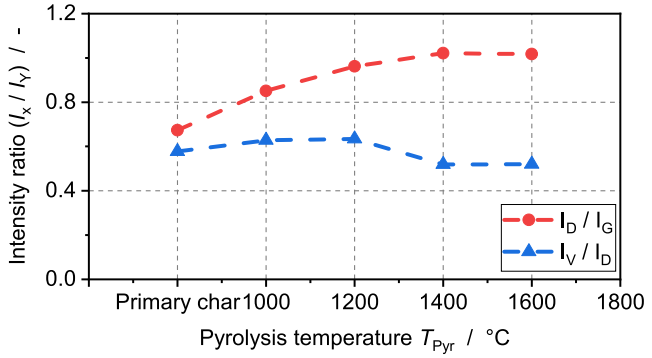

Fig. 9. Ratios of intensity maxima I_D/I_G and I_V/I_D as a function of pyrolysis temperature.

the assumption that due to a low K/Si ratio, K may be deactivated by bonds to Si.

The average sizes of ash nanoparticles as a function of pyrolysis temperature is depicted in Fig. 14. For the evaluation of average particle size, between 650 and 900 particles were analyzed that were larger than 5 nm. The presence of an ash film was not taken into account for

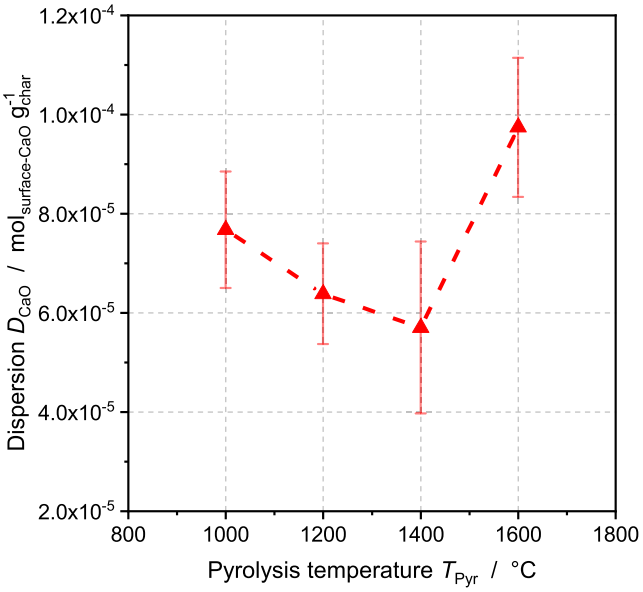

Fig. 10. CaO dispersion of secondary chars determined by TPR in a pTGA with CO_2 at 300 °C as a function of pyrolysis temperature.

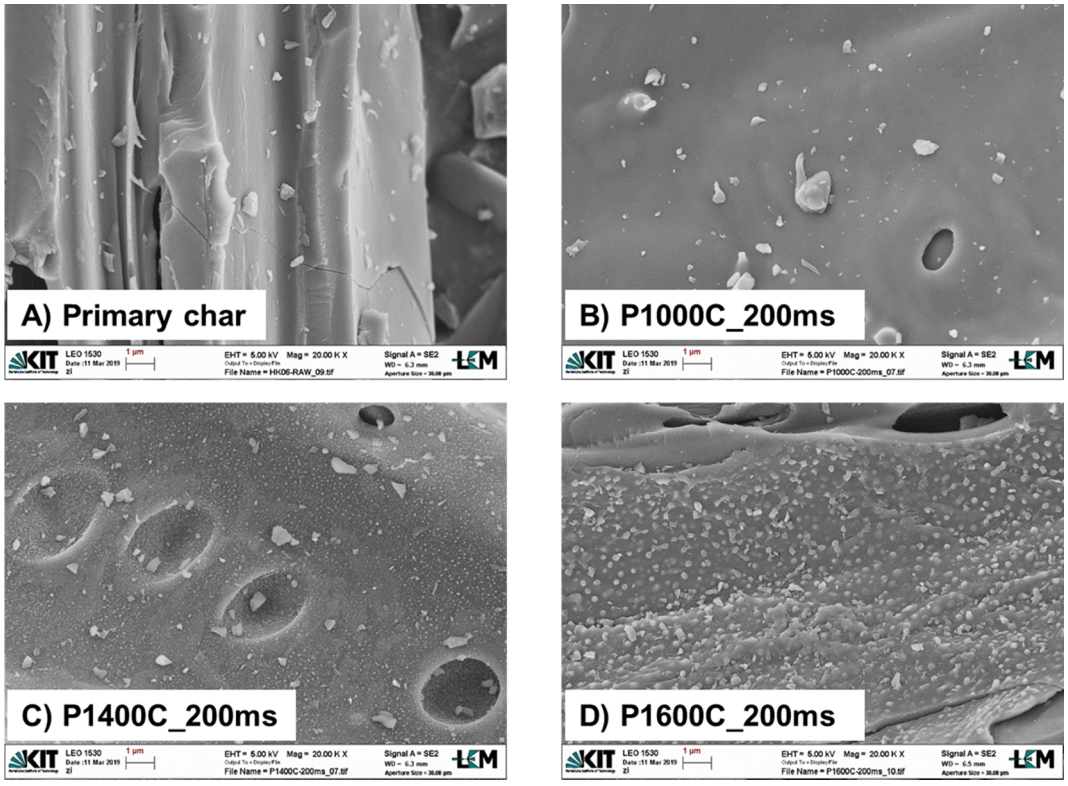

Fig. 11. SEM images of primary and secondary chars with 20,000× magnification.

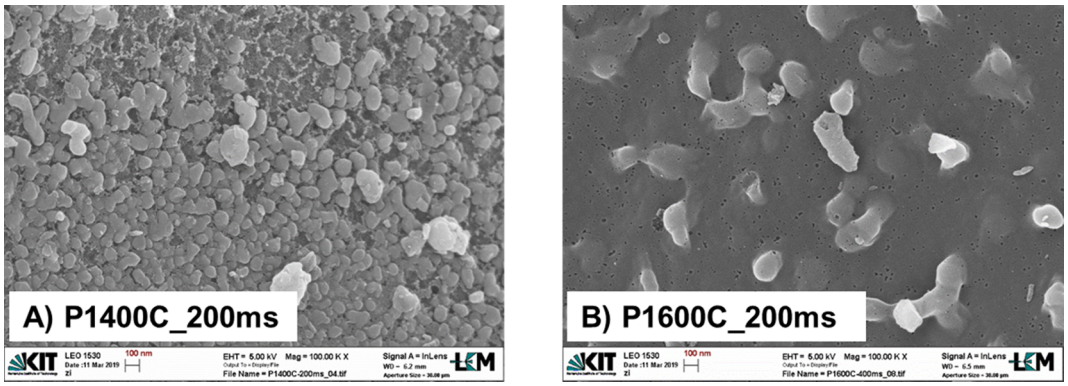

Fig. 12. SEM images of two secondary chars (P1400C_200ms and P1600C_200ms) with 100,000× magnification.

this analysis. Average particle size slightly decreases from primary char to P1000C_200ms. Taking into account the large standard deviation of the analysis, it can be assumed that the ash nanoparticles on both samples may have almost the same size. Increasing the pyrolysis temperature from 1000 °C to 1400 °C leads to an increase in average particle size from approx. 10 nm to 18 nm. This is in good accordance with the Tammann temperature T_{Ta} = 1307 °C where mobility of CaO particles increases significantly. The largest ash particles were obtained at 1600 °C with an average size of approx. 32 nm. Sintering of ash particles during pyrolysis was proven quantitatively by the particle size analysis as well as qualitatively observed via SEM images beforehand. However, increasing particle sizes do not necessarily have to involve a decrease in initial conversion rate R_0 of the gasification reaction with CO_2 as it can be seen for the char sample P1600C_200ms having the highest value for R_0 among the secondary chars.

To sum up, TEM-EDX images allowed for the identification of highly

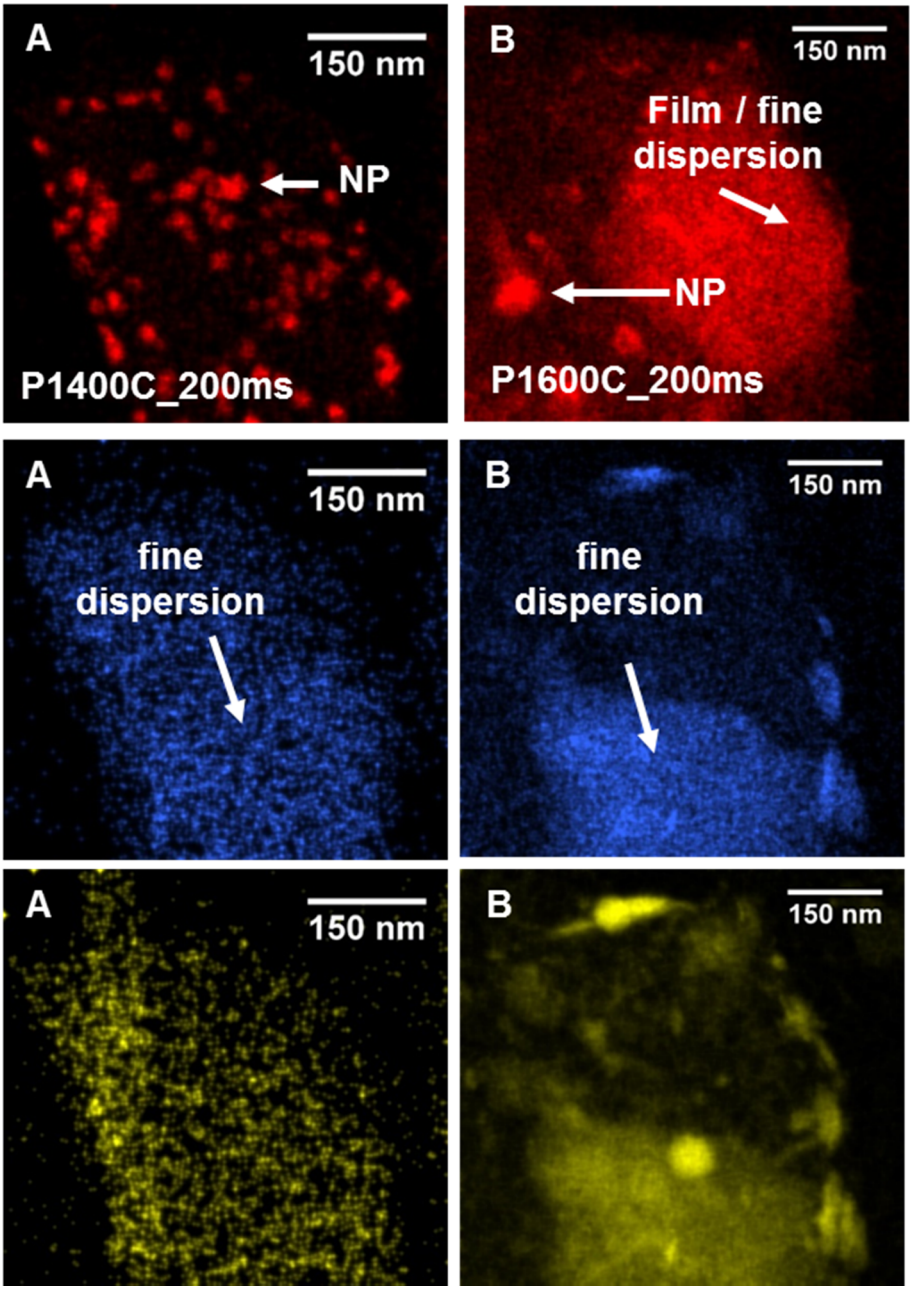

Fig. 13. TEM-EDX images of two secondary chars (P1400C_200ms (A) and P1600C_200ms (B)) visualizing the elements Ca (red), K (blue) and Si (yellow).

dispersed Ca compounds at a pyrolysis temperature of 1600 °C. Even the formation of a CaO film or thin layer can be deduced from SEM and TEM images. The high initial conversion rate R_0 of P1600C_200ms can be attributed to this thin layer of CaO. Due to the ash layer, a large contact area between both gas phase and catalyst as well as catalyst and carbon support is generated. The fact that a uniform thin layer of ash particles on the carbon matrix catalyzes the gasification reaction with CO_2 supports the catalysis mechanisms described by Lobo & Carabineiro [30] and Cazorla-Amoros et al. [57] where the diffusion of a gaseous reactant through the catalyst layer plays a significant role.

Furthermore, the shape of the conversion curves and conversion rates depicted in Figs. 2 and 3 can be explained by the presence of

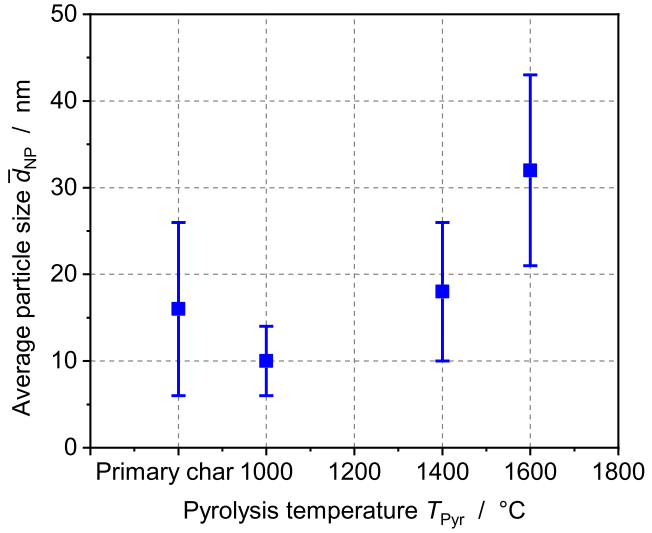

Fig. 14. Average sizes of ash nanoparticles as a function of pyrolysis temperature.

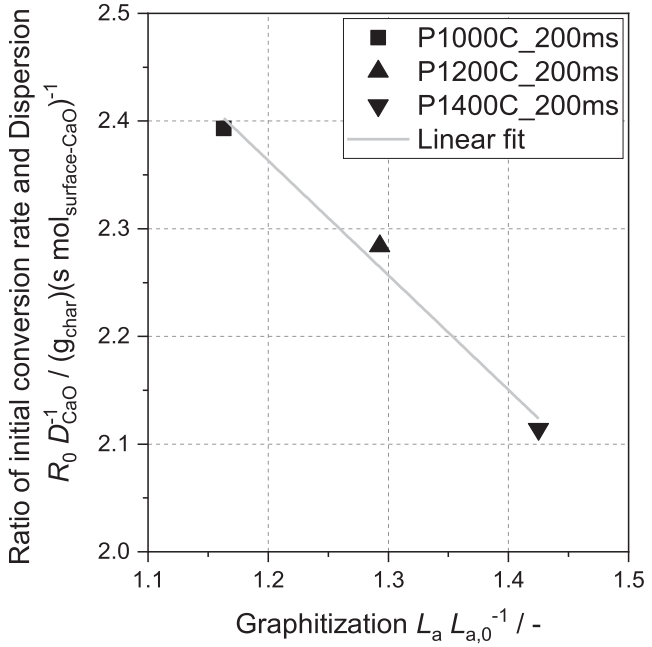

Fig. 15. The ratio of initial conversion rate R_0 and CaO dispersion D_{CaO} as a function of graphitization degree defined as $L_a\ L_{a,0}^{-1}$.

catalytic gasification induced by Ca. During calcium catalyzed gasification, the conversion rate decreases due to thermal deactivation processes of calcium particles which are mainly sintering [52]. This phenomenon can be observed for all samples except P1400C_200ms. From the constant conversion rate $\frac{dX}{dt}$ of P1400C_200ms can be deduced that the gasification of this sample is not or only to a small extent influenced by catalytic reactions. From both, long gasification time and linear shape of the conversion curve, it can be concluded that the uncatalyzed carbon gasification is the dominant reaction for the sample P1400C_ms [44,70].

4.6. Influence of graphitization and ash dispersion on initial conversion rate R_0

In order to clarify the influence of graphitization on initial conversion rate R_0 of gasification with CO_2, the ratio of R_0 and CaO dispersion D_{CaO} is formed for pyrolysis temperatures between 1000 °C and 1400 °C. In Fig. 15, the ratio $R_0\ D_{CaO}^{-1}$ is shown as a function of graphitization degree which is defined as the ratio of $L_a\ L_{a,0}^{-1}$. In this temperature range, which is later referred to as regime 1 (see Fig. 16), it can be seen that graphitization does have an impact on the initial conversion rate. The ratio $R_0\ D_{CaO}^{-1}$ decreases linearly with increasing graphitization and consequently, with increasing pyrolysis temperature up to 1400 °C. Thus, when excluding the catalytic activity of CaO via formation of the ratio $R_0\ D_{CaO}^{-1}$, increasing graphitization degree has a linear negative influence on char reactivity. However, both influences must be taken into account when investigating thermal deactivation due to thermal stress during high-temperature pyrolysis.

5. Summary and conclusions

Thermal deactivation of beech wood chars during secondary pyrolysis in a drop-tube reactor is presented. The effect of pyrolysis conditions on initial conversion rate R_0 during gasification, graphitization and ash dispersion was investigated. Gasification experiments for the determination of R_0 were conducted in a thermogravimetric analyzer using CO_2 at 750 °C. A linear decrease in the initial conversion rate between 1000 °C and 1400 °C was observed. However, a strong increase of R_0 at 1600 °C was encountered. Micropore surface area of the secondary chars showed no correlation with the initial conversion rate during gasification with CO_2. Graphitization of the carbon matrix was determined using X-ray diffraction and Raman spectroscopy suggesting the growth of aromatic clusters and graphite crystals for increasing pyrolysis temperatures. Furthermore, CaO dispersion was analyzed quantitatively and qualitatively using TPR at 300 °C as well as SEM/TEM. CaO dispersion D_{CaO} decreases steadily between 1000 °C and 1400 °C whereas a strong increase can be observed at 1600 °C which is in good accordance with the development of the initial conversion rate R_0 as a function of pyrolysis temperature. SEM/TEM images indicate the formation of a thin CaO layer at 1600 °C which is presumably responsible for the strong increase in initial conversion rate R_0 at this temperature. When excluding the catalytic activity of CaO via formation of the ratio $R_0\ D_{CaO}^{-1}$, increasing graphitization degree has a linear negative influence on char reactivity between 1000 °C and 1400 °C pyrolysis temperature.

Fig. 16 shows the most important experimental results of the present work summed up in one graph being the initial conversion rate R_0, CaO dispersion D_{CaO} and graphitization defined as $L_a\ L_{a,0}^{-1}$. In regime 1, the initial conversion rate and CaO dispersion decrease linearly with increasing pyrolysis temperature. Graphitization increases linearly with increasing pyrolysis temperature up to 1600 °C. However, the initial conversion rate R_0 of the char pyrolyzed at 1600 °C increases significantly despite showing the highest degree of graphitization. A strong correlation between initial conversion rate R_0 and CaO dispersion D_{CaO} is visible. D_{CaO} increases significantly for P1600C_200ms presumably due to the formation of a thin ash layer catalyzing the gasification reaction with CO_2.

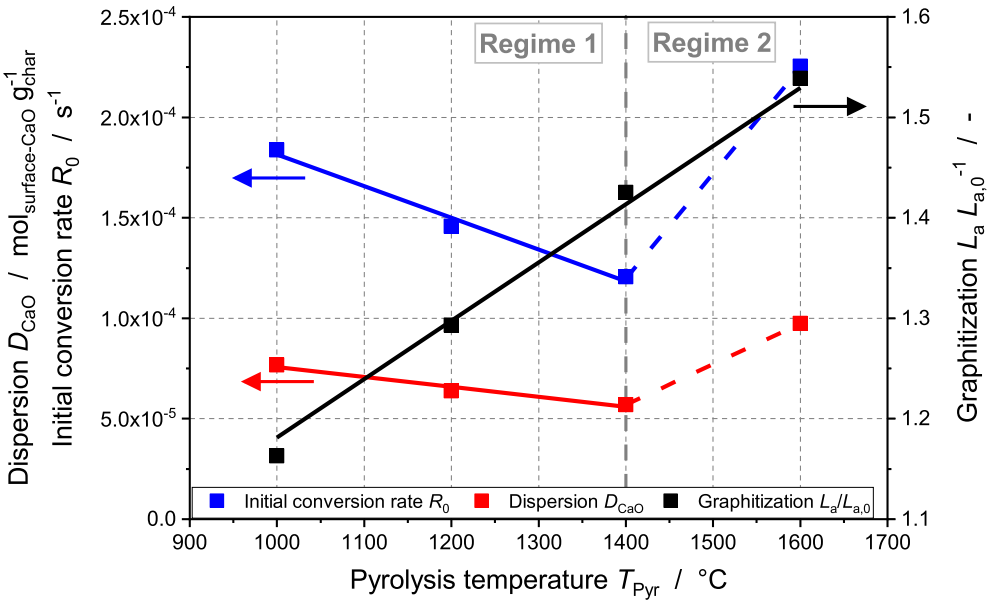

Fig. 16. Summary of the most important experimental results (CaO dispersion D_{CaO}, initial conversion rate R_0 and graphitization degree $L_a\ L_{a,0}^{-1}$) for the secondary chars.

In summary, secondary pyrolysis conditions have an influence on both graphitization of the carbon matrix and ash morphology which in turn affect the initial conversion rate R_0 during gasification with CO_2. Further research should investigate the formation of the observed catalyzing thin ash layer at high pyrolysis temperatures and its influence on the heterogeneous gasification reactions with CO_2 and H_2O.

6. Glossary

Symbol	Description	Unit
A	Specific surface area	$m^2\ g^{-1}$
B_a	FWHM of the (1 0 0)-Peak	cm^{-1}
B_c	FWHM of the (0 0 2)-Peak	cm^{-1}
D	Dispersion	$mol\ g^{-1}$
d	Distance between two lattice planes	m
$\bar{d}_{NP}$	Average particle size	m
$\frac{dX}{dt}$	Conversion rate	s^{-1}
I_D	Maximum intensity of the D-Peak	a.u.
I_G	Maximum intensity of the G-Peak	a.u.
I_V	Maximum intensity of the Valley-Peak	a.u.
K_a	Structural constant for Scherrer equation	-
K_c	Structural constant for Scherrer equation	-
$l_{H1\text{-}3}$	Length of the oven heating zones 1-3	m
L_a	Radial expansion of graphene layers	m
$L_{a,0}$	Radial expansion of graphene layers of the primary char	m
L_c	Stacking height of graphene layers	m
m	Mass	g
M_{CO_2}	Molar mass of CO_2	$g\ mol^{-1}$
n	Integer multiple	-
n_{CO_2}	Chemisorbed molar amount of CO_2	mol
R_0	Initial conversion rate	s^{-1}
R_m	Specific conversion rate	s^{-1}
R_X	Conversion rate	s^{-1}
t	Time	s
T	Temperature	°C
U	Accelerating voltage	V
X	Conversion	-
λ	Wave length	m
θ_a	Position of the (100)-Peak	°
θ_c	Position of the (002)-Peak	°

Subscripts	Description
CO_2	Carbon dioxide
surface-CaO	Superficial calcium oxide
Chem	Chemisorbed amount
Hü	Hüttig
melt	Melting point
MSA	Micropore surface area
Pyr	Pyrolysis
Stab	Stabilizing segment
Ta	Tamman

Abbreviations	Description
DR	Dubinin-Radushkevich
EDX	Energy-dispersive X-ray spectroscopy
EFG	Entrained-flow gasification
Eq.	Equation
Fig.	Figure
FWHM	Full-width at half maximum
HTSI	Heat treatment severity index
IAM-AWP	Institute for Applied Materials - Applied Materials Physics
ICP-OES	Inductively coupled plasma optical emission spectrometry
KIT	Karlsruhe Institute of Technology
LEM	Laboratory for Electron Microscopy
pTGA	Pressurized Thermogravimetric Analyzer
SEM	Scanning electron microscopy
TEM	Transmission electron microscopy
TPR	Temperature-programmed reaction
wt.	Weight
XRD	X-ray diffractometry

CRediT authorship contribution statement

Christoph Schneider: Conceptualization, Methodology, Validation, Investigation, Data curation, Writing - original draft, Visualization, Supervision, Project administration. **Stella Walker:** Methodology, Validation, Investigation, Data curation, Writing - review & editing. **Aekjuthon Phounglamcheik:** Methodology, Validation, Investigation, Data curation, Writing - review & editing. **Kentaro Umeki:** Resources, Writing - review & editing, Supervision. **Thomas Kolb:** Resources, Writing - review & editing, Supervision.

Declaration of Competing Interest

The authors declare that they have no known competing financial interests or personal relationships that could have appeared to influence the work reported in this paper.

Acknowledgements

The authors gratefully acknowledge the financial support by the Deutsche Forschungsgemeinschaft (DFG) (121384/22-1) and the Helmholtz Association of German Research Centers (HGF), within the research program Energy Efficiency, Materials and Resources (EMR). The present work contributes to the Helmholtz Virtual Institute for Gasification Technology - HVIGasTech (VH-VI-429, http://www.hvigastech.org/). The authors also acknowledge the financial support of Swedish national strategic research environment, Bio4Energy, and Swedish Centre for Biomass Gasification. Further acknowledgement goes to Dr. Thomas Bergfeldt and co-workers from IAM-AWP as well as Dr. Radian Popescu and Dipl.-Ing. Volker Zibat from LEM for the char analyses and many fruitful discussions.

Appendix A. Supplementary data

Supplementary data to this article can be found online at https://doi.org/10.1016/j.fuel.2020.118826.

References

[1] Dahmen N, Abeln J, Eberhard M, Kolb T, Leibold H, Sauer J, et al. The bioliq process for producing synthetic transportation fuels. WIREs Energy Environ 2017;6(3):e236https://doi.org/10.1002/wene.236.
[2] Higman C. State of the gasification industry-the updated worldwide gasification database. In: Gasification Technology Conference, Colorado Springs; 2013.
[3] Kolb T, Aigner M, Kneer R, Müller M, Weber R, Djordjevic N. Tackling the challenges in modelling entrained-flow gasification of low-grade feedstock. J Energy Inst 2016;89(4):485–503. https://doi.org/10.1016/j.joei.2015.07.007.
[4] Hurt R, Sun J-K, Lunden M. A Kinetic Model of Carbon Burnout in Pulverized Coal Combustion. Combust Flame 1998;113(1):181–97. https://doi.org/10.1016/S0010-2180(97)00240-X.
[5] Radovic LR, Steczko K, Walker PL, Jenkins RG. Combined effects of inorganic constituents and pyrolysis conditions on the gasification reactivity of coal chars. Fuel Process Technol 1985;10(3):311–26. https://doi.org/10.1016/0378-3820(85)90038-4.
[6] Senneca O, Salatino P, Masi S. Microstructural changes and loss of gasification reactivity of chars upon heat treatment. Fuel 1998;77(13):1483–93. https://doi.org/10.1016/S0016-2361(98)00056-8.
[7] Salatino P, Senneca O, Masi S. Assessment of thermodeactivation during gasification of a bituminous coal char. Energy Fuels 1999;13(6):1154–9. https://doi.org/10.1021/ef9900334.
[8] Russell NV, Gibbins JR, Williamson J. Structural ordering in high temperature coal chars and the effect on reactivity. Fuel 1999;78(7):803–7. https://doi.org/10.1016/S0016-2361(98)00210-5.
[9] Russell NV, Gibbins JR, Man CK, Williamson J. Coal char thermal deactivation under pulverized fuel combustion conditions. Energy Fuels 2000;14(4):883–8. https://doi.org/10.1021/ef990241w.
[10] Zanzi R, Sjöström K, Björnbom E. Rapid high-temperature pyrolysis of biomass in a free-fall reactor. Fuel 1996;75(5):545–50. https://doi.org/10.1016/0016-2361(95)00304-5.
[11] Zhang S-Y, Lu J-F, Zhang J-S, Yue G-X. Effect of Pyrolysis Intensity on the Reactivity of Coal Char. Energy Fuels 2008;22(5):3213–21. https://doi.org/10.1021/ef800245z.
[12] Di Blasi C. Combustion and gasification rates of lignocellulosic chars. Prog Energy Combust Sci 2009;35(2):121–40. https://doi.org/10.1016/j.pecs.2008.08.001.
[13] Ishimaru K, Hata T, Bronsveld P, Nishizawa T, Imamura Y. Characterization of sp2- and sp3-bonded carbon in wood charcoal. J Wood Sci 2007;53(5):442–8. https://doi.org/10.1007/s10086-007-0879-7.
[14] Lu L, Sahajwalla V, Kong C, Harris D. Quantitative X-ray diffraction analysis and its application to various coals. Carbon 2001;39(12):1821–33. https://doi.org/10.1016/S0008-6223(00)00318-3.
[15] Guo P, Saw WL, van Eyk PJ, Stechel EB, de Nys R, Ashman PJ, et al. Gasification reactivity and physicochemical properties of the chars from raw and torrefied wood, grape marc, and macroalgae. Energy Fuels 2017;31(3):2246–59. https://doi.org/10.1021/acs.energyfuels.6b02215.
[16] Oberlin A. Carbonization and graphitization. Carbon 1984;22(6):521–41. https://doi.org/10.1016/0008-6223(84)90086-1.
[17] Ferrari AC, Robertson J. Interpretation of Raman spectra of disordered and amorphous carbon. Phys. Rev. B 2000;61(20):14095–107. https://doi.org/10.1103/PhysRevB.61.14095.
[18] Ferrari AC, Robertson J. Raman spectroscopy of amorphous, nanostructured, diamond-like carbon, and nanodiamond. Philos Trans Ser A Math Phys Eng Sci 2004;362.
[19] Morin M, Pécate S, Hémati M, Kara Y. Pyrolysis of biomass in a batch fluidized bed reactor: Effect of the pyrolysis conditions and the nature of the biomass on the physicochemical properties and the reactivity of char. J Anal Appl Pyrol 2016;122:511–23. https://doi.org/10.1016/j.jaap.2016.10.002.
[20] Cetin E, Moghtaderi B, Gupta R, Wall TF. Influence of pyrolysis conditions on the structure and gasification reactivity of biomass chars. Fuel 2004;83(16):2139–50. https://doi.org/10.1016/j.fuel.2004.05.008.
[21] Septien S, Valin S, Peyrot M, Dupont C, Salvador S. Characterization of char and soot from millimetric wood particles pyrolysis in a drop tube reactor between 800°C and 1400°C. Fuel 2014;121:216–24. https://doi.org/10.1016/j.fuel.2013.12.026.
[22] Lu L, Kong C, Sahajwalla V, Harris D. Char structural ordering during pyrolysis and combustion and its influence on char reactivity. Fuel 2002;81(9):1215–25. https://doi.org/10.1016/S0016-2361(02)00035-2.
[23] Guerrero M, Ruiz MP, Millera Á, Alzueta MU, Bilbao R. Characterization of Biomass Chars Formed under Different Devolatilization Conditions: Differences between Rice Husk and Eucalyptus. Energy Fuels 2008;22(2):1275–84. https://doi.org/10.1021/ef7005589.
[24] Trubetskaya A, Jensen PA, Jensen AD, Steibel M, Spliethoff H, Glarborg P, et al. Comparison of high temperature chars of wheat straw and rice husk with respect to chemistry, morphology and reactivity. Biomass Bioenergy 2016;86:76–87. https://doi.org/10.1016/j.biombioe.2016.01.017.
[25] Guizani C, Jeguirim M, Valin S, Peyrot M, Salvador S. The Heat Treatment Severity Index: A new metric correlated to the properties of biochars obtained from entrained flow pyrolysis of biomass. Fuel 2019;244:61–8. https://doi.org/10.1016/j.fuel.2019.01.170.
[26] Senneca O, Apicella B, Russo C, Cerciello F, Salatino P, Heuer S, et al. Pyrolysis and thermal annealing of coal and biomass in CO2 -rich atmospheres. Energy Fuels 2018;32(10):10701–8. https://doi.org/10.1021/acs.energyfuels.8b02417.
[27] Mahinpey N, Gomez A. Review of gasification fundamentals and new findings: Reactors, feedstock, and kinetic studies. Chem Eng Sci 2016;148:14–31. https://doi.org/10.1016/j.ces.2016.03.037.
[28] Irfan MF, Usman MR, Kusakabe K. Coal gasification in CO2 atmosphere and its kinetics since 1948: A brief review. Energy 2011;36(1):12–40. https://doi.org/10.1016/j.energy.2010.10.034.
[29] Lobo LS. Intrinsic kinetics in carbon gasification: Understanding linearity, “nanoworms” and alloy catalysts. Appl Catal B 2014;148–149:136–43. https://doi.org/10.1016/j.apcatb.2013.09.048.
[30] Lobo LS, Carabineiro SAC. Kinetics and mechanism of catalytic carbon gasification. Fuel 2016;183:457–69. https://doi.org/10.1016/j.fuel.2016.06.115.
[31] Wood BJ, Sancier KM. The Mechanism of the Catalytic Gasification of Coal Char: A Critical Review. Catal Rev 2006;26(2):233–79. https://doi.org/10.1080/01614948408078065.
[32] Huang Y, Yin X, Wu C, Wang C, Xie J, Zhou Z, et al. Effects of metal catalysts on CO2 gasification reactivity of biomass char. Biotechnol Adv 2009;27(5):568–72. https://doi.org/10.1016/j.biotechadv.2009.04.013.
[33] Baker RTK, Chludzinski JJ. Catalytic gasification of graphite by calcium and nickel-calcium. Carbon 1985;23(6):635–44. https://doi.org/10.1016/0008-6223(85)90223-4.
[34] Bouraoui Z, Dupont C, Jeguirim M, Limousy L, Gadiou R. CO2 gasification of woody biomass chars: The influence of K and Si on char reactivity. C R Chim 2016;19(4):457–65. https://doi.org/10.1016/j.crci.2015.08.012.
[35] Dupont C, Jacob S, Marrakchy KO, Hognon C, Grateau M, Labalette F, et al. How inorganic elements of biomass influence char steam gasification kinetics. Energy 2016;109:430–5. https://doi.org/10.1016/j.energy.2016.04.094.
[36] Kapteijn F, Abbel G, Moulijn JA. CO2 gasification of carbon catalysed by alkali metals: Reactivity and mechanism. Fuel 1984;63(8):1036–42. https://doi.org/10.1016/0016-2361(84)90184-4.
[37] Kirtania K, Axelsson J, Matsakas L, Christakopoulos P, Umeki K, Furusjö E. Kinetic study of catalytic gasification of wood char impregnated with different alkali salts. Energy 2017;118:1055–65. https://doi.org/10.1016/j.energy.2016.10.134.
[38] Kopyscinski J, Habibi R, Mims CA, Hill JM. K2CO3-Catalyzed CO2 Gasification of Ash-Free Coal: Kinetic Study. Energy Fuels 2013;27(8):4875–83. https://doi.org/10.1021/ef400552q.
[39] Aho A, DeMartini N, Pranovich A, Krogell J, Kumar N, Eränen K, et al. Pyrolysis of pine and gasification of pine chars – Influence of organically bound metals. Bioresour Technol 2013;128:22–9. https://doi.org/10.1016/j.biortech.2012.10.093.
[40] Duman G, Uddin MA, Yanik J. The effect of char properties on gasification reactivity. Fuel Process Technol 2014;118:75–81. https://doi.org/10.1016/j.fuproc.2013.08.006.
[41] Kramb J, Gómez-Barea A, DeMartini N, Romar H, Doddapaneni TRKC, Konttinen J. The effects of calcium and potassium on CO2 gasification of birch wood in a fluidized bed. Fuel 2017;196:398–407. https://doi.org/10.1016/j.fuel.2017.01.101.
[42] Lahijani P, Zainal ZA, Mohamed AR, Mohammadi M. CO2 gasification reactivity of biomass char: Catalytic influence of alkali, alkaline earth and transition metal salts. Bioresour Technol 2013;144:288–95. https://doi.org/10.1016/j.biortech.2013.06.059.
[43] Mitsuoka K, Hayashi S, Amano H, Kayahara K, Sasaoaka E, Uddin MA. Gasification of woody biomass char with CO2: The catalytic effects of K and Ca species on char gasification reactivity. Fuel Process Technol 2011;92(1):26–31. https://doi.org/10.1016/j.fuproc.2010.08.015.
[44] Struis RPWJ, Cv S, Stucki S, Prins R. Gasification reactivity of charcoal with CO2.

Part II: Metal catalysis as a function of conversion. Chem Eng Sci 2002;57(17):3593–602. https://doi.org/10.1016/S0009-2509(02)00255-5.
[45] Zhang Y, Ashizawa M, Kajitani S, Miura K. Proposal of a semi-empirical kinetic model to reconcile with gasification reactivity profiles of biomass chars. Fuel 2008;87(4):475–81. https://doi.org/10.1016/j.fuel.2007.04.026.
[46] Zhang Y, Hara S, Kajitani S, Ashizawa M. Modeling of catalytic gasification kinetics of coal char and carbon. Fuel 2010;89(1):152–7. https://doi.org/10.1016/j.fuel.2009.06.004.
[47] Kapteijn F, Porre H, Moulijn JA. CO2 gasification of activated carbon catalyzed by earth alkaline elements. AIChE J 1986;32(4):691–5. https://doi.org/10.1002/aic.690320421.
[48] Marquez-Montesinos F, CorderoRodríguez-Mirasol J, Rodríguez JJ. T. CO2 and steam gasification of a grapefruit skin char. Fuel 2002;81(4):423–9. https://doi.org/10.1016/S0016-2361(01)00174-0.
[49] Kuznetsov PN, Kolesnikova SM, Kuznetsova LI. Steam gasification of different brown coals catalysed by the naturally occurring calcium species. Int J Clean Coal Energy 2013;2(01):1.
[50] Hognon C, Dupont C, Grateau M, Delrue F. Comparison of steam gasification reactivity of algal and lignocellulosic biomass: Influence of inorganic elements. Bioresour Technol 2014;164:347–53. https://doi.org/10.1016/j.biortech.2014.04.111.
[51] Argyle M, Bartholomew C. Heterogeneous Catalyst Deactivation and Regeneration: A Review. Catalysts 2015;5(1):145–269. https://doi.org/10.3390/catal5010145.
[52] Cazorla-Amoros D, Linares-Solano A, Salinas-Martinez de Lecea C, Yamashita H, Kyotani T, Tomita A, et al. XAFS and thermogravimetry study of the sintering of calcium supported on carbon. Energy Fuels 1993;7(1):139–45.
[53] Vannice MA, Joyce WH. Kinetics of catalytic reactions. New York (NY): Springer; 2005.
[54] Kuznetsov PN, Kuznetsova LI, Mikhlin YL. Chemical forms and distribution of naturally occurring calcium in brown coal chars. Fuel 2015;162:207–10. https://doi.org/10.1016/j.fuel.2015.09.015.
[55] Cazorla-Amoros D, Linares-Solano A, Salinas-Martinez de Lecea C, Joly JP. A temperature-programmed reaction study of calcium-catalyzed carbon gasification. Energy Fuels 1992;6(3):287–93. https://doi.org/10.1021/ef00033a008.
[56] Zhang Y, Ashizawa M, Kajitani S. Calcium loading during the dewatering of wet biomass in kerosene and catalytic activity for subsequent char gasification. Fuel 2008;87(13):3024–30. https://doi.org/10.1016/j.fuel.2008.03.009.
[57] Cazorla-Amorós D, Linares-Solano A, Lecea CS-Md, Joly JP. Calcium-carbon interaction study: Its importance in the carbon-gas reactions. Carbon 1991;29(3):361–9. https://doi.org/10.1016/0008-6223(91)90205-W.
[58] Linares-Solano A, Almela-Alarcón M, Lecea CS-Md. CO2 chemisorption to characterize calcium catalysts in carbon gasification reactions. J Catal 1990;125(2):401–10. https://doi.org/10.1016/0021-9517(90)90313-9.
[59] Cazorla-Amoros D, Linares-Solano A, Salinas-Martinez de Lecea C, Nomura M, Yamashita H, Tomita A. Local structure of calcium species dispersed on carbon: Influence of the metal loading procedure and its evolution during pyrolysis. Energy Fuels 1993;7(5):625–31.
[60] Guizani C, Jeguirim M, Valin S, Limousy L, Salvador S. Biomass chars: the effects of pyrolysis conditions on their morphology, structure, chemical properties and reactivity. Energies 2017;10(6):796. https://doi.org/10.3390/en10060796.
[61] Strandberg A, Holmgren P, Wagner DR, Molinder R, Wiinikka H, Umeki K, et al. Effects of pyrolysis conditions and ash formation on gasification rates of biomass char. Energy Fuels 2017;31(6):6507–14. https://doi.org/10.1021/acs.energyfuels.7b00688.
[62] Stoesser P, Schneider C, Kreitzberg T, Kneer R, Kolb T. On the influence of different experimental systems on measured heterogeneous gasification kinetics. Appl Energy 2018;211:582–9. https://doi.org/10.1016/j.apenergy.2017.11.037.
[63] Stoesser P. Investigation of solid phase processes during the conversion of biogenic slurry in entrained flow gasifiers. Munich: Dr. Hut; 2020.
[64] Feng B, Bhatia SK, Barry JC. Variation of the crystalline structure of coal char during gasification. Energy Fuels 2003;17(3):744–54. https://doi.org/10.1021/ef0202541.
[65] Saikia BK, Boruah RK, Gogoi PK. A X-ray diffraction analysis on graphene layers of Assam coal. J Chem Sci 2009;121(1):103–6.
[66] Tuinstra F, Koenig JL. Raman spectrum of graphite. J Chem Phys 1970;53(3):1126–30. https://doi.org/10.1063/1.1674108.
[67] Rhim Y-R, Zhang D, Fairbrother DH, Wepasnick KA, Livi KJ, Bodnar RJ, et al. Changes in electrical and microstructural properties of microcrystalline cellulose as function of carbonization temperature. Carbon 2010;48(4):1012–24. https://doi.org/10.1016/j.carbon.2009.11.020.
[68] Haynes WM. CRC Handbook of Chemistry and Physics, 92nd Edition. 92nd ed. Hoboken: CRC Press; 2011.
[69] Dupont C, Nocquet T, Costa JAD, Verne-Tournon C. Kinetic modelling of steam gasification of various woody biomass chars: Influence of inorganic elements. Bioresour Technol 2011;102(20):9743–8. https://doi.org/10.1016/j.biortech.2011.07.016.
[70] Kramb J, DeMartini N, Perander M, Moilanen A, Konttinen J. Modeling of the catalytic effects of potassium and calcium on spruce wood gasification in CO2. Fuel Process Technol 2016;148:50–9. https://doi.org/10.1016/j.fuproc.2016.01.031.
[71] Tremel A, Spliethoff H. Gasification kinetics during entrained flow gasification – Part I; Devolatilisation and char deactivation. Fuel 2013;103:663–71. https://doi.org/10.1016/j.fuel.2012.09.014.
[72] Liu H, Luo C, Kato S, Uemiya S, Kaneko M, Kojima T. Kinetics of CO2/Char gasification at elevated temperatures: Part I: Experimental results. Fuel Process Technol 2006;87(9):775–81. https://doi.org/10.1016/j.fuproc.2006.02.006.
[73] Franklin RE. The structure of graphitic carbons. Acta Cryst 1951;4(3):253–61. https://doi.org/10.1107/S0365110X51000842.
[74] Di Blasi C. Modeling chemical and physical processes of wood and biomass pyrolysis. Prog Energy Combust Sci 2008;34(1):47–90. https://doi.org/10.1016/j.pecs.2006.12.001.

Fuel 267 (2020) 117179

Contents lists available at ScienceDirect

Fuel

journal homepage: www.elsevier.com/locate/fuel

Full Length Article

Determination of active sites during gasification of biomass char with CO_2 using temperature-programmed desorption. Part 2: Influence of ash components

Sonia Rincón Prat[b], Christoph Schneider[a,*], Thomas Kolb[a,c]

[a] Karlsruhe Institute of Technology, Engler-Bunte-Institute, Fuel Technology, EBI-ceb, Engler-Bunte-Ring 3, 76131 Karlsruhe, Germany
[b] Universidad Nacional de Colombia, Departamento de Ingeniería Mecánica y Mecatrónica, Grupo de Investigación en Biomasa y Optimización Térmica de Procesos, BIOT, Carrera 30 No 45A-03, Bogotá, Colombia
[c] Karlsruhe Institute of Technology, Institute for Technical Chemistry, ITC-vgt, Hermann-von-Helmholtz-Platz 1, 76344 Eggenstein-Leopoldshafen, Germany

ARTICLE INFO

Keywords:
Biomass char
Gasification kinetics
Surface chemistry
Temperature-programmed desorption
Active sites
Inorganic ash components
Catalytically active sites

ABSTRACT

The present work is the second part of a study conducted with the aim to determine the amount of active sites present on the surface of a biomass char participating in the gasification reaction with CO_2 using the temperature programmed desorption (TPD) technique. In part 1, the methodology and experimental results during TPD of partially gasified samples of beech wood char (WC1600) using CO_2 as gasification agent are presented. This work focusses on the influence of the main inorganic ash components of WC1600 on the CO_2 and CO signals obtained during TPD of partially gasified char samples. Furthermore, an activated carbon with ash content lower than 1 wt-% is impregnated with Ca and K and partially gasified followed by a TPD analysis. CO_2 and CO signals obtained during TPD result from decomposition of oxygenated surface complexes and decomposition reactions of ash components. During gasification, three different kinds of sites are present on the surface of the char: stable, reactive and catalytically active sites. The latter are a measure of the catalytic influence of inorganic matter during char gasification. From the analysis of the TPD spectra, it can be concluded that gasification of WC1600 is dominated by the catalytic influence exerted by Ca and K. Formation of oxygenated surface complexes on WC1600 is limited, possibly due to the high temperature at which the sample was pyrolyzed (1600 °C). However, a direct correlation between specific conversion rate and the amount of reactive and catalytically active sites is developed from the experimental results, corrected by the contribution of ash decomposition.

1. Introduction

The knowledge of biomass char gasification kinetics is necessary for process and reactor design. It is the slowest reaction taking place inside the gasifier determining its size and the process conditions in the gasification plant. As char gasification is a heterogeneous gas–solid reaction, it is dependent not only on temperature and on concentration of gasifying agent but also on the origin and the physical and chemical characteristics of the solid char. Most of the studies concentrate on the determination of global formal kinetic parameters that are restricted to the raw material and the processing conditions and that do not take into account the change in specific conversion rate as the reaction proceeds [1–3]. Variation in specific conversion rate is considered by a structural term describing the change of physical char properties, i.e. the char surface [4]. Moreover, the great variety of experimental set-ups and conditions implemented during experimentation make the results on same raw materials difficult to compare. Studies on the intrinsic reaction rate and the derivation of kinetic expressions that lie on the fundamental mechanism of the char gasification reaction are limited. The most widely accepted mechanism for the gasification of char with CO_2 or H_2O is the oxygen exchange mechanism in which gasification takes place via formation and decomposition of carbon–oxygen intermediates [1,2]. From a fundamental point of view in a kinetic expression of carbon (or char) gasification, the specific conversion rate should be proportional to the surface concentration of the reactant gas (at constant temperature). Assuming constant partial pressure of the reactant gas (pseudo-zero-order reaction), the surface concentration of the gaseous reactant is described by the chemisorption isotherm which is proportional to the surface concentration of carbon atoms participating in the gasification reaction. The determination of these carbon atoms is still one of the current challenges in the study of the char gasification kinetics. Lizzio et al. [5] introduced the concept of reactive surface area

* Corresponding author.
E-mail addresses: slrinconp@unal.edu.co (S. Rincón Prat), ch.schneider@kit.edu (C. Schneider), thomas.kolb@kit.edu (T. Kolb).

https://doi.org/10.1016/j.fuel.2020.117179
Received 9 September 2019; Received in revised form 29 November 2019; Accepted 21 January 2020
Available online 11 February 2020
0016-2361/

as a measure of the amount of carbon atoms participating in the gasification reaction. They stated that during gasification the char surface contains stable C-O and unstable C(O) complexes formed on stable and reactive sites. The reactive surface area (RSA) is the number of carbon atoms which are able to form carbon oxygen intermediates (unstable C(O) complexes) and are decomposed subsequently to desorb as gaseous product.

The present work is the second part of a study aiming for a better understanding concerning the role of chemical properties of the char surface in the mechanism of biomass char gasification with CO_2. A methodology for measurement of stable C-O and unstable C(O) complexes based on the temperature-programmed desorption (TPD) technique proposed by Lizzio et al. [5] is applied using a beech wood biomass char. An analysis of the obtained CO and CO_2 spectra presented in part 1 [6] shows that the TPD signals are not only a result of decomposition of oxygenated surface complexes followed by desorption of gaseous products but also of decomposition of ash constituents, as both processes yield in oxygenated gases (CO and CO_2) during the desorption phase of TPD experiments [5,7].

Only little work concerning the analysis of released gases during TPD of coal or biomass char after gasification that considers the effect of ash components can be found in literature. In their work, Lizzio et al. [5] measured total and stable complexes using TPD experiments for partially gasified chars with different ash contents (bituminous coal char, polyvinylidene chloride (Saran) char and a Ca-loaded and demineralized lignite). For the quantification of the complexes, they only used the CO signal as they assumed that the CO_2 signal arises from decomposition reactions of ash, especially the decomposition of $CaCO_3$. Kyotani et al. [7] proposed in their study on the catalytic influence of mineral matter during gasification with H_2O of brown coal that H_2O, CO_2 and CO released during TPD, after partial gasification of the samples, is the consequence of the presence of Ca, Mg, Na and Fe. In another work, the same group [8] concludes that the mechanism responsible for the release of gas species detected in the TPD spectra is closely related to the catalytic activity of mineral matter during gasification. They state that the amount of oxygen contained in inorganic species and in carbon–oxygen complexes after gasification is a measure of carbon specific conversion rate. In the more recent works of Klose and Wölki [2] and Guizani et al. [9], who made TPD analysis of partially gasified biomass char samples using CO_2 or H_2O as gasifying agent, there is no mention of the possibility of ash decomposition reactions resulting in the release of CO_2 and CO during TPD.

Based on the conclusions presented in part 1 of this study [6] this paper concentrates on the analysis of TPD spectra of partially gasified beech wood char samples from the point of view of the influence of its ash components. First, a summary of relevant results presented in literature concerning desorption of oxygenated surface complexes and decomposition of ash components from biomass char and coal char that influence TPD spectra is presented. Then, experimental results of TPD of partially gasified samples of a low ash content commercial activated carbon impregnated with the main ash components of the beech wood char under study (Ca and K) is given. The findings are finally applied to the results of TPD spectra obtained for partially gasified samples presented in the first part of this study [6] and conclusions about the influence of decomposition of ash components in the TPD spectra and its relationship to the gasification process are drawn.

2. Literature review on TPD behavior of oxygen surface complexes and biomass ash components

2.1. Carbon oxygen surface complexes and their decomposition behavior during TPD

Carbon oxygen surface complexes are present in the form of oxygenated groups on the surface of carbon materials. They act not only as surface intermediates in gasification reactions (and other) but also determine the surface chemistry of the material, influencing its application as catalyst or as adsorbent, among others [10,11]. They form on the edges of the basal plane of the graphite layer of carbon materials where unsaturated carbon atoms are present and on defects, dislocations and discontinuities present on these basal planes [12]. Oxygen surface groups form acidic, basic or neutral structures that decompose during TPD at different temperature ranges yielding CO, CO_2 and H_2O. Fig. 1 shows the most common oxygenated groups found in carbon materials with their typical decomposition temperatures and the released gases during decomposition. Groups not shown in the figure like lactols, aldehydes, ketones and chromenes can also be present in low amounts [13,14]. Decomposition temperatures of oxygenated surface complexes are influenced by the structure of the carbon material, the heating rate and the experimental system [15]. Therefore, they appear in a wide interval during TPD. General trends show that the CO_2 releasing oxygen groups desorb in the lower temperature range (between 100 °C and 700 °C). Carboxylic anhydrides desorb yielding equimolar amounts of CO_2 and CO at intermediate temperatures (350 °C to 620 °C). Complexes releasing CO desorb at higher temperatures (550 °C to 1000 °C) [11]. According to Calo and Hall [16], oxygenated groups yielding CO_2 (e.g. carboxylic acid, anhydrides and lactones) are formed preferably in the mesopores of the carbon structure because of their large size. At the same time, smaller structures that yield CO during desorption (e.g. carbonyl, ketone and ethers) are formed in the micropores.

During TPD, CO and CO_2 signals appear overlapped. Thus, TPD

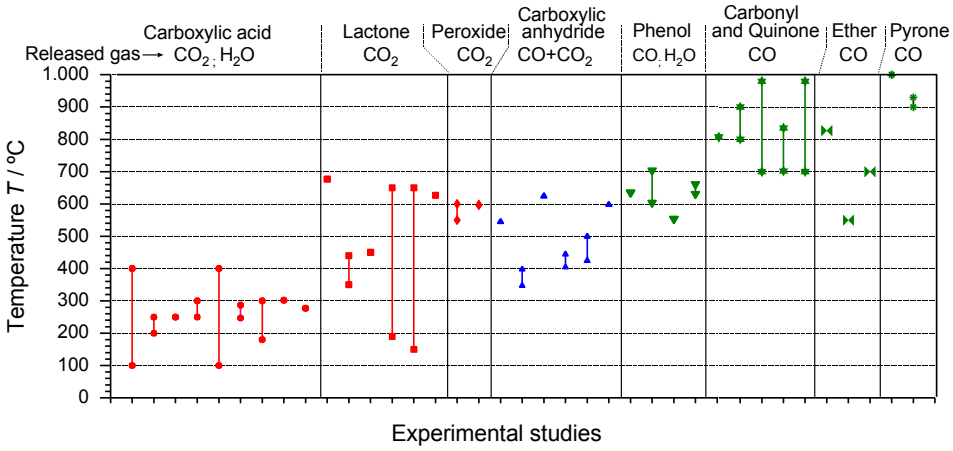

Fig. 1. Decomposition temperatures of different functional groups present as oxygenated surface complexes on carbon materials. Summarized from data compiled by Ishii and Kyotani [20] and Tremblay et al. [14].

peaks can be assigned to different functional groups. The assignment is often accompanied by other techniques like acid-base titration, infrared spectroscopy (FT-IR) and X-ray photoelectron spectroscopy (XPS) [17–19]. Moreover, the desorption behavior of complexes adsorbed in the micropores can be influenced by its location within the pore and the neighboring complexes. As pointed out by Calo and Hall [16], CO, which is the primary desorption product of the complexes in micropores, has a high probability of interacting with other complexes and free sites on the surface undergoing a secondary oxidation reaction to form CO_2. The reaction takes place at intermediate temperatures. At low temperatures (lower than 400 °C), C(O) complexes are inactive whereas at very high temperatures, the equilibrium of the oxidation reaction is shifted to the CO side. The authors state that CO_2 formation from secondary oxidation of CO can be either minimized by using low heating rates during TPD (in their work lower than 20 K/min) as the concentration of evolved CO within the pores remains low. On the other hand, very high heating rates should be used (higher than 500 K/min) in order to minimize the residence time of released CO within the micropores.

Figueiredo et al. [10] studied the formation of oxygenated surface complexes based on the CO and CO_2 evolution during TPD of activated carbon from coconut shell char partially oxidized in 5% O_2 in N_2 at 425 °C. TPD experiments were performed using a heating rate of 5 K/min in He atmosphere. They concluded that the evolving CO_2 originates from desorption of carboxylic anhydrides and lactones with maxima at 603 °C and 631 °C respectively. No evolution of CO_2 is observed at lower temperatures. The evolution of CO is attributed to desorption of carboxylic anhydrides (accompanied by CO_2 evolution), phenols and carbonyl/quinones with maxima at 603 °C, 674 °C and 821 °C respectively. Szymanski et al. [13] conducted deconvolution of the CO_2 and CO signals of TPD profiles of demineralized commercial activated carbon oxidized with nitric acid. The obtained CO_2 profile is composed of five peaks, although two of them with maxima at 290 °C and 430 °C show the higher contributions. This signal is attributed to the decomposition of carboxylic compounds at lower temperatures and to anhydrides, lactones or lactols at higher temperatures followed by desorption of CO_2. The CO profile shows the presence of four peaks in the temperature range between 250 °C and 700 °C which are attributed to the decomposition of carbonyl and carboxylic groups at lower temperatures and phenol and quinone groups at higher temperatures. Zhou et al. [18] studied the formation of oxygenated surface groups on a carbon nanofiber submitted to different heat treatments including oxidation in air and O_2 at temperatures between 400 °C and 600 °C. They characterized the surface oxygen complexes by deconvolution of TPD spectra together with FT-IR and XPS measurements. TPD was performed under Ar atmosphere at 10 K/min until 1000 °C. Additionally to the surface complexes already determined by other authors they attribute CO peaks obtained at low temperatures (lower than 300 °C) to adsorbed CO. Samples that were submitted to high temperatures under Ar atmosphere (900 °C and 1700 °C) before oxidation showed a CO_2 peak at high temperatures (above 800 °C) that could not be identified and is referred to as desorbed unknown group. They also conclude that high temperature treatment (oxidation at 600 °C and heating in Ar at 1700 °C) causes a higher degree of graphitization of the carbon nanofibers and consequently, a decrease in number of surface oxygenated groups.

2.2. Decomposition behavior of biomass ash components during TPD

Biomass ash is composed of high concentrations of alkali and alkaline earth metallic species (AAEM), mainly K and Ca together with small fractions of Na and Mg. Si, Al and Fe are also present in ash whereas the highest contribution is exerted by Si [21–23]. Studies on decomposition of ash components are based on TPD, differential scanning calorimetry (DSC), thermogravimetric analysis (TGA) and in some cases X-ray diffraction measurements. Experimental work is made on the more representative components of char and/or biomass char ashes and their mixtures. Following a summary of the main findings about the decomposition behavior during TPD of individual ash components and biomass char ash is presented.

2.2.1. Decomposition of individual components

After gasification, AAEM are generally present as carbonates [23,24]. During TPD in inert atmosphere, $CaCO_3$ decomposes according to the decarboxylation reaction in solid state (R6), yielding CO_2 in the temperature interval between 600 and 800 °C [25–28]. Formation of CO according to (R7) takes place to a very small extent at slightly lower temperatures [29].

Regarding K_2CO_3 its decomposition according to reaction (R8) takes place at temperatures above 900 °C–1150 °C [30,31]. Arvelakis et al. [31] state that this reaction occurs after melting of K_2CO_3 at temperatures near 900 °C. However, contrary to the findings about the reaction of $CaCO_3$ in presence of C, Kopyscinski et al. [32] found that reaction of K_2CO_3 according to reaction (R9) predominates as only CO was detected in their experiments in TGA in N_2 atmosphere. This reaction takes place at temperatures above 700 °C [32]. $CaCO_3$ and K_2CO_3 decomposition (according to reactions (R6) and (R8)) is inhibited by the presence of CO_2 [27,29,33,34].

$$CaCO_3 \leftrightarrows CaO + CO_2 \quad (R6)$$

$$CaCO_3 + C \rightarrow CaO + 2CO \quad (R7)$$

$$K_2CO_3 \leftrightarrows K_2O + CO_2 \quad (R8)$$

$$K_2CO_3 + 2C \rightarrow 2K + 3CO \quad (R9)$$

During heat treatment, gaseous K formed after decomposition of K_2O (generated according to R8) can escape the sample [35]. Zhao et al. [35] observed in samples of K_2CO_3 submitted to heating in a fixed bed reactor at 900 °C during 120 min under N_2 atmosphere a loss of 20% of the original K. Nzihou et al. [23] indicate that alkali compounds tend to suffer evaporative losses during pyrolysis and gasification conditions due to their high vapor pressures.

Decomposition reactions of silicon take place in presence of C with CO evolution by different reactions yielding SiO, SiC and/or Si. According to Biernacki and Wotzak [36] and Henderson and Tant [37], these reactions take place above 1300 °C. Hüttinger and Nill [38] indicate that the reaction of silica with C begins at 800 °C. This affirmation is however not supported on experimental evidence or a literature reference. Interactions between SiO_2 and AAEM to form silicates can also influence TPD spectra as these reactions take place with CO_2 release [28,31,39]. Calcium silicates form after $CaCO_3$ decomposition to CaO at temperatures above 650 °C [28]. Potassium silicate formation takes place via reaction of K_2CO_3 with SiO_2 at temperatures as low as 600 °C [31,40]. Thermodynamic calculations made by Anicic et al. [39] indicate that at molar ratios SiO_2:K_2CO_3 below 1:1 the presence of CO_2 exerts a high inhibiting influence, so that almost 50% of the original K_2CO_3 remains in equilibrium without decomposition.

Mg- and Na- compounds are present in much smaller quantities as Ca- and K-compounds in biomass ash so it is expected that their influence in TPD signals is of minor importance. Their decomposition should follow similar pathways as for Ca (Group IA) and K (Group IIA), respectively. $MgCO_3$ undergoes thermal decomposition at low temperatures between 113 °C and 550 °C [41]; Na_2CO_3 decomposes above 1000 °C. In presence of SiO_2 sodium silicate is formed (with CO_2 evolution) at temperatures as low as 800 °C [42]. The reaction of Na_2CO_3 with carbon resulting in CO evolution takes place at temperatures above 800 °C [43].

The presence of Fe can also influence TPD spectra. After gasification, due to reaction of Fe with CO_2, it is present as FeO in the char ash. During TPD in presence of C the oxide is reduced with CO evolution at temperatures over 700 °C [44]. Kyotani et al. [8] identified Fe_3O_4 as the

predominant Fe compound in coal char during gasification with H_2O. They conclude that during TPD it is reduced to FeO in the presence of C producing CO. This reaction takes place at temperatures higher than 750 °C. Al_2O_3 is stable a temperatures lower than 1000 °C so it is expected that this component do not exert any influence in the TPD signals [45].

2.2.2. Decomposition of biomass char ash

Few studies deal with the decomposition behavior of biomass char ash. Li et al. [46] studied the thermal decomposition of raw biomass ash and artificial mixtures representative for biomass ashes by TGA under air atmosphere. They divided the mass loss in three temperature stages: low temperature between 70 °C and 250 °C, moderate temperature between 350 °C and 450 °C and high temperature between 600 °C and 1100 °C. Mass loss of artificial mixtures at low and high temperature stages are attributed to the presence of K_2O, whereas mass loss in the low temperature range is attributed to dehydration of the alkali oxide. Mass loss at the moderate temperature stage is attributed to the presence of CaO. Raw biomass ash did not show mass loss at moderate temperatures, which they ascribe to the combination of CaO to other Ca compounds having different decomposition temperatures. According to Arvelakis et al. [31] below 800 °C, weight loss of biomass ash during heating in nitrogen is due to $CaCO_3$ decomposition according to (R6). Between 850 °C and 1150 °C, K_2CO_3 reacts with SiO_2 yielding CO_2 and above 1150 °C, mass loss is attributed to decomposition of K_2CO_3 according to (R8).

3. Materials and methods

3.1. Characterization of raw material

3.1.1. Biomass char

In the present work a high temperature char (WC1600) produced from a bark-less beech wood is used. The biomass was milled and pyrolyzed in two steps up to 500 °C and 1600 °C, respectively. Thereafter, the char obtained was sieved to a 50–100 μm fraction. Carbon content of the char amounts to 97.4 wt-% daf and ash content to 6.68 wt-% d. Ash composition analysis of WC1600 determined by inductively coupled plasma optical emission spectrometry (ICP-OES) is presented in Table 1. Cl and S were below detection limits. A detailed description of the production procedure and its characterization is presented in part 1 of the present study [6].

3.1.2. Impregnated activated carbon

The behavior of the main ash components of WC1600 (K and Ca) is investigated with a commercially available activated carbon (AC1) having ash content lower than 1 wt-% (Merck CAS 7440-44-0, particle diameter < 100 μm, BET specific surface area 740 m^2/g). AC1 was impregnated with calcium nitrate (AC1Ca) and potassium nitrate (AC1K), the ash concentration was determined by ICP-OES. For impregnation, a round bottom flask was filled with 5 g of AC1 and the correspondent solution of metal salt in demineralized water. Subsequently, the flask was attached to a vacuum rotary evaporator (Heidolph VV 2000). The flask was lowered into a water bath, which was tempered at 55 °C, and rotated with 30 min^{-1}. Using a vacuum pump, the pressure was decreased to 170 mbar. After approx. four hours, the liquid was completely evaporated. Finally, the impregnated char was dried for 12 h at 105 °C. Values for Ca, K and Si concentration for the raw activated carbon material and the two impregnated samples are given in Table 1.

Table 1
Ca, K and Si mass fractions of WC1600, raw activated carbon (AC1) and the two impregnated samples AC1Ca and AC1K measured by ICP-OES.

Sample	Ca mg/g_C	K mg/g_C	Si mg/g_C
WC1600	26.19	2.94	6.01
AC1	0.80	0.69	2.81
AC1Ca	26.45	0.69	2.81
AC1K	0.80	25.02	2.81

3.2. Experimental

The detailed experimental set-up and procedure, as well as the approach used for the correction of the TPD signals are presented in detail in section 3 of part 1 of the present study [6]. Summarizing, WC1600 is partially gasified in 80 vol-% CO_2 in Ar at 820 °C up to carbon conversion degrees of 0.25, 0.50, 0.75, 0.90 and 1. After gasification, the samples were cooled to 200 °C either in reaction atmosphere or in Ar atmosphere. Subsequently, a TPD under Ar at 3 K/min until 900 °C is performed. As proposed by Lizzio et al. [5] by cooling in Ar atmosphere the amount of stable surface complexes formed in the gasification reaction can be determined from the released CO_2 and CO during the TPD step. The obtained volume fractions using this procedure are noted as $y_{CO_2,stable}$ and $y_{CO,stable}$. If the cooling step is performed in CO_2 atmosphere, the amount of total complexes (stable and unstable) is measured. Volume fractions obtained using this procedure are called $y_{CO_2,total}$ and $y_{CO,total}$.

The impregnated activated carbon samples AC1Ca and AC1K were gasified to a conversion degree of 20% using 80 vol-% CO_2 in Ar at 800 °C. The samples were then cooled to 200 °C in a CO_2 atmosphere followed by TPD until a final temperature of 900 °C, with a heating rate of 3 K/min and flow of Ar 100 ml/min (same parameters used by the WC1600 samples). As cooling is performed under reaction atmosphere evolved CO_2 and CO are assigned as $y_{CO_2,total}$ and $y_{CO,total}$.

3.3. Data analysis

3.3.1. Determination of released CO and CO_2 amounts and calculation of the quantity of reactive sites

The determination of the CO and CO_2 amounts released during the TPD experiments and the calculation of the quantity of reactive sites is performed according to the procedure described in section 3.4 of Part 1 of the present study [6] (Eq. numbers refer to Part 1). Volume fractions of Ar ($y_{Ar}(t)$), CO_2 ($y_{CO_2}(t)$) and CO ($y_{CO}(t)$) are calculated from the ion current signals of the mass spectrometer using Eq. (3) to (6). With these values, the molar flows of CO_2 and CO are calculated using Eq. (11). The amount of desorbed gas species n_{CO} and n_{CO_2} is determined by integration of the molar flows using Eq. (12) and the determination of the total quantity of reactive sites is performed by applying Eq. (13).

3.3.2. Determination of the maximal theoretical amounts of released CO_2 and CO from the initial ash content

Theoretical maximum amounts of released CO_2 and CO originated from ash decomposition reactions can be deduced from the initial content of the corresponding inorganic element in ash presented in Table 1, and the stoichiometry of the reactions presented in Section 2.2. As an example, maximal theoretical CO_2 evolution of sample AC1Ca due to the thermal decomposition of $CaCO_3$ (R6) is calculated as follows: First, the maximal available amount of calcium carbonate is determined from the Ca content of the sample assuming that all Ca forms the carbonate. Then, the corresponding amount of CO_2 that evolves according to (R6) is determined. The same procedure is used for each reaction considered in chapter 4.

4. Results and discussion

4.1. CO and CO_2 release during TPD of AC1Ca and AC1K

CO_2 and CO signals during TPD of AC1Ca and AC1K are depicted in

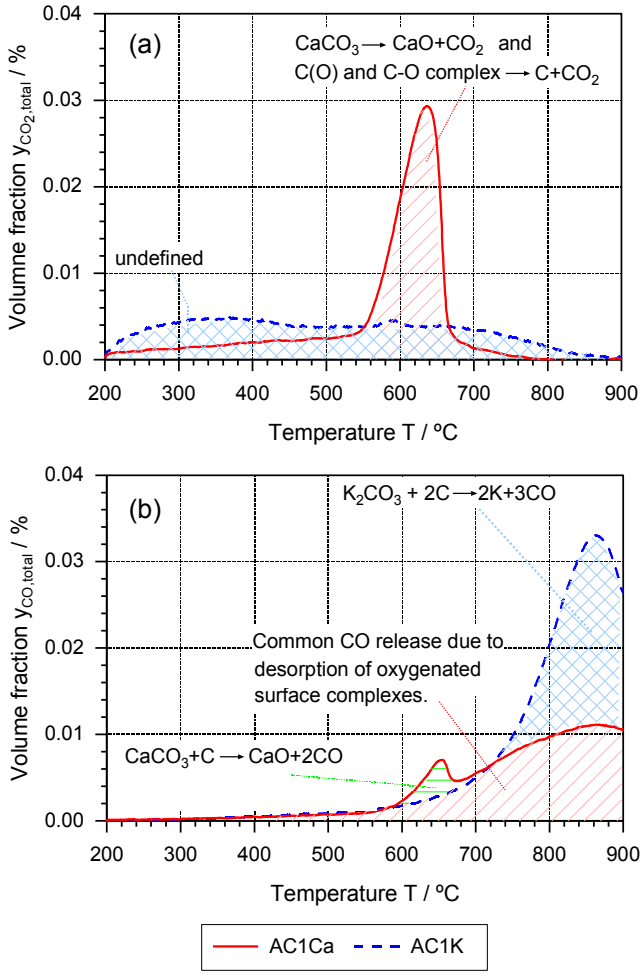

Fig. 2. TPD spectra during determination of total surface complexes for the impregnated activated carbon samples AC1Ca and AC1K submitted to gasification at 800 °C and 80 vol-% CO_2 until 20% carbon conversion. The cooling step before TPD is performed under CO_2 atmosphere. (a) CO_2 and (b) CO release.

Fig. 2. Table 2 presents a comparison between experimental amounts of released CO_2 and CO and the maximal theoretical values that can be calculated from the samples according to their initial ash composition and to selected decomposition reactions using the methodology presented in Section 3.3.2.

The CO_2 spectrum of sample AC1Ca, presented in Fig. 2(a), shows a pronounced peak at 630 °C that does not appear in the sample AC1K. Thus, its formation can be attributed in part to the decomposition of $CaCO_3$ according to (R6). As presented in Section 2.2.1 under TPD conditions this reaction is favored over reaction (R7) and takes place in the temperature interval at which this peak appears. The presence of $CaCO_3$ in the sample after cooling can be explained as follows: During gasification, $CaCO_3$ undergoes continuous decomposition, according to (R7), and formation, according to reverse reaction of (R6). The latter is favoured due to the presence of CO_2. This sequence is proposed to be the mechanism responsible of the catalytic effect exerted by the presence of Ca during gasification [29]. By cooling in CO_2, all CaO forms the carbonate and due to the lower temperatures, its decomposition is stopped. Therefore, Ca is present as its carbonate $CaCO_3$ in the sample at 200 °C. During the following TPD, the carbonate decomposes according to (R6) yielding CO_2 in the gas phase. Row A.1 of Table 2 shows the calculated amount of CO_2 that might be released from the sample as a result of $CaCO_3$ decomposition according to (R6) using the initial Ca content in the ash. In row A.2 of the same table the experimentally released CO_2 during TPD, indicated with diagonal hatch pattern on Fig. 2a, is presented. The higher value of the experimental CO_2 amount indicates the presence of oxygenated surface complexes, such as carboxylic anhydride and lactone groups, that are formed during gasification and desorb in this temperature interval [10,13]. In the present case, the desorbed oxygenated surface complexes correspond to the sum of stable and unstable complexes as cooling was performed under CO_2 atmosphere (for a detailed explanation of the experimental procedure refer to section 3.3 of part 1 of the present study [6]). The calculated amount of desorbed CO_2, following the procedure of section 3.3.2, constitutes the maximum CO_2 evolution from $CaCO_3$ decomposition that can arise from the sample as it is assumed that all Ca is available for the formation of the carbonate. The true CO_2 amount will however be lower as it depends on the availability of Ca on the surface to undergo $CaCO_3$ formation and decomposition during TPD. Moreover, Ca availability is directly related to the amount that is catalytically active during gasification since the amount of carbonate that undergoes the decomposition-formation mechanism during gasification is the one that decomposes during subsequent TPD [8]. Availability of Ca depends on Ca dispersion in the sample and the occurrence of sintering during gasification [8,24,47].

As can be seen from the CO_2 release of sample AC1K presented in Fig. 2(a), the presence of potassium exerts an influence on this signal in the whole temperature range. No evidence on decomposition of K-compounds on ash yielding CO_2 or CO at temperatures lower than 600 °C was found in literature. Thermal decomposition of K_2CO_3 according to (R8) takes place at temperatures higher than 900 °C so the occurrence of this reaction is improbable at the conditions used in the present work. A source of CO_2 from the K containing sample at temperatures above 600 °C can arise from the formation of potassium silicate. However, the released CO_2 would be negligible due to the low Si content of the sample. This can be supported by calculating the maximal CO_2 amount that evolves from the initial Si content in the sample (see Table 1) and reaction of SiO_2 with K_2CO_3 to form $K_2O(SiO_2)$ and CO_2. Applying the procedure depicted in Section 3.3.2, the calculated value corresponds to only 0.89% of the total experimentally released

Table 2
Calculated and experimental CO_2 and CO amounts according to proposed decomposition reactions during TPD of samples AC1Ca and AC1K.

		Released mass of gas species during TPD per initial carbon mass $mg_i/g_{c,0}$
A	**CO_2 evolution attributed to $CaCO_3$ = CaO + CO_2**	
A.1	Calculated from the initial Ca content of sample AC1Ca and the stoichiometry of the reaction.	29.04
A.2	Experimental value from TPD of sample AC1Ca (area identified with diagonal hatch pattern of Fig. 2a).	39.35
B	**CO evolution according to K_2CO_3 + 2C = 2 K + 3 CO**	
B.1	Calculated from initial K content of sample AC1K and the stoichiometry of the reaction.	26.88
B.2	Experimental value from TPD of sample AC1K (calculated as the sum of the areas marked with cross hatch pattern and diagonal hatch pattern on Fig. 2b).	63.72
B.3	Experimental value from TPD of sample AC1K minus common CO evolution (area identified with diagonal hatch pattern on Fig. 2b).	30.32

CO_2 determined from the cross hatched area of Fig. 2. A similar behavior in the CO_2 signal is observed in the WC1600 samples analyzed in part 1 of the present study (as presented in Fig. 3 and Fig. 4 of part 1 [6]). There, it is concluded that this CO_2 release cannot be the result of desorption of oxygenated surface complexes as preheated and unconverted char samples of WC1600 show a similar CO_2 spectrum. Desorption of oxygenated surface complexes yielding CO_2 from sample AC1K is rather unlikely. The considerable amount of CO_2 that desorbs from oxygenated surface complexes from sample AC1Ca shows a possible influence of the presence of Ca in the formation of oxygen surface complexes yielding CO_2 during TPD. Finally, at approx. 590 °C the CO_2 signal of sample AC1K shows a small peak that can be the result of decomposition of $CaCO_3$ formed from the original Ca content of the sample presented in Table 1.

Fig. 2(b) shows the CO signals during TPD for both samples AC1K and AC1Ca. As expected, CO release takes place at higher temperatures than CO_2. Excluding the peak at 650 °C from sample AC1Ca, both signals seem to have the same course up to approx. 730 °C. Afterwards, the signal of the sample AC1K exhibits a faster increase until reaching a maximum at 850 °C. Enhanced CO evolution of sample AC1K after 730 °C can be attributed to decomposition of K_2CO_3 according to (R9) which predominates over the thermal decomposition following (R8) [32]. During gasification, K undergoes reactions that include a continuous decomposition and formation of the carbonate by means of (R9) and the reverse reaction of (R8). K_2O needed for the formation of the carbonate arises from reaction of elemental K with CO_2 in an intermediate step [48,49]. By stopping the gasification reaction, K is present in the sample mainly as K_2CO_3 and during cooling in CO_2 remaining K_2O reacts to K_2CO_3 according to the reverse reaction of (R8). At 200 °C, catalytically active K, or the one that undergoes K_2CO_3 formation and decomposition, is present in the sample as K_2CO_3. During subsequent heating at TPD conditions, the carbonate decomposes following (R9). Table 2 section B shows the calculated CO amount that arises from (R9) using the initial K content of the impregnated sample (row B.1) and the CO released during the experiment using two approaches (row B.2 and row B.3). Row B.2 includes the whole CO amount released from sample AC1K (sum of areas indicated with cross and diagonal hatched patterns on Fig. 2(b)). In Row B.3 the value of the additional CO evolution of sample AC1K over sample AC1Ca is shown (area of the cross-hatched pattern on Fig. 2(b)). The obtained experimental value presented in row 3 is close to the calculated value from the initial K content of the sample. Consequently, it can be stated that the CO curve of the sample AC1K results from two contributions: One that is common for both samples, and therefore independent of impregnation, and other that originates from the decomposition of K_2CO_3 present in the sample. CO evolution due to decomposition of K_2CO_3 amounts to 42% of the total evolved CO of sample AC1K.

Regarding the common CO evolution, as the original ash content of the samples is very small (< 1 wt-%), decomposition reactions of common ash components should not have a relevant influence on the CO signal. Si present in both samples (see Table 2) which is typically present as silicon oxide, decomposes in presence of C at high temperatures (1300 °C) [36,37]. Moreover, it would rather tend to form calcium or potassium silicates with CO_2 evolution at lower temperatures [28,31]. K present in the sample AC1Ca could also be a source of CO through K_2CO_3 decomposition. However, the calculated amount of CO that would evolve using the initial K content of the sample and (R9) amounts to only 1,26% of the total area marked with diagonal hatch pattern of Fig. 2(b). The common CO release should then be the result of desorption of oxygenated complexes yielding CO like phenols, carbonyl/quinones and ether groups that are formed on the samples during gasification. The presence of a high amount of oxygenated complexes yielding CO is related to a sample having a high amount of micropores [16] which should be the case of the activated carbon samples used in the present work.

Finally, the origin of the CO peak at 650 °C of the sample AC1Ca (identified with horizontal hatch pattern in Fig. 2(b)) can be associated with the decomposition of $CaCO_3$ in presence of C according to (R7). This reaction takes place to a smaller extent than thermal decomposition of $CaCO_3$ [29]. The mass of CO released calculated by this peak area amounts to 2,11 $g_{CO}/g_{C,0}$. Based on the stoichiometry of reaction (R7) it is calculated that this amount would be released from an initial Ca content of 1,51 $mg/g_{C,0}$ which represents 5,7% of the Ca present in the sample. Another possible origin is the desorption of carboxylic anhydride that, as shown in Fig. 1, decomposes yielding CO and CO_2 in the temperature interval in which this peak appears (shifted to the higher temperatures). However, as the occurrence of this peak depends on the presence of Ca in the sample the most likely cause of its appearance is the decomposition according to (R7).

From the previous analysis, it can be concluded that the presence of Ca and K in samples of partially gasified activated carbon exerts a big influence on the CO_2 and CO spectra obtained during subsequent TPD. CO_2 and CO release is the result of a combination of desorption of oxygenated surface complexes and decomposition reactions of carbonates of Ca and K. Both are formed during gasification under CO_2 atmosphere and participate in the gasification reaction. TPD spectra can be interpreted as follows:

- The peak of the CO_2 signal of the sample impregnated with Ca (AC1Ca) is in its major fraction the result of decomposition of $CaCO_3$ according to (R6). Extra CO_2 evolution can be attributed to decomposition of oxygen surface complexes followed by desorption of CO_2.
- CO evolution at temperatures higher than 700 °C for sample AC1K results from decomposition of K_2CO_3 (according to (R9)) and decomposition of oxygen surface complexes followed by desorption of CO.
- Regardless of impregnation, CO release shows for both samples (AC1K and AC1Ca) a common course. This release is attributed to decomposition of oxygenated surface complexes formed during gasification followed by desorption of CO.
- CO_2 release does not exhibit a common course comparing both samples. Moreover, sample AC1K does not show a CO_2 signal arising from decomposition of oxygenated surface complexes. Consequently, formation of oxygenated surface complexes yielding CO_2 seems to be promoted by the presence of Ca in the sample.
- Decomposition of $CaCO_3$ in presence of C according to (R7) takes place to a smaller extent than thermal decomposition (R6) giving a peak in the CO spectrum of the sample AC1Ca at 650 °C.
- The presence of K exerts an influence on the CO_2 signal that could not be explained from evidence found in the literature available. The same influence was detected in samples of partially gasified WC1600 as presented in part 1 of the present study [6].

4.2. CO and CO_2 release during TPD of completely gasified WC1600

TPD profiles of ash of samples of WC1600 completely gasified (X_C = 1) using the procedures for determination of total and stable complexes (described in section 3.3 of part 1 of the present study [6]) are presented in Fig. 3.

CO_2 signals show the characteristic peaks at 610 °C ($y_{CO_2,total}$) and 430 °C ($y_{CO_2,stable}$) that also appear in the WC1600 samples partially gasified as presented in Figs. 3 and 4 of part 1 of the present study [6]. From the analysis of the preceding section, the origin of the peak at 610 °C can be attributed to the decomposition of $CaCO_3$ that is present in the sample after cooling in CO_2. Both CO_2 peaks of samples AC1Ca and WC1600 appear in the same temperature interval, with a small difference of 20 K. The experimental amount of CO_2 that is released from this peak amounts to 0,0092 $g_{CO2}/g_{C,0}$ while the maximal CO_2 amount that would evolve from the initial Ca content in the sample of WC1600 (reported in Table 1) following the decomposition reaction of

(R6) increases to 0,033 $g_{CO2}/g_{C,0}$. This result indicates that only a fraction of Ca in ash of WC1600 is capable to undergo $CaCO_3$ decomposition. As stated above, this fraction corresponds to the quantity of Ca that is catalytically active during the gasification process as it is able to undergo formation and decomposition of $CaCO_3$ at gasification conditions. As reported by Radovic et al. [47] and Cazorla-Amorós et al. [24] the catalytic activity of the metal during gasification is dependent on Ca-dispersion in the sample. Non-active Ca may be sintered in the matrix of the ash sample [24].

When the procedure for determination of stable complexes is applied, the CO_2 atmosphere is changed to Ar at gasification temperature after reaching the desired carbon conversion degree. Consequently, recombination of CaO (originated from decomposition of $CaCO_3$ following the decomposition and formation mechanism responsible for the catalytic influence exerted by Ca on the gasification reaction with CO_2) to form $CaCO_3$ does not take place. Moreover, remaining $CaCO_3$ decomposes to CaO and CO_2 at gasification temperature. After cooling, the amount of Ca that participates in the gasification reaction is present as CaO and consequently, during the subsequent TPD, the peak at 600 °C does not appear. The CO_2 peak at 430 °C observed in Fig. 3 must originate from a compound whose formation is inhibited by the presence of CO_2 during cooling, as this peak does not appear in the signal of $y_{CO_2,total}$. From the literature review, only Mg compounds decompose at temperatures lower than 500 °C but yield CO_2 instead of CO [41]. Hall and Calo [16] obtained a similar CO_2 peak centered at 427 °C in their TPD studies of oxidized coal char. However, no indication about the origin of this peak is given. A possibility arises from desorption of chemisorbed CO_2 on CaO. Linares-Solano et al. [50] pointed out that, at temperatures lower than 300 °C, CO_2 chemisorption on CaO predominates over the carbonation reaction (reverse reaction of (R6)). Considering the experimental conditions used in the present work, as the atmosphere is changed at gasification temperature from CO_2 to Ar, all $CaCO_3$ should decompose to CaO with CO_2 release. It is possible that during the rapid cooling a small amount of CO_2 remains chemisorbed on the sample and is later desorbed during the subsequent TPD. This aspect should be further investigated.

Another possible source of CO_2 during TPD is the formation of potassium silicate. However, no CO_2 is detected in the temperature range at which this reaction takes place (above 650 °C) so its occurrence is unlikely. Finally none of the CO_2 signals show the continuous evolution in the whole temperature interval that appears in the partially gasified samples of WC1600 (see Fig. 3 and Fig. 4 of part 1 of the present study [6]) and the sample AC1K (see Fig. 3). Thus, the presence of C in the sample must have an influence on the event that causes the appearance of this signal.

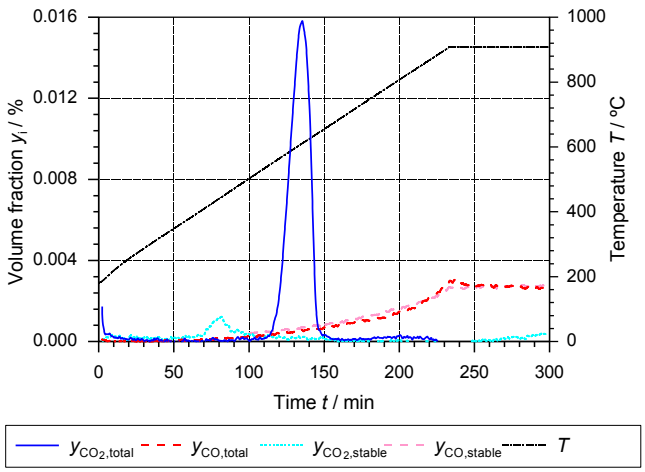

Fig. 3. CO_2 and CO release during TPD for determination of surface complexes for ash of WC1600 submitted to total gasification at 820 °C and 80 vol-% CO_2.

CO signals of both $y_{CO,total}$ and $y_{CO,stable}$ show the same course as the one obtained from blank experiments indicating that no decomposition of ash components yielding CO takes place. The present results confirm that K_2CO_3 decomposition in the studied temperature range takes only place in presence of C according to (R9). Moreover, no thermal decomposition of K_2CO_3 according to (R8) occurs as no CO_2 is detected in the high temperature region. As reported in the literature this reaction takes place at temperatures higher than 900 °C [30].

From the above presented results on TPD of ash remaining after gasification of WC1600 with CO_2 it can be stated that:

- Only a fraction of Ca present in ash of WC1600 undergoes $CaCO_3$ decomposition. This fraction is related to the quantity of Ca that is catalytically active during CO_2 gasification.
- After cooling in Ar atmosphere Ca in ash of WC1600 is present as CaO. Consequently during TPD the pronounced peak at approx. 600 °C, attributed to $CaCO_3$ decomposition, does not appear.
- Chemisorbed CO_2 on CaO can be the source of the small peak at approx. 430 °C of the signal of stable complexes $y_{CO_2,stable}$.
- Contrary to the results on the partially gasified samples, a release of CO_2 at low temperatures does not take place. Consequently, release of CO_2 at low temperatures depends on the presence of C in the sample.
- Decomposition of ash components yielding CO does not take place during TPD of ash obtained after total gasification of WC1600.

4.3. Comparison of spectra from ash and partially gasified samples of WC1600

Based on the conclusions about the course of the CO_2 and CO signals during TPD obtained so far an attempt is made to identify the contributions of both ash decomposition reactions and desorption of oxygen surface complexes during TPD of WC1600 samples partially gasified in CO_2 atmosphere. The results for these samples obtained for 0.25, 0.50, 0.75 and 0.90 carbon conversion degrees are presented in detail in part 1 of the present study [6].

Regarding Figs. 3 and 4 of part 1 of the present study [6], CO_2 signals of total surface complexes are dominated by the pronounced peak at 600 °C that is characteristic for $CaCO_3$ decomposition. The peak shows small variations in height and maximum peak temperature. The CO_2 signal of stable complexes is characterized by the peak at 430 °C possibly due to chemisorbed CO_2. Additionally to these characteristic peaks the course of the CO_2 signals of both total ($y_{CO_2,total}$) and stable ($y_{CO_2,stable}$) complexes show a common behavior that extends over the whole temperature range studied. It can be identified by overlapping the signals of $y_{CO_2,total}$ and $y_{CO_2,stable}$ as shown in Fig. 3 of part 1 of the present study [6]. As the signal is common for both stable and total complexes it should evolve from a compound that remains stable at gasification conditions and consequently does not participate in the gasification reaction. As shown in Fig. 4(a), it corresponds to the signal of $y_{CO_2,stable}$ without the peak at 430 °C. Latter is taken from the signal of stable CO_2 ($y_{CO_2,stable}$) of the sample completely gasified ($X_C = 1$) presented in Fig. 3. It has been shown that the common CO_2 release is not caused by desorption of oxygen surface complexes as it appears on degassed samples that have not been submitted to partial gasification. From the analysis presented in sections 4.1 and 4.2, it is also concluded that it emerges during TPD when C and K are present in the sample.

A detailed analysis of the CO_2 signals of the samples gasified up to $X_C = 0.90$ carbon conversion degree (both stable and total CO_2) show a deviation to higher values starting from approx. 650 °C onwards compared to the common CO_2 course. This can be seen in detail in Fig. 4(b) where the area corresponding to the additional CO_2 (hatched area) and the course of this additional release (dashed line) show a peak at approx. 820 °C. At the same time, the CO signals show a steep increase (see $X_c = 0.90$ in Fig. 4(a) and (b) of part 1 of the present study [6]),

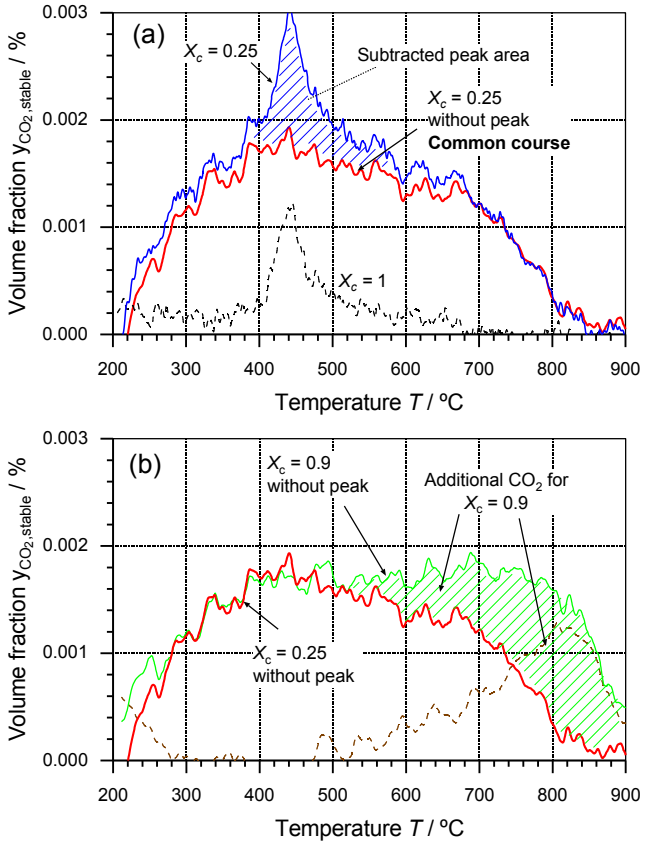

Fig. 4. CO_2 evolution during TPD for determination of stable surface complexes for ash of WC1600, gasification at 820 °C and 80 vol-% CO_2. (a) Graphical determination of common course of the CO_2 signal. (b) Graphical determination of additional CO_2 release at X_C = 0.90.

compared to the signals obtained at X_c = 75%. At X_c = 0.90, released CO values are the highest of all conversion degrees. This behavior is contrary to that observed from 25% to 75% conversion where the CO signal is shifted towards lower values. The enhanced CO_2 and CO evolution at 90% conversion may be explained by the initial structure of WC1600 and its development during gasification. Due to the high temperature at which the sample was pyrolyzed (1600 °C), the graphitic structure of WC1600 became highly ordered so that places for the formation of oxygenated surface complexes are limited [12]. Thus, the gasification reaction is predominantly caused by the catalytic influence exerted by the main ash components Ca and K. At high conversion degrees (X_c = 0.90) collapsing of the carbon structure gives rise to the formation of edges and imperfections on the basal planes of the graphite layers were formation of oxygenated surface complexes is favored. It would be expected that in some point at a conversion degree higher than X_c = 0.90 further collapsing of the char matrix occurs and the amount of surface complexes declines rapidly until reaching total conversion. Based on the decomposition temperatures of oxygenated surface complexes presented in Fig. 1, the origin of these newly formed complexes that are released as CO_2 cannot be fully explained as CO_2 evolution usually does not take place at temperatures higher than 700 °C. A possible source of this CO_2 evolution is the occurrence of a secondary reaction within the pores of the sample between released CO and the surface of the carbon [16], as presented in the literature review.

CO release of the samples of WC1600 obtained using the procedure for determination of total complexes ($y_{CO,total}$) (Fig. 4(b) of part 1 of the present study [6]), show a similar course as the CO signal of sample AC1K (Fig. 3(b)). These samples were cooled under CO_2 atmosphere. Consequently, as presented in section 4.1, the CO signal is the result of decomposition of K_2CO_3 according to (R9) and desorption of oxygenated surface complexes (stable and unstable). The tendency of the CO signal towards lower values as the conversion is increased from X_c = 0.25 to X_c = 0.75 can be ascribed to the tendency of K to volatize during gasification, as reported by several authors [22,23,32]. Another possible explanation for this behavior is a reduction in the amount of C that is available for K_2CO_3 decomposition with an increment in the carbon conversion. The steep increase in CO evolution at X_c = 0.90 is due to an enhanced formation of active sites in the structure of the carbon matrix at high conversion degrees. When CO_2 is changed to Ar at gasification temperature, (R9) takes place until all K_2CO_3 has decomposed to K and CO and new formation of the carbonate does not occur. Consequently, CO evolution is not affected by K_2CO_3 decomposition and should be then the product of the sole decomposition of oxygenated surface complexes followed by desorption of CO. Additionally, as shown in Fig. 4(a) of part 1 of the present study [6], the CO signals of these samples ($y_{CO,stable}$) show a similar behavior as the one obtained for $y_{CO,total}$ in which the curves are shifted to lower values of CO as the conversion degree increases from X_c = 0.25 to X_c = 0.75. Therefore, although the CO signal of $y_{CO,stable}$ is not affected by decomposition of K_2CO_3 its presence during gasification exerts an influence on the formation of active sites that remain stable during gasification.

4.4. Quantification of catalytically active and reactive sites during gasification of WC1600

Following the procedure for the determination of reactive sites proposed by Lizzio et al. [5], $y_{CO_2,stable}$ and $y_{CO,stable}$ are subtracted from $y_{CO_2,total}$ and $y_{CO,total}$ at each conversion degree (for $y_{CO_2,stable}$ the peak at 430 °C is excluded from the calculation as shown in Fig. 5(a)). As the results are influenced by the presence of ash in the samples, they are not only representative for the amount of reactive sites participating in the gasification reaction. Moreover, $y_{CO_2,total}$ and $y_{CO,total}$ include the amounts of CO_2 and CO that evolve when Ca and K undergo the conversion mechanisms that are responsible for their catalytic influence during gasification. Consequently, the CO_2 and CO spectra obtained following the procedure proposed by Lizzio et al. [5] in the present work are a measure for reactive sites and catalytically active sites representing the amount of K and Ca in ash that exerts a catalytic influence during gasification with CO_2.

The course of the obtained CO_2 signal for each conversion degree is presented in Fig. 5(a) together with the CO_2 signal of ash of the completely gasified sample (X_c = 1). In this figure, the strong influence of the presence of Ca in the TPD signal, and consequently during gasification, is noticeable as the peaks are very similar to that of the sample at X_c = 1. Moreover, as conversion increases the course of the signals tends to be similar to the one at X_c = 1. Contrary to the tendency of K to volatilize, Ca remains in the char during gasification [32]. Assuming that the catalytically active Ca remains constant during gasification it can be quantified by the amount of desorbed CO_2 of the sample completely gasified (X_c = 1) when cooling is performed in CO_2. Fig. 6(a) shows the calculated CO_2 amounts released from reactive plus catalytically active sites (bars marked with diagonal hatch pattern) obtained from the curves presented in Fig. 5(a). The calculated amounts for all conversion degrees (X_c = 0.25 to X_c = 0.90) are higher than the CO_2 amount released at X_c = 1. Extra CO_2 in samples partially gasified indicates that reactive sites participate in the gasification reaction. These reactive sites form oxygenated surface complexes, such as, lactone, peroxide or carboxylic anhydride that decompose and desorb as CO_2 in a similar temperature interval at which $CaCO_3$ decomposition takes place (as can be seen in Fig. 1). As shown in Fig. 6(a), the calculated extra CO_2 evolution is more pronounced in the early stages of gasification up to X_c = 0.5. From this conversion degree onwards, the amount of evolved CO_2 remains almost constant. Bars marked with crossed hatch pattern show the CO_2 amounts corresponding to stable

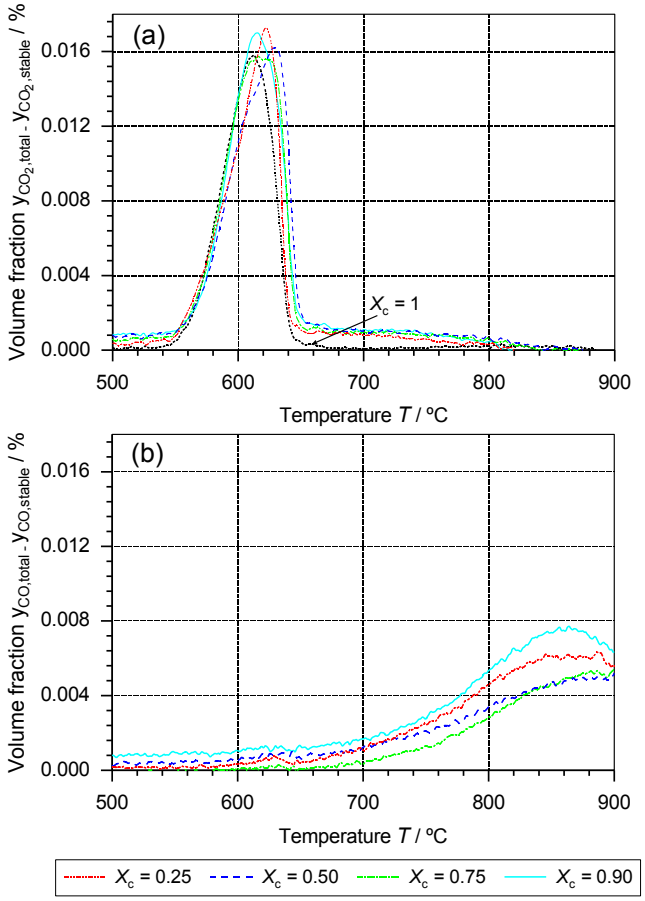

Fig. 5. TPD spectra as a function of temperature for carbon conversion degrees after partial gasification WC1600 accounting for catalytically active ash components and unstable surface complexes; a) CO_2 b) CO release.

sites. These are calculated from the CO_2 signals of Fig. 4(a) of part 1 of the present study [6] without the peak at 430 °C. The bars show a small decrease up to X_c = 0.75 followed by the increase at X_c = 0.90 attributed to the formation of oxygenated surface complexes. The slight decrease can be related to loss of K during gasification that, as stated in section 4.1, is responsible for the CO_2 evolution of the common course of the CO_2 signal.

Regarding CO, the curves presented in Fig. 5(b) show a similar course as the one obtained for total and stable complexes having a slight tendency to lower values as the conversion degree increases from X_c = 0.25 to X_c = 0.75 followed by the steep increase for the sample obtained until X_c = 0.90. In this case, it is not possible to set a baseline or to separate the contributions related to catalytically active sites due to the presence of K and reactive sites. K_2CO_3 decomposition takes place only in presence of C (according to (R9)). Consequently, oxygenated surface complexes must be present in the sample. The maximal CO amount that would evolve from K_2CO_3 decomposition using the initial K content of WC1600 presented in Table 1 and the stoichiometry of reaction of (R9) amounts to 0,0036 $g_{CO2}/g_{C,0}$. As it is the case for Ca, not all K is located on the char surface but rather in the carbon bulk of the char particle. Thus, not all K is available for carbonate formation and decomposition under gasification conditions. Moreover, the amount of K that is active during gasification can change continuously due to volatilization. However, for both CO and CO_2, the sum of the two contributions is a measure for the amount of sites on the surface of the char available for the gasification reaction. Released CO amounts corresponding to the sum of reactive sites plus catalytically active sites are calculated from the curves presented in Fig. 5(b) and presented in Fig. 6(b) (bars marked with diagonal hatch pattern). Crossed hatched bars of the same figure show the CO amounts released from stable complexes calculated from the curves presented in Fig. 4(a) of part 1 of the present study [6]. The results indicate that the ratio of reactive sites plus catalytically active sites vs. stable sites remains constant over the conversion degrees studied (see Fig. 4(b)). In the present work, the amount of reactive plus catalytically active sites for all conversion degrees studied amounts to 54% of the CO released in total. It seems reasonable to state that the presence of K has an influence in the formation of both stable and reactive surface complexes.

The amount of reactive plus catalytically active sites was calculated using Eq. 13 of part 1 of the present study [6]. The CO and CO_2 molar amounts in the bars marked with diagonal hatch pattern of Fig. 6 represent the differences of $(n_{CO,total} - n_{CO,stable})$ and $(n_{CO_2,total} - n_{CO_2,stable})$, respectively. This equation was originally defined assuming that desorbed CO and CO_2 were a measure of reactive sites only. However, as the obtained CO and CO_2 signals include the effect of decomposition and desorption of unstable surface complexes together with decomposition of catalytically active ash components, the calculated amount includes both contributions and is therefore designated as $x_{reactive+catalytic}$ in the present work.

The relation between the specific conversion rate R_m (see Eq. 1 of

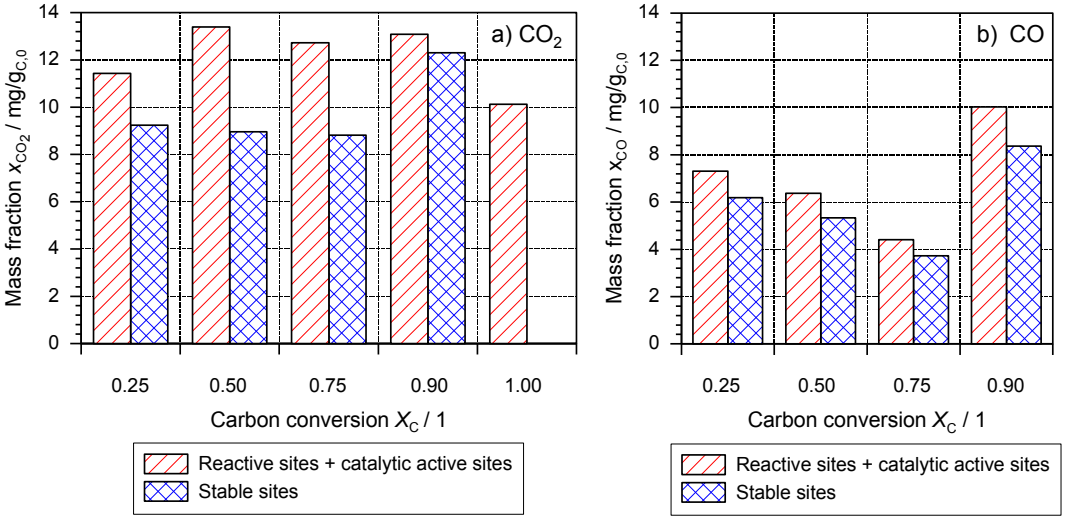

Fig. 6. CO_2 (a) and CO (b) amounts released as function of carbon conversion of WC1600 for catalytic active ash components, reactive surface complexes and stable surface complexes.

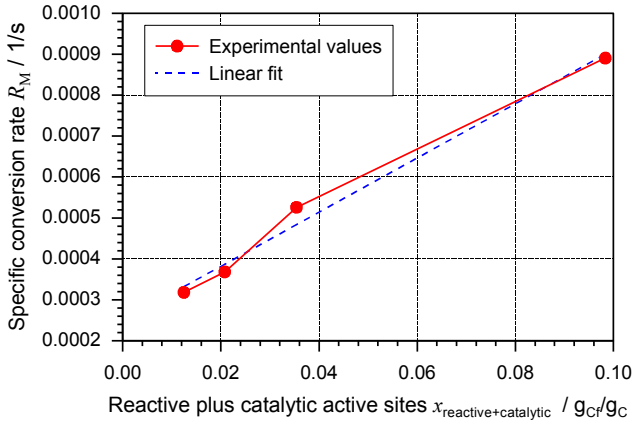

Fig. 7. Specific conversion rate vs. $x_{reactive+catalytic}$ for the gasification of WC1600 at 820 °C in 80 vol-% CO_2.

Table 3
Specific conversion rate constants k reported Lizzio et al. [5] and determined in present work. Calculated values of reactive sites using the TPD method and Eq. 1 of part 1 of the present work.

Fuel	Gasification temperature °C	k s^{-1}
Bituminous coal char [5]	820	0.003373
Saran char [5]	860	0.005947
Demineralized lignite char [5]	700	0.001366
Beech wood char (present work)	820	0.006616

part 1 [6]) and $x_{reactive+catalytic}$ (see Eq. 13 of part 1 [6]) is presented in Fig. 7. A linear correlation between R_m and $x_{reactive+catalytic}$ can be observed which is in accordance with Eq. 1 of part 1 of the present study [6]. As stated by Lizzio et al. [5], this equation implies that the surface concentration of active sites available for the gasification reaction (C_{C_f}) should be proportional to the specific conversion rate during the gasification reaction, as the specific conversion rate constant k depends only on temperature. The calculated values of $x_{reactive+catalytic}$ seem to be a quantitative measure for C_{C_f}. Moreover, this approach is able to include the effect of the catalytic influence exerted during gasification by the presence of K and Ca in ash of the sample.

Eq. (4) is an analytical expression for the linear fit of the experimental values presented in Fig. 7.

$$R_m = 0.006616 s^{-1} x_{reactive+catalytic} + 0.000249 s^{-1} \quad (4)$$

In conformity with Eq. 1 of part 1 of the present work [6], the slope of the linear fit (0.006616 s^{-1}) is a measure of the specific conversion rate constant k at T = 820 °C between X_C = 0.25 and X_C = 0.90. Mean values obtained by Lizzio et al. [5] using the same approach for the gasification of coal chars of different origins are presented in Table 3. As indicated in the literature review, they attempted to eliminate the influence of ash decomposition by only using the CO signal in their calculations. As shown in the table, despite the different materials the obtained values are of the same order of magnitude. However, it should be taken into account that the specific conversion rate constant k is exponentially dependent on temperature. Thus, a comparison of the values should be made with caution. For specific conversion rates lower than 0.0003 s^{-1} (or X_C < 0.25), the correlation is not proven, as the linear fit does not reach the zero value (y-intercept is 0.000249 s^{-1}).

5. Summary

During gasification of WC1600 with CO_2, three different kinds of sites on the char surface can be observed: stable and reactive sites as proposed and defined by Lizzio et al. [5] and additionally catalytically active sites which represent the influence of catalytically active components of ash. Release of CO_2 and CO during TPD of partially gasified samples of WC1600 using CO_2 as gasification agent is the result of decomposition of oxygenated surface complexes followed by desorption of the gaseous products as well as decomposition of carbonates of Ca and K. Decomposition of $CaCO_3$ is identified as the main source of CO_2 and that of K_2CO_3 as the main source of CO. The released amounts of CO_2 and CO are a measure of the catalytic influence of each metal in the gasification reaction. Moreover, the presence of Ca and K promote the creation of stable sites as well as reactive sites where oxygenated surface complexes are formed.

Due to the high pyrolysis temperature of the char investigated (WC1600), the char presumably exhibits a high grade of graphitization limiting the availability of active sites for the formation of oxygenated surface complexes. Hence, the catalytic gasification induced by Ca and K is the dominating process. Only at higher carbon conversion degrees (X_C = 0.90), an enhanced formation of both stable and reactive sites is observed.

A linear correlation between specific conversion rate R_m and the amount of reactive plus catalytically active sites is derived from the experimental data. This indicates that the calculated value is an appropriate measure of the available sites (reactive and catalytically active) on the char surface participating in the gasification reaction of WC1600 with CO_2.

Future experiments will focus on a wider range of experimental conditions in order to investigate the applicability of the correlation for the conversion rate in entrained-flow gasification. For now, the presented correlation for the conversion rate is only valid for one parameter set. Varying gasification temperature and CO_2 partial pressure is essential in order to further validate this model and extend the previous data set.

Declaration of Competing Interest

The authors declare that they have no known competing financial interests or personal relationships that could have appeared to influence the work reported in this paper.

Acknowledgments

The authors gratefully acknowledge the financial support by the Helmholtz Association of German Research Centres (HGF) in the frame of the Helmholtz Virtual Institute for Gasification Technology – HVIGasTech (VH-VI-429) and the German Academic Exchange Service (DAAD) for funding the research visits of Prof. Rincón Prat at KIT.

References

[1] Di Blasi C. Combustion and gasification rates of lignocellulosic chars. Prog Energy Combust Sci 2009;35(2):121–40. https://doi.org/10.1016/j.pecs.2008.08.001.
[2] Klose W, Wölki M. On the intrinsic reaction rate of biomass char gasification with carbon dioxide and steam. Fuel 2005;84(7):885–92. https://doi.org/10.1016/j.fuel.2004.11.016.
[3] Mahinpey N. Review of gasification fundamentals and new findings: Reactors, feedstock, and kinetic studies. Chem Eng Sci 2016;148:14–31. https://doi.org/10.1016/j.ces.2016.03.037.
[4] Irfan M, Usman M, Kusakabe K. Coal gasification in CO_2 atmosphere and its kinetics since 1948: a brief review. Energy 2011;36:12–40. https://doi.org/10.1016/j.energy.2010.10.034.
[5] Lizzio AA, Jiang H, Radovic LR. On the kinetics of carbon (Char) gasification: Reconciling models with experiments. Carbon 1990;28(1):7–19. https://doi.org/10.1016/0008-6223(90)90087-F.
[6] Schneider C, Rincon S, Kolb T. Determination of active sites during gasification of biomass char with CO_2 using temperature-programmed desorption. Part 1: Methodology & Desorption Spectra. Fuel 2019. https://doi.org/10.1016/j.fuel.2019.116726.
[7] Kyotani T, Karasawa S, Tomita A. A TPD study of coal chars in relation to the catalysis of mineral matter. Fuel 1986;65(10):1466–9. https://doi.org/10.1016/0016-2361(86)90125-0.
[8] Kyotani T, Zhang Z, Hayashi S, Tomita A. TPD study on H_2O-gasified and O_2-chemisorbed coal chars. Energy Fuels 1988;2(2):136–41. https://doi.org/10.1021/

ef00008a006.
[9] Guizani C, Jeguirim M, Gadiou R, Escudero Sanz FJ, Salvador S. Biomass char gasification by H_2O, CO_2 and their mixture: evolution of chemical, textural and structural properties of the chars. Energy 2016;112:133–45. https://doi.org/10.1016/j.energy.2016.06.065.
[10] Figueiredo JL, Pereira MFR, Freitas MMA, Órfão JJM. Characterization of Active Sites on Carbon Catalysts. Ind. Eng. Chem. Res. 2007;46(12):4110–5. doi:10.1021/ie061071v.
[11] de la Puente G, Pis JJ, Menéndez JA, Grange P. Thermal stability of oxygenated functions in activated carbons. J Anal Appl Pyrol 1997;43:125–38. https://doi.org/10.1016/S0165-2370(97)00060-0.
[12] Marsh H, Heintz E, Rodriguez-Reinoso F. Introduction to carbon techologies. Alicante: Universidad de Alicante; 1997.
[13] Szymański GS, Karpiński Z, Biniak S, Świątkowski A. The effect of the gradual thermal decomposition of surface oxygen species on the chemical and catalytic properties of oxidized activated carbon. Carbon 2002;40(14):2627–39. doi:10.1016/S0008-6223(02)00188-4.
[14] Tremblay G, Vastola FJ, Walker Jr PL. Thermal desorption analysis of oxygen surface complexes on carbon. Carbon 1978;16(1):35–9.
[15] Figueiredo, JL, Pereira MFR, Freitas MMA, Órfao JJM. Modification of the surface chemistry of activated carbons. Carbon 1999;37(9):1379–89. doi:10.1016/S0008-6223(98)00333-9.
[16] Hall P, Calo J. Secondary interactions upon thermal desorption of surface oxydes from coal chars. Energy Fuels 1989;3(3):370–6. https://doi.org/10.1021/ef00015a020.
[17] Boehm HP. Surface oxides on carbon and their analysis: a critical assessment. Carbon 2002;40(2):145–9. https://doi.org/10.1016/S0008-6223(01)00165-8.
[18] Zhou JH, Sui ZJ, Zhu J, Li P, Chen D, Dai YC, et al. Characterization of surface oxygen complexes on carbon nanofibers by TPD, XPS and FT-IR. Carbon 2007;45(4):785–96. https://doi.org/10.1016/j.carbon.2006.11.019.
[19] Kundu S, Wang Y, Muhler M. Thermal stability and reducibility of oxygen-containing functional groups on multiwalled carbon nanotube surfaces: a quantitative high-resolution XPS and TPD/TPR study. J Phys Chem C 2008;112(43):16869–78. https://doi.org/10.1021/jp804413a.
[20] Ishii T, Kyotani T. Temperature Programmed Desorption. In: Inagaki M, Kang F, editors. Materials Science and Engineering of Carbon: Characterization Elsevier; 2016. https://doi.org/10.1016/C2014-0-03769-0.
[21] Du C, Liu L, Qiu P. Importance of volatile AAEM species to char reactivity during volatile–char interactions. RSC Adv 2017;7(17):10397–406. https://doi.org/10.1039/C6RA27485D.
[22] Matsuoka K, Yamashita T, Kuramoto K, Suzuki Y, Takaya A, Tomita A. Transformation of alkali and alkaline earth metals in low rank coal during gasification. Fuel 2008;87(6):885–93. https://doi.org/10.1016/j.fuel.2007.05.031.
[23] Nzihou A, Stanmore B, Sharrock P. A review of catalysts for the gasification of biomass char, with some reference to coal. Energy 2013;58:305–17. https://doi.org/10.1016/j.energy.2013.05.057.
[24] Cazorla-Amoros D, Linares-Solano A, Salinas-Martinez de Lecea C, Yamashita H, Kyotani T, Tomita A, et al. XAFS and thermogravimetry study of the sintering of calcium supported on carbon. Energy Fuels 1993;7(1):139–45. https://doi.org/10.1021/ef00037a022.
[25] Mu J, Perlmutter DD. Thermal decomposition of carbonates, carboxylates, oxalates, acetates, formates, and hydroxides. Thermochim Acta 1981;49(2):207–18. https://doi.org/10.1016/0040-6031(81)80175-X.
[26] Rodriguez-Navarro C, Ruiz-Agudo E, Luque A, Rodriguez-Navarro AB, Ortega-Huertas M. Thermal decomposition of calcite: Mechanisms of formation and textural evolution of CaO nanocrystals. Am Miner 2009;94(4):578–93. https://doi.org/10.2138/am.2009.3021.
[27] Dollimore D, Tong P, Alexander KS. The kinetic interpretation of the decomposition of calcium carbonate by use of relationships other than the Arrhenius equation. Thermochim Acta 1996;282–283:13–27. https://doi.org/10.1016/0040-6031(95)02810-2.
[28] Sinkó K, Pöppl M, Gábor M, Migály B. Study of the binary $CaCO_3$-SiO_2 system by quantitative DTA. J Therm Anal 1988;33(3):1003–11. https://doi.org/10.1007/BF02138623.
[29] McKee DW. Catalytic effects of alkaline earth carbonates in the carbon-carbon dioxide reaction. Fuel 1980;59(5):308–14. https://doi.org/10.1016/0016-2361(80)90215-X.
[30] Lehman RL, Gentry JS, Glumac NG. Thermal stability of potassium carbonate near its melting point. Thermochim Acta 1998;316(1):1–9. https://doi.org/10.1016/S0040-6031(98)00289-5.
[31] Arvelakis S, Jensen PA, Dam-Johansen K. Simultaneous thermal analysis (STA) on ash from high-alkali biomass. Energy Fuels 2004;18(4):1066–76. https://doi.org/10.1021/ef034065+.
[32] Kopyscinski J, Rahman M, Gupta R, Mims CA, Hill JM. K_2CO_3 catalyzed CO_2 gasification of ash-free coal. Interactions of the catalyst with carbon in N_2 and CO_2 atmosphere. Fuel 2014;117:1181–9. https://doi.org/10.1016/j.fuel.2013.07.030.
[33] Hyatt EP, Cutler IB, Wadsworth ME. Calcium carbonate decomposition in carbon dioxide atmosphere. J Am Ceram Soc 1958;41(2):70–4. https://doi.org/10.1111/j.1151-2916.1958.tb13521.x.
[34] Brown I. Thermodynamic modelling of reactions in materials chemistry. Chemistry in New Zealand 2014.
[35] Zhao H, Xu W, Song Q, Zhuo J, Yao Q. Effect of steam and SiO_2 on the release and transformations of K_2CO_3 and KCl during biomass thermal conversion. Energy Fuels 2018;32(9):9633–9. https://doi.org/10.1021/acs.energyfuels.8b02269.
[36] Biernacki JJ, Wotzak GP. Stoichiometry of the C + SiO_2 reaction. J Am Ceram Soc 1989;72(1):122–9. https://doi.org/10.1111/j.1151-2916.1989.tb05964.x.
[37] Henderson JB, Tant MR. A study of the kinetics of high-temperature carbon-silica reactions in ablative polymer composite. Polym Compos 1983;4:233–7. https://doi.org/10.1002/pc.750040408.
[38] Hüttinger KJ, Nill JS. A method for the determination of active sites and true activation energies in carbon gasification: (II) experimental results. Carbon 1990;28(4):457–65. https://doi.org/10.1016/0008-6223(90)90039-2.
[39] Anicic B, Lin W, Dam-Johansen K, Wu H. Agglomeration mechanism in bioass fluidized bed combustion – Reaction between potassium carbonate and silica sand. Fuel Process Technol 2018;173:182–90. https://doi.org/10.1016/j.fuproc.2017.10.005.
[40] Vassilev S, Baxter D, Andersen L. Vassileva Ch. An overview of the composition and application of biomass ash. Part 1. Phase-mineral chemical composition and classification. Fuel 2013;105:40–76.
[41] Kahn N, Dollimore D, Alexander K, Wilburn FW. The origin of the exothermic peak in the thermal decomposition of basic magnesium carbonate. Thermochim Acta 2001;367–368:321–33. https://doi.org/10.1016/S0040-6031(00)00669-9.
[42] Newkirk A, Aliferis I. Drying and decomposition of sodium carbonate. Anal Chem 1958;30(5):982–4. https://doi.org/10.1021/ac60137a031.
[43] Fox D, White A. Effect of sodium carbonate upon gasification of carbon and production of producer gas. Ind Eng Chem Res 1931;23(3):259–66. https://doi.org/10.1021/ie50255a011.
[44] Furimsky E, Sears P, Suzuki T. Iron-catalyzed gasification of char in CO_2. Energy Fuels 1988;2(5):634–9. https://doi.org/10.1021/ef00011a005.
[45] Thy P, Lesher CE, Jenkins BM. Experimental determination of high-temperature elemental losses from biomass slag. Fuel 2000;79(6):693–700. https://doi.org/10.1016/S0016-2361(99)00195-7.
[46] Li Q, Meng A, Li L, Zhou H, Zhang Y. Investigation of biomass ash thermal decomposition by thermogravimetry using raw and artificial ashes. Asia-Pac J Chem Eng 2014;9(5):726–36. https://doi.org/10.1002/apj.1817.
[47] Radović LR, Walker PL, Jenkins RG. Importance of carbon active sites in the gasification of coal chars. Fuel 1983;62(7):849–56. https://doi.org/10.1016/0016-2361(83)90041-8.
[48] McKee DW. Gasification of graphite in carbon dioxide and water vapor – the catalytic effects of alkali metal salts. Carbon 1982;20(1):59–66. https://doi.org/10.1016/0008-6223(82)90075-6.
[49] Spiro C, McKee D, Kosky P, Lamby E. Catalytic CO_2-gasification of graphite versus coal char. Fuel 1983;62(2):180–4. https://doi.org/10.1016/0016-2361(83)90194-1.
[50] Linares-Solano A, Almela-Alarcón M. Salinas-Martínez de Lecea C. CO_2 chemisorption to characterize calcium catalyst in carbon gasification reactions. J Catal 1990;125(2):401–10. https://doi.org/10.1016/0021-9517(90)90313-9.

Fuel 267 (2020) 116726

Contents lists available at ScienceDirect

Fuel

journal homepage: www.elsevier.com/locate/fuel

Full Length Article

Determination of active sites during gasification of biomass char with CO_2 using temperature-programmed desorption. Part 1: Methodology & desorption spectra

Christoph Schneider[a,*], Sonia Rincón Prat[b], Thomas Kolb[a,c]

[a] Karlsruhe Institute of Technology, Engler-Bunte-Institute, Fuel Technology, EBI-ceb, Engler-Bunte-Ring 1, 76131 Karlsruhe, Germany
[b] Universidad Nacional de Colombia, Departamento de Ingeniería Mecánica y Mecatrónica, Grupo de Investigación en Biomasa y Optimización Térmica de Procesos, BIOT, Carrera 30 No 45A-03, Bogotá, Colombia
[c] Karlsruhe Institute of Technology, Institute for Technical Chemistry, ITC-vgt, Hermann-von-Helmholtz-Platz 1, 76344 Eggenstein-Leopoldshafen, Germany

ARTICLE INFO

Keywords:
Biomass char
Gasification kinetics
Surface chemistry
Temperature-programmed desorption
Active sites

ABSTRACT

Based on a carbon conversion mechanism for the gasification of carbon with CO_2, a method for the determination of active sites during gasification of biomass char is presented. Beech wood char was partially gasified in CO_2 followed by a temperature-programmed desorption (TPD) in order to determine total and stable surface complexes as a function of carbon conversion degree. The experiments were conducted in a temperature controlled quartz glass reactor coupled with a mass spectrometer for the detection of desorbed gas species (CO and CO_2). Similar CO_2 signals for total and stable surface complexes are observed for all carbon conversion degrees. Increased release of CO during the determination of total and stable surface complexes is detected for $X_C = 0.9$ carbon conversion degree. The desorption spectra of CO and CO_2 during TPD cannot completely be explained by the underlying mechanistic model. The measured concentration profiles indicate that the gas species released during TPD may originate from decomposition of surface complexes but also from decomposition of ash components. CO and CO_2 arising from of ash components or surface complexes must be differentiated in order to determine reactive surface area (RSA) as a function of carbon conversion degree which is then transferred into a kinetic rate expression for the specific conversion rate R_m. This paper describes the methodology applied for the determination of RSA and discusses the raw data obtained during TPD. In part 2, a detailed analysis concerning the origin of the released gases during TPD is conducted.

1. Introduction

The biomass gasification process has gained wide attention following the discussion on utilization of renewable sources for production of chemicals and the supply of power and heat. The syngas from entrained flow gasification of biogenic residues is suitable for the production of a wide variety of liquid fuels (gasoline, diesel), gaseous fuels (synthetic natural gas) and chemicals (methanol, dimethyl-ether – DME, ethanol, ammonia), as well as electric power (gas turbines and integrated gasification combined cycle plants) [1]. The present work is part of the research activities of the BtL bioliq® project which includes a gasification step in a 5 MW_{th} input high-pressure oxygen-blown entrained flow gasifier (EFG). As feedstock for the gasifier, a suspension fuel (slurry) based on pyrolysis oil and char, produced from biogenic residues (e.g. straw) in a fast pyrolysis process is used. [2]. The slurry is fed to the gasifier via a burner, inside the reactor the liquid phase of the slurry droplets evaporates rapidly. Subsequently, the char is heated up and undergoes a secondary pyrolysis process characterized by high heating rates. Downstream of the gasifier flame zone the secondary char reacts with H_2O and CO_2 to the final syngas. As the heterogeneous secondary char gasification is the rate-determining step of the gasification process, understanding the complex physical and chemical processes that take place during the gasification reactions has been identified as one of the knowledge gaps that restrict mathematical modelling and design of technical entrained flow gasifiers.

2. Literature review

The heterogeneous gasification of char particles is controlled by process parameters, i.e. temperature, partial pressure of the reactant gas and process pressure as well as the chemical and physical properties of the char. Char properties change as char conversion proceeds, which

* Corresponding author.
E-mail addresses: ch.schneider@kit.edu (C. Schneider), slrinconp@unal.edu.co (S. Rincón Prat), thomas.kolb@kit.edu (T. Kolb).

https://doi.org/10.1016/j.fuel.2019.116726
Received 9 September 2019; Received in revised form 19 November 2019; Accepted 21 November 2019
Available online 10 December 2019
0016-2361/

in turn causes changes in char conversion rate with progressing conversion degree. Although the properties of biomass chars have been studied extensively [3], less attention has been paid to the fundamental understanding of the reaction mechanisms and the role of the variable chemical and physical properties of the char during the gasification process. The relevant physical properties are total internal surface area, porosity, pore size distribution and char carbonaceous structure and ordering [4]. Chemical properties of char affecting conversion rate are related to active sites and functional groups available at the char surface as well as to the presence of catalytic minerals embedded as ash in the char particle.

The oxygen exchange mechanism presented in R1 to R3 [5] is widely accepted as reaction mechanism describing the carbon/char gasification with CO_2.

$$C_f + CO_2 \xrightarrow{k_1} C(O) + CO \quad (R1)$$

$$C(O) + CO \xrightarrow{k_2} C_f + CO_2 \quad (R2)$$

$$C(O) \xrightarrow{k_3} CO \quad (R3)$$

C_f represents an active site on the char surface and C(O) a carbon-oxygen intermediate, respectively. Assuming first-order dependency on carbon concentration and pseudo zero-order dependency on gas concentration, the specific conversion rate R_m can be written according to the fundamental kinetic expression [6]

$$R_m = -\frac{1}{m_C(t)}\frac{dm_c}{dt} = \frac{1}{1 - X_C(t)}\frac{dX_C}{dt} = kC_{C_f} \quad (1)$$

where C_{C_f} is the surface concentration of active sites available for the reaction, X_C the carbon conversion degree and $\frac{dX_C}{dt}$ the carbon conversion rate. For modeling of the char gasification process, the concentration of carbon active sites has to be determined as a function of carbon conversion degree. The carbon conversion degree can be expressed by a mass balance with $m_C(t)$ as the time dependent and $m_{C,0}$ as the initial carbon mass:

$$X_C(t) = \frac{m_{C,0} - m_C(t)}{m_{C,0}} \quad (2)$$

Wölki [7] presented a detailed summary of kinetic expressions for biomass char gasification with H_2O and CO_2 under atmospheric pressure. These expressions do not take into account the evolution of chemical or physical properties of chars during gasification reaction. Thus, they are only valid for a certain carbon conversion degree range [3,8]. Other authors have included a term that accounts for changes in physical properties in the kinetic equations. In a review on combustion and gasification rates of ligno cellulosic chars, Di Blasi [3] presented expressions that include a structural term which depends exclusively on char conversion degree. More complex particle models account for the variation of physical properties of the char during gasification in terms of porosity, pore diameter and length as well as total surface area. Lizzio et al. [9] give a summary of five coal gasification models that include general expressions for the variation of structural parameters e.g. the random pore model (RPM) of Bathia and Perlmutter [10] describing growth and collapse of the pore structure of a char particle during conversion. Regarding biomass char gasification, Gómez-Barea and Leckner [11] present a summary of existing structural models. The RPM and its modifications (MRPM) have been successfully used in some cases concerning biomass char gasification [12–16]. Moreover, Fatehi and Bai [17] as well as Singer and Ghoniem [18] propose models describing the evolution of a multimodal pore structure. Experimental values for the variation of structural properties i.e. specific surface area, pore size distribution and porosity of biomass char during gasification can be found in literature [4,19–21]. Although these structural models describe the evolution of carbon conversion and conversion rate, their application is restricted as the model parameters are very difficult to be determined experimentally.

Studies on the reaction kinetics of biomass char gasification addressing the influence of chemical properties use the theory of active sites developed in the working group of Walker. The approach was presented originally by Laine et al. [22] in 1963 and further developed until the early nineties [6,9,23]. The theory is based on the mechanistic understanding of catalytic heterogeneous reactions where the catalytic activity is proportional to the active surface area (ASA) of the catalyst. As presented in reactions R1 to R3, gasification proceeds via oxygenated surface complexes, so-called carbon-oxygen intermediates (C(O)). Thus, the quantity of these complexes available for the reaction is a direct measure of the specific conversion rate. A first approximation of the quantification of the surface area available for the reaction is the utilization of the total accessible surface area (TSA) determined by physical adsorption and applying the Brunauer-Emmett-Teller (BET) [24] or Dubinin-Radushkevich (DR) [25] models. The evolution of TSA during char gasification can be predicted by the models mentioned above. These approaches assume either that the gasification reactions occur everywhere on the char surface (TSA) or that there is a linear relationship between ASA and TSA. However, this model concept is not able to explain the correlation between char surface and conversion rate, since chars of similar TSA can show significantly different conversion rates and a linear relationship between conversion rate and TSA has not been reported [4,6,20,22].

The quantification of the surface area available for the reaction can be accomplished by measurement of the amount of oxygenated surface complexes formed during gasification by the temperature-programmed desorption technique. Oxygenated surface complexes are bound on the surface of carbonaceous materials in the form of oxygen functional groups, such as lactones, carbonyls, anhydrides, phenols, ethers and quinones. During desorption, the bonds of these functional groups are destroyed resulting in the release of the gaseous species such as CO, CO_2 and H_2O [26–30].

Laine et al. [22] proposed an approach based on their research on the carbon – oxygen reaction of highly purified graphitized carbon black. They determined the active surface area from the quantity of surface complexes formed on in situ partially oxidized samples through chemisorption experiments with oxygen at 300 °C followed by a desorption *in vacuo* up to 950 °C. They define the unoccupied active surface area (UASA), which corresponds to the term reactive surface area used later in the present work, as the quantity of active sites at which the reaction occurs and no formation of stable complexes takes place. Stable complexes are defined as being formed during reaction remaining on the surface at reaction conditions i.e. blocking active sites for further reaction. Wölki [7] presents a summary of numerous investigations that followed the procedure proposed by Laine et al. [22] for the measurement of ASA on chars using O_2, CO_2 and H_2O as reactive gases. Although in these investigations no linear relationship between specific conversion rate and experimentally determined ASA was found, it could be concluded that ASA depends on temperature and partial pressure of the reactive gas. The value of ASA is only a small fraction of the total surface area (TSA). These findings reveal that a suitable approach for the experimental determination of available active sites during char conversion is the UASA and not the ASA from low temperature chemisorption [9,31]. 23 years after Laine et al. [10], Lizzio et al. [9] introduced the concept of reactive surface area (RSA) as a measure for active sites that are capable to chemisorb the reactant gas dissociatively but do not form a stable complex (C-O). These authors add an extra step (R4 and R5) to the oxygen exchange mechanism presented before accounting for the formation of a stable C-O complex from a carbon–oxygen intermediate during gasification.

$$C_f + CO_2 \xrightarrow{k_1} C(O) + CO \quad (R1)$$

$$C(O) + CO \xrightarrow{k_2} C_f + CO_2 \quad (R2)$$

$$C(O) \xrightarrow{k_4} C\text{-}O \quad \text{(R4)}$$

$$C\text{-}O \xrightarrow{k_5} C(O) \quad \text{(R5)}$$

$$C\text{-}C(O) \xrightarrow{k_6} CO + C_f \quad \text{(R3*)}$$

The carbon–oxygen intermediate C(O) desorbs either as CO (R3*), leaving a new active carbon site C_f or forms a stable complex C–O (R4). This mechanism is based on the assumption that reactions R4 and R5 are in equilibrium at constant temperature. Furthermore, it is assumed that stable complexes C-O cannot be desorbed. Accounting for a closed carbon balance, the reaction R3* has been slightly modified as compared to literature. R3* produces a new carbon active site as long as excess carbon is available [9].

The determination of RSA requires experiments at reaction temperature either using temperature programmed desorption (TPD) or transient kinetics (TK) [7,9]. The method of transient kinetics proposed by Freund [32] for the study of desorption of oxygen surface complexes allows a direct determination of RSA. After gasification to a desired carbon conversion degree, the flow of reacting gas is changed to inert gas and the desorption of oxygen containing gases is continuously recorded. The quantity of desorbed gases corresponds to the number of reactive sites available at the experimental conditions chosen. The suitability of the method was intensively studied and proven by Radovic et al. [9,33,34]. The method was also applied by other authors concerning the study of gasification reactions of coal chars [35,36]. The TPD method was successfully used by several authors for the determination of surface complexes of partially gasified char samples [8,9,37–39]. RSA is determined indirectly based on a two-step procedure proposed by Lizzio et al. [9]. In a first experiment (procedure 1), a partially gasified sample is quenched in reactant gas. As the activation energies for adsorption and migration of oxygen species are lower than the activation energy for desorption, the desorbed unstable C(O) complexes are quickly replaced by new C(O) complexes in the presence of excess CO_2 during the quench procedure [40]. Thus, all carbon oxygen intermediates (stable C-O and unstable C(O) complexes) are preserved. In a second experiment (procedure 2) using the same gasification conditions, the flow of reactant gas is switched to inert gas at reaction temperature. In this case, unstable C(O) complexes desorb while stable C-O complexes remain on the char surface. The quantification of total surface complexes (TSC) (procedure 1) and stable complexes (procedure 2) is accomplished by submitting the samples to temperature-programmed desorption, measuring the amount of released oxygen-containing gases. RSA is calculated as the difference between total and stable surface complexes. A detailed description of the experimental procedure is given in chapter 3.

Research that concentrates on the measurement of the formation of active sites during gasification of biomass char is rare. Klose & Wölki [8] presented experimental results in 2005 on the quantification of RSA using the TPD procedure for the gasification of beech wood char and oil palm shell char with CO_2 and H_2O. They determined kinetic parameters for the intrinsic reaction rate using a Langmuir-Hinshelwood type rate expression and found a linear relationship between the measured RSA and the reaction rate. Zoulalian et al. [41] developed a mathematical model that accounts for the evolution of RSA with increasing carbon conversion degree. The theoretical results are in good agreement with the experimental work presented by Lizzio et al. [9] and Klose & Wölki [8]. Guizani et al. [4] studied variations in chemical and physical properties of beech wood char during gasification with CO_2, H_2O and its mixtures. They conducted TPD experiments of partially gasified samples, where the flow of reactive gas was switched to nitrogen and quickly cooled down after reaching the desired conversion degree. Interpreting the concentration over temperature profiles of the released gas species, they qualitatively determined possible oxygenated functional groups present in the samples based on literature data.

In order to further improve the fundamental understanding of phenomenological changes during char gasification, in this work, an experimental method for quantification of total, stable and unstable complexes during gasification of a biomass char based on the method proposed by Lizzio et al. [9] and Klose & Wölki [8] is applied. However, special focus is put on the interpretation of the gas species profiles in order to determine the contributions of desorption of oxygenated surface complexes and possible influence of ash decomposition reactions during TPD. The validity of the mechanism based on Lizzio et al. [9] is applied to describe the gasification process of a biomass char pyrolyzed in a drop-tube reactor. The experimental determination of total surface complexes (TSC), stable complexes (C-O in equilibrium with C(O) in R4 and 5) and unstable complexes (C(O) leading to the formation and desorption of gaseous CO in R3*) is presented.

$$C_f + CO_2 \overset{k_{1,2}}{\leftrightarrow} C(O) + CO \quad \text{(R1-R2)}$$

$$C(O) \overset{k_{4,5}}{\leftrightarrow} C\text{-}O \quad \text{(R4-R5)}$$

$$C\text{-}C(O) \xrightarrow{k_6} CO + C_f \quad \text{(R3*)}$$

3. Materials and methods

3.1. Biomass char characterization

The biomass char used in this study was produced from a bark-less beech wood. Wood chips were chopped and fed to a screw-pyrolysis reactor which is described elsewhere [42,43]. The primary pyrolysis was conducted at 500 °C at a residence time of five minutes for the solid material. The resulting char was milled and sieved to particle sizes in the range of 50 to 150 µm. The char underwent a secondary pyrolysis in a drop-tube reactor at 1600 °C in order to produce a char with low volatile content under high heating rates and short residence time (200 ms), i.e. the char was produced under typical conditions of entrained-flow gasification (EFG). The char (WC1600) [44] was sieved to a 50–100 µm fraction. Physical and chemical data of the biomass char can be found in Table 1.

3.2. Experimental set-up

Experiments in terms of partial gasification and temperature-programmed desorption (TPD) at atmospheric pressure were carried out in

Table 1
Properties of WC1600.

Proximate analysis/wt.-%, ad	
Moisture	1.1
Ash content	6.6
Volatiles	4.6
Fixed carbon	87.7
Ultimate analysis/wt.-%, daf	
C	97.4
H	< 0.1
O (diff)	1.6
N	1.0
Ash composition analysis/wt.-%	
Na_2O	0.5
K_2O	9.1
MgO	1.6
CaO	30.1
Fe_2O_3	2.6
Al_2O_3	3.5
SiO_2	25.8
Structural parameters	
Specific Surface Area/$m^2\ g^{-1}$	62.1
Skeletal density/g cm^{-3}	2.0
Hg intrusion porosity/%	83.4

a chemisorption analyzer (MicrotracBEL, BELCAT-II). A schematic drawing of the reactor system is given in the supplementary material section. The reactor consists of two concentric quartz glass tubes. The reactant gas is introduced through the outer tube to be heated up to reaction temperature. The char sample is positioned between two quartz wool layers in the inner tube of the reactor (inner diameter d = 8 mm). The sample temperature is monitored by a type K thermocouple. Gas species (CO, CO_2, Ar) are continuously analyzed by a quadrupole mass spectrometer (MS) (IPI, GAM 400). The char sample is quenched by cooling the external surface of the outer reactor tube with air at ambient temperature.

3.3. Experimental procedure

Raw biomass char was gasified up to conversion degrees Xc of 0.25, 0.50, 0.75 and 0.90. Prior to each gasification procedure, the char sample was degassed for 1 h at 900 °C in flowing Ar and cooled down to gasification temperature. In the next step, partial gasification up to the desired carbon conversion degree at 820 °C and atmospheric pressure in 80 vol–% CO_2 and 20 vol-% Ar was conducted. A sample mass of 30 mg and a total volume gas flow of $\dot{V}_{in,STP}$ = 100 ml min^{-1} were applied in order to avoid transport limitations. With these process parameters, a maximum reduction of CO_2 concentration due to reaction below 3 vol-% was assured, i.e. the chemisorption analyzer was operated as differential reactor.

For the determination of total surface complexes (TSC), the sample was quenched to 200 °C in reactant gas atmosphere. After the CO concentration detected in the off-gas reached baseline level, i.e. no more gasification took place, the gas atmosphere was switched to Ar. Subsequently, a TPD was performed in flowing Ar ($\dot{V}_{STP}$= 50 ml min^{-1}) with a heating rate of 3 K/min to a final temperature of 900 °C. This temperature was kept constant for 1 h to achieve complete desorption of surface complexes. Volume fractions of CO and CO_2 ($y_{CO,total}$ and $y_{CO_2,total}$) were measured in the off-gas and plotted over time (see Fig. 3).

For the determination of stable C-O complexes, the experimental procedure was modified. After gasifying the char to the desired carbon conversion degree, the gas atmosphere was switched to Ar at reaction temperature in order to desorb all unstable C(O) complexes. After the CO and CO_2 concentrations reached zero level, the char sample was quenched in flowing Argon to 200 °C. Again, a TPD was performed as described previously and volume fractions of CO and CO_2 ($y_{CO,stable}$ and $y_{CO_2,stable}$) were measured (see Fig. 3).

In both experimental procedures, quenching from 820 °C to 400 °C was achieved within 5 min. The time required for the additional cooling to 200 °C was 7 min. In order to set a base line for the CO and CO_2 signals, blank experiments without char sample using only Ar as carrier gas were performed following the same heating program as the one for the determination of total surface complexes. Here, no CO_2 signal was observed, the CO signal, however, showed a continuous increase beginning at approx. 450 °C up to 0,003 vol-% at 900 °C. This baseline signal was subtracted from all CO signals obtained.

3.4. Data analysis

3.4.1. Gas phase analysis

Calibration of the MS was carried out for CO, CO_2 and Ar before and after each experiment. Mass flow controllers of the chemisorption analyzer were also checked versus a volumetric flowmeter (Ellutia, 7000 GC Flowmeter). The following equations were used to assign ion currents of a certain mass-to-charge ratio to the corresponding gas volume fractions of Ar and CO_2 [45]:

$$I_{40}(t) = S_{Ar} p_{total} y_{Ar}(t) \tag{3}$$

$$I_{44}(t) = S_{CO_2} p_{total} y_{CO_2}(t) \tag{4}$$

Here, $I_{m/z}$ is the ion current of a certain mass-to-charge ratio (m/z), S_i is the sensitivity of the gas species i, p_{total} is the total pressure (1 bar) and y_i is the volume fraction of the gas species i. Difficulties in the determination of the CO concentration arise from fragmentation of CO_2. This effect needs to be taken into account by a relative intensity a_{28} at a mass-to-charge ratio of 28:

$$a_{28} = \frac{I_{28}}{I_{44}} \tag{5}$$

$$I_{28}(t) = S_{CO_2} a_{28} p_{total} y_{CO_2}(t) + S_{CO} p_{total} y_{CO}(t) \tag{6}$$

Experimental values for a_{28} in the range of 0.090–0.095 are in good agreement with literature [46]. Sensitivities S_i and relative intensity a_{28} were determined for each experiment. Calibrations were carried out with 3 vol-% CO, 5 vol-% CO_2 and 80 vol-% CO_2 in Argon.

3.4.2. Calculation of carbon conversion degree

Considering only the Boudouard Reaction, the carbon conversion degree X_C can be calculated by a carbon balance according to following equations (Eqs. 7–10):

$$\frac{dX_C}{dt} = \frac{y_{CO}(t)}{2} \frac{M_C}{m_C} \dot{n}_{out}(t) \tag{7}$$

$$\dot{n}_{out}(t) = (\dot{n}_{Ar,in} + \dot{n}_{CO_2,in}) \frac{1}{1 - 0.5 y_{CO,out}(t)} \tag{8}$$

M_C represents the molar mass of carbon, m_C the converted mass of carbon which was calculated from the CO signal in the exhaust gas by a carbon balance (Eq. 7) and $\dot{n}_{out}$ the molar gas flow of the exhaust gas which can be calculated from the inlet gas flows of Ar and CO_2 and the measured CO concentration in the off-gas. The converted mass of carbon m_C can be calculated as:

$$m_C = \frac{M_C}{2} \int_0^{t_{end}} y_{CO}(t) \dot{n}_{out}(t) dt \tag{9}$$

Finally, the time dependent carbon conversion degree $X_C(t)$ is calculated by:

$$X_C(t) = \frac{\int_0^t y_{CO}(t) \dot{n}_{out}(t) dt}{\int_0^{t_{end}} y_{CO}(t) \dot{n}_{out}(t) dt} \tag{10}$$

Specific conversion rate R_m as a function of carbon conversion degree is calculated according to Eq. 1.

3.4.3. Analysis of released CO and CO_2 signals during TPD

Molar flows of CO_2 and CO during TPD are determined according to Eq. 11 with i being either CO or CO_2. This equation takes into account the increment in the gas flow due to the released gas during TPD. The amount of desorbed gas species n_{CO} and $n_{CO_2}$is determined by integration of Eq. 11 (see Eq. 12).

$$\dot{n}_i(t) = y_i(t) \left(1 + \frac{y_{CO_2}(t)}{y_{Ar}(t)} + \frac{y_{CO}(t)}{y_{Ar}(t)}\right) \frac{p_{STP} \dot{V}_{Ar}}{R T_{STP}} \tag{11}$$

$$n_i = \int_0^{t_{end}} \dot{n}_i(t) dt \tag{12}$$

The total quantity of active sites where surface complexes are formed is calculated assuming that one surface complex contains one oxygen atom. The number of complexes is determined by summing up the amount of oxygen atoms released in CO and CO_2 during TPD. This approach is valid for total, stable and unstable complexes using the corresponding CO and CO_2 signals. In the present work, the mass specific quantity of reactive sites $x_{reactive}$ is expressed as the mass fraction of carbon atoms on which surface complexes participating in the gasification reaction are formed (C_f) divided by the actual mass of carbon according to the following expression [22].

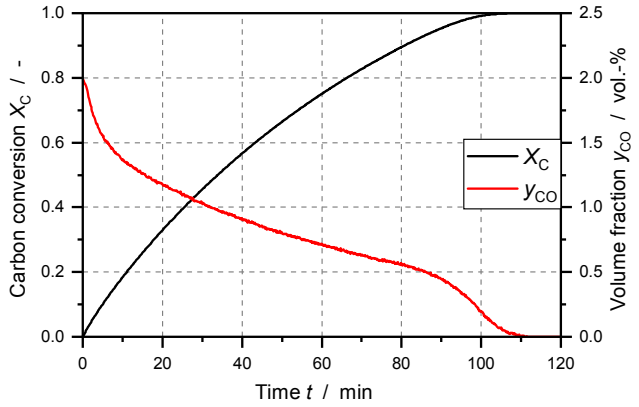

Fig. 1. Carbon conversion and CO volume fraction as a function of time; gasification of WC1600 at 820 °C with 80 vol-% CO_2 and 20 vol-% Ar at atmospheric pressure in the chemisorption analyzer.

$$x_{\text{reactive}} = \left[(n_{\text{CO,total}} - n_{\text{CO,stable}}) + 2(n_{\text{CO}_2\text{,total}} - n_{\text{CO}_2\text{,stable}})\right] \frac{M_C}{m_{C,0}(1 - X_C)} \quad (13)$$

$m_{C,0}$ corresponds to the initial mass of unconverted carbon and X_C to the carbon conversion degree defined in Eq. 10. M_C is the molar mass of carbon.

4. Results and discussion

4.1. Gasification experiment

Fig. 1 shows an example of the experimentally obtained volume fraction of CO in the exhaust gas of the chemisorption analyzer and the calculated carbon conversion degree (Eq. 10) during complete gasification of WC1600 at 820 °C in a mixture of 80 vol-% CO_2 and 20 vol-% Ar. The CO concentration has a maximum value of 2 vol-% at the beginning of the gasification process and decreases steadily. At 90% conversion degree, a steep decrease in CO concentration is observed.

Fig. 2 shows the char conversion rate and the specific conversion rate (calculated according to Eqs. 7 and 1, respectively) as a function of carbon conversion degree for the experiment shown in Fig. 1. The conversion rate decreases steadily over the whole conversion process; in the range Xc = 0.15–0.9 the char conversion rate shows an almost linear decrease. For Xc = 0–0.15 and even more pronounced for Xc > 0.9, a steeper decrease is observed. Specific conversion rate R_m increases slowly until Xc = 0.6 carbon conversion degree is reached. From this point, R_m increases significantly as the remaining carbon

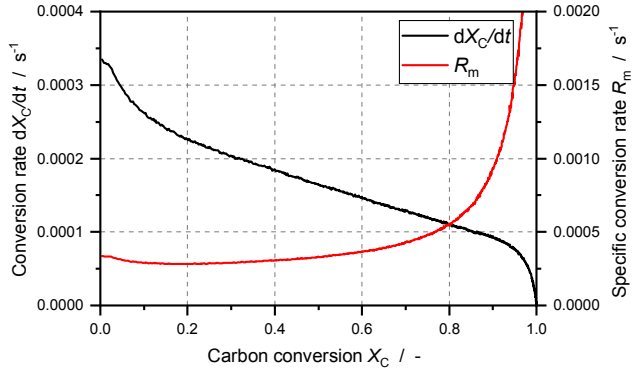

Fig. 2. Conversion rate and specific conversion rate as a function of carbon conversion; gasification of WC1600 at 820 °C with 80 vol-% CO_2 and 20 vol-% Ar at atmospheric pressure in the chemisorption analyzer.

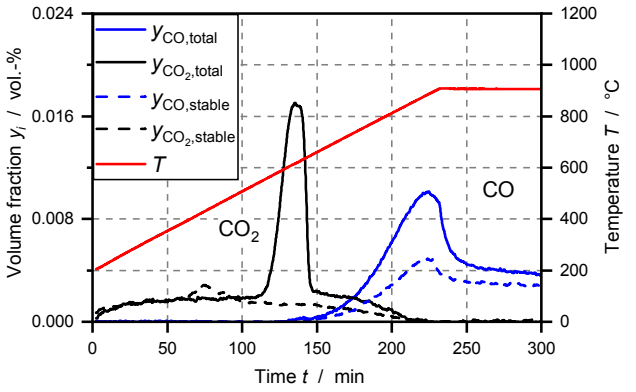

Fig. 3. TPD spectra for the WC1600 char samples gasified up to Xc = 0.75; gasification of WC1600 at 820 °C with 80 vol-% CO_2 and 20 vol-% Ar at atmospheric pressure in the chemisorption analyzer; total and stable complexes desorbed as CO_2 and CO.

mass approaches zero. Reported values for R_m and conversion rate are in the range of literature data [8].

4.2. Temperature-programmed desorption spectra

Fig. 3 shows the desorption spectra of CO and CO_2 for the detection of total and stable surface complexes exemplarily for Xc = 0.75 carbon conversion degree. Similar spectra are obtained for all experiments with different carbon conversion degrees.

As it is assumed by the reaction mechanism proposed by Lizzio et al. [9], total and stable surface complexes must originate from oxygenated carbon atoms on the char surface (also noted as carbon–oxygen intermediates). The release of CO_2 during TPD may arise from the decomposition of lactones between 190 °C and 650 °C [26]. During the TPD experiments carried out, CO_2 desorption starts at 200 °C and is observed over almost the whole temperature range investigated. At 850 °C, complete desorption of CO_2 is achieved. CO_2 shows a similar trend up to 380 °C for both TPD-procedures i.e. total and stable complexes. Above 380 °C, differences in total and stable CO_2 can be observed. Between 380 and 500 °C, the CO_2 signal of the stable complex curve is above the signal of the total complexes, showing a reproducible maximum at 430 °C. Regarding the mechanisms considered, total CO_2 has to be higher than stable CO_2. Extra CO_2 evolution must arise from other reactions where CO_2 is released during the desorption step in the experiments for determination of stable complexes.

Concerning the analysis of total surface complexes, a dominant CO_2 peak between 550 °C and 650 °C is observed. At higher temperatures, the CO_2 signal of the total complexes remains slightly higher than the one of the stable complexes. The difference in the signals may be attributed to the formation of oxygenated complexes on the char surface during gasification, which are released as CO_2.

Regarding the release of CO arising from oxygenated carbon complexes on the char surface, it may originate from the decomposition of carbonyls, ethers and quinones within a temperature range of 700 °C to 980 °C [26]. During the TPD experiments, the CO signal begins to increase at 600 °C with a maximum near 900 °C. CO signals of total and stable complexes show a similar course but with a higher value for the total surface complexes. In the isothermal part of the TPD at 900 °C the CO does not reach baseline level.

The experimental data reported in Fig. 3 some features that do not correspond to the underlying mechanistic model by Lizzio et al. [9]:

(i) CO_2 release around T = 430 °C implies higher amount of stable complexes than total complexes.
(ii) CO signal does not reach baseline line level in the isothermal part of the TPD at 900 °C.

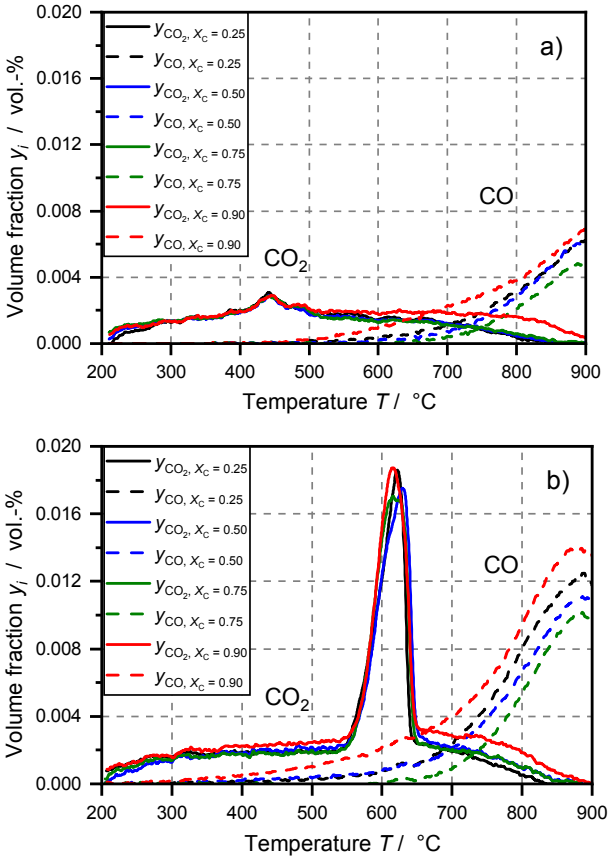

Fig. 4. TPD spectra of CO_2 and CO for the gasification of WC1600 as function of temperature with increasing carbon conversion for (a) stable surface complexes (b) total surface complexes. Gasification of WC1600 at 820 °C with 80 vol-% CO_2 and 20 vol-% Ar at atmospheric pressure in the chemisorption analyzer.

As all our experiments were reproduced, there is no evidence for experimental error. The deviations observed need considerations beyond the mechanistic models for the uncatalyzed heterogeneous char gasification reaction. Part 2 of our research report is focused on the explanation of these effects, which are due to:

(i) Decomposition processes of inherent ash components [47–50].
(ii) Desorption of chemisorbed CO_2 at low temperatures [51].
(iii) CO forming reactions from silica with carbon above 800 °C [52,53].

Basic experiments to show the influence of ash decomposition are given in Section 4.3 of this paper.

4.3. Effect of X_C on desorption spectra

Fig. 4 shows desorption spectra of CO and CO_2 during the determination of total and stable surface complexes for the four carbon conversion levels studied (Xc = 0.25, 0.50, 0.75 and 0.90) as a function of temperature.

The release of CO_2 from stable surface complexes (see Fig. 4 (a)) shows exactly the same profile for all conversion degrees. Only for 90% conversion degree, the high temperature section (650–900 °C) is slightly more pronounced.

The consistency in the profiles may be explained either by:

(i) The same amount of stable C-O complexes during gasification for all carbon conversion degrees observed.
(ii) No formation of stable complexes, CO_2 is released only by ash decomposed during TPD then the same CO_2-release profile irrespective of conversion degree would be expected. If the amount of ash remained constant during gasification, the same quantity must decompose during TPD.

The CO_2 signal of total complexes also shows a similar profile with a peak between 550 °C and 600 °C for all carbon conversion degrees (Fig. 4(b)). A difference can be observed for the sample with Xc = 0.9, where a slightly higher CO_2 signal is detected at T > 700 °C.

Regarding CO, the signals for both stable and total surface complexes decrease slightly from Xc = 0.25 to 0.75 followed by a steep increase for the Xc = 0.9 case. For both stable and total complexes, the signals of the chars at Xc = 0.25, 0.50 and 0.75 conversion have the same form while the signal of the sample for Xc = 0.90 shows an increased release of CO between 500 °C and 850 °C. Possible interpretations for the increased CO signal are:

(i) Enhanced formation of oxygenated surface complexes at Xc = 0.9.
(ii) Decomposition of potassium carbonates at temperatures higher than 700 °C mainly yielding CO [54,55].

In conclusion, CO and CO_2 released during TPD may arise from either desorption of oxygenated surface complexes or ash decomposition reactions. Total and stable complexes released as CO_2 follow the same trend for each conversion degree. Stable complexes show a reproducible peak at approx. 430 °C, which is higher than the CO_2 signal of the total surface complexes. Assuming that this peak cannot arise from desorption of surface complexes, it has to be the result of ash decomposition reactions favored by the experimental procedure applied for the determination of stable complexes. In order to clarify the observed effects, the influence of ash decomposition reactions on the detected signals was investigated by TPD experiments of samples, which were not subjected to gasification and with ash samples resulting from complete gasification of the char.

4.4. Desorption spectra of unconverted and completely gasified char sample

In order to evaluate the influence of ash decomposition reactions on the obtained desorption spectra blank experiments were performed where no surface complexes should have been formed. Here, the procedure for the determination of stable surface complexes was applied. The first experiment was conducted with WC1600 using the same heating program as for the determination of stable complexes but using Ar rather than CO_2 in the gasification segment i.e. there was no production or conversion of carbon-oxygen intermediates. In the second experiment, a complete conversion of the char sample was first carried out in a CO_2 atmosphere. Both sample underwent the standard TPD procedure for stable complex detection, i.e. Ar quench and desorption. The obtained desorption spectra are shown in Fig. 5. For comparison, the desorption spectra of the determination of stable complexes at X_C = 0.25 conversion degree is included in Fig. 5.

The CO_2 signal (see Fig. 5(a)) shows the highest intensity for the unconverted char and decreases with conversion degree. As the unconverted char was not subjected to CO_2 and potential surface complexes must have been desorbed in the heating pretreatment under Ar atmosphere prior to TPD, the CO_2 release cannot arise from the desorption of stable complexes. This result indicates that part of the CO_2 release of the samples submitted to gasification originates from decomposition reactions of ash components inherent in the char. The decrease of the CO_2 signals for increasing carbon conversions may be the result of sintering processes of Ca particles leading to a lower Ca dispersion [56]. Thus, a lower amount of carbon in the immediate vicinity of the Ca particles can react to form $CaCO_3$, which then decomposes during TPD releasing CO_2.

Furthermore, the CO_2 signal of the unconverted char (X_C = 0) shows a different course as compared to the samples gasified up to

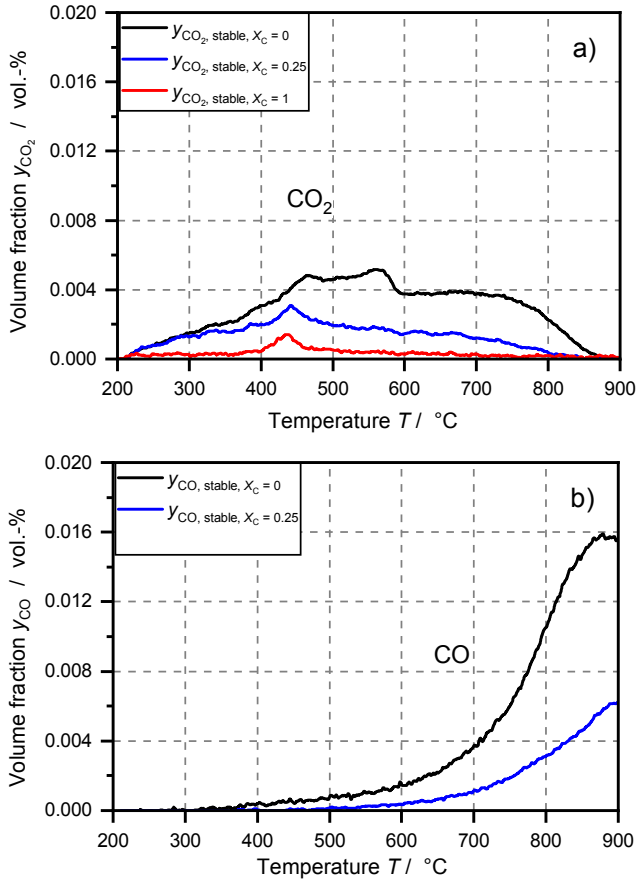

Fig. 5. TPD spectra for the determination of stable complexes of WC1600 for carbon conversion degrees of (a) Xc = 0/0.25/1 for CO_2 and (b) Xc = 0/0.25 CO release.

X_C = 0.25 and X_C = 1 conversion degree. This implies that gaseous CO_2 during gasification exerts an instantaneous effect over the configuration of the sample surface that causes a change either in the configuration, volatilization or inactivation of ash components immediately after changing the atmosphere from Ar to CO_2.

Fig. 5(b) shows the CO release during the determination of stable complexes for the unconverted char (X_C = 0) as well as X_C = 0.25 and X_C = 1 conversion degree. Similar to the CO_2 signal (see Fig. 5(a)), the intensity of CO decreases with increasing carbon conversion degree. However, the course of the CO signal is similar to the signals during determination of total and stable surface complexes (see Fig. 4). The high intensity at X_C = 0 conversion degree may be the result from CO forming reactions of carbon and silica which is present in the quartz wool layers surrounding the sample [52]. The CO signal at X_C = 1 conversion degree was the same one as used as base line and subtracted from the CO signals obtained in all the other TPD experiments, as it was assumed to be a systematic error for the determination of RSA. Thus, no CO signal for X_C = 1 is depicted.

For the calculation of RSA by difference of total and stable surface complexes, the effects of ash decomposition and silica-carbon reactions need to be taken into account. Part 2 of the paper will address this issue in detail.

5. Summary

Based on the carbon conversion mechanism proposed by Lizzio et al. [9] for the gasification of carbon with CO_2, a method for the determination of active sites during gasification of biomass char is presented. The investigations were conducted with beech wood char that underwent secondary pyrolysis in a drop-tube reactor at 1600 °C in order to imitate entrained-flow gasification conditions. This secondary char was partially gasified in CO_2 followed by a temperature-programmed desorption in order to determine total and stable surface complexes as a function of carbon conversion degree. The experiments were conducted in a temperature controlled quartz glass reactor at atmospheric pressure coupled with a mass spectrometer for the detection of desorbed gas species spectra.

The observed desorption spectra of CO and CO_2 during TPD cannot completely be explained by the underlying mechanistic model. Discrepancies arise from the following findings:

- CO_2 release around T = 430 °C implies higher amount of stable complexes than total complexes.
- CO signals of total and stable complexes do not reach baseline line level in the isothermal part of the TPD at T = 900 °C.

The interpretation of the obtained TPD spectra as function of carbon conversion degree are summarized as follows:

- Similar CO_2 signals for total and stable surface complexes are observed for all carbon conversion degrees. This may be explained by either:
  - o the amount of stable C-O does not depend on gasification progress, i.e. is similar for all carbon conversion degrees.
  - o observed CO_2 is released only by ash decomposed during TPD.
- Increased release of CO during the determination of total and stable surface complexes at X_C = 0.9 may originate from:
  - o Enhanced formation of oxygenated surface complexes at Xc = 0.9.
  - o Decomposition of potassium carbonates at temperatures higher than T = 700 °C mainly yielding CO.

The measured CO_2 and CO concentration spectra indicate that the gas species released during TPD may originate from desorption of surface complexes as well as from decomposition of ash components. Both signals must be differentiated in order to determine reactive surface area (RSA) as a function of carbon conversion degree to be implemented in Eq. 1 describing the specific char conversion rate R_m.

Part 2 of the paper addresses the influence of inorganic matter on CO_2 and CO signals obtained from TPD. An activated carbon is impregnated with Ca and K being the main components of beech wood char. A direct relationship between specific conversion rate and the amount of reactive sites is presented.

Declaration of Competing Interest

The authors declare that they have no known competing financial interests or personal relationships that could have appeared to influence the work reported in this paper.

Acknowledgments

The authors gratefully acknowledge the financial support by the Helmholtz Association of German Research Centres (HGF) in the frame of the Helmholtz Virtual Institute for Gasification Technology – HVIGasTech (VH-VI-429) and the German Academic Exchange Service (DAAD) for funding the research visits of Prof. Rincón at KIT.

Appendix A. Supplementary data

Supplementary data to this article can be found online at https://doi.org/10.1016/j.fuel.2019.116726.

References

[1] Kolb T, Aigner M, Kneer R, Müller M, Weber R, Djordjevic N. Tackling the challenges in modelling entrained-flow gasification of low-grade feedstock. J. Energy Inst. 2016;89(4):485–503. https://doi.org/10.1016/j.joei.2015.07.007.

[2] Eberhard M, Santo U, Böning D, Schmid H, Michelfelder B, Zimmerlin B, et al. Der bioliq®-Flugstromvergaser - ein Baustein der Energiewende. Chem. Ing. Tech. 2018;90(1–2):85–98. https://doi.org/10.1002/cite.201700086.

[3] Di Blasi C. Combustion and gasification rates of lignocellulosic chars. Prog. Energy Combust. Sci. 2009;35(2):121–40. https://doi.org/10.1016/j.pecs.2008.08.001.

[4] Guizani C, Jeguirim M, Gadiou R, Escudero Sanz FJ, Salvador S. Biomass char gasification by H_2O, CO_2 and their mixture: evolution of chemical, textural and structural properties of the chars. Energy 2016;112:133–45. https://doi.org/10.1016/j.energy.2016.06.065.

[5] Laurendeau NM. Heterogeneous kinetics of coal char gasification and combustion. Prog. Energy Combust. Sci. 1978;4(4):221–70. https://doi.org/10.1016/0360-1285(78)90008-4.

[6] Radović LR, Walker PL, Jenkins RG. Importance of carbon active sites in the gasification of coal chars. Fuel 1983;62(7):849–56. https://doi.org/10.1016/0016-2361(83)90041-8.

[7] Wölki M. Über die wahre Reaktionsgeschwindigkeit der Vergasung von Biomassepyrolysat mit Kohlendioxid und Wasserdampf. Kassel: Kassel Univ. Press; 2005.

[8] Klose W, Wölki M. On the intrinsic reaction rate of biomass char gasification with carbon dioxide and steam. Fuel 2005;84(7):885–92. https://doi.org/10.1016/j.fuel.2004.11.016.

[9] Lizzio AA, Jiang H, Radovic LR. On the kinetics of carbon (Char) gasification: reconciling models with experiments. Carbon 1990;28(1):7–19. https://doi.org/10.1016/0008-6223(90)90087-F.

[10] Bhatia SK, Perlmutter DD. A random pore model for fluid-solid reactions: I. Isothermal, kinetic control. AIChE J. 1980;26(3):379–86. https://doi.org/10.1002/aic.690260308.

[11] Gómez-Barea A, Leckner B. Modelling of biomass gasification in fluidized bed. Prog. Energy Combust. Sci. 2010;36(4):444–509. https://doi.org/10.1016/j.pecs.2009.12.002.

[12] Duman G, Uddin MA, Yanik J. The effect of char properties on gasification reactivity. Fuel Process. Technol. 2014;118:75–81. https://doi.org/10.1016/j.fuproc.2013.08.006.

[13] Rincón S, Gómez A, Klose W. Gasificación de biomasa residual de procesamiento agroindustrial. kassel university press GmbH; 2011.

[14] Wang G, Zhang J, Shao J, Liu Z, Wang H, Li X, et al. Experimental and modeling studies on CO 2 gasification of biomass chars. Energy 2016;114:143–54. https://doi.org/10.1016/j.energy.2016.08.002.

[15] Struis RPWJ, von Scala C, Stucki S, Prins R. Gasification reactivity of charcoal with CO_2 Part I: Conversion and structural phenomena. Chem. Eng. Sci. 2002;57(17):3581–92. https://doi.org/10.1016/S0009-2509(02)00254-3.

[16] Zhang Y, Ashizawa M, Kajitani S, Miura K. Proposal of a semi-empirical kinetic model to reconcile with gasification reactivity profiles of biomass chars. Fuel 2008;87(4):475–81. https://doi.org/10.1016/j.fuel.2007.04.026.

[17] Fatehi H, Bai X-S. Structural evolution of biomass char and its effect on the gasification rate. Appl. Energy 2017;185:998–1006. https://doi.org/10.1016/j.apenergy.2015.12.093.

[18] Singer SL, Ghoniem AF. An adaptive random pore model for multimodal pore structure evolution with application to char gasification. Energy Fuels 2011;25(4):1423–37. https://doi.org/10.1021/ef101532u.

[19] Gómez A, Klose W, Rincón S. Thermogravimetrische Untersuchungen zur Entwicklung des Porensystems bei der einstufigen Teilvergasung von Biomasse. Chem. Ing. Tech. 2008;80(5):631–9. https://doi.org/10.1002/cite.200700159.

[20] Fu P, Hu S, Xiang J, Yi W, Bai X, Sun L, et al. Evolution of char structure during steam gasification of the chars produced from rapid pyrolysis of rice husk. Bioresour. Technol. 2012;114:691–7. https://doi.org/10.1016/j.biortech.2012.03.072.

[21] Bouraoui Z, Jeguirim M, Guizani C, Limousy L, Dupont C, Gadiou R. Thermogravimetric study on the influence of structural, textural and chemical properties of biomass chars on CO_2 gasification reactivity. Energy 2015;88:703–10. https://doi.org/10.1016/j.energy.2015.05.100.

[22] Laine NR, Vastola FJ, Walker Jr PL. The importance of active surface area in the carbon-oxygen reaction. J. Phys. Chem. 1963;67(10):2030–4.

[23] Radovic LR. Importance of carbon active sites in coal char gasification—8 years later. Carbon 1991;29(6):809–11. https://doi.org/10.1016/0008-6223(91)90020-J.

[24] Brunauer S, Emmett PH, Teller E. Adsorption of gases in multimolecular layers. J. Am. Chem. Soc. 1938;60(2):309–19.

[25] Dubinin MM, Zaverina ED, Radushkevich LV. Sorption and structure of active carbons. I. Adsorption of organic vapors. Zh. Fiz. Khim. 1947;21(3):151–62.

[26] Figueiredo JL, Pereira MFR, Freitas MMA, Órfão JJM. Modification of the surface chemistry of activated carbons. Carbon 1999;37(9):1379–89. https://doi.org/10.1016/S0008-6223(98)00333-9.

[27] Figueiredo JL, Pereira MFR, Freitas MMA, Órfão JJM. Characterization of active sites on carbon catalysts. Ind. Eng. Chem. Res. 2007;46(12):4110–5. https://doi.org/10.1021/ie061071v.

[28] Figueiredo JL, Pereira MFR. The role of surface chemistry in catalysis with carbons. Catal. Today 2010;150(1–2):2–7. https://doi.org/10.1016/j.cattod.2009.04.010.

[29] Szymanski GS, Karpinski Z, Biniak S, Swiatkowski A. The effect of the gradual thermal decomposition of surface oxygen species on the chemical and catalytic properties of oxidized activated carbon. Carbon 2002;40(14):2627–39. https://doi.org/10.1016/S0008-6223(02)00188-4.

[30] Tremblay G, Vastola FJ, Walker PL. Thermal desorption analysis of oxygen surface complexes on carbon. Carbon 1978;16(1):35–9. https://doi.org/10.1016/0008-6223(78)90113-6.

[31] Walker PL, Taylor RL, Ranish JM. An update on the carbon-oxygen reaction. Carbon 1991;29(3):411–21. https://doi.org/10.1016/0008-6223(91)90210-A.

[32] Freund H. Gasification of carbon by CO_2: a transient kinetics experiment. Fuel 1986;65(1):63–6. https://doi.org/10.1016/0016-2361(86)90143-2.

[33] Kyotani T, Yamada H, Yamashita H, Tomita A, Radovic LR. Use of transient kinetics and temperature-programmed desorption to predict carbon/char reactivity: the case of copper-catalyzed gasification of coal char in oxygen. Energy Fuels 1992;6(6):865–7.

[34] Radovic LR, Jiang H, Lizzio AA. A transient kinetics study of char gasification in carbon dioxide and oxygen. Energy Fuels 1991;5(1):68–74.

[35] Kapteijn F, Meijer R, Moulijn JA, Cazorla-Amóros D. On why do different carbons show different gasification rates: a transient isotopic CO_2 gasification study. Carbon 1994;32(7):1223–31. https://doi.org/10.1016/0008-6223(94)90106-6.

[36] Zhu ZB, Furusawa T, Adschiri T, Nozaki T. Characterization of coal char reactivity by the number of active sites during CO2 gasification. Prepr. Pap., Am. Chem. Soc., Div. Fuel Chem; (United States) 1989;34:1.

[37] Lizzio A, Radovic LR. Temperature-programmed desorption studies of coal char gasification. Prepr. Pap. (Am. Chem. Soc., Div. Fuel Chem.) 1989:102–11.

[38] Laine NR, Vastola FJ, Walker Jr PL. The role of the surface complex in the carbon-oxygen reaction. Proceedings of the Fifth Carbon Conference. 1963. p. 211.

[39] Kyotani T, Karasawa S, Tomita A. A TPD study of coal chars in relation to the catalysis of mineral matter. Fuel 1986;65(10):1466–9. https://doi.org/10.1016/0016-2361(86)90125-0.

[40] Ranish JM, Walker PLJR. Desorption turnover numbers for the carbon-oxygen reaction. Prepr. Pap., Am. Chem. Soc., Div. Fuel Chem; (United States) 1987;32:4.

[41] Zoulalian A, Bounaceur R, Dufour A. Kinetic modelling of char gasification by accounting for the evolution of the reactive surface area. Chem. Eng. Sci. 2015;138:281–90. https://doi.org/10.1016/j.ces.2015.07.035.

[42] Morgano MT, Leibold H, Richter F, Seifert H. Screw pyrolysis with integrated sequential hot gas filtration. J. Anal. Appl. Pyrol. 2015;113:216–24. https://doi.org/10.1016/j.jaap.2014.12.019.

[43] Stoesser P, Ruf J, Gupta R, Djordjevic N, Kolb T. Contribution to the understanding of secondary pyrolysis of biomass-based slurry under entrained-flow gasification conditions. Energy Fuels 2016;30(8):6448–57. https://doi.org/10.1021/acs.energyfuels.6b00935.

[44] Stoesser P, Schneider C, Kreitzberg T, Kneer R, Kolb T. On the influence of different experimental systems on measured heterogeneous gasification kinetics. Appl. Energy 2018;211:582–9. https://doi.org/10.1016/j.apenergy.2017.11.037.

[45] Kienitz H, Aulinger F. Massenspektrometrie: VerlagChemie 1968.

[46] Linstrom PJ, Mallard WG. NIST Chemistry WebBook, NIST Standard Reference Database Number 69. Gaithersburg MD: National Institute of Standards and Technology.

[47] Mu J, Perlmutter DD. Thermal decomposition of carbonates, carboxylates, oxalates, acetates, formates, and hydroxides. Thermochim Acta 1981;49(2):207–18. https://doi.org/10.1016/0040-6031(81)80175-X.

[48] McKee DW. Catalytic effects of alkaline earth carbonates in the carbon-carbon dioxide reaction. Fuel 1980;59(5):308–14. https://doi.org/10.1016/0016-2361(80)90215-X.

[49] Rodriguez-Navarro C, Ruiz-Agudo E, Luque A, Rodriguez-Navarro AB, Ortega-Huertas M. Thermal decomposition of calcite: mechanisms of formation and textural evolution of CaO nanocrystals. Am. Mineral. 2009;94(4):578–93. https://doi.org/10.2138/am.2009.3021.

[50] Dollimore D, Tong P, Alexander KS. The kinetic interpretation of the decomposition of calcium carbonate by use of relationships other than the Arrhenius equation. Thermochim Acta 1996;282–283:13–27. https://doi.org/10.1016/0040-6031(95)02810-2.

[51] Linares-Solano A, Almela-Alarcón M, Lecea CS-Md. CO2 chemisorption to characterize calcium catalysts in carbon gasification reactions. J. Catal. 1990;125(2):401–10. https://doi.org/10.1016/0021-9517(90)90313-9.

[52] Hüttinger KJ, Nill JS. A method for the determination of active sites and true activation energies in carbon gasification: (II) Experimental results. Carbon 1990;28(4):457–65. https://doi.org/10.1016/0008-6223(90)90039-2.

[53] Henderson JB, Tant MR. A study of the kinetics of high-temperature carbon-silica reactions in an ablative polymer composite. Polym. Compos. 1983;4(4):233–7. https://doi.org/10.1002/pc.750040408.

[54] Kopyscinski J, Rahman M, Gupta R, Mims CA, Hill JM. K_2CO_3 catalyzed CO_2 gasification of ash-free coal. Interactions of the catalyst with carbon in N_2 and CO_2 atmosphere. Fuel 2014;117:1181–9. https://doi.org/10.1016/j.fuel.2013.07.030.

[55] Lehman RL, Gentry JS, Glumac NG. Thermal stability of potassium carbonate near its melting point. Thermochim Acta 1998;316(1):1–9. https://doi.org/10.1016/S0040-6031(98)00289-5.

[56] Cazorla-Amoros D, Linares-Solano A, Salinas-Martinez de Lecea C, Yamashita H, Kyotani T, Tomita A, et al. XAFS and thermogravimetry study of the sintering of calcium supported on carbon. Energy Fuels 1993;7(1):139–45.

Glossary

Symbol: Description (Unit)
a_{28}: Relative intensity (–)
C_{Cf}: Concentration of active sites of fixed carbon (mol/g)

d: Diameter (m)
$\frac{dX}{dt}$: Conversion rate (1/s)
$I_{m/z}$: Ion current of a mass-to-charge ratio (A)
k: Specific conversion rate constant (g/(mol s))
M: Molar mass (g/mol)
m: Mass (g)
$\dot{n}$: Molar flow (mol/s)
p_{total}: Total system pressure (bar)
R_m: Specific conversion rate. 1/s
S: Calibration sensitivity (A/bar)
T: Temperature (K)
t: Time (S)
X: Conversion degree (-)
y: Volume fraction (vol.-%)

Subscripts

28: Mass-to-charge ratio 28
C: Carbon
f: Fixed carbon
i: Gas species
in: Inlet gas flow
m/z: Mass-to-charge ratio
out: Outlet gas flow

Abbreviations

ad: Air dried
Ar: Argon
ASA: Active surface area
BET: Brunauer-Emmett-Teller
Ca: Calcium
daf: Dry ash free
DR: Dubinin-Radushkevich
EFG: Entrained-flow gasification
MRPM: Modified random pore model
RPM: Random pore model
RSA: Reactive surface area
TK: Transient kinetics
TPD: Temperature-programmed desorption
TSA: Total surface area
TSC: Total surface complexes
UASA: Unoccupied active surface area
vol.: Volume
wt.: Weight

Applied Energy 211 (2018) 582–589

Contents lists available at ScienceDirect

Applied Energy

journal homepage: www.elsevier.com/locate/apenergy

On the influence of different experimental systems on measured heterogeneous gasification kinetics

P. Stoesser[a], C. Schneider[b], T. Kreitzberg[c], R. Kneer[c], T. Kolb[a,b,*]

[a] Karlsruhe Institute of Technology, Institute for Technical Chemistry, ITC-vgt, Hermann-von-Helmholtz-Platz 1, 76344 Eggenstein-Leopoldshafen, Germany
[b] Karlsruhe Institute of Technology, Engler-Bunte-Institute, Fuel Technology, EBI-ceb, Engler-Bunte-Ring 3, 76131 Karlsruhe, Germany
[c] RWTH Aachen, Institute for Heat and Mass Transfer, WSA, Augustinerbach 6, 52056 Aachen, Germany

HIGHLIGHTS

- Investigation of the influence of experimental systems on observed reactivity.
- Comparison of the four most used experimental systems in literature.
- Identification of four fundamentally different reaction domains.
- All setups give valid results if operated in a specific range of process parameters.
- The relevant process conditions for each system are reported.

ARTICLE INFO

Keywords:
Boudouard reaction
Reaction regimes
Thermogravimetric analyzer
Fluidized-bed
Fixed-bed
Drop-tube

ABSTRACT

The objective of this study was to gain further insight into the characteristic behavior of reaction systems for establishment of intrinsic and effective particle gasification kinetics. A wood-derived char was subjected to the carbon dioxide-containing atmospheres of four different reaction systems: a thermogravimetric analyzer (TGA), a fluidized-bed reactor (FBR), a fixed-bed reactor (FFB) and a drop-tube reactor (DTR). All systems contained the same CO_2 partial pressure of 800 mbar at atmospheric pressure. A temperature span from 700 to 1600 °C and residence times from 200 ms to over 8 h were investigated. Reactivities spanning five orders of magnitude were observed. The gasification experiments resulted in the identification of four fundamentally different reaction domains; two were classified as true particle behavior, while the observed reaction rates of the other two domains are mainly dominated by the characteristics of the reaction system applied. The domains were referred to as: chemical control, particle diffusion control, bed diffusion control, and system response control. Within the present work, the occurrence of these reaction domains is discussed in regard to the physical nature of the experiments, and implications towards the measurement of reliable particle kinetics are formulated.

1. Introduction

Utilization of low-grade biogenic and fossil fuels in enhanced gasification processes (e.g. high-pressure entrained-flow gasification, EFG) allows for the production of high-quality synthesis gas which can be converted into liquid fuels and chemicals or used for power and heat generation via Integrated Gasification Combined Cycle (IGCC) systems. In the future, EFG will play an increasingly important role in satisfying the demand for basic chemicals and power [1,2]. In entrained-flow gasification, the fuel is converted via thermal and thermochemical processes such as heat-up, drying and pyrolysis of the solid phase, and the subsequent heterogeneous gasification reactions of the resulting char in a CO_2- and H_2O-rich atmosphere [3]. For the achievement of high cold gas efficiencies, complete char conversion is essential. In this context, the heterogeneous reactions are considered as the rate-limiting step for complete fuel conversion under technical gasification conditions. This motivates the determination of kinetic data for char gasification in diverse laboratory-scale experiments.

A tremendous amount of kinetic data for solid-fuel conversion is available in the literature; most of them established by thermogravimetric analyzers, fixed-bed-, drop-tube- or fluidized-bed reactors. Fig. 1 compares the number of papers reporting the use of different systems for measurements of kinetic data in terms of CO_2 gasification. The chart, summarizing experiments for coal and biomass gasification, is based on two review papers by Irfan et al. [4] and Di Blasi [5]. The majority of experiments which were considered in this study (100 in

* Corresponding author at: Karlsruhe Institute of Technology, Institute for Technical Chemistry, ITC-vgt, Hermann-von-Helmholtz-Platz 1, 76344 Eggenstein-Leopoldshafen, Germany.
E-mail address: Thomas.kolb@kit.edu (T. Kolb).

https://doi.org/10.1016/j.apenergy.2017.11.037
Received 22 December 2016; Received in revised form 22 October 2017; Accepted 4 November 2017

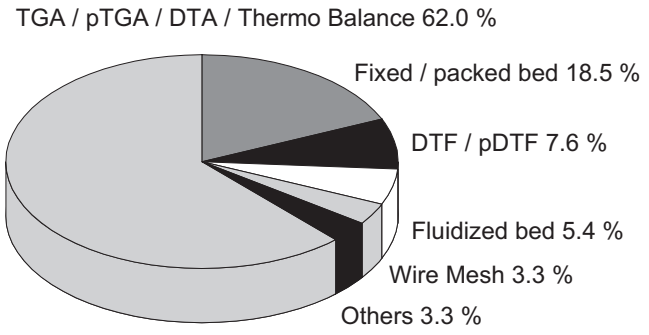

Fig. 1. Use of different reaction systems for determination of gasification kinetics with CO_2 (based on [4,5]).

total), have been carried out in thermogravimetric systems (62.0%), followed by fixed-bed reactors (18.5%), and drop-tube furnaces (7.6%). Recent publications with contributions to the field of reaction kinetics of gasification reinforce this trend. Numerous research groups use thermogravimetric analyzers to determine reaction kinetic [6–12] while some favor fixed-bed reactors [13–15]. Furthermore, kinetic data is also determined with drop-tube furnaces [11,16] and fluidized-bed reactors [17]. However, the latter two reaction systems are still less frequent. Combined, these four systems claim well over 90 % of the results generated to date in terms of heterogeneous gasification kinetics.

The heterogeneous gasification kinetics derived in literature are commonly the reactions of solid carbon with CO_2 and H_2O, referred to as Boudouard- and heterogeneous water-gas reaction. Heterogeneous reactions are characterized by the occurrence of reactant fluxes through interface surfaces. In the case of the Boudouard reaction, the reaction takes place at the solid surface. The steps in heterogeneous conversion of porous solid carbon with CO_2 are: (1) reactant film diffusion, (2) reactant pore diffusion, (3) reactant adsorption, (4) chemical reaction, (5) product desorption, (6) product pore diffusion, (7) product film diffusion. Since most of these steps depend on partial pressures and temperature, applying considerably different reaction conditions can result in different reaction behaviors. The observed reaction rate of a porous carbon particle can be depicted in an Arrhenius plot (Fig. 2). It describes the temperature dependency of the reaction rate and was divided into three regimes where the reaction is governed by different mechanisms by Rossberg and Wicke [18].

In regime I, the reaction rate is solely affected by the before-mentioned reaction steps 3–5 because of constant reactant gas concentrations throughout the particle. This regime is often referred to as chemically controlled or quasi-homogeneous regime. Here, increasing the temperature leads to higher reaction rates with a slope proportional to

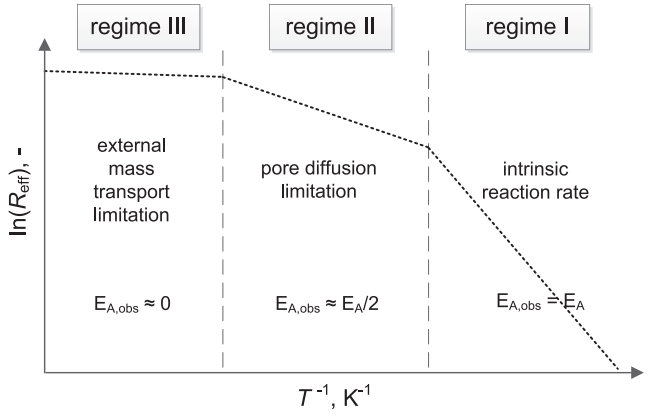

Fig. 2. The three reaction regimes representing the change in reaction rate of porous carbon with temperature according to Rossberg and Wicke [18].

the intrinsic activation energy E_A. At a certain temperature, due to the exponential nature of the reaction rate, mass transport becomes noticeable. In the resulting regime II, the dominant factor limiting the reaction rate is diffusion of the reactant gas through the porous particle. Here, the observed activation energy is approximately $E_A/2$ [18]. At even higher temperatures (regime III), the resistance of the external mass transport (film diffusion) is the predominant process affecting the reaction rate. Due to the weak temperature dependency of the diffusive mass transport in contrast to the chemical reaction, the observed reaction rate increases only slightly with temperature [19].

A transition to lower observed activation energies at high temperature is reported by authors applying all different kinds of reactors [6,13,14,20–24]. In most cases, there are explanations or suggestions given by the authors. While some authors conclude that in their case, this is caused by a transition to another regime according to Rossberg and Wicke [18], others suspect fuel-specific effects, such as ash transformation, thermal annealing and structural effects, causing the observed reactivity to deviate from the intrinsic trend at high temperature.

Since the majority of experiments reported in the literature use either different reaction systems or different fuels and are hence not directly comparable, our goal was to conduct a systematic investigation of the influence of the four most used reaction systems on observed reactivity. Special care had to be taken to guarantee, that the fuel did not undergo changes in composition, structure or reactivity on its way from feeding to the gasification segments of the different reaction systems. In a previous study [25], it was shown that a differing change of fuel properties in different systems prior to the gasification segment can be largely suppressed by an appropriate thermal pre-treatment of the fuel. If the resulting chars contain low amounts of volatiles, their physical and chemical properties will most likely not be changed significantly during in-situ pyrolysis in the reaction system used for kinetic studies and therefore should result in similar reactivity values. Consequently, at first a wood char was produced at high temperature and low residence time. This char was then conditioned and characterized. Subsequently, the Boudouard reactivity was determined in four different reaction systems: a thermogravimetric analyzer (TGA), representing a non-flow through fixed-bed, a fluidized-bed reactor (FBR), representing a stirred-tank, a free-fall fixed bed reactor (FFB), representing a flow-through fixed-bed, and a drop-tube reactor (DTR), representing an entrained-flow reactor. All systems used the same CO_2 partial pressure at atmospheric conditions (80% CO_2, 1 bar). A total temperature span of 700–1600 °C and residence times from 200 ms to over 8 h were investigated. Reactivities spanning five orders of magnitude were observed. Detailed results and conclusions concerning the importance of interpreting results from the reaction systems applied are discussed in the course of this work.

2. Materials and methods

A systematic investigation was performed using the same high-temperature wood char, four different reaction systems, and the equal CO_2 partial pressure of 800 mbar in N_2/Ar at atmospheric pressure. Following the generation of char, the setup of the reaction systems as well as the corresponding data analysis are explained.

2.1. Fuel characterization

The char used in this study was derived from a bark-less soft wood. Wood chips were chopped to sizes of approximately 1 mm and fed to a screw-pyrolysis reactor, described in the literature [26,27]. A temperature of 500 °C was chosen. The solids had a residence time of 5 min and were cooled in an inert, tar-free atmosphere. The produced char was further milled and sieved to particle sizes between 50 and 150 µm. To produce a high-temperature char with low volatile content as the one inside the hot flame zone of an entrained-flow gasifier, the char was

Table 1
Proximate analysis data of WC1600.

Water-content wt.%	Ash-content wt.%, wf	Volatile-content wt.%, wf	HHV MJ/kg, wf
2.6	6.4	1.1	31.7

Table 2
Ultimate analysis data of WC1600.

C m%, waf	H	O (diff.)	N m%, wf	S	Cl
98.7	< 0.1	< 0.1	0.86	0.34	0.30

Table 3
Ash composition analysis data of WC1600.

Na_2O m%	K_2O	MgO	CaO	Fe_2O_3	Al_2O_3	SiO_2
0.5	9.1	1.6	30.1	2.6	3.5	25.8

Table 4
Morphological data of WC1600.

Specific surface area m^2/g	Skeletal density g/cm^3	Hg-intrusion porosity vol.%
62.1	2.03	55.3

then subjected to the hot inert atmosphere of the drop-tube furnace which was one of the reactors further used to study kinetics and is described below. The temperature was 1600 °C, the residence time 200 ms. The produced char was cooled in an inert, tar-free atmosphere. It was then sieved to a 50–100 µm and a 100–150 µm fraction. Both char fractions were dried for 24 h at 105 °C in air. Both chemical and physical data of the resulting high-temperature char, further referred to as WC1600, can be found in Tables 1–4.

The high temperature char WC1600 consisted of almost pure carbon with a very low content of volatiles and an ash content of around 6 wt. %. The minor amounts of catalytically active metals such as Ca and K can be regarded as inert within this study. The literature reports strong deactivation of both metals at high temperatures by either evaporation or sintering [5,28]. In the case of potassium it is also known that remaining amounts are only detectable since K is bound by silicates, which protects them from volatilization but also renders them inert in terms of catalysis [28].

To prove the important assumption that the chemical and physical structure of the high-temperature char is not changed during introduction into the applied reaction systems, WC1600 was once again pyrolyzed, collected, and characterized. Two char samples were therefore pyrolyzed one more time in a) the drop-tube reactor, applying the same pyrolysis conditions (1600 °C, 200 ms), and b) the TGA used in this study, applying longer residence times (1200 °C, 30 min). In both cases, no notable change in fuel properties was observed, except a decrease in specific surface area of less than 10% in the case of the drop-tube pyrolysis. It can therefore be concluded, that the WC1600 char was highly unlikely to behave differently in the reaction systems studies and that the effects observed can be to a great extent attributed to the systems themselves.

2.2. Fluidized bed reactor (FBR)

The experimental setup of the fluidized bed reactor consists of three major components: A gas feeding system with thermal mass flow controllers, a small-scale fluidized bed reactor, and a Fourier transform infrared (FTIR) spectrometer for product gas analysis. Small batches (~5 mg) of pulverized solid fuel are supplied to a fluidized bed consisting of alumina (Al_2O_3) particles while simultaneously analyzing the exhaust gas.

The fluidized bed reactor consists of two coaxial ceramic pipes mounted in a stainless-steel reactor head. The fluidizing gas is fed in through the reactor head and flows downwards through the annular gap between the two pipes to the bottom of the reactor. The reactant gas (in this case CO_2 in N_2) enters the inner reactor pipe (d = 55 mm) through a porous distributor plate made from sintered silica glass and fluidizes the bed. The distributor plate creates a homogeneous inflow and is impermeable to the Al_2O_3 bed particles. Further details on homogeneity, mixing and fluidization conditions of the bed can be found in [29,17]. The feed gas flow for the present experiments has been approximately 100 l(STP)/h. The bed temperature is measured separately by an S-type thermocouple placed in a ceramic shielding inside the fluidized bed. Gaseous reaction products are fed into the FTIR-gas analyzer sampling at 0.56 Hz. A system schematic can be found in the supplementary material section.

The establishment of kinetic parameters is based on the dimensionless carbon conversion X, which represents the mass fraction of reacted solid carbon. This analysis procedure has been described in detail by the authors in [29,17] and is briefly described in the following:

The carbon conversion curve can be derived experimentally (X_{exp}) from the temporal concentrations of the reactor exhaust gas species discharging the reacted carbon from the reactor - namely CO. It can also be computed by a model approach (X_{mod}), which can be interpreted using the characteristic reaction rate r_0 as an adjustable fit-parameter. In this case, the uniform reaction model (Eq. (2)) has been adopted for the calculation of X_{mod}. The calculated conversion X_{exp} of solid carbon C_s into gaseous products is based on a carbon-species balance of the feed gas stream and the stream leaving the reactor, yielding the following expressions:

$$\frac{\partial X_{exp}}{\partial t} = \frac{1}{2}\frac{M_C}{m_C}\left(\frac{\dot{m}_{N_2}}{M_{N_2}} + \frac{\dot{m}_{CO_2}}{M_{CO_2}}\right)\frac{y_{CO}(t)}{1-0.5y_{CO}(t)} \quad (1)$$

In Eq. (1), $\dot{m}$ indicates the feed gas mass flow, divided into the individual species N_2 and CO_2. The variable $y_{CO}(t)$ denotes the time dependent gas concentration of the reaction product CO, measured by FTIR. The experimental carbon conversion curves X_{exp} are calculated by numerical integration over time of Eq. (1). The characteristic reaction rate is then determined by iteratively fitting the model prediction X_{mod} to the experimental data X_{exp}. A conversion-over-time graph including the fit can be found in the supplementary material section.

2.3. Thermogravimetric analyzer (TGA)

A high-pressure thermogravimetric analyzer (Rubotherm GmbH, Germany) is used to perform reaction kinetic measurements at low temperatures. The apparatus allows for a total pressure of up to 40 bar. The reactor and the balance system are coupled by a magnetic suspension and are mechanically not connected to each other. It allows for a wide range of different gas atmospheres (CO_2, CO, H_2O, H_2, O_2, Ar and N_2). The heating elements which are located in the pressure vessel are protected by a constant purge flow of Argon. Maximum temperatures of 1200 °C are applicable. The balance has a resolution of 10 µg. A system schematic can be found in the supplementary material section.

In the following experiments, a total gas flow of 200 ml(STP)/min was set. A sample mass of approx. 2 ± 0.1 mg was placed in a ceramic crucible (inner diameter 16 mm; height of wall 10 mm). After evacuating the pressure vessel to ensure an oxygen free atmosphere, the reaction chamber was purged with argon. The fuel samples were heated up at a constant heating rate of 20 K/min to reaction temperature

followed by 20 min holding time to ensure stable conditions. The samples were then gasified in CO_2/Ar atmosphere until complete conversion of the fuel was reached. Reaction temperatures between 700 and 1200 °C were set. Temperature and mass loss of the sample due to gasification were measured continuously.

$$X(t) = \frac{m(t) - m_0}{m_0 - m_\infty} = 1 - \exp\{-Rt\} \quad (2)$$

The conversion was derived by a mass balance (Eq. (2)), where m_0 is the initial sample mass before reaction and m_∞ the final sample mass after reaction. Reactivity values were derived using the TGA signal in the rage of 20 and 50 % carbon conversion. In this range, the measured carbon conversion was fitted with the uniform conversion model applying a least-squares approach to derive a characteristic value for R. A conversion-over-time graph including the fit can be found in the supplementary material section.

2.4. Free-fall fixed bed reactor (FFB)

The free-fall fixed-bed reactor consists of a heated alumina pipe with a length of 1 m and an inner diameter of 20 mm which is heated by 3 separate external electrical heaters, each 200 mm in length. The pipe is filled with multiple layers of inert material up to the middle of the heated length of the reactor. Coarse alumina beads are used in combination with small layers of increasingly finer broken alumina bits. At the top, a small layer of coarse alumina beads follows, in which sample fuel can settle and still be widely distributed. This design also avoids a drastic increase in pressure drop from ash built-up, although total deposited ash amounts are usually very low, the amount of runs not high and the influence of ash deposition therefore negligible. This was also confirmed by reproduction measurements at the end of each measurement campaign which always yielded identical results compared to measurements conducted at the beginning of the campaigns. Fuel is entered from a feeder inside an inert housing at the top of the reaction tube. The feeder allows fuel amounts of approximately 1.5–200 mg per run. Dosed fuel is then transported to the top of the fixed bed via inert gas-flow (approximately 1/4 of the total gas flow) inside a coaxial alumina pipe which ends approximately 30 mm above the top of the fixed-bed material. The rest of the gas which also contains a fraction of reactant was introduced inside the annular gap between reaction pipe and dosing pipe. At the end of the reaction tube, the gas is cooled, filtered, and analysed by standard analytics. CO and CO_2 are recorded over time. The pressure inside the reaction zone is controlled with a vacuum pump to be at atmospheric level. Deviations were less than ± 5 mbar. A system schematic can be found in the supplementary material section.

In the experiments conducted, a total gas-flow of 1 l(STP)/min of a 80 vol.% CO_2 in N_2 mixture was used. Nitrogen was introduced through the fuel dosing pipe. Carbon dioxide was introduced through the annular gap. The dried fuel was purged with nitrogen inside the dosing-chamber. It was then fed in amounts of 1.8–14.4 mg, depending on the reaction time and hence the resulting CO concentration peaks. For each reactor setting validation runs were made to ensure that the amount of fuel was not influencing the results. Reaction temperatures between 800 and 1200 °C were applied. Measurements at each temperature were repeated at least 3 times; deviations were negligible.

Conversion and reactivity values were derived identically to Section 2.2. A conversion-over-time graph including the fit can be found in the supplementary material section.

2.5. Method: Drop-tube reactor (DTR)

The drop-tube reactor consists of a heated alumina pipe with a length of 2.1 m and an inner diameter of 20 mm which is heated by 3 separate external electrical heaters (top and bottom 200 mm, middle 900 mm in length). An isothermal zone of close to 900 mm is achieved for all practical conditions. A Schenck Process Pure Feed DP-4 inside a closed housing is used to continuously feed the fuel to the reactor. The dosed mass over time curve is recorded. Due to very low fuel mass flow rates of 1 g/min and below, deviations of approximately 10% have to be accepted with this setup. This, however, has no effect on the reaction since all experiments are conducted with a high CO_2 stoichiometric factor of at least 10. Similar to Section 2.4, a coaxial alumina dosing pipe is used to feed inert gas and fuel to the reactor. It ends at the beginning of the isothermal zone. There, the gas is mixed with the reaction gas from the annular gap between dosing pipe and reaction pipe. At the outlet, the hot reaction gas is cooled by an inert gas quench to temperatures below 400 °C. The gas then passes through a gas cyclone in which the particles are collected at temperatures between 300 and 350 °C. The gas is then cooled and filtered by a candle filter to collect fines to protect the downstream pressure valves. Gas samples are continuously taken from the hot exit of the reaction tube prior to the gas quench. Sample gases are filtered, cooled, and analyzed by standard analytics and a Varian micro-GC cp-4900. Stationary CO_2- and CO-concentrations are recorded. Two electrically controlled valves regulate the reactor pressure to be at 5 mbar above atmospheric pressure; deviations were less than ± 1 mbar. A system schematic can be found in the supplementary material section.

The dried and flushed fuel was introduced to the reactor with mass flow rates between 0.5 and 1.0 g/min. The total gas-flow rate was 12–20 l(STP)/min, depending on the reaction temperature. It was adjusted to achieve uniform reaction times of 200 ms inside the isothermal zone. A constant flow of 2.0 l(STP)/min Ar was used as tracer for the analytics. The rest of the inert gas consisted of N_2. The heating zones were adjusted to result in isothermal zones of 900–1600 °C. Both analytics (standard and micro-GC) recorded comparable values. For data analysis, the micro-GC data was chosen.

Reactivity values were gained by fitting Eq. (3), similarly to the data analysis of the free-fall fixed- bed- and fluidized-bed reactors.

$$X = \frac{0.5 y_{CO} \dot{V}^{STP}_{gas,in}}{(1 - 0.5 y_{CO}) V^{STP}} \frac{M_C}{\dot{m}_{in} x_C} = 1 - \exp\{-R\tau\} \quad (3)$$

However, unlike the in-stationary Eq. (2), here, the carbon balance of feed and product gas results in a steady-state carbon conversion.

3. Results and discussion

In this chapter the results of the systematic investigation are shown and discussed. First, Sections 3.1-3.4 discuss the results of the four studied reaction systems individually. Subsequently, in Section 3.5, a discussion follows, comparing the reaction systems applied in regard to their ability to generate data for reliable reaction kinetics and in regard to their limitations.

3.1. Fluidized bed reactor (FBR)

The observed reactivities in the range of $1 * 10^{-3}$ to $4.7 * 10^{-2}\,s^{-1}$ established in the fluidized-bed reactor (Fig. 3) suggest a reaction domain under chemical control, referred to as regime I by Rossberg and Wicke [18]. The resulting activation energy is 232 kJ/mol. At around $4.7 * 10^{-2}\,s^{-1}$, the observed reactivity approaches constant values and yields an activation energy of approximately 0 kJ/mol. In this system, the rate is determined by the recorded concentration of product gas (CO) over time. On its way from the reaction zone to the analytical device CO is unavoidably backmixed in pipes, bends and other volumes such as filters and coolers, resulting in a broader signal distribution with reduced peak height. Even if an infinitely fast change of conditions occurs, any technical system, such as a chemical reactor, will show a finite response signal according to the pulse response theory. Since nothing faster than the pulse response can be observed in a system, the observed reactivity is approaching constant values even when the

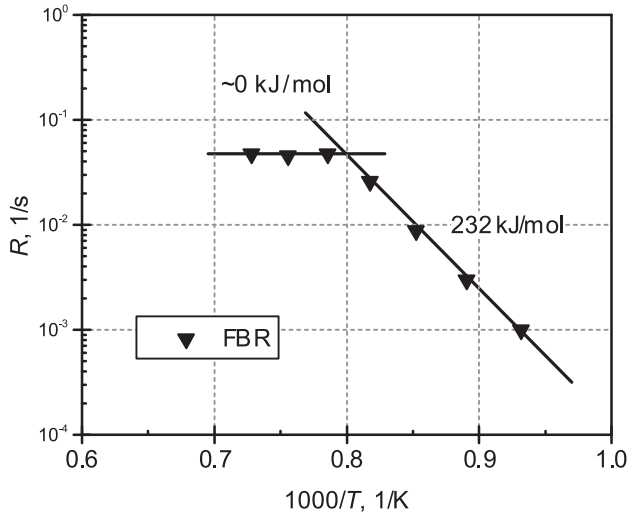

Fig. 3. Arrhenius plot of the fluidized-bed reactor (FBR) results, WC1600, d_p 100–150 µm, 80 vol.% CO_2 in N_2.

reaction temperature increases and the reaction rate in the reaction zone increases further. This is also demonstrated by the reciprocal value of R which roughly corresponded to the system pulse response. In this case 1/R was 21 s – fitting the system response time.

We refer to this reaction domain as response control. It does not represent true particle behavior and is not a regime according to Rossberg and Wicke [18] but is solely a characteristic of the reaction system applied. It is inherent to any type of non-steady system with external gas analytics operating at high reaction rates.

3.2. Thermogravimetric analyzer (TGA)

The TGA measurements resulted in reactivities under chemical control from $3.5 * 10^{-5}$ to $3.0 * 10^{-3}$ s^{-1} (Fig. 4). The activation energy was derived as 238 kJ/mol. In the range of $3.0 * 10^{-3}$ to $2.0 * 10^{-2}$ s^{-1}, a second domain established. Here, the observed activation energy dropped to 129 kJ/mol. While in TGA up to the top of the crucible, convection and diffusion are responsible for mass transfer, inside the free space of the crucible and inside the particle bed, diffusion is the only mechanism of mass transport [21]. Due to increasing reaction rates at elevated temperature, either a local depletion of the reactant CO_2 or a local accumulation of the product gas CO, causing

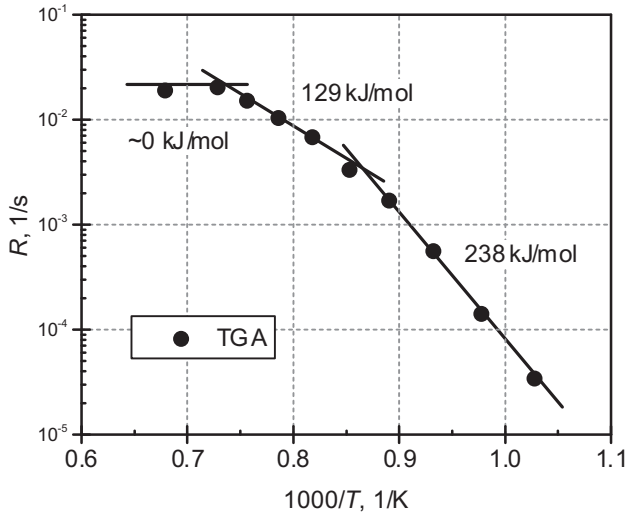

Fig. 4. Arrhenius plot of the thermogravimetric analyzer (TGA) results, WC1600, d_p 50–100 µm, 80 vol.% CO_2 in Ar.

inhibition of the Boudouard reaction are likely. Own numeric simulations and experimental studies varying the crucible geometry showed that the height of the crucible had no influence on the observed reactivity. Solely the change of crucible bottom surface area, changing the bed height, had a major impact on the observed reactivity. Additionally, increasing the sample mass with unchanged geometry drastically decreases the observed reactivity, clearly showing, that the reaction is influenced by non-ideal system behavior. In return, a particle monolayer can greatly reduce the non-ideality of TG measurements at high reactivities [30]. Nonetheless, the measurements of the present work were conducted with a monolayer and still show signs of mass transfer limitations at elevated temperatures. Possible explanations might be that on one hand, an ideal distribution of particles resulting in a true monolayer is usually not trivial to achieve. On the other hand, the influence of the particle-wall contact can become considerate at high reactivity. Since this cannot be prevented in a crucible, even a monolayer will show signs of limitation caused by non-ideal diffusion of reactant- and product gases.

We refer to this reaction domain as bed diffusion control. It does not represent true particle behavior and is not a regime according to Rossberg and Wicke [18] but is solely a characteristic of the reaction system and experimental method applied. It is inherent to any type of system applying particle beds operating at high reaction rates.

At even higher temperatures, with reactivities of $2.0 * 10^{-2}\,s^{-1}$, the observed activation energy drastically decreases to around 0 kJ/mol. We attribute this behavior to response control. This reaction domain is not a regime according to Rossberg and Wicke [18]. It is caused by the non-steady nature of an isothermal TG experiment, in which the gas flow is switched from inert to reactant at a certain point in time [30]. Backmixing throughout the system volume causes a steady rise of the CO_2 concentration at the sample rather than a spontaneous change from inert to set-point. This is usually indicated by a slow increase of the carbon conversion rate at the beginning of the reaction, in contrast to the ideal conversion over time curve, which has its highest gradient at the beginning. When the fuel reactivity reaches a critical level, reactant gas is rapidly consumed as it reaches the particle bed. Here, the observed conversion rates represent the rate of CO_2 built-up inside the crucible, rather than the intrinsic fuel reactivity. In this case, the reciprocal value of the response controlled reactivity yielded around 50 s. This duration can be seen as the system-specific response time.

3.3. Free-fall fixed bed reactor (FFB)

Fig. 5 shows the results of the free-fall fixed-bed reactor. In the range of $6.6 * 10^{-4}$ to $3.0 * 10^{-2}\,s^{-1}$, a reaction domain under chemical control is observed. The activation energy in this domain is 236 kJ/mol. In the reactivity range of $3.0 * 10^{-2}$ to $7.5 * 10^{-2}\,s^{-1}$, a decrease in activation energy occurs. Even though the experimental data does not fit very well in this range, an activation energy of approximately 125 kJ/mol can be derived. As in other fixed bed reactors, in the FFB a particle bed can develop during fuel injection. Although the aim was to distribute the fuel as widely as possible, the possibility of local regions in which particles are stacked or deposited in small pockets where the gas flow was minimal cannot be excluded. Also, as discussed in Section 3.2, the particle-wall influence cannot be excluded in this system. As a result, a local depletion of reactant gas (CO_2) or local accumulation of inhibiting product (CO) reduces the observed reactivity. Similar to Section 3.2, we refer to this reaction domain as bed diffusion control.

At reactivities of approximately $7.5 * 10^{-2}$ s^{-1}, the activation energy drops to 0 kJ/mol. Similar to Section 3.1, this can be explained by response control caused by backmixing of product gas (CO) while it is transported from the reaction zone to the analytic device. Here, the reciprocal value of the highest observable reactivity equaled 13 s, which was also the response time of the system applied.

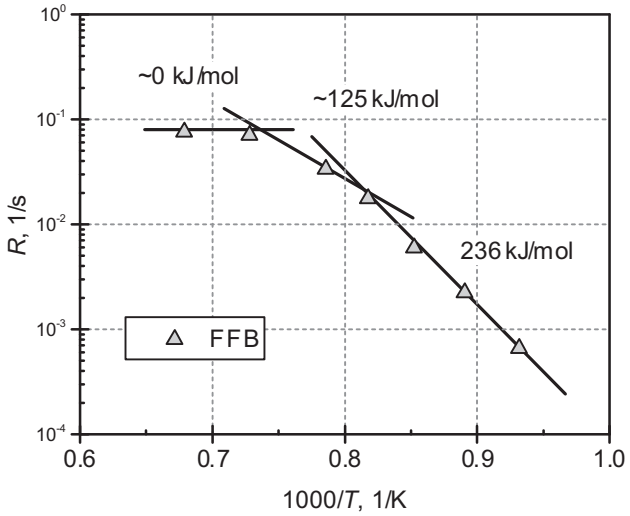

Fig. 5. Arrhenius plot of the free-fall fixed-bed reactor (FFB) results, WC1600, d_p 50–100 µm, 80 vol.% CO_2 in N_2.

3.4. Drop-tube reactor (DTR)

Similar to the other systems, the DTR was also able to operate in the reaction domain under chemical control, representing regime I according to Rossberg and Wicke [18]. The domain was found in the reactivity range of $7.3 * 10^{-3}$ to $7.2 * 10^{-2}\,s^{-1}$ (Fig. 6). Here, an activation energy of 229 kJ/mol was observed. However, the drop-tube reactor was operated at its lowest conversion limit in this case. Since lower temperatures demand for exponentially higher residence time, conversion levels obtained in a stationary system with given low residence time quickly drop to marginal levels. In return, a stationary operation is not limited by response control. Here, carbon conversion is stationary over time while the time characteristic of a system only applies to changes over time. This was the main reason for the DTR to be able to observe the Boudouard reaction under particle diffusion control in the reactivity range of $7.2 * 10^{-2}$ to $4.5\,s^{-1}$. Particle diffusion control is the regime in which the internal mass transfer of reactant gas inside the porous fuel is limiting the overall reaction rate, as described in Section 1. It is referred to by Rossberg and Wicke [18] as regime II and represents true particle behavior. The observed activation energy in this domain was around 147 kJ/mol.

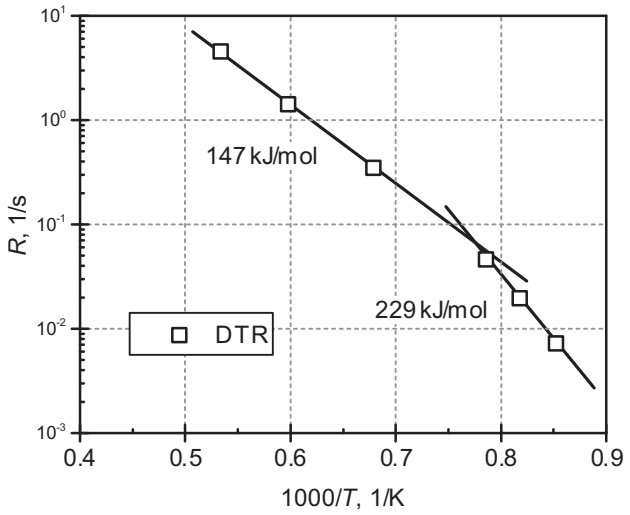

Fig. 6. Arrhenius plot of the drop-tube reactor (DTR) results, WC1600, d_p 50–100 µm, 80 vol.% CO_2 in N_2/Ar.

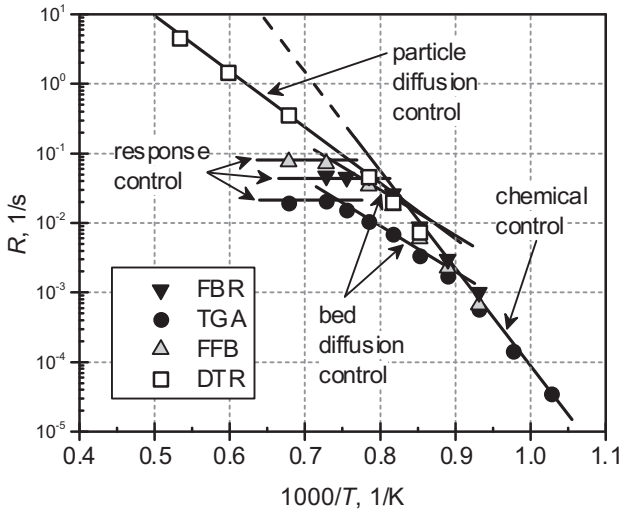

Fig. 7. Arrhenius plot of all experiments conducted.

3.5. System comparison

A complete overview of all experiments conducted is given by Fig. 7. From the individual results of the four systems studied, a total of ten reaction domains were identified. These belong to four principal domains referred to as chemical-, particle diffusion-, bed diffusion- and response control. Only two of these four domains (chemical- and particle diffusion control) can be considered valid for intrinsic or effective kinetics since they represent true particle behavior according to regimes I and II, defined by Rossberg and Wicke [18]. The other two (bed diffusion- and response control) do not represent true particle behavior. These reaction domains can be seen as system characteristics, caused by the operational method rather than by true particle behavior. It is important to note that the absolute values obtained in this study are only valid for the fuel, conditions, and systems applied. The positions of the reaction domains are likely to change when using different settings, but the principle will remain the same. This should be kept in mind when comparing the four systems as follows.

First, all methods were able to determine intrinsic reaction data under chemical control. This is quite astounding, considering different gas-solid contacts, different in-situ temperature histories, different analytic devices and mathematical models for data processing, steady and non-steady operation, vastly different temperatures and reaction timescales and different particle size in the case of the FBR. Nonetheless, the activation energies obtained all fall into a narrow band of 229–238 kJ/mol.

Despite the fact that the DTR was able to establish kinetics under chemical control, due to its inherent low residence time it was limited towards low temperatures due to decreasing conversion levels. On the other hand, it was not restricted by response control due to its stationary operation and was therefore capable of generating data for determining effective kinetics under particle diffusion control at high temperatures. Here, all other methods were limited by response control, due to their non-steady operation. In both, FBR and FFB, the fuel dosing leads to a rapid change in gas concentrations over time, while in TGA, the switch from inert to reactant gas represents a significant pulse. These two experimental methods result in the same effect: Response control by backmixing of either product gas (CO) on its way to the analytics or reactant gas (CO_2) on its way to the reaction zone. These phenomena should not be confused with the reaction regime III according to Rossberg and Wicke [18] (Section 2) which is likely to occur only at extreme temperatures in the case of heterogeneous gasification reactions [31].

Besides response control, the fixed-bed reactors (TGA and FFB) additionally showed bed diffusion control, in which either a depletion

of reactant gas (CO_2) or accumulation of product gas (CO) inhibits the reaction. The FFB with its flow-through particle bed was able to reach intrinsic reactivities 10 times higher than the TGA before being limited by bed diffusion control. This suggests that a forced flow through the particle bed greatly enhances gas transport. In the reactor with close-to-ideal mass transfer (FBR), the domain under chemical control could be further extended to higher temperatures resulting in approximately 50 % higher achievable reactivities before system limitations occurred.

The system limitations, which result in the occurrence of bed diffusion- and response control, can be greatly reduced by appropriate measures. However, despite shifting and changing the extent of the reaction domains, the occurrence of the mentioned limitations cannot be completely excluded. Regardless, all types of systems studied in this publication contributed to valuable information. Each system possesses a range of validity in which it should be operated, depending on the system setup, fuel, and conditions applied.

4. Summary and conclusions

A systematic investigation comparing four different reaction systems for the determination of heterogeneous gasification kinetics was conducted. The reactors chosen were a fluidized-bed reactor (FBR), a thermogravimetric analyzer (TGA), a free-fall fixed-bed reactor (FFB), and a drop-tube reactor (DTR). These four reactor types represent over 90% of applied reaction systems for heterogeneous gasification studies in literature. A wood char pyrolysed at high temperature was produced as fuel for the investigation. Numerous pre-studies showed that this high-temperature fuel was not changed by the reaction systems prior to reaching the point in time where the gasification reaction takes place. The Boudouard reaction was selected as heterogeneous reaction. The same CO_2 partial pressure of 800 mbar at a total pressure of 1 bar was chosen for all systems. Temperatures and residence times correlated to the specific capabilities of the reaction systems. Individual experimental methods and mathematical interpretation of results of each system were used. Observed reactivities, determined by all four reaction systems, were plotted in an Arrhenius diagram, and discussed.

A total of four different principal reaction domains were identified: Chemical control, particle diffusion control, bed diffusion control, and system response control. While the former two represent true particle behavior, the latter two can be seen as system characteristics. All systems were able to operate under chemical control determining intrinsic reactivities. The derived activation energy in this reaction domain lies within a narrow band of 229–238 kJ/mol. At high temperature, the stationary DTR was able to determine effective reactivities under particle diffusion control while the non-steady systems (FBR, TGA, FFB) showed response control. The fixed-bed reactors (TGA and FFB) showed additional reaction domains under bed diffusion control.

The positions and extent of the four reaction domains observed can vary, depending on the system setup, fuel specification, and operating conditions applied. However, their occurrence in principle cannot be prevented.

Based on the findings of this work, further conclusions concerning the measurement of reliable kinetics are:

- Reaction systems for the measurement of kinetic data of heterogeneous gasification reactions may show true particle behavior as well as system characteristics.
- Applying different systems may give new insights into the true particle reaction behavior over a wide range of conditions.
- Relying on a single method requires special care to avoid misinterpretations of the results.

Acknowledgments

The authors gratefully acknowledge the financial support by the Deutsche Forschungsgemeinschaft (DFG) (121384/22-1) and the Helmholtz Association of German Research Centres (HGF) in the frame of the Helmholtz Virtual Institute for Gasification Technology – HVIGasTech (VH-VI-429).

Appendix A. Supplementary material

Supplementary data associated with this article can be found, in the online version, at http://dx.doi.org/10.1016/j.apenergy.2017.11.037.

References

[1] Dahmen N, Abeln J, Eberhard M, Kolb T, Leibold H, Sauer J, et al. The bioliq process for producing synthetic transportation fuels. WIREs Energy Environ 2016. http://dx.doi.org/10.1002/wene.236.
[2] Higman C. State of the gasification industry-the updated worldwide gasification database. In: Gasification Technologies Conference, Colorado Springs, 16th October; 2013.
[3] Kolb T, Aigner M, Kneer R, Müller M, Weber R, Djordjevic N. Tackling the challenges in modelling entrained-flow gasification of low-grade feedstock. J Energy Inst 2016;89(4):485–503. http://dx.doi.org/10.1016/j.joei.2015.07.007.
[4] Irfan MF, Usman MR, Kusakabe K. Coal gasification in CO_2 atmosphere and its kinetics since 1948: a brief review. Energy 2011;36(1):12–40. http://dx.doi.org/10.1016/j.energy.2010.10.034.
[5] Di Blasi C. Combustion and gasification rates of lignocellulosic chars. Prog Energy Combust Sci 2009;35(2):121–40. http://dx.doi.org/10.1016/j.pecs.2008.08.001.
[6] Lin L, Strand M. Investigation of the intrinsic CO_2 gasification kinetics of biomass char at medium to high temperatures. Appl Energy 2013;109:220–8. http://dx.doi.org/10.1016/j.apenergy.2013.04.027.
[7] Huo W, Zhou Z, Wang F, Wang Y, Yu G. Experimental study of pore diffusion effect on char gasification with CO_2 and steam. Fuel 2014;131:59–65.
[8] Malekshahian M, Hill JM. Kinetic analysis of CO_2 gasification of petroleum coke at high pressures. Energy Fuels 2011;25(9):4043–8. http://dx.doi.org/10.1021/ef2009259.
[9] Liu L, Liu Q, Cao Y, Pan W-P. The isothermal studies of char-CO_2 gasification using the high-pressure thermo-gravimetric method. J Therm Anal Calorim 2015;120(3):1877–82. http://dx.doi.org/10.1007/s10973-015-4476-5.
[10] Roberts DG, Harris DJ. High-pressure char gasification kinetics: CO inhibition of the C-CO_2 reaction. Energy Fuels 2012;26(1):176–84. http://dx.doi.org/10.1021/ef201174k.
[11] Tremel A, Spliethoff H. Gasification kinetics during entrained flow gasification – Part II: intrinsic char reaction rate and surface area development. Fuel 2013;107:653–61. http://dx.doi.org/10.1016/j.fuel.2012.10.053.
[12] Zhang R, Wang QH, Luo ZY, Fang MX, Cen KF. Coal char gasification in the mixture of H_2O, CO_2, H_2, and CO under pressured conditions. Energy Fuels 2014;28(2):832–9. http://dx.doi.org/10.1021/ef4018527.
[13] Zhou L, Zhang G, Schurz M, Steffen K, Meyer B. Kinetic study on CO_2 gasification of brown coal and biomass chars: reaction order. Fuel 2016;173:311–9. http://dx.doi.org/10.1016/j.fuel.2016.01.042.
[14] Ren L, Yang J, Gao F, Yan J. Laboratory study on gasification reactivity of coals and petcokes in CO_2/steam at high temperatures. Energy Fuels 2013;27(9):5054–68. http://dx.doi.org/10.1021/ef400373y.
[15] Li C, Zhao J, Fang Y, Wang Y. Effect of pressure on gasification reactivity of three Chinese coals with different ranks. Front Chem Eng China 2010;4(4):385–93. http://dx.doi.org/10.1007/s11705-010-0501-1.
[16] Matsumoto K, Takeno K, Ichinose T, Ogi T, Nakanishi M. Gasification reaction kinetics on biomass char obtained as a by-product of gasification in an entrained-flow gasifier with steam and oxygen at 900–1000 °C. Fuel 2009;88(3):519–27. http://dx.doi.org/10.1016/j.fuel.2008.09.022.
[17] Kreitzberg T, Haustein HD, Gövert B, Kneer R. Investigation of gasification reaction of pulverized char under N_2/CO_2 atmosphere in a small-scale fluidized bed reactor. J Energy Res Technol 2016;138(4):42207. http://dx.doi.org/10.1115/1.4032791.
[18] Rossberg M, Wicke E. Transportvorgänge und Oberflächenreaktionen bei der Verbrennung graphitischen Kohlenstoffs. Chemie Ingenieur Technik 1956;28(3):181–9. http://dx.doi.org/10.1002/cite.330280309.
[19] Huo W, Zhou Z, Wang F, Yu G. Mechanism analysis and experimental verification of pore diffusion on coke and coal char gasification with 5CO26. Chem Eng J 2014;244:227–33. http://dx.doi.org/10.1016/j.cej.2014.01.069.
[20] Roberts DG, Hodge EM, Harris DJ, Stubington JF. Kinetics of char gasification with CO_2 under regime II conditions: effects of temperature, reactant, and total pressure. Energy Fuels 2010;24(10):5300–8. http://dx.doi.org/10.1021/ef100980h.
[21] Nowak B, Karlström O, Backman P, Brink A, Zevenhoven M, Voglsam S, et al. Mass transfer limitation in thermogravimetry of biomass gasification. J Therm Anal Calorim 2013;111(1):183–92. http://dx.doi.org/10.1007/s10973-012-2400-9.
[22] Kajitani S, Hara S, Matsuda H. Gasification rate analysis of coal char with a pressurized drop tube furnace. Fuel 2002;81(5):539–46. http://dx.doi.org/10.1016/S0016-2361(01)00149-1.
[23] Liu H, Zhu H, Kaneko M, Kato S, Kojima T. High-temperature gasification reactivity with steam of coal chars derived under various pyrolysis conditions in a fluidized bed. Energy Fuels 2010;24(1):68–75. http://dx.doi.org/10.1021/ef9004994.
[24] Ollero P, Serrera A, Arjona R, Alcantarilla S. Diffusional effects in TGA gasification experiments for kinetic determination. Fuel 2002;81(15):1989–2000. http://dx.doi.org/10.1016/S0016-2361(02)00126-6.

[25] Mueller A, Haustein HD, Stoesser P, Kreitzberg T, Kneer R, Kolb T. Gasification kinetics of biomass- and fossil-based fuels: comparison study using fluidized bed and thermogravimetric analysis. Energy Fuels 2015;29(10):6717–23. http://dx.doi.org/10.1021/acs.energyfuels.5b01123.
[26] Stoesser P, Ruf J, Gupta R, Djordjevic N, Kolb T. Contribution to the understanding of secondary pyrolysis of biomass-based slurry under entrained-flow gasification conditions. Energy Fuels 2016;30(8):6448–57. http://dx.doi.org/10.1021/acs.energyfuels.6b00935.
[27] Morgano MT, Leibold H, Richter F, Seifert H. Screw pyrolysis with integrated sequential hot gas filtration. J Anal Appl Pyrol 2015;113:216–24. http://dx.doi.org/10.1016/j.jaap.2014.12.019.
[28] Bai J, Li W, Li C-Z, Bai Z, Li B. Influences of minerals transformation on the reactivity of high temperature char gasification. Fuel Process Technol 2010;91(4):404–9. http://dx.doi.org/10.1016/j.fuproc.2009.05.017.
[29] Haustein HD, Kreitzberg T, Gövert B, Massmeyer A, Kneer R. Establishment of kinetic parameters of particle reaction from a well-stirred fluidized bed reactor. Fuel 2015;158:263–9. http://dx.doi.org/10.1016/j.fuel.2015.05.038.
[30] Gomez A, Mahinpey N. Kinetic study of coal steam and CO_2 gasification: a new method to reduce interparticle diffusion. Fuel 2015;148:160–7. http://dx.doi.org/10.1016/j.fuel.2015.01.071.
[31] Roberts DG, Harris DJ. Char gasification with O_2 CO_2 and H_2O: effects of pressure on intrinsic reaction kinetics. Energy Fuels 2000;14(2):483–9. http://dx.doi.org/10.1021/ef9901894.

Glossary

Symbol: Description (Unit)
E_A*:* Activation energy (kJ/mol)
M*:* Molar weight (g/mol)
m*:* Mass (g)
$\dot{m}$*:* Mass flow (g/s)
V*:* Molar volume (l/mol)
$\dot{V}$*:* Volumetric flow (l/s)
R*:* Reactivity (1/s)
T*:* Temperature (K)
t*:* Time (s)
X*:* Conversion degree (–)
y*:* Molar fraction (–)
x*:* Mass fraction (–)
τ*:* Residence time (s)
Subscripts: Description
eff: Effective
exp: Experimental
mod: Model
obs: Observed
0: Initial
∞*:* Final
Abbreviations: Description
DTR: Drop-tube reactor
EFG: Entrained-flow gasification
FBR: Fluidized-bed reactor
FFB: Free-fall fixed-bed reactor
KIT: Karlsruhe Institute of Technology
RWTH: Rheinisch-Westfälische Technische Hochschule
STP: Standard temperature and pressure
TGA: Thermogravimetric analyzer
vol.: Volume
waf: Water and ash free
wf: Water free
wt.: Weight